Air Force Institute of Technology
AFIT Scholar

3-21-2019

Flow Behavior in Radial Rotating Detonation Engines

Scott A. Boller

Follow this and additional works at: https://scholar.afit.edu/etd

Part of the Heat Transfer, Combustion Commons, Other Aerospace Engineering Commons, and the Propulsion and Power Commons

Flow Behavior in Radial Rotating Detonation
Engines

THESIS

Scott A. Boller, Captain, USAF

AFIT-ENY-MS-19-M-205

AFIT-ENY-MS-19-M-205

FLOW BEHAVIOR IN RADIAL ROTATING DETONATION ENGINES

THESIS

Presented to the Faculty

Department of Aeronautics and Astronautics

Graduate School of Engineering and Management

Air Force Institute of Technology

Air University

Air Education and Training Command

in Partial Fulfillment of the Requirements for the

Degree of Master of Science in Aeronautical Engineering

Scott A. Boller, B.S.

Captain, USAF

March 2019

AFIT-ENY-MS-19-M-205

FLOW BEHAVIOR IN RADIAL ROTATING DETONATION ENGINES

Scott A. Boller, B.S.
Captain, USAF

Committee Membership:

Dr. Marc D. Polanka, PhD
Chairman

Dr. Frederick R. Schauer, PhD
Member

Maj Levi M. Thomas, PhD
Member

AFIT-ENY-MS-19-M-205

Abstract

Recent progress has been made in demonstrating Radial Rotating Detonation Engine (RRDE) technology for use in a compact Auxiliary Power Unit with a rapid response time. Investigation of RRDEs also suggests an increase in stable operating range, which is hypothesized to be due to the additional degree of freedom in the radial direction which the detonation wave can propagate. This investigation seeks to determine if the detonation wave is in fact changing its radial location. High speed photography was used to capture chemiluminescence of the detonation wave within the channel to examine its radial location, which was found to vary based on operating condition. One wave detonations tended to operate near the inner radius of the channel near the nozzle, whereas two wave detonations tended to operate near the outer radius of the channel. Normalized detonation velocity was found to increase with detonation radius, from $< 0.5v_{D,CJ}$ near the inner radius to $0.7v_{D,CJ}$ near the outer edge. Additionally, the power generation of the RRDE integrated with a radial inflow turbocharger was examined over a broad range of reactant mass flow rates, equivalence ratios, and compressor and turbine back pressures. The addition of a flow straightening device was shown to have no appreciable impact on performance. Compressor back pressure was found to increase performance but placed the compressor near its surge line, whereas turbine back pressure decreased performance.

iv

Acknowledgements

When men are arrived at the goal, they should not turn back - Plutarch

The author would like to thank the entire D-Bay team. Special thanks to Joshua Codoni for help with setting up and operating the high speed camera, Curtis Rice for assistance with setting up the research facilities and instrumentation, Riley Huff for device operation support, Matthew Fotia and Andrew Naples for their research guidance, Fred Schauer for allowing the author to use his laboratory, and Marc Polanka for his constant efforts.

The author would also like to thank his lovely wife for her support and patience in this endeavor, as well as his family and friends for their love and support.

Scott A. Boller

Table of Contents

List of Figures

List of Tables

List of Abbreviations

Abbreviation		Page

List of Symbols

Symbol		Page

FLOW BEHAVIOR IN RADIAL ROTATING DETONATION ENGINES

I. Introduction

1.1   The Rotating Detonation Engine

The Rotating Detonation Engine (RDE) is an advanced combustion concept utilizing a detonative combustion mode in lieu of the deflagrative mode typical of traditional combustors. In theory detonation combustion offers several advantages over deflagration combustion.

Detonations are a supersonic combustion processes coupled with a shock wave, where the increase in pressure and temperature from the shock wave provides the conditions necessary to initiate combustion. The combustion in turn releases energy to sustain the shock wave, producing a self-sustaining Detonation Wave (DW). Because the reactants are pressurized by a shock prior to combustion, although the pressure declines during the combustion event itself, there is a net pressure gain, producing Pressure Gain Combustion (PGC). The availability of this additional pressure allows for more propulsive or work potential from the flow relative to constant pressure combustion.

An additional benefit of the supersonic detonation cycle is that combustion occurs without offering the reacting gases time to expand, so combustion is essentially isochoric. Isochoric heat addition produces a lower entropy increase than isobaric heat addition, resulting in a greater potential for the flow to produce work in the form of thrust or shaft power. This is illustrated in the $P - v$ diagram in Figure 1. As compared to the Brayton cycle that approximates the flow through a conventional jet
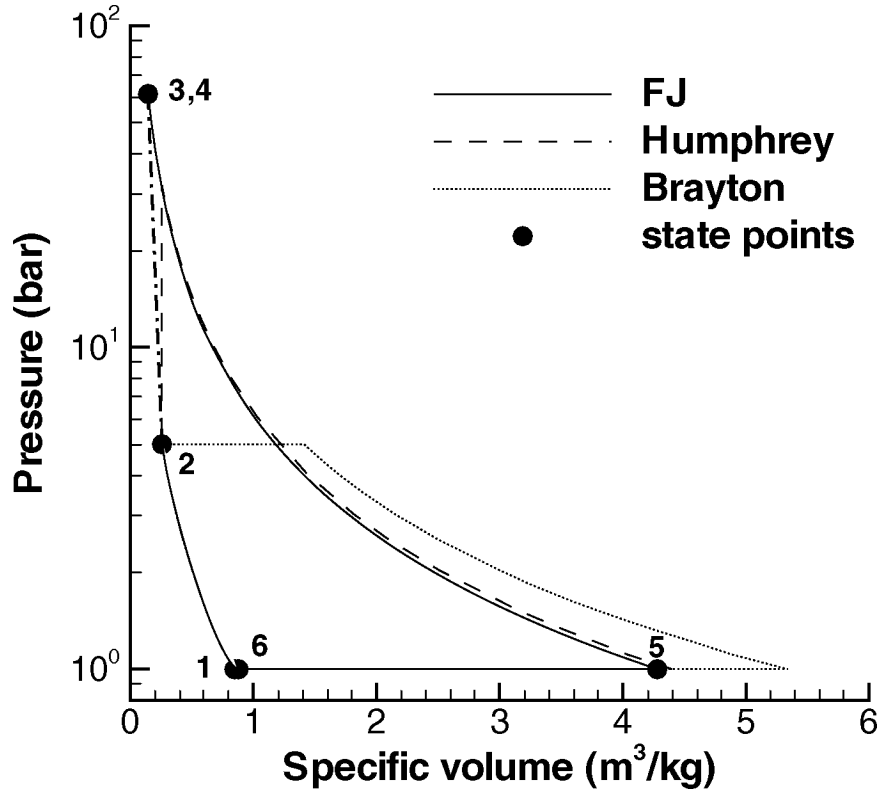
Figure 1. Thermodynamic cycle comparison for stoichiometric propane-air combustion at an initial condition of $T_1 = 300K$ and $P_1 = 1BAR$ from Wintenberger and Shepherd, 2006 [1].

engine or gas turbine engine, the Humphrey and Fickett-Jacobs (FJ) cycles approximate the thermodynamic cycle of a detonation. The pressure rise after State 2 in the Detonation cycles produces additional area under the curve relative to the constant pressure heat addition Brayton cycle, which is available to be converted into work.

RDEs provide an architecture for the DW to exist in, allowing them to take advantage of the thermodynamic benefits of the detonation cycle. Axial RDEs form an annular channel with reactants injected at one end as shown in Figure 2 (a). The DW propagates azimuthally through the reactants at the base of the channel perpendicular to the axial mean flow direction on $\mathcal{O}(km/s)$ as shown in Figure 3, with the channel walls providing confinement to enable the detonation to persist. Reactants are continuously refreshed at the base of the channel, providing a new
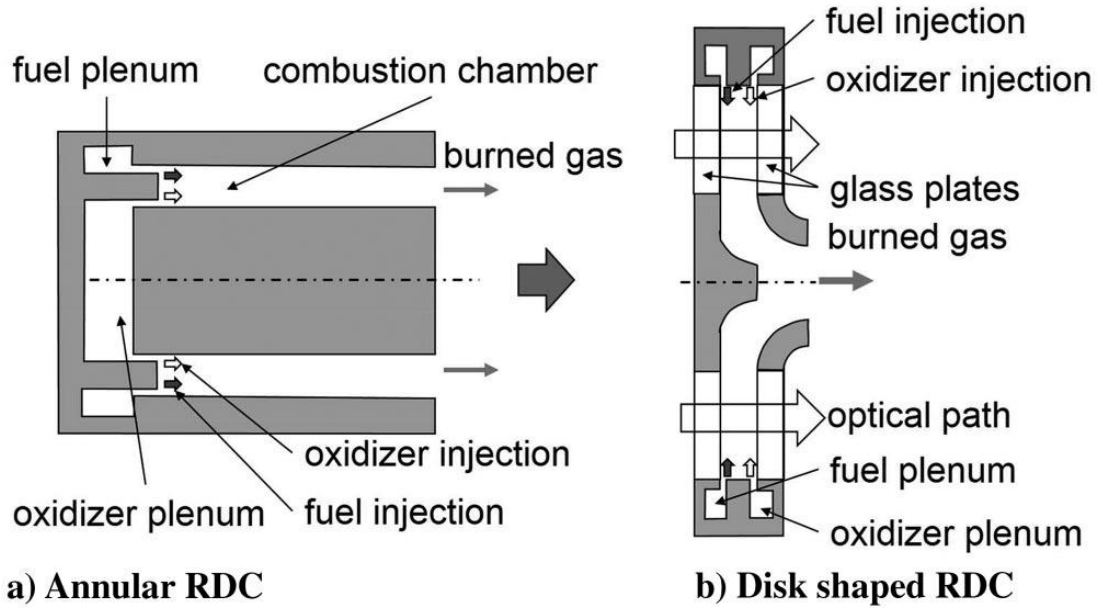
Figure 2. Comparison of RDE cross sections for a) Annular (Axial) RDEs and b) Disk shaped (radial) RDEs from Nakagami et al. [2].

supply of reactants for the DW to propagate into in subsequent cycles. Following detonation the products are exhausted axially.

Radial Rotating Detonation Engines (RRDEs) provide a similar architecture to Axial RDEs. Detonable reactants are continuously injected at the outer radius as shown in Figure 2 (b), and are confined by the upper and lower surfaces of the channel. The DW continuously propagates azimuthally around the channel, consuming the reactants which continue to flow along a radially inward mean flow direction. The products of the detonation are then turned axially and exhausted.

While thermodynamic considerations drove much of the initial interest in detonation combustion, RDEs also offer an additional advantage over many other combustors in that the flow time and therefore distance required for combustion is much shorter due to the detonative heat release. Whereas many traditional combustors used in jet engines are on the order of half a meter in length, RRDEs can be made a fraction of that length, reducing the overall size and weight of the powerplant. This rapid energy release behavior is beneficial in general, but especially so in high speed flows

3
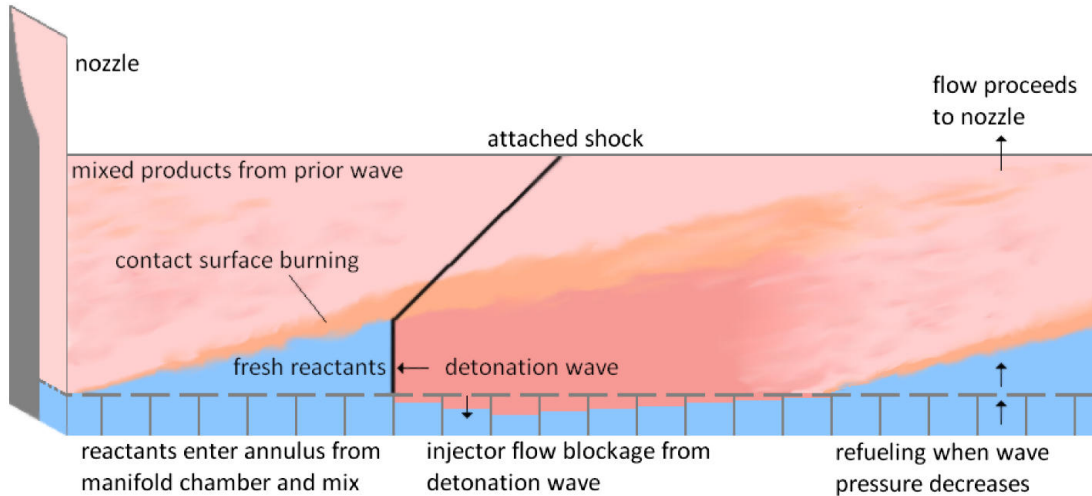
Figure 3. Sketch of the flowfield structure within an Axial RDE from Lu and Braun [3].

where residence time in the combustor is minimal, such as the engines of high speed aircraft, and in high power density powerplants where volume must be minimized, such as aircraft Auxiliary Power Units (APUs) where both space and weight are at a premium.

Power density and rapid response are desirable characteristics for a power source such as an APU. However, these are a necessity for a power generation source designed to be used on aircraft with a high output power requirement. The potential to use the RRDE as a compact power generation source with rapid response is therefore especially attractive for application to Directed Energy (DE) weapon systems (i.e. lasers, microwaves) on small tactical aircraft where space comes at a premium, such as the DE systems shown in the concept art in Figure 4. DE systems are under consideration for integration into both large AFSOC airframes such as the AC-130 gunship and smaller tactical fighters, with a target weight of 680 kg (1500 lbs) for the entire fielded system [4].

The design of laser systems at AFRL/RD has transitioned away from the heavy, bulky chemical DE systems that use and produce hazardous chemicals towards lighter

Figure 4. Directed energy target engagement concept art [4].

and compact electrically powered solid-state DE systems that have few moving parts [4]. The power of the DE systems under consideration ranges from $30kW$ for smaller defensive systems and technology demonstrators [4] to $1MW$ for anti-ballistic missile systems [5]. In concept, these DE weapons will be operated on battery power, with the batteries recharged by an onboard power source fueled by the aircraft's primary fuel supply, allowing rapid firing of the DE system[4]. This power may have traditionally been provided by the aircraft engine, but an RDE APU could serve as an alternative.

A generic schematic of an electrical generator is shown in Figure 5. Air flows through the compressor and into the combustor, where it is mixed with fuel and ignited, releasing thermal energy. The products are then expanded through the turbine, which powers the compressor and the electrical generator. In theory, an RDE could replace the traditional combustor in this system resulting in a more compact and thermally efficient system, increasing the power density relative to traditional

5
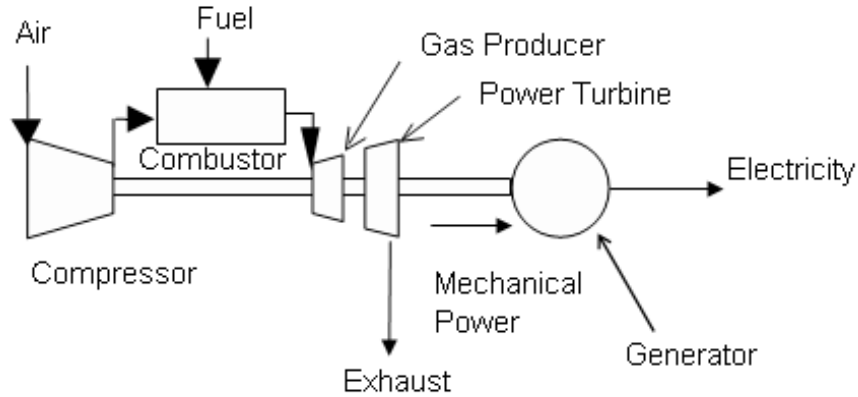
Figure 5. Schematic of a gas turbine engine driven generator [6].

combustor technology.

1.2 Objectives

The present work strives to achieve several objectives. To better understand the response of different parameters on the ideal wave speed, a theoretical experiment was conducted using detonation solving software. Specifically, the sensitivity of the ideal $H_2 - Air$ Chapman–Jouguet (CJ) DW speeds to variations in initial pressure and temperature, and equivalence ratio was conducted, as well as an investigation to the response of the DW to re-ingesting products into the reactant mixture.

Previous research suggested that the radial location of the DW within the detonation channel, or detonation radius r_D, of an RRDE was variable, a behavior which was not confirmed due to lack of visual access to the detonation channel itself. To better understand the behavior of the DW in the RRDE configuration, visual confirmation of the DW location was required.

In addition to the detonation visualization effort, investigation of the test article reconfigured with a radial inflow turbine in place of the nozzle was desired. Specifically, the response of the RRDE's power output to the addition of a post-turbine flow straightening collar and restrictions in the compressor and turbine exit area was

6

required. The effect of DW propagation direction on the output power, as well as the repeatability of the turbine's power from test to test and day to day were also considered.

In support of developing this system to work on operationally relevant fuels, investigation of the RRDE's ignition characteristics and response to gaseous hydrocarbon fuels Ethylene (C_2H_4) and air was required. Specifically, whether the RRDE would work as-configured, and if so the operating conditions over which operation was possible, were desired.

1.3 Thesis Description

To aid the research effort the relevant literature related to the subject was consulted, as described in Chapter II. A review of combustion chemistry and DW fundamentals was first conducted. Combustor types were then reviewed, with an emphasis on detonation-based propulsion systems such as axial and radial RDEs. To better understand the use and limitations the equipment used in testing, a review of literature regarding commonly used detonation flow instrumentation was conducted. Because this technology must eventually be fielded, a review of literature related to RDE design considerations and auxiliary power units was performed.

Chapter III describes the experimental setup used to accomplish the research objectives. The baseline experimental device used in previous research as well as its instrumentation is first described, followed by a description of the test facilities used, including the reactant measurement systems. Modifications required for this effort are then described. The metallic channel plate was replaced with a visually transparent channel plate through which chemiluminescence of the DWs could be observed using a high speed camera. This enabled tracking of the DW radial location, which could be used to determine the mean radius at which the detonation propagates ($\bar{r_D}$). Having

a radial measurement as well as a frequency measurement, the mean velocity of the DWs could then be calculated and compared with the CJ wave speed to evaluate the performance of the DW. Because turbomachinery integration testing was required, the turbomachinery setup and related instrumentation is then described. In particular, the new flow straightening device and compressor and turbine back pressure methods are described. Finally, modifications required to begin gaseous hydrocarbon testing are described.

Chapter IV discusses the results of this research. The chapter begins with a discussion on the anticipated wave speeds based on equilibrium CJ theory. Because instrumentation is unable to determine the precise conditions within the high temperature detonation channel, the sensitivity of the DW speed at a known global equivalence ratio to changes in pressure, temperature, and reingestion of post-detonation products is first examined. The modes observed, flowfield behavior, and general trends observed are described first, and confirm that the DW radius varies, with one wave operation generally occurring at a lower radius and two wave operation at a larger radius. However, the operating modes varied from those observed in previous research, and the introduction of polycarbonate reactants to the detonation flow field were shown to be a possible contributer.

Testing with an integrated turbocharger demonstrated that increasing compressor back pressure generally increased shaft power, whereas increasing turbine back pressure decreased shaft power. Adding the flow straightening collar had a negligible impact on performance. Data was collected at a similar condition over multiple days to establish repeatability of the configuration, which showed power fell along curve within $\pm 5\%$. Preliminary indications also showed that DW direction had minimal to no impact on performance.

Finally, a preliminary investigation into operability with gaseous hydrocarbon

fuels is discussed. Although detonation was not initiated, only a limited range of tests was conducted due to time constraints, and the operating point was based on previous work with a different fuel which may not be directly transferable. Several potential methods which could enhance operability are also discussed.

II. Literature Review

To develop detonation-based combustor technology used in Rotating Detonation Engines (RDEs), a review of the necessary fundamentals and research to date is necessary. As its name implies, the RDE uses a Detonation Wave (DW) for combustion, as opposed to the deflagration mode employed in most current combustors. This has the potential to provide a more thermally efficient combustion cycle, reducing the fuel consumption required for a given output power. This chapter begins with a discussion of fundamentals of combustion chemistry in Section 2.1. Combustion topics specific to detonations are discussed in Section 2.2. Discussion and comparison of deflagration combustors and relevant detonation combustor types is provided in Section 2.3. Flow measurement and control techniques commonly used in detonation flows are examined in Section 2.4. A discussion of some RDE design considerations is presented in Section 2.5 Finally, Section 2.6 provides an overview of Auxiliary Power Unit fundamentals with RDE integration in mind.

2.1 Combustion Chemistry

Combustion is the chemical process by which fuel and oxidizer (reactants) are converted into spent products and thermal energy. This process occurs at the subatomic level, with electron bonds in the reactant atoms/molecules breaking and recombining to intermediate ions and eventually products. Stoichiometry is the condition where there is a precisely balanced combination of fuel and oxidizer such that combustion converts all reactants into products. For a simple $H_2 - O_2$ reaction, this can be determined on a molar basis by examining the chemical reaction $aH_2 + bO_2 \Rightarrow cH_2O$. Arbitrarily setting $b = 1$ for convenience, the chemical equation is stoichiometrically balanced if $a = c = 2$, giving $2H_2 + O_2 \Rightarrow 2H_2O$.

Because many practical combustion devices use air as the oxidizer instead of pure oxygen, this process must be modified to account for the constituents and relative proportions of air. As a first approximation, air can be considered to be a mixture of 21% diatomic oxygen (O_2) and 79% diatomic nitrogen (N_2) by volume. For this case, an arbitrary hydrocarbon burning in air can have its stoichiometric coefficients determined using [7]

$$C_xH_y + a(O_2 + 3.76N_2) \Rightarrow xCO_2 + (y/2)H_2O + 3.76aN_2 \tag{1}$$
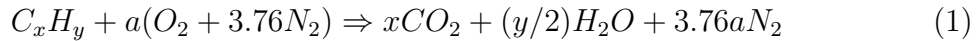
where

$$a = x + y/4 \tag{2}$$

Note that this equation can be used for combustion of H_2 by noting that this is a special case where $x = 0$ and $y = 2$.

The fuel to air ratio, (F/A), is a fundamental concept underlying all combustion devices. Essentially, it is the ratio of the mass of fuel to the mass of air consumed in combustion.

$$(F/A) = \frac{m_{fuel}}{m_{air}} \tag{3}$$

The stoichiometric fuel to air ratio, $(F/A)_{stoich}$, can be defined as the (F/A) ratio corresponding to the stoichiometric condition. For arbitrary hydrocarbon combustion in air, $(F/A)_{stoich}$ may be calculated as [7]

$$(F/A)_{stoich} = \frac{1}{4.76a}\frac{MW_{fuel}}{MW_{air}} \tag{4}$$

where MW is the molecular weight. $(F/A)_{stoich}$ for combustion of fuels of interest with air is given in Table 1. Expressed in terms of the mass flow rate, $\dot{m}$, (F/A)

Table 1. Fuel Stoichiometric Properties

Fuel	MW_{fuel}	Oxidizer	$MW_{oxidizer}$	x	y	a	$(F/A)_{stoich}$
H_2	2.016	O_2	32.00	0	2	$\frac{1}{2}$	1.260E-1
H_2	2.016	Air	28.86	0	2	$\frac{1}{2}$	2.935E-2
C_2H_4	28.054	Air	28.86	2	4	3	6.807E-2

becomes

$$(F/A) = \frac{\dot{m}_{fuel}}{\dot{m}_{air}} \tag{5}$$

which is particularly relevant when considering systems that have continuous combustion.

The equivalence ratio, ϕ, is defined as the ratio of the actual (F/A) to the stoichiometric (F/A),

$$\phi = \frac{(F/A)}{(F/A)_{stoich}} \tag{6}$$

where a $\phi = 1$ corresponds to the stoichiometric mixture. For $\phi > 1$ indicates excess fuel is present and the mixture is said to be rich; conversely $\phi < 1$ indicates excess oxidizer is present and the mixture is said to be lean.

Given a specific fuel/oxidizer combination and an equivalence ratio, a (F/A) is implied. With algebraic rearrangement, this can be expressed as

$$\dot{m}_{fuel} = \phi(F/A)_{stoich}\dot{m}_{air} \tag{7}$$

This equation can be readily used with appropriate flow metering to achieve a desired equivalence ratio, as discussed in Section 2.4.3.

The preceding discussion on combustion has assumed an idealized combustion event where all reactants are either consumed to produce reactants, or are present in some excess of either fuel (rich combustion) or oxidizer (lean combustion), and are represented by global reactions. In reality this is not the case. For all equilibrium mixtures some degree of dissociation will be present. However, for high temperature

12

mixtures such as the post-detonation mixture, this effect becomes particularly important. Many chemical reactions have been found to conform to the Arrhenius equation [8],

$$k_c = CT^\eta e^{-\epsilon_0/kT} \tag{8}$$

where k_c is the reaction's rate constant, T is the mixture's temperature on an absolute temperature scale, C is a proportionality constant, η is a temperature dependency coefficient, ϵ_0 is related to the activation energy, and k is the Boltzmann constant. C, η, and ϵ_0 are all specific to a elementary reaction and are independent of temperature. Thus, k_c has both a power law and an exponential dependence on temperature, making it sensitive to mixture temperature. The practical result of this effect is that the reactions will not proceed to completion as given by the global reactions, but will instead proceed to some intermediate state, the degree to which is determined by the available energy, which results in an equilibrium, or maximum entropy, state, with a lower energy release and therefore lower final temperature. The equilibrium state and composition for a combustion reaction can then be determined using the elementary reactions and initial state and composition of the reaction, given values for C, η, and ϵ_0 for all relevant elementary reactions. A code used to determine the equilibrium state of a mixture as described by Gordon et al. and McBride et al. [9, 10] is the NASA Chemical Equilibrium with Applications (CEA) code, which is widely available online at `https://cearun.grc.nasa.gov/` [11].

2.2 Detonation Wave Fundamentals

A Detonation Wave (DW) is a supersonic combustion event coupled with a shock wave. The shock wave increases the pressure of the reactant mixture, providing the necessary activation energy required to initiate combustion. In turn, the combustion event provides the necessary increase in energy to drive the shock wave, perpetuating

the cycle.

In this section DW models are considered in Section 2.2.1. The structure of real DW is then explored in Section 2.2.2. Section 2.2.3 discusses the importance of the detonation cell size, and how this parameter varies with various operating conditions. Section 2.2.4 explains the process of Deflagration to Detonation Transition, a process by which detonation initiated can be realized.

2.2.1 Detonation Wave Models.

Several models have been proposed for the structure of a DW. One of the simplest, and most instructive, physics-based DW structure models is the so-called Zeldovich-Neumann-Döring, or ZND, model shown in Figure 6 [7, 12]. This model proposes a 1-D DW where the shock wave adiabatically increases the pressure and temperature of the reactant mixture. Combustion of the reactants before and during the shock is assumed to be negligible. Post-shock, the heated and pressurized reactants enter an induction zone where the fuel molecules begin to break down. Following the induction zone the reactants are rapidly combusted due to the high temperatures and pressures. This combustion decreases the pressure and density of the fluid while further increasing its temperature, and the products are accelerated by this energy release.

While the ZND model provides a model for the DW, it does not provide a closure condition permitting determination of the final state of the products. This condition is provided by the Chapman–Jouguet (CJ) condition, as depicted in Figure 7 [7, 12]. The Rayleigh line represents the 1-D solution to the mass and momentum conservation equations, and can be expressed as [12]

$$\frac{P_2}{P_1} = \left(1 + \gamma_1 M_1^2\right) - \left(\gamma_1 M_1^2\right) \frac{v_2}{v_1} \tag{9}$$

14
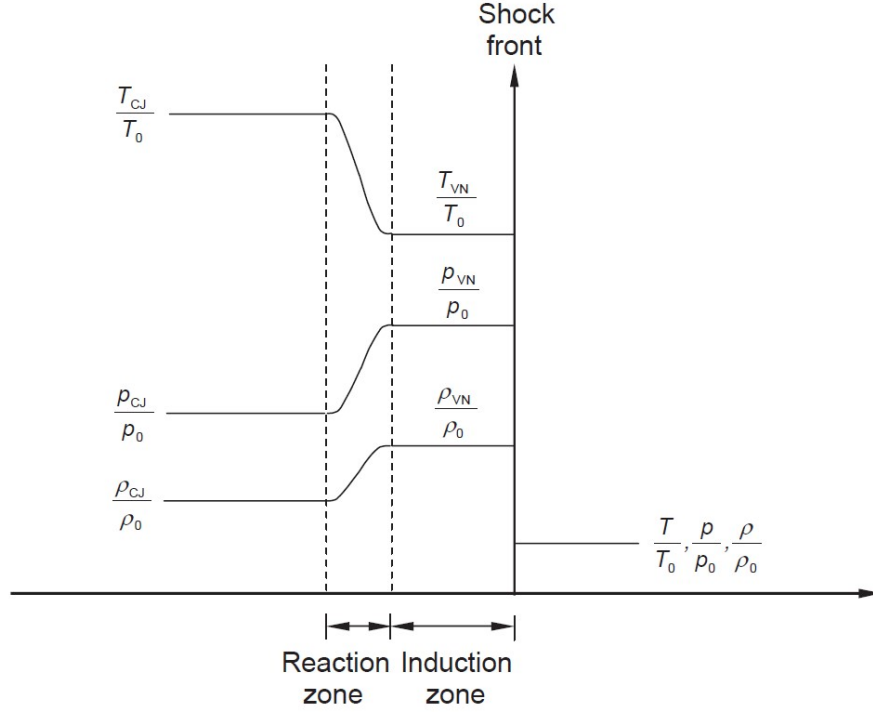
Figure 6. ZND model from Lee [12]

The Hugoniot curve represents the 1-D solution to the mass, momentum, and energy equations, and for a perfect gas can be expressed as [12]

$$\left(\frac{P_2}{P_1} + \alpha\right)\left(\frac{v_2}{v_1} - \alpha\right) = \beta \tag{10}$$

which has the form of a rectangular hyperbola, where

$$\alpha = \frac{\gamma_2 - 1}{\gamma_2 + 1} \tag{11}$$

$$\beta = \frac{\gamma_2 - 1}{\gamma_2 + 1}\left(\frac{\gamma_1 + 1}{\gamma_1 - 1} - \frac{\gamma_2 - 1}{\gamma_2 + 1} + 2q'\right) \tag{12}$$

$$q' = \frac{q}{p_1 v_1} \tag{13}$$

Both of these equations must necessarily be satisfied for conservation, so a physical solution must occur at the intersection of these curves. Analysis by Chapman [13]

15
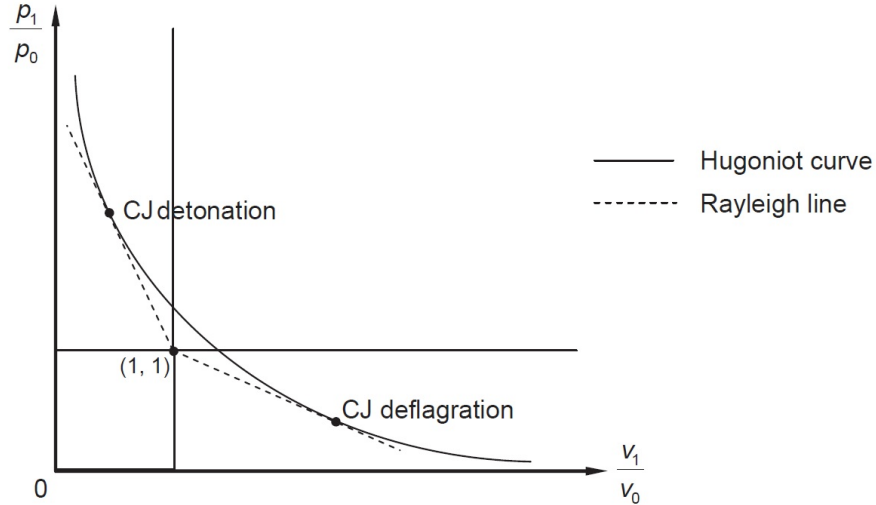
Figure 7. Rayleigh lines and the Hugoniot curve, with points of tangency indicated. Tangency points corresponds to a CJ Detonation (Upper CJ point) and a CJ Deflagration (Lower CJ point) are indicated. From Lee [12].

and Jouguet [14] found that a detonation will naturally move towards the Upper CJ point, which is the upper tangency solution of the Rayleigh line and the Hugoniot curve, resulting in a stable DW at this point. DWs existing to the left of this point are strong/overdriven and will decay; conversely, DWs to the right of this point are weak/underdriven and will accelerate. Notably, the pressure is increased relative to the pre-shock pressure, providing Pressure Gain Combustion (PGC), and the post-detonation flow has accelerated to the sonic condition [12, 7].

Also of note, the upper right and lower left quadrants are inaccessible, corresponding to non-physical solutions. The lower right quadrant corresponds to deflagration combustion, which experiences a net pressure decrease. Most deflagration will occur to the left of the CJ deflagration point, with the conditions corresponding to the CJ deflagration or to the right of a CJ deflagration rarely or never occurring in nature [12, 7].

Detonation parameters for a ZND/CJ DW can be estimated from equations de-

rived from these models, assuming $P_2 >> P_1$, giving [7]

$$T_2 = \frac{2\gamma_2^2}{\gamma_2 + 1}\left(\frac{c_{p,1}}{c_{p,2}}T_1 + \frac{q}{c_{p,2}}\right) \quad (14)$$

$$v_D = \left[2(\gamma_2 + 1)\gamma_2 R_2\left(\frac{c_{p,1}}{c_{p,2}}T_1 + \frac{q}{c_{p,2}}\right)\right]^{1/2} \quad (15)$$

$$\frac{\rho_2}{\rho_1} = \frac{\gamma_2 + 1}{\gamma_2} \quad (16)$$

Note that in this case the subscript 1 corresponds to the pre-detonation condition, whereas the subscript 2 corresponds to the post-detonation condition. The final temperature of the products is then a function of the initial temperature, the heat addition, q, the ratio of specific heats, γ, and the specific heat at constant pressure, c_p. The Detonation Velocity, v_D, has similar dependencies but is also a function of the Specific Gas Constant, R, noting that R, c_p, and γ are linked through the equation $\gamma = \frac{c_p}{c_p - R}$. Notably, in the limit as $P_2 >> P_1$, the density ratio is simply a function of γ.

In practice, the solution of these equations is non-trivial because $c_{p,2}$ and γ_2 are a function of T_2 due to the equilibrium solution discussed in Section 2.1. Thus the equilibrium solution for these parameters must be solved before these parameters are known. The NASA CEA code mentioned in Section 2.1 has a built-in calculator for detonations, which can be readily used to calculated the equilibrium solution for these parameters assuming a CJ detonation [9, 10].

2.2.2   Real Detonation Wave Structure.

In reality, the simplified laminar ZND wave structure does not occur. Instead, a series of turbulent, continuously generated and extinguishing cellular structures are generated by a dynamic wavefront. Figure 8 shows a sketch of the DW front. Note

that the DW does indeed have a shock followed by an induction zone, similar to the ZND model. However, several other structures not predicted by the ZND model exist. The DW front is composed of alternating Mach stems and incident shocks. Where these waves intersect, a transverse shock forms to correct the pressure differential. The intersection of these three waves forms a so-called triple point. A turbulent shear layer also extends from the triple point due to the velocity slip condition within the flow, a form of the classic Helmholtz instability. The trace of the intersection of the triple point trajectories form the boundary of the DW cell structure, which appear similar to fish scales. The lateral distance between triple point intersections is defined as the detonation cell size (λ). The λ for a given mixture is one of the most important parameters for the development of any detonation based combustion device, as λ sets the minimum dimension of the detonation channel [15, 16, 17, 18]. Specifically, the detonation channel must be wide enough to accommodate at least one detonation cell, or a DW cannot be sustained and will transition back to deflagration. Further discussion on λ can be found in Section 2.2.3.

The progression of a real DW can be seen in Figure 9. In a through d, there are two overdriven Mach waves flanking an incident shock. Where these Mach waves and the incident shock intersect is a triple point with the corresponding shear layers. As the two Mach waves intersect in e the reaction zone is decoupled and an unburned fuel pocket forms which is convected downstream, away from the detonation reaction zone as shown in f-i. Following the intersection of the two triple points, the new reaction zone that forms is overdriven, becoming a Mach wave with a coupled reaction zone as shown in j-l. Simultaneously, the two Mach waves flanking it have decayed to the point where they have become underdriven incident shocks. This process is repeated as the DW propagates through the reactant mixture. Note the DW is revealed to be highly unsteady, and is characterized by the continuous generation and decay of

18
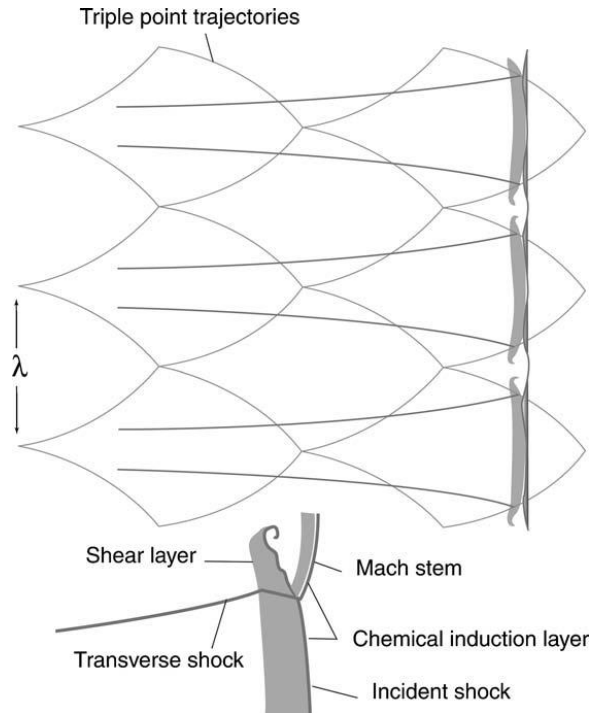
Figure 8. Sketch of a DW front from Lee & Radulescu [19]

reaction zones.

DWs are inherently unsteady and 3-D in nature, but with confinement of sufficient aspect ratio they can be made essentially planar. As noted by Lee [12], a cell size to channel height ratio of $\lambda/h \approx$ 6-10 essentially eliminates modes in the smallest length scale, leaving a near-planar DW. This is the case for the DW in Figure 10. Note that the spacing between the intersections is higher in the lower pressure case, corresponding to a larger cell size. Due to the unsteadiness in a DW, pockets of fuel can become detached from the reaction zone and convected away from the wave front. This is shown in Figures 9 and 11. These pockets are eventually consumed by deflagration [20]. This effect seems to be especially probable where the triple points collide, bringing multiple turbulent and high pressure structures into close proximity with each other and the unburned gases in the induction/reaction zone.

Unsteadiness at the DW front also manifests in an unsteady velocity of the wave front. Figure 12 shows that the velocity distribution of the wavefront within the deto-

19
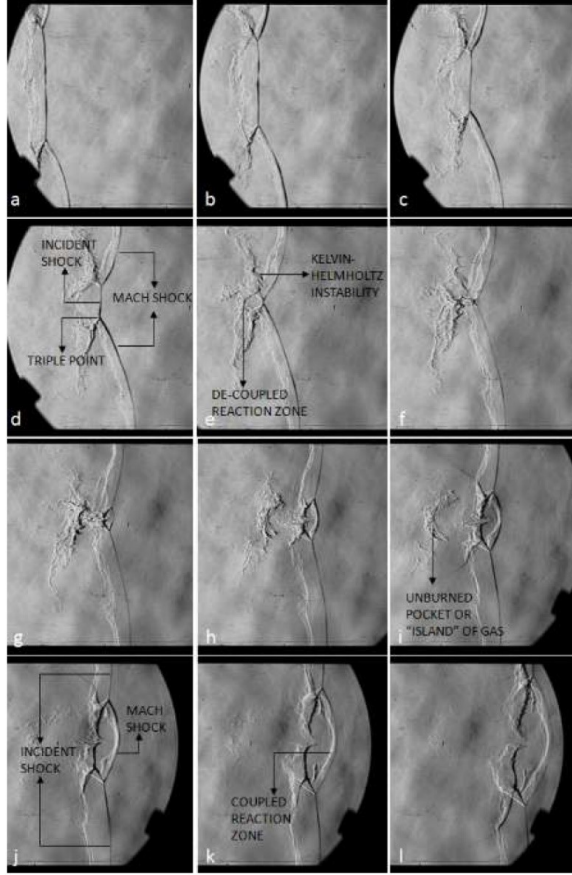
Figure 9. Detonation of a $CH_4 + 2O_2$ mixture at an initial pressure of **3.5kPa**, with images at **11ms** intervals. From Maxwell et al. **[20]**.

nation cell along the centerline normalized by the CJ velocity varies from a maximum of near 1.8 then decays to a minimum of less than 0.6. Note that the highest velocity is achieved as the cell is initiated, when it is overdriven by the intersection of waves at the triple point. This steadily decays as the DW within the cell propagates and becomes underdriven.

2.2.3 Detonation Cell Size.

As noted in Section 2.2.2, λ is one of the most important parameters in a detonation environment. While data regarding λ is limited in the pressure, temperature, and composition ranges relevant to RDEs, it is known to be a function of the pres-
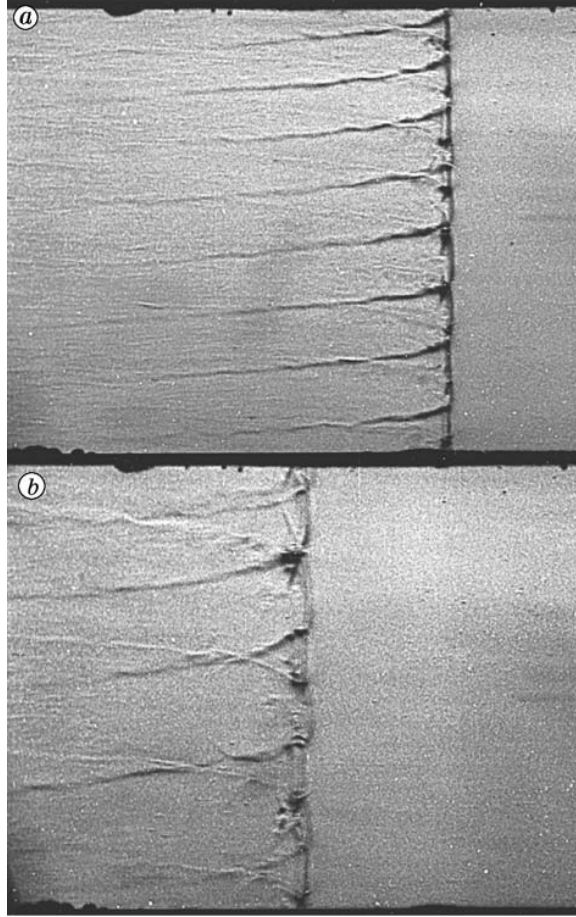
Figure 10. DW front propagating from left to right in an $H_2 - O_2 - 40\%Ar$ mixture at initial pressures of (a) 13 kPa and (b) 8 kPa from Radulescu [19].

sure, temperature, and chemical composition of the pre-shock reactant mixture, to include equivalence ratio and diluent concentration. Babbie et al. [23, 15] found λ is minimized at an equivalence ratio of approximately one, as shown in Figure 13. Varying the equivalence ratio away from one and the presence of diluents increase λ. Increasing the initial pressure and temperature decreases λ. This behavior was experimentally observed at elevated initial pressures for hydrogen-air detonations at initial pressures between 1 and 10 atm and equivalence ratios between 0.65 and 1. At lower initial pressures, Lee and Radulescu [19] also observed decreasing cell size as pressure increased, as seen in Figure 10.

Figure 14 shows the behavior of λ as a function of ϕ. Note the minimum cell size
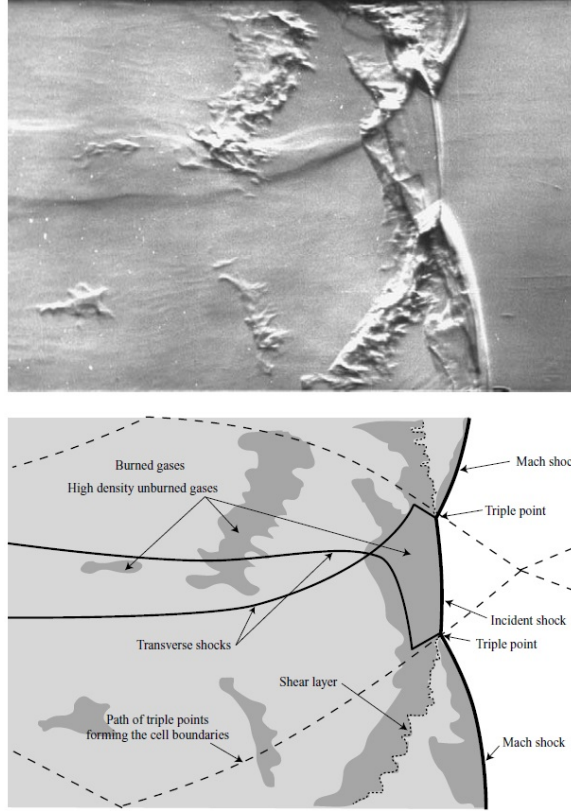
Figure 11. Detonation of a $CH_4 + 2O_2$ mixture at an initial pressure of 3.4kPa. Note that unburned fuel pockets have become detached from the DW front and are being transported aft of the wavefront. From Radulescu et al. [21].

is located at approximately $\phi = 1$ for a selection of common detonation fuels. Away from $\phi = 1$ the cell size increases monotonically. Figure 15 shows that as temperature increases, the detonation cell size tends to decrease. Therefore, increasing fuel initial temperature may lead to increased detonability. Figure 15 also shows that at increasing percentages of H_2O in the pre-detonation mixture, the cell size tends to increase. H_2O acts as a diluent, or non-participating species, which only affects the detonation by absorbing energy, reducing the final temperature and v_D per the relations given for the ZND model. This has interesting implications for practical detonation combustors. Whereas the experiments conducted utilized a precisely controlled percentage of steam in the detonation, the amount of steam in a detonation propulsion device is influenced in part by how effectively it can purge products from the previous
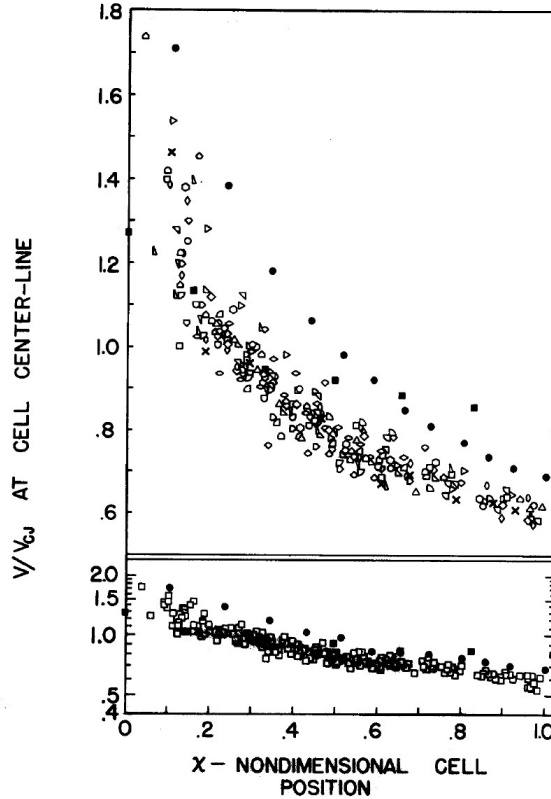
Figure 12. λ decreases as initial temperature increases. Additionally, λ increases with increasing percentage of H_2O diluent. From Strehlow and Crooker [22].

combustion process from the detonation channel. If the reactants are mixed with the products from the previous reaction, the net result is a weaker detonation, a lower v_D, and reduced product temperature, as determined by Edwards [25].

2.2.4   Deflagration to Detonation Transition.

Deflagration to Detonation Transition (DDT) is the process by which deflagration combustion is accelerated and transitions to a detonation [12]. This is in contrast to a direct initiation, by which the shock wave and energy required for detonation are introduced by a process external to the reactants, initiating the detonation directly without the flame acceleration process. A common direct initiation technique involves using conventional high explosives to provide the necessary shock wave strength and energy required to initiate a DW [12]. While this method is effective, it produces

23
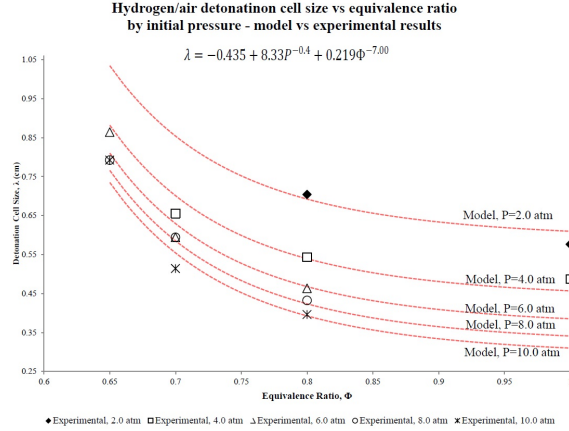
Figure 13. Detonation cell size from Babbie et al. [15]. Note that cell size decreases with increasing ϕ and initial pressure.

excessive overpressure, creates transient effects, and requires special handling and storage procedures that increasing setup time. The DDT process bypasses many of these issues.

To initiate a DW, special procedures are required to provide the correct conditions. If a flame is initiated via introduction of a spark, flame, or other conventional deflagration initiation method, the reactant mixture may simply deflagrate within the channel. The invention of so-called DDT devices has allowed for reliable and convenient detonation initiation using fuels which are traditionally combusted with deflagration, which may be safer to work with and have fewer storage and handling requirements than high explosives [15]. These devices work by filling a tube with a reactant mixture and initiating deflagration at one end. As the deflagrating flame advances through the tube, it encounters solid or fluidic barriers which reflect pressure waves, further increasing the temperature and pressure, and increasing the velocity of the flow, i.e. providing flame acceleration [27]. If the mixture is sufficiently reactive this feedback loop process eventually results in a flame which is propagating at supersonic velocity, at which point the flame will transition to a coupled shock-combustion wave, i.e. a DW [12]. Thus, DDT is achieved in the DDT device. This may then be

24
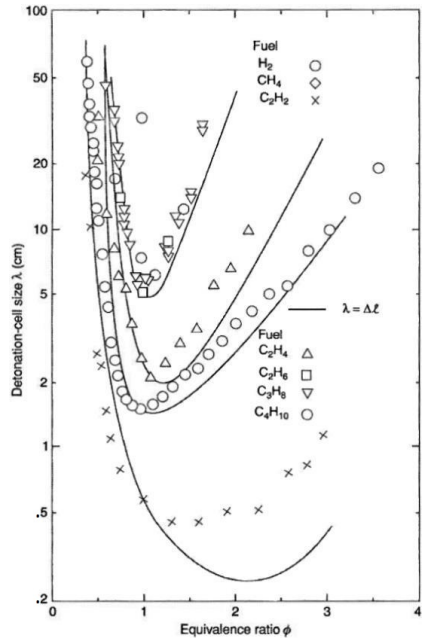
Figure 14. λ **increases monatonically away from** $\phi = 1$ **for a variety of common detonation fuels. From Knysttautas et al. [24].**

used to initiate detonation in another reactant mixture, with the shock and energy from the DDT device serving as the initiation mechanism for either a direct initiation or an accelerated DDT.

2.3 Combustor Types and Comparison

A variety of combustion concepts exist at varying levels of technical maturity and usage. Currently, the vast majority of combustion devices operate in the deflagration mode. Advanced combustion devices may employ a variety of detonation-based pressure gain combustion schemes. Examples of such engines include Pulsed Detonation Engines (PDEs), Axial RDEs, and Disk or Radial RDEs (RRDEs). While detonation based combustion is not currently widely used, active research is being pursued to develop these concepts into operationally viable systems [28, 3, 29]. While both RDEs and PDEs used detonation-based combustion, they achieve it in different ways.

Typically the total pressure for deflagration is approximately constant, with some
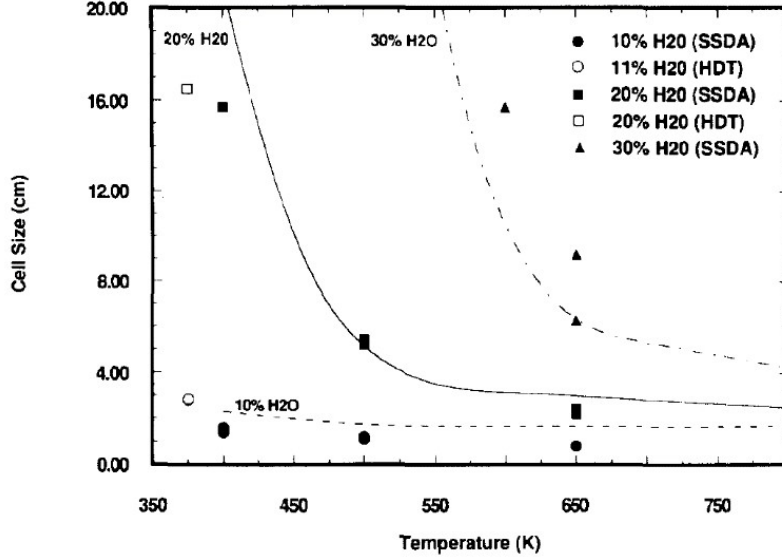
25

Figure 15. λ decreases as initial temperature increases. Additionally, λ increases with increasing percentage of H_2O diluent. From Ciccarelli et al. [26].

losses [30]. By contrast, detonation combustion results in pressure ratios notionally in the range of $P_2/P_1 \approx 13 - 35$. Similarly, deflagration results in $T_2/T_1 \approx 7.5$, whereas detonations result in $T_2/T_1 \approx 8 - 21$ [7].

The remainder of this section begins with a discussion of deflagration type combustors in Section 2.3.1, which are currently the standard. A discussion on PDEs is presented in Section 2.3.2 to provide the reader with a reference point in detonation combustion, as PDEs are perhaps the most widely known and understood detonation-based propulsion device. Section 2.3.3 explores both axial type RDEs (Section 2.3.3.1), again for reference to a more common and well understood similar configuration, and radial type RDEs (Section 2.3.3.2), which are the subject of the current research, as well as a discussion on their flowfields (Section 2.3.3.3).

2.3.1 Deflagration Combustors.

As the most commonly used combustion mode, several classes of deflagration-type combustors exist. These are primarily divided into premixed or nonpremixed, and

26

laminar or turbulent. Most propulsion and power generating systems utilize turbulence as a mechanism to reduce flame length [7], which reduces the required combustor length, ultimately reducing the weight of the powerplant. Conventional gas turbine engines such as those used on aircraft operate with non-premixed turbulent combustion, whereas the spark ignition internal combustion engines used on automobiles are in the premixed turbulent combustion regime. Certain gas turbine engines may also incorporate premixed regions to reduce NO_x emissions [7].

Combustors are typically sized to minimize length subject to the maximum flame length. Combustors such as the Ultra Compact Combustor (UCC) seek to reduce the combustor length further by adding a circumferential swirling velocity component, allowing for more residence time at a given axial location [31]. By reducing the engine's length, the engine's overall weight can also be reduced, resulting in better thrust to weight performance. RDEs may also offer a more compact solution than traditional combustions, as discussed in Section 2.3.3.

2.3.2   Pulse Detonation Engines.

The PDE is an example of a detonation-based PGC engine. PDEs serve as a useful benchmark comparison to RDEs because 1) they operate on a thermodynamically similar cycle and 2) they represent a more well known, well developed technology that has been flight tested on at least one occasion [32].

PDEs operate on a Fill-Fire-Purge cycle [33]. Reactants are first injected into the PDE and mixed, forming a detonable mixture. These reactants are then ignited, which begin to deflagrate. Flow blockages such a Shchelkin spiral inside the PDE tube initiate a DDT, and with sufficient length the PDE can obtain detonation. The products then blow down the PDE tube, and purge air is introduced. Because of this cycle, the PDE must ignite and transition from deflagration to detonation every

cycle. Additionally, the products are accelerated axially by the detonation. Because of this, the PDE has an upper limit to its operating frequency, and significant length is required to achieve DDT.

The PDE used by Rouser et al. utilized a $5cm$ DIA, $1.2m$ long PDE tube, of which $0.9m$ was dedicated to achieving DDT. The operational frequency of this PDE was on the order of $10Hz$. In contrast, the RRDE used by Huff et al. [34] and McClearn et al. [35] had an axial length measured in cm, and an operational frequency in the kHz range. Similar trends were noted by Lu and Braun [3] in their overview of detonation engine technologies. This reduction in axial length for RDEs is due to the fact that 1) the DW is moving perpendicular to the flow path and 2) detonation in an RDE need only be initiated once, after which detonation occurs essentially continuously; RDE's operational frequency is primarily limited by the combustion chemistry affecting the DW velocity and the constraints on mass flow. Both PDEs and RDEs produce comparable specific impulse, as shown in Figure 16.
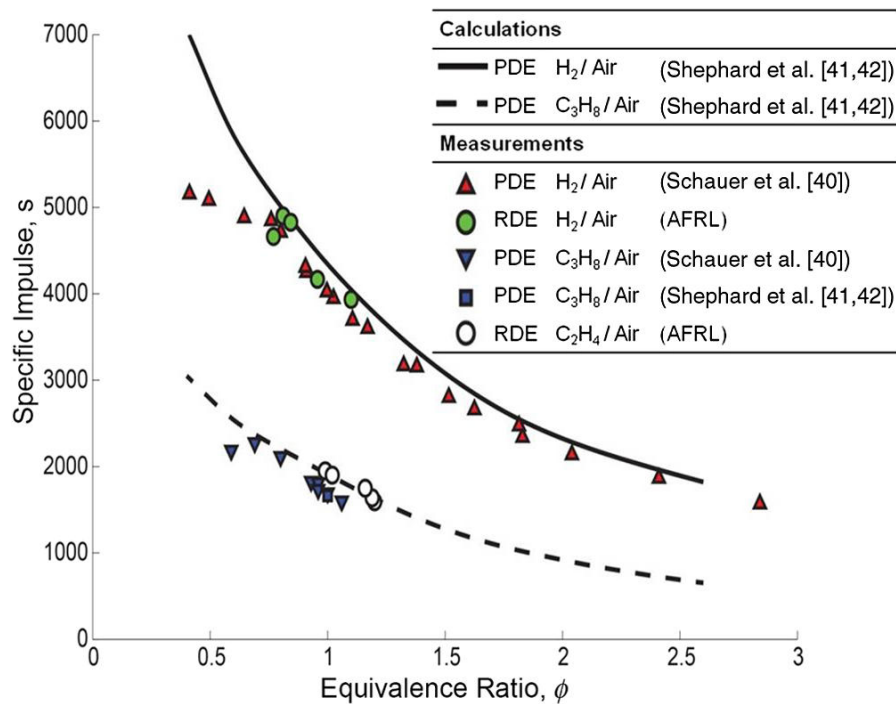
Figure 16. Comparison of PDE and RDE specific impulses. From Rankin et al. [28].

Due to the cyclical nature of the PDE's output products integration of the PDE with turbomachinery can be challenging. Rouser et al. [33] were successful integrating a PDE combustor with an automotive turbocharger. The PDE achieved power that was consistently higher than the same combustor was able to achieve while operating in a deflagration mode, as shown in Figure 17. However there were significant fluctuations in both rotor speed and power that corresponded to passage of the DW through the turbine. This behavior is generally considered to be undesirable, as most turbomachinery is designed for quasi-steady operation.
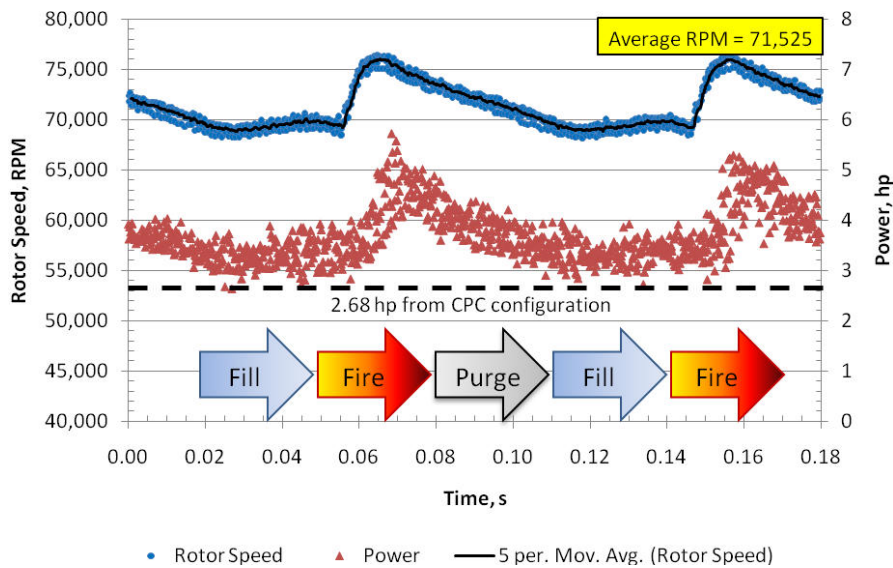
Figure 17. Variation in PDE driven rotor speed and power. From Rouser et al. [33].

2.3.3 Rotating Detonation Engines.

RDEs are currently being tested in both axial configurations as discussed in Section 2.3.3.1 and radial configurations as discussed in Section 2.3.3.2. Both classes of RDE notionally transition to detonation once, after which the detonation persists in the channel indefinitely, provided reactants are continuously supplied. Additionally, both classes of RDE operate with a DW that travels perpendicular to the mean flow direction, as opposed to the PDE, where the DW travels in the direction of the mean

29

flow. Because RDEs operate with PGC, the potential exists for local flow reversal at the fuel and oxidizer injection ports as the DW passes. This has been observed experimentally by Nakagami et al. [2]. Following flow reversal, depending on pressures and potentially geometric factors, the flow through the injectors will resume, although in general the fuel and oxidizer injectors need not recover simultaneously [2]. While PDEs also achieve PGC, they are able to avoid this flow reversal by using timed valves to close the flow path during detonation; this is not currently possible in RDEs due to the significantly higher operational frequency. Further details of the RDE flowfield are discussed in Section 2.3.3.3. A long term goal of RDEs is to transition from the gaseous fuels used in research devices to heavier liquid hydrocarbon fuels, which are a necessity for any logistically supportable system, and are safer to store and use [28, 3].

2.3.3.1 Axial RDEs.

Axial RDEs are being investigated for a number of applications, including replacement of traditional aircraft main combustors, rocket main combustors, and similar systems [29]. Axial RDEs are annular with a primarily axial flow path and transverse DW propagation. Figure 18 shows the cross section of one such axial RDE, along with a photograph of its operation. Fuel and oxidizer are injected near the inner radius of the annulus, defined as the region between the inner body and outer body, that forms the detonation channel. The DW traverses the base of the channel, where reactants are combusted forming a high temperature and pressure stream of products, which continue moving axially to exhaust. The ratio between the injector area and the channel longitudinal cross section area is defined as the Throat Area Ratio (AR_t). This particular RDE has an aerospike plug nozzle installed, which bulges in the channel to form a minimum nozzle area. The ratio between the channel area

and the minimum nozzle area is defined as the Nozzle Area Ratio, (AR_n) For nozzles without this choke point, $AR_n = 1$. Both area ratios affect the choking behavior of the RDE, which in turn affects performance.
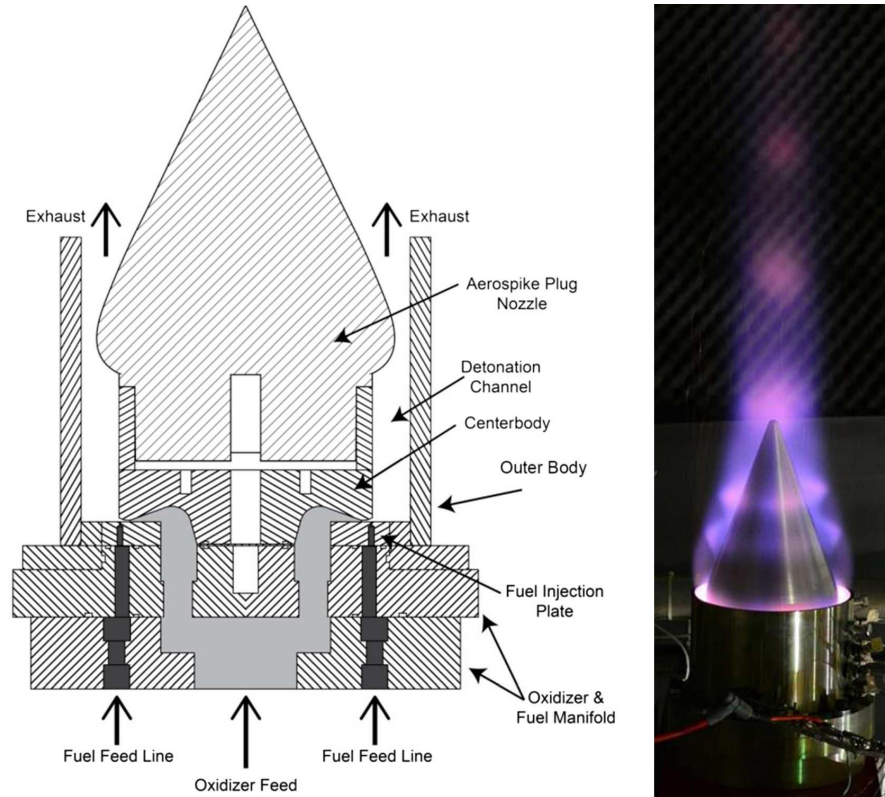
Figure 18. Axial RDE cross section and operation photograph [28]

Figure 19 shows a collection of cross sections for various types of axial RDEs. The even bluff body and recessed bluff bodies both have minimal aerodynamic considerations beyond combustion, and would be used primarily for research only. The open aerospike is analogous to a nozzle and is more representative of a propulsion device that would operate unchoked. The choked aerospike is similar to the open aerospike, but would be operated in a system that would encounter choked flow. The converging-diverging nozzle configuration would be used to accelerate the exhaust flow to supersonic axial velocity, and could notionally be used in a rocket RDE configuration.
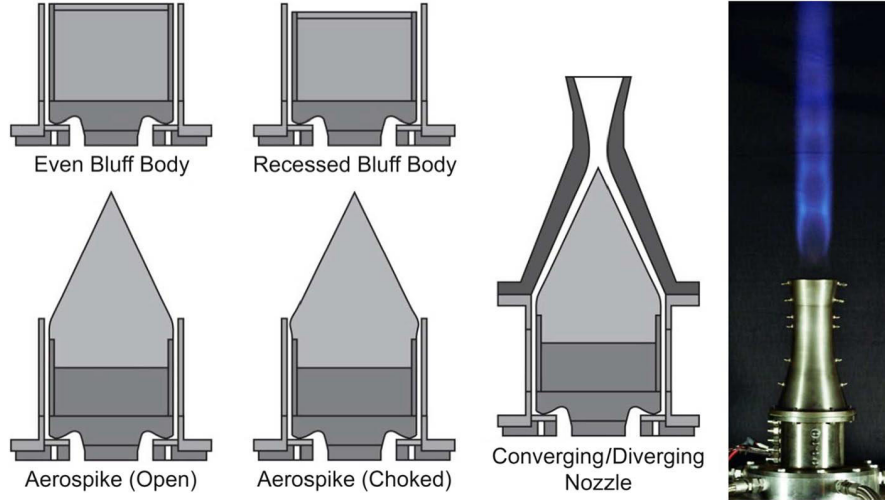
Figure 19. Cross sections for various types of axial RDEs and operation photograph [28]

Unlike PDEs, which ignite and undergo DDT every cycle, the DW in an RDE propagates indefinitely after the initial DDT. Thus, the operational frequency of an axial RDE is related to the radius at which the DW propagates (r_D), the detonation velocity (v_D), and the number of DWs that exist in the channel (N_D), and is limited by the recovery time from when reactants undergo flow reversal and when reactant flow is reestablished through the injectors. This makes a typical RDE considerably more compact than a PDE. Additionally, because of the magnitude of v_D combustion in an RDE occurs over a very short axial length, meaning that RDEs can potentially be made even shorter than traditional deflagration-type combustors, and with increased thermodynamic efficiency.

Axial RDEs have been integrated with turbomachinery by Naples et al. [36]. A T63 engine was modified by replacing its stock (deflagration) combustor with an axial RDE and operated for over 20 minutes in the modified configuration, with no damage noted to the turbomachinery. Due to the presence of the rotating DW, pressure fluctuations of 25% of the mean pressure were measured at Station 4, the inlet of the high pressure turbine, compared to 6% with the stock combustor as shown

32

in Figure 20, which did not appear to damage the turbomachinery. These pressure fluctuations were attenuated to levels comparable with the stock combustor by the time the flow traversed the high pressure turbine at Station 4.5, the entrance to the low pressure turbine.
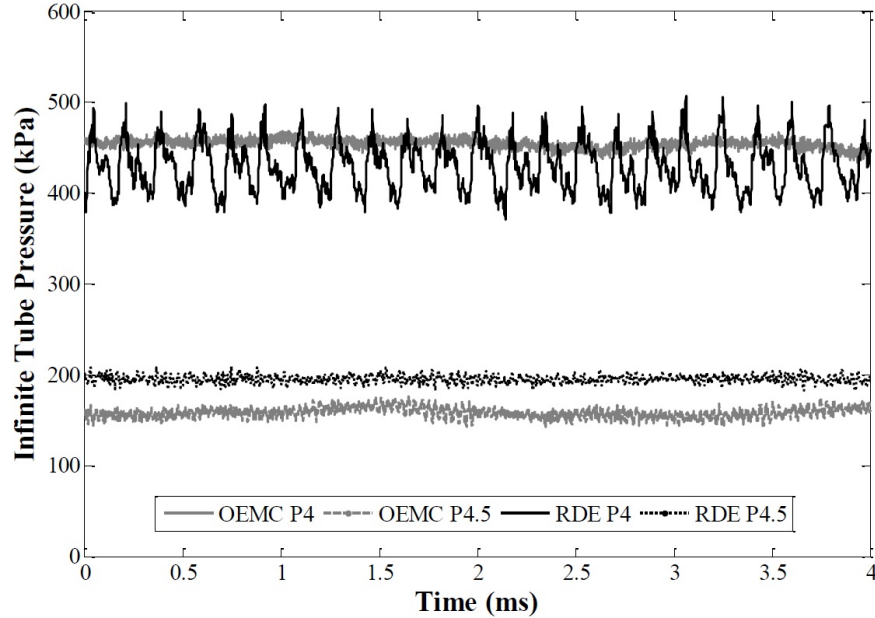
Figure 20. RDE driven turbine pressure fluctuations at Station 4 (lower lines) and Station 4.5 (upper lines) [36].

2.3.3.2 Radial RDEs.

Development of RRDEs followed that of axial RDEs by several decades, with early work being accomplished in the mid 1990s by Bykovskii et al. [37, 38, 39]. The RRDE has a detonation channel shaped like a disk, with fuel and oxidizer injected at the inner or outer radius. In this configuration, there is a transverse DW with products moving radially, which are then turned axially and exhausted. Two types of RRDEs exist: radial inflow RRDEs and radial outflow RRDEs. The present research uses a radial inflow RRDE.

Radial inflow RDEs have reactants which are injected at the outer radius, which

are then consumed by the azimuthally propagating DW, with the products moving axially towards the center as shown in Figure 21. Bykovskii's experimental device consisted of two parallel, planar circular plates with an opening in the center of one of them for exhaust, with a cylindrical wall at the outer radius through which reactants were injected. CH_4, H_2, and C_2H_2 fuels and O_2 oxidizer were used for early experiments [37], followed by H_2, CH_4, and sprayed liquid kerosene and diesel fuel with atmospheric air as the oxidizer for later experiments [38]. These experiments proved the radial configuration was viable for an RDE. Subsequent work with radial inflow RDEs has been accomplished by Nakagami et al. [40, 2] with $C_2H_4 - O_2$ and Huff et al. [41, 34, 35, 42, 43] with $H_2 - Air$. Huff et al. also integrated a radial inflow turbocharger with their RRDE to examine power generation potential.
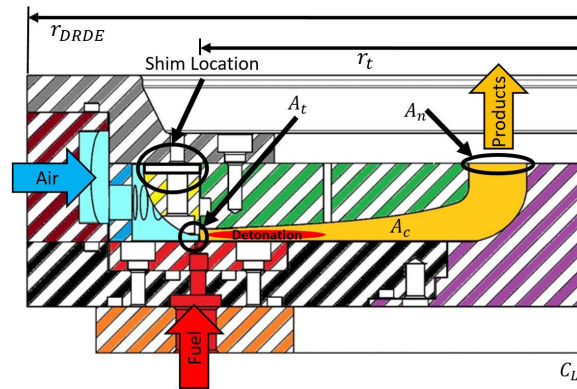
Figure 21. Radial inflow RRDE schematic [41]

The RRDE used in the present work, which is the same RRDE used by Huff with modifications described in Chapter III, has the oxidizer (air) injected at the outer radius. The oxidizer is then choked to a minimum area at the throat, denoted as A_t. Fuel is injected into the airstream using a jet in crossflow injection scheme, as described in Section 2.5.2. There is a backward facing step on the radially inward side of the throat, which promotes fuel-oxidizer mixing. Following this step, the channel is designed to have a constant area as the flow moves radially inward until the nozzle, denoted as A_c. The cross section area at the nozzle exit is denoted A_n. The ratio

34

between A_t and A_c is defined as the throat area ratio, $AR_t = \frac{A_t}{A_c}$. The ratio between A_n and A_c is defined as the nozzle area ratio, $AR_n = \frac{A_n}{A_c}$. The geometry metrics for the RRDE can then be specified in terms of A_c, AR_t, and AR_n.

The radial inflow RRDE appears to provide increased operability range and stability compared to the annular type RDE. Specifically, Huff [41] hypothesized the DW can move its radial position (r_D) to match the mass flow rate and time scales it is experiencing as shown in Figure 22, which is not possible in annular type RDEs due to the presence of the center body, in effect giving the RRDE an additional degree of freedom. At sufficiently high mass flux ($\dot{m}''$), depending on conditions such as ϕ and AR_n, transition from one wave to two wave and then multi-wave operation was observed as shown in Figure 23, where additional DW fronts are generated allowing combustion of the increased reactant mass; this behavior is also observed in annular type RDEs. The plots in Figure 23 show several features of note. With the exception of one data point for the $AR_n = 0.5$ case, there is a sharp decline in $v_D/v_{D,CJ}$ at the transition from one to two wave operation. Huff calculated all wave speeds at a fixed radius of $r_D = 7.0cm$, as there was no way to determine the radial location of the DW with certainty. This sharp change in behavior could be explained by the radial location of the DW changing, with one wave detonations located at a smaller radius and multiple wave operation located at a larger radius. Thus, the two wave detonation cases may not actually have a lower $v_D/v_{D,CJ}$, but rather be traversing a longer distance. These phenomena suggest that the RRDE is capable of automatically adjusting its operating conditions to a stable condition, which is a desirable behavior, over a much wider range than is possible in annular type RDEs.

Radial inflow RRDEs lend themselves to integration with a radial inflow turbine, which replaces the nozzle. This was examined by Huff [41] in the extended examination of the RRDE behavior in the configuration shown in Figure 24, The top channel
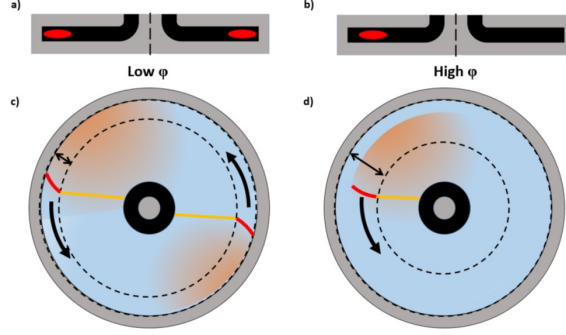
Figure 22. Hypothesized DW radial shift. From Huff [41]

.

plate was also replaced with a modified variant designed to accept the nozzle guide vane ring and lengthened axially to enclose the turbine. This configuration is used in the present work with additional modifications described in Chapter III.

Huff [41] and Huff et al. [44] were able to demonstrate proof of concept with this configuration by generating power for a compressor connected to the radial inflow turbine. An example RPM profile for a test is shown in Figure 25. First the air, then the fuel were released before detonation initiation and the device reaches an equilibrium state. At the point of ignition, the turbine RPM experiences a rapid increase, beginning to plateau within $0.5s$ of startup. These tests established the potential for rapid power generation with this configuration. The test concludes when the fuel is turned off, at which point the DW is extinguished and the rotor speed immediately begins to drop.

Figure 26 shows the achieved performance for different combinations of IGV angle, ϕ, and $\dot{m}''$. As $\dot{m}''$ increases, specific power tends to increase as well. Also, for each $\dot{m}''$ the specific power at $\phi = 0.6$ is higher than at $\phi = 0.5$ as expected. However, at the $\dot{m}'' = 75$ and 100 the specific power is higher for the NGV angle of 32 degrees than it is for 39 degrees. This behavior was not expected, and the reason for this change in behavior is unknown.

It was also noted that the turbine experienced no significant damage from either

36
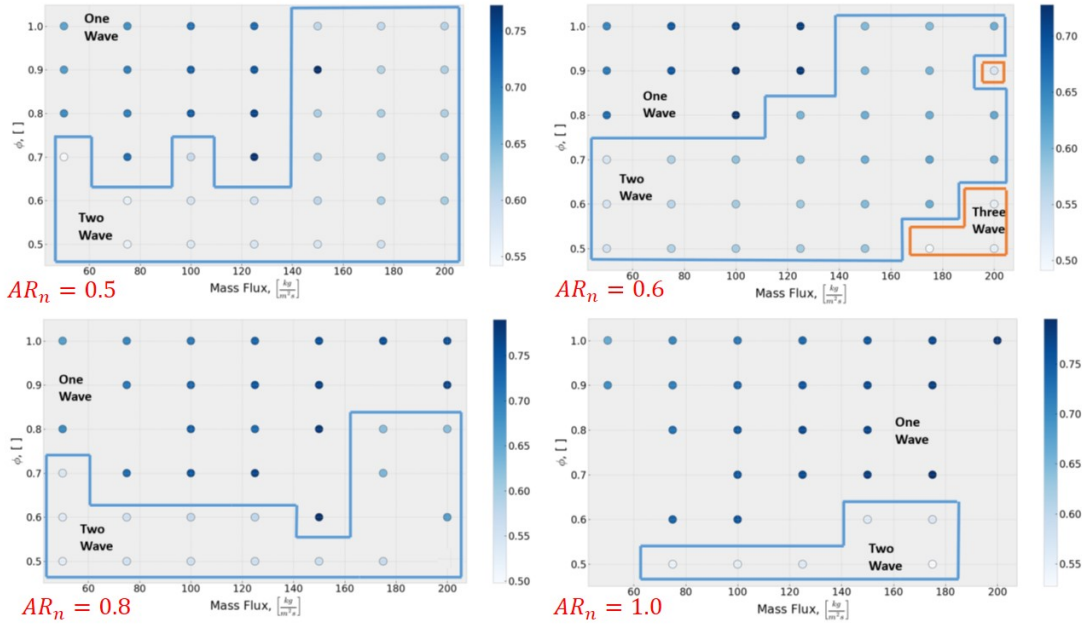
Figure 23. RRDE operability maps at Channel Height $= 4.5mm, AR_t = 0.2$. **Colored by** $v_D/v_{D,CJ}$. **Compiled from Huff [41], with** AR_n **labels added for clarity.**
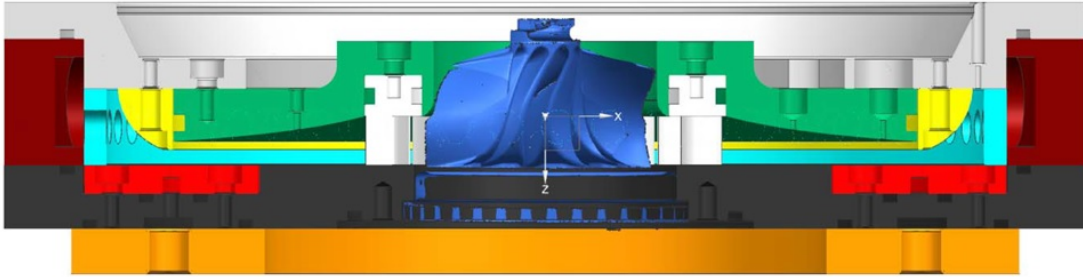
Figure 24. RRDE with turbine integrated in place of nozzle. Image courtesy of R. Huff, AFRL/RQTC.

heating or the DW during testing, and produced an audibly markedly reduced acoustic signature compared to operation without a turbine. However, they noted that power extraction was sub-optimal. Suggested reasons included sub-optimal component design due to uncertainty in the operating environment at the time of design/manufacture, using a turbine which was incapable of fully extracting all available power, and potential interactions with the DW. Specifically, the direction of propagation of the DW, and the effect that this will have for flow propagating through the NGV ring, was unknown. The present work investigates the effect of the DW propaga-

37
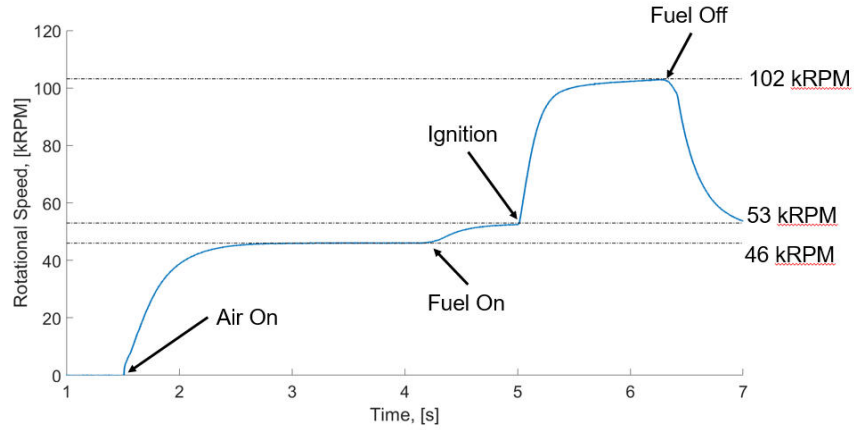
Figure 25. RRDE specific power vs RPM with turbine installed. From Huff et al. [44].
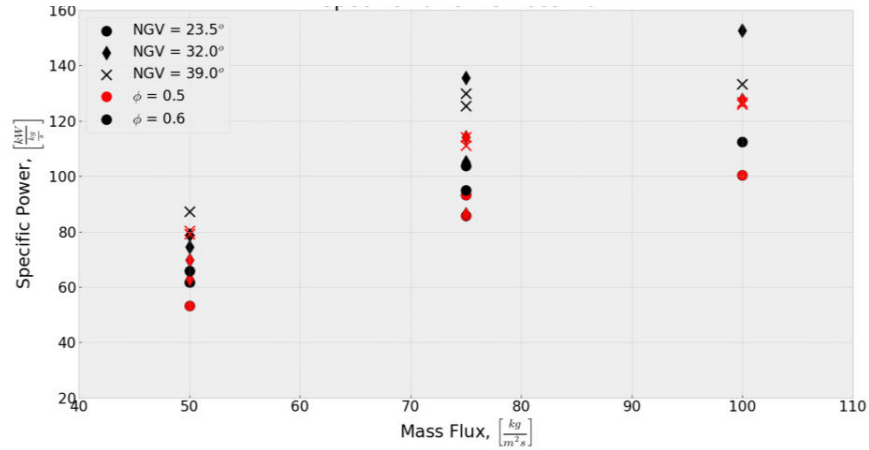
Figure 26. Turbine Tip Speed vs NGV Angle with turbine installed. From Huff et al. [44].

tion direction on performance using additional modifications described in Chapter III noted above. The remaining issues can be addressed with further design refinements in future engineering efforts.

Radial outflow RRDEs have been used in at least one instance by Higashi et al. [45]. The radial outflow RRDE has a similarly planar channel, but reactants are injected at the inner hub and propelled outward by the radial compressor into the detonation channel where they are consumed by the DW, then expanded through the turbine at the outer radius as shown in Figure 27. This configuration offers a compact power generation source, with the compressor and turbine co-located on
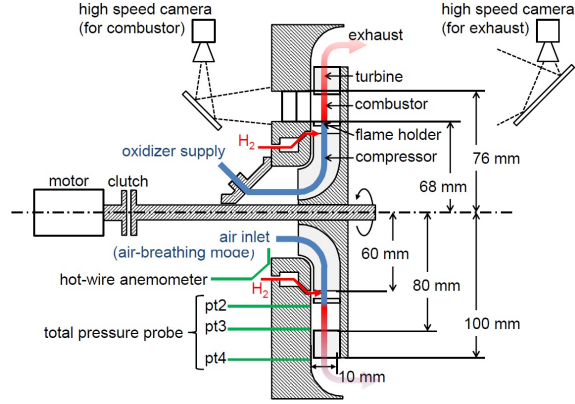
Figure 27. Radial outflow RRDE schematic. From Higashi et al. [45]

the same disk. However, while a gain of 160 RPM was achieved over the starting rotational rate of 2700 RPM, this configuration produced DWs propagating at less than half the CJ speed, and the flow though the turbines diverged greatly from the design value.

2.3.3.3 RDE Flowfields.

DWs in an RDE produce a unique detonation flowfield due to their boundary conditions. Many experiments conducted to study DWs consider well mixed, stationary reactants bounded by walls within the test section. In contrast most experimental RDEs are non-premixed, with flowing reactants, an open boundary on the upper surface, and flow through the lower boundary. Figure 28 shows a CFD generated flowfield for a premixed axial type RDE. Region A is immediately aft of the DW. Region B is the oblique shock wave, caused by post-detonation flow expansion. Region C is the shear layer between the freshly reacted products and older products from the previous DW. The intersection of the DW, oblique shock, and shear layer forms the triple point. Region D is a secondary shock caused by injection of reactants. Region E is the boundary between the unreacted reactants (bottom) and products from the previous DW (top). Secondary, autoignition burning occurs at this interface,

consuming on the order of 10% of the fuel prior to the arrival of the DW, resulting in lower performance compared to detonation-only combustion[46, 3]. The region in the vicinity of Region F has ceased injection of reactants due to the DW pressure. The streamlines aft of the DW curve upward, indicating the flow has expanded and accelerated axially.
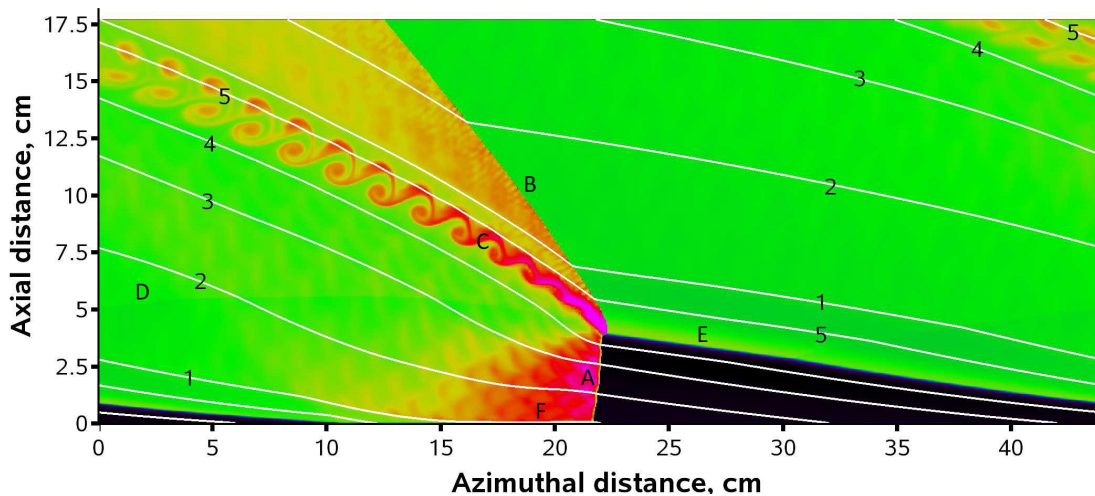
Figure 28. DW flowfield in an axial RDE. DW propagates from left to right. The flowfield is shown in the DW reference frame. Streamlines extending from various points labeled 1-5 are shown. Modified from Schwer and Kailasanath [46] with the addition of lettered regions of interest.

This flowfield can be approximated by a detonation with side relief, as modeled by Sichel and Foster [47], shown in Figure 29. This model examines the behavior of a DW traveling along a solid boundary at the lower surface with a height h corresponding to the reactant height at a detonation velocity velocity $v_D = C$. The model predicts the slip line is angled upward by an angle δ due to the expansion of the post-detonation products by a Prandtl-Meyer expansion fan. This upward angle of the flow creates an effective blockage for the flow over the DW, modeled as inert products, causing the oblique shock at an angle θ. This will reach an equilibrium when the flow direction and pressure at the interface match. While not shown, for real flow the difference in velocity along this shear layer result in a Kelvin-Helmholtz type instability causing

vortices along the slip line. While this model does not consider injection of new reactants from the wall boundary, it reasonably predicts most of the flow features observed, which may be due to the fact that v_D is much greater than the velocity of the reactants being injected at the boundary.
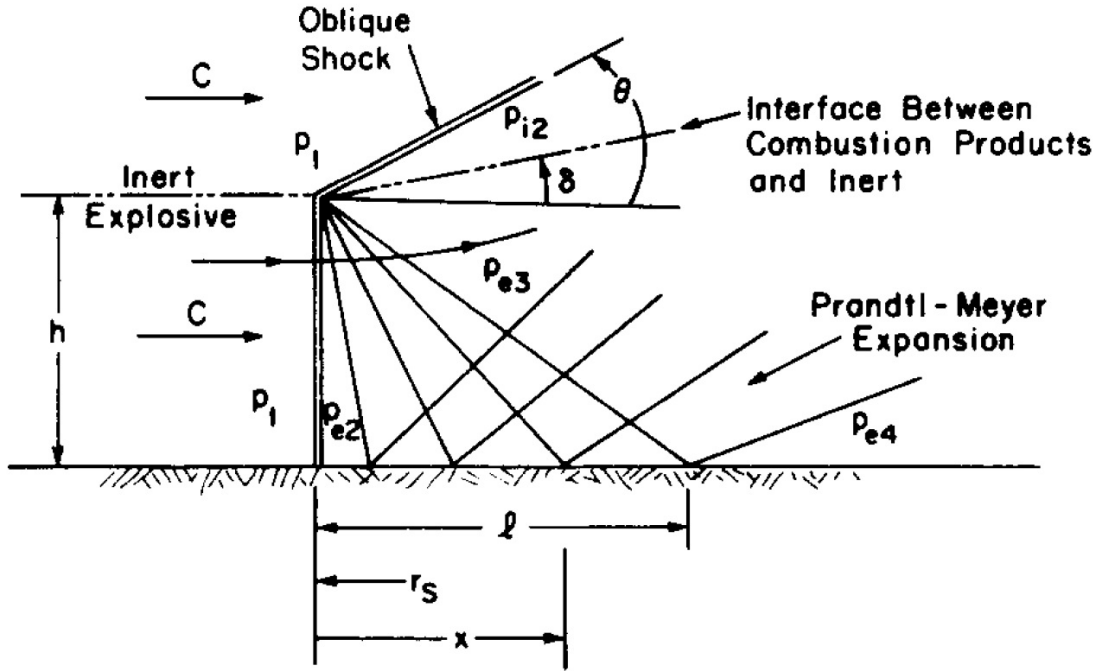
Figure 29. Sketch of a DW with side relief. DW propagates from right to left. From Sichel and Foster [47].

A modification to this model to more accurately describe the flow within an RDE is described by Yu et al. [48], as shown in Figure 30. In this model, the detonation wave is inclined forward. In the DW frame of reference, the reactants have velocity components both due to the DW velocity and due to the axial movement of the reactants as they are injected. This results in a relative angle between the reactant flow and the base of the channel, which is the same as the angle of the slip line separating the reactants from the products from previous cycles ahead of the DW. An expansion fan also appears on the lower edge of the DW, as flow reversal through the injectors allows relief. A second slip line, between the post-detonation products

41

and fresh reactants, also appears.
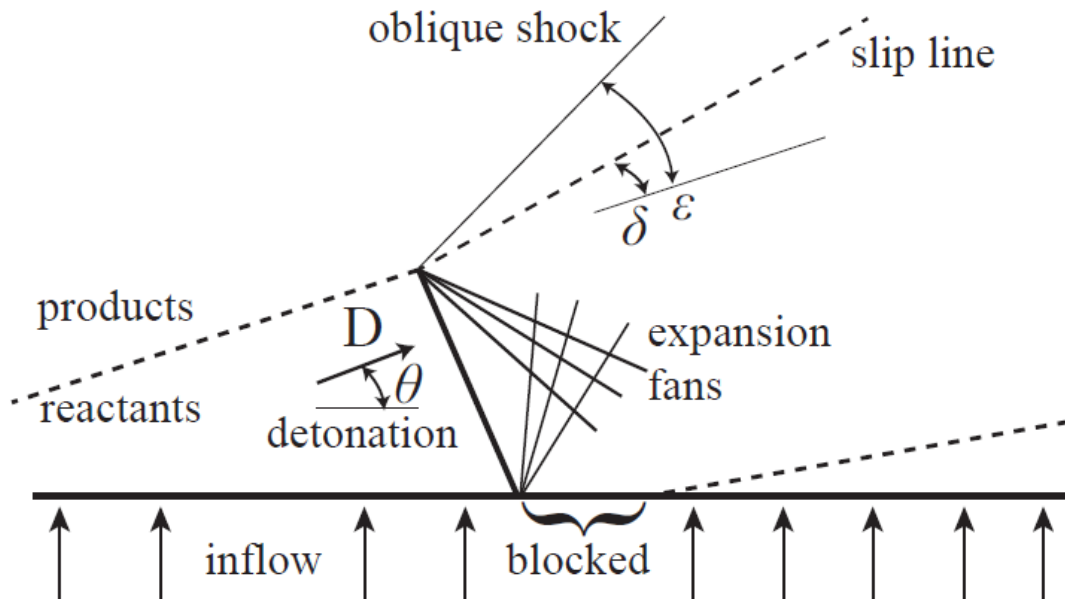
Figure 30. Sketch of a DW in an RDE flowfield. DW propagates from right to left. From Yu et al. [48].

Computational evaluation of the RDE flow structure demonstrates that the temperature of the inert products bounding the reactant mixture also affects the DW structure. Houim and Fievisohn [49] used chemically reactive 2-D CFD to examine the behavior of a DW in an RDE analog bounded by inert gases representing detonation products from previous cycles resulting in impedances of 0.29, 0.55, 0.71, 1.00, 1.73, and ∞ (solid wall). The impedance was defined as $Z \equiv \frac{R_I}{R_R} = \sqrt{\frac{T_R}{T_I}}$, where the subscript "R" denotes a reactant property and the subscript "I" denotes a inert gas property. The reactant temperature was held fixed at $T_R = 300K$, with T_I set to 100, 300, 600, 1000, or $3500K$, resulting in the variation in impedance. Note that as T_I increases, Z decreases. This analysis found that an impedance of 0.29, 1.73, of ∞ resulted in a stable detonation, an impedance of 0.55 resulted in a marginal detonation, and an impedance of 0.71 or 1.00 resulted in a failed detonation.

The highest impedance case ($Z = 1.73$), corresponding to an inert gas temperature

42

of $100K$, resulted in a detonation wave similar to that predicted by the DW wide side relief model sketched in Figure 29 as shown in Figure $31(a)$. This detonation wave has an oblique shock attached to the upper edge of the DW at the inert gas interface. The pressures rise across the normal shock preceding the DW and the oblique shock in the products, then decreasing as the product gases expand behind the DW front.

In comparison, the low impedance case ($Z = 0.29$), corresponding to an inert gas temperature of $3500K$, resulted in a detonation wave with a detached shock propagating through the inert gas ahead of the DW in the reactants, connected by an oblique shock connecting the two wave fronts as shown in Figure $31(b)$. This case more closely approximates the flow in an RDE, where the inert product gases from the previous cycle will have an elevated temperature. Blast waves, caused by unsteady interactions of shock waves, emanate from the upper edge of the DW front into the inert gas behind the detached shock, reinforcing it. The pressures rise across the normal shock preceding the DW and the detached shock, then decrease in the expansion region aft of these waves. Note the slip line separating the post-detonation products from the inert gas is steeper in the lower impedance case. The $Z = 0.55$ case, corresponding to an inert gas temperature of $1000K$, resulted in an intermittent oscillation between the attached and detached shock behavior.

RRDEs have been observed to have a similar DW flowfield to the axial type RDEs. Figure 32 shows a sketch of an experimental visualization of a non-premixed radial type RDE. To the author's knowledge, no high fidelity CFD simulations of an RRDE have been published for comparison. The experiment showed that the DW has similar behavior to the axial type RDE's DW, with the detonation occurring at a standoff distance from the reactants, possibly due to mixing. The pressure waves from the detonation cause injection of reactants to cease. Oxygen injection resumes once the channel pressure is reduced enough to permit this, followed by resumption of fuel
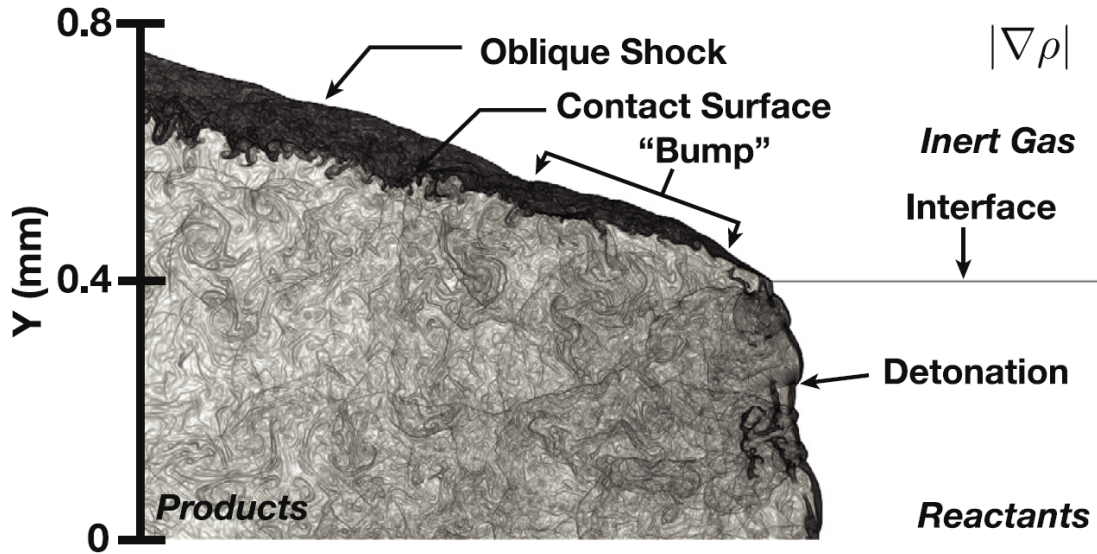
(a) High Impedance Products (Z=1.73)
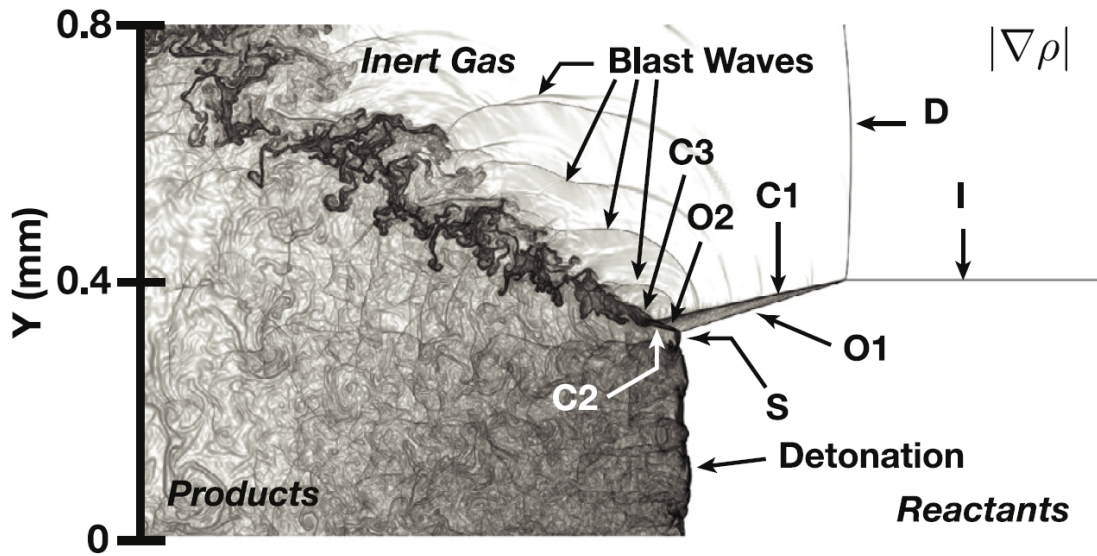
(b) Low Impedance Products (Z=0.29)

Figure 31. The effect of product impedance on RDE DW structure. Numerical Schlieren ($|\nabla\rho|$) results shown for (a) a high impedance case and (b) a low impedance case. Images from Houim and Fievisohn [49].

injection. The fuel and oxidizer are then able to mix before the DW passes again.
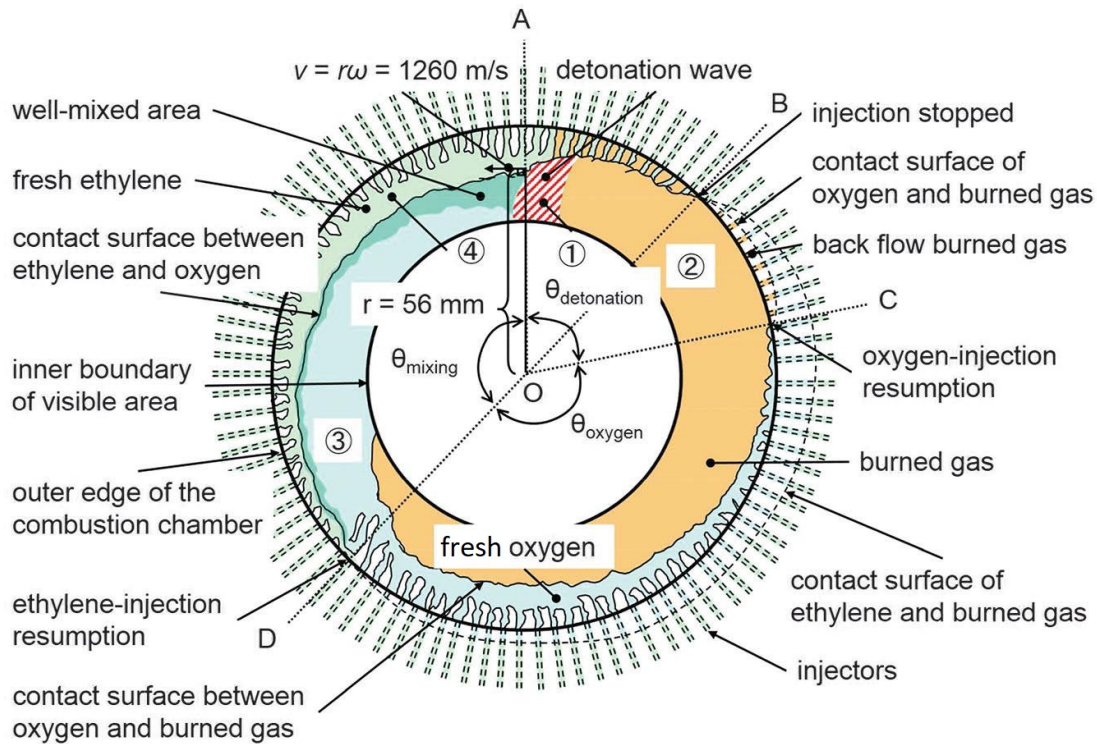
Figure 32. Sketch of a DW flowfield in an RRDE. DW propagates counterclockwise. From Nakagami et al. [2]. Image modified to correct a spelling error in "fresh oxygen".

2.4 Detonation Flow Instrumentation

A variety of high performance flow measurement and control devices are used for aerospace engineering applications. Flow measurement and control devices used in detonation flows are exposed to extremes of pressure, temperature, and frequency that demand instrumentation designed to withstand these conditions. Additionally, precise flow rate measurements are required to accurately determine the conditions under which these devices are operating, such as mass flow rate and equivalence ratio.

The remainder of this section begins with a discussion of pressure measurement devices commonly used in detonation flowfields and the challenges associated with them in Section 2.4.1. A discussion of high speed photography and high frequency

reactive flow visualization is presented in Section 2.4.2. Flow metering, by which mass flow and hence reaction chemistry is controlled, is explored in Section 2.4.3.

2.4.1 Pressure Measurement.

Due to the high pressures, temperatures, and frequencies experienced in an RDE, the pressure measurement devices used are selected to operate in this environment. Commonly used pressure measurement devices include Capillary Tube Attenuated Pressure (CTAP) devices and Infinite Tube Pressure (ITP) devices [50]. Kiel probes have also been used with limited application.

CTAP devices, as their name implies, attenuate pressure fluctuations. This is accomplished by placing the pressure transducer at the end of a long tube as shown in Figure 33 and relying on viscous dissipation within the tube to dampen fluctuations. The result is a pressure measurement of the average pressure [50]. Due to the standoff length of the tube, the pressure transducer is also protected from temperatures at the pressure source. While in theory any pressure transducer can be used in the CTAP device, in practice high speed probes are not used in this application because of the excessive data file sizes and the fact that only average pressures are being recorded.
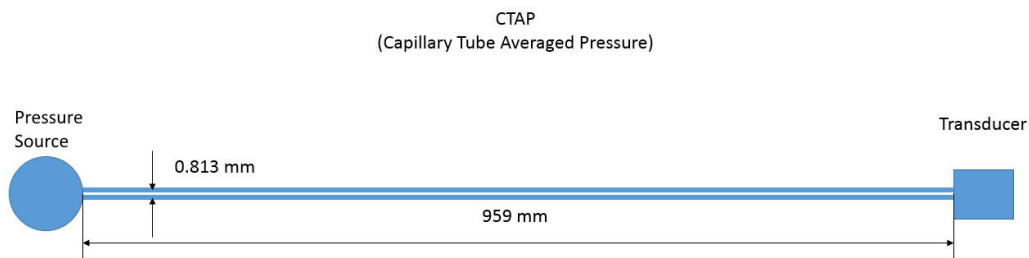
Figure 33. Schematic sketch of a notional CTAP measurement device from Stevens et al. [50]

The design of a CTAP measurement device is principally concerned with attenuation of the pressure. Stevens [50] utilized an estimate from White [51] that considered

46

the flow to be essentially steady at the nondimensional time $t^* = 0.75$, where

$$t^* = \frac{\nu t}{r_0^2} \tag{17}$$

The length of the tube required to attenuate the pressure was then be estimated as

$$L = at = \frac{at^* r_0^2}{\nu} \tag{18}$$

where a is the speed of sound within the tube, r_0 is the tube diameter, and ν is the kinematic viscosity of the fluid within the probe.

There are significant violations of the assumptions in this analysis. White [51] estimated the flow reached a steady state at $t^* = 0.75$ from analysis of starting flow in a circular tube after the application of a pressure gradient over the length of the tube with uniformly zero velocity as the initial condition. The nondimensional time cited was for this case specifically, with a constant pressure gradient, as opposed to the oscillating pressure gradient considered in an RDE. Additionally, the continuity and momentum equations solved to produce this result were for incompressible flow. Naples et al. [52] found that the pressure wave within the tube propagates as a shock well correlated to the Riemann shock tube problem, which implies supersonic, compressible propagation of the pressure wave. It is unclear what the effect of the viscous interaction with the shock will be over the length of the tube. As such this estimate should be regarded as a first order approximation of the required length to attenuate the pressure wave when a DW is the pressure source.

ITP devices are designed to measure high frequency pressure fluctuations in environments that cannot have a high speed pressure transducer mounted directly for reasons of extreme temperatures, etc. [53], similar to a CTAP. The principal difference is that the ITP's pressure probe is high frequency, located much closer to the

pressure source, and placed perpendicular to the tube axis, as shown in Figure 34. The end of the tube opposite of the pressure source can be closed, open (as shown), or open to a closed volume[53]. Due to the transducer being perpendicular to the tube the pressure transducer is also not directly impacted by the shock traveling down the tube, extending its survivability [50]. Due to the proximity of the pressure probe to the pressure source it is capable of detecting the high frequency pressure fluctuations, while still offering some protection from extreme temperatures. This high speed signal can be post-processed with a Fast Fourier Transform (FFT) to determine the cyclic frequency of the pressure fluctuations. In an RDE, this can be correlated to the DW frequency (f_D) in the channel. With a known radius at which the DW is propagating (r_D), the average v_D can then be determined as [34, 35]

$$v_D = 2\pi r_D f_D \tag{19}$$

If multiple DWs are present, this equation is modified as

$$v_D = 2\pi r_D \left(\frac{f_D}{N_D}\right) \tag{20}$$

where N_D is the number of DWs present in the channel.
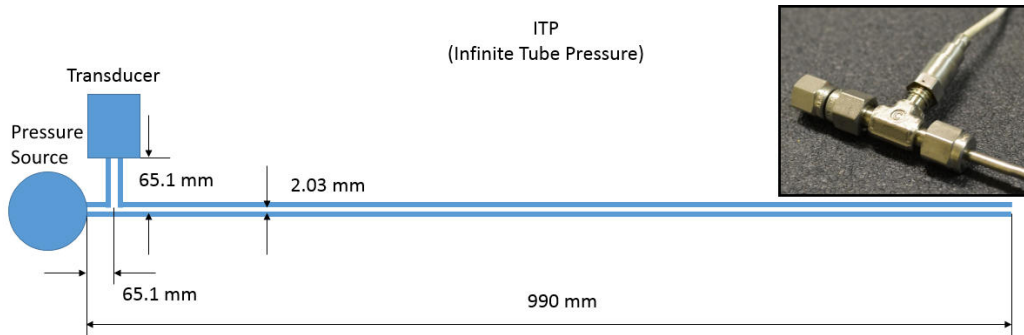
Figure 34. Schematic sketch of a notional ITP measurement device from Stevens et al. [50]

The pressure measurements from an ITP themselves can be of limited value without careful calibration and quantification of the specific configuration's interactions with the pressure frequency spectrum. Due to acoustic interactions within the device, including resonance in the cavity where the transducer connects and/or off of the end cap (if present) to the tube, the pressure response can be amplified or attenuated and phase lagged [53]. Specifically, the time varying pressure at a position x along the tube axis can be modeled as

$$P_x(t) = P_0 e^{-\alpha x} cos(\omega t - bx) \tag{21}$$

where P_0 is the source pressure, α is an attenuation factor, x is the axial distance from the source pressure, t is the time, ω is the natural frequency, and b is a phase lag factor.

For ITP design, the tube itself should have minimal sharp curvature to prevent reflections of pressure waves. Additionally, the pressure transducer should be located as close to the pressure source as possible to minimize attenuation and phase lag, and the volume of the cavity between the transducer face and the tube should be minimized to minimize acoustic interaction [50, 53].

Naples et al. [54] demonstrated that although the ITP can generally capture the fundamental frequency of the non-linear signal produced by the DW, the signal experiences significant attenuation $\mathcal{O}50 - 90\%$ and changes the perceived shape of the DW as compared to the PCB piezoelectric pressure transducer signal as shown in Figure 35. Furthermore the degree of attenuation and wave shape were sensitive to the construction of the ITP itself. Therefore, in general the ITP can only be relied on for the fundamental frequency of the detonation.

The Kiel probes is a pressure probe designed to measure stagnation pressure. The probe is comprised of a chamfered cowling surrounding a tube open normal to the
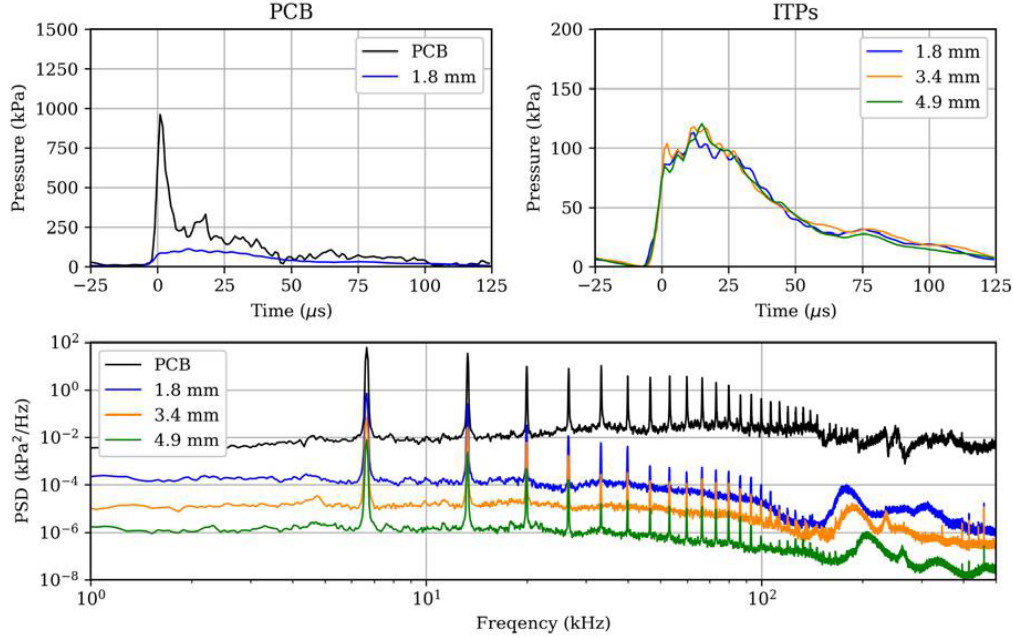
Figure 35. Differences in the frequency response and wave shape produced by an ITP compared to a PCB truth signal. Note the differing vertical axis for the upper two plots. From Naples et al. [54]

flow direction on one end and connected to a pressure transducer at the opposing end, as shown in Figure 36. This offers the pressure transducer some protection from the detonation environment. Due to the design of the shroud surrounding the probe it is insensitive to flow angle over approximately a 90° range, with a 10% or less error in this range [50, 55]. Due to the fact that the probe protrudes into the flow and experiences stagnation pressures and temperatures the lifespan of the Kiel probe is measured in milliseconds in a detonation environment, giving very limited functionality. However, the probe can be used effectively upstream of the detonation for reactant flow measurements [50].

2.4.2 High Speed Photography.

High speed photography is frequently employed to assist in understanding detonation flowfields. While specifics will depend on the camera model and manufacturer,
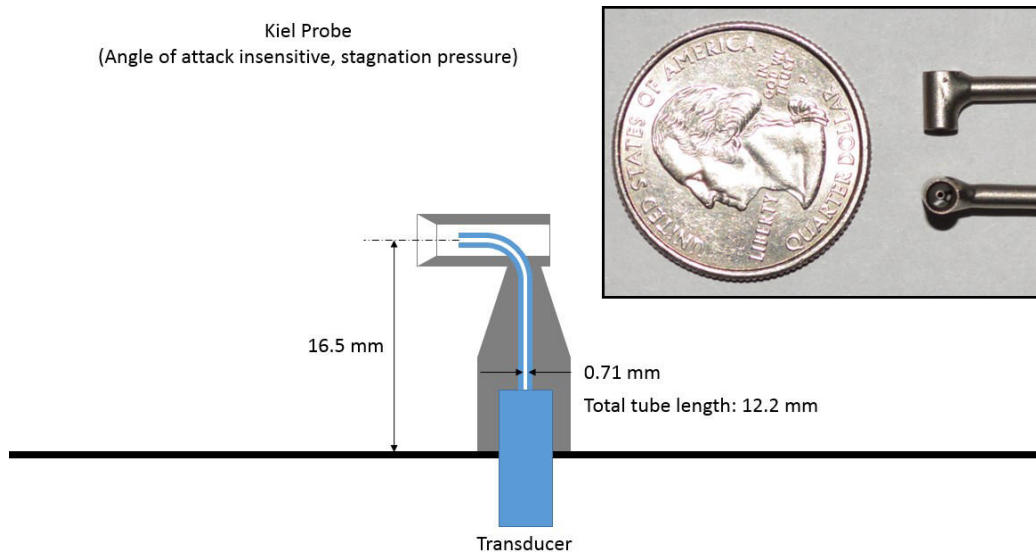
Figure 36. Schematic sketch of a notional Kiel Probe measurement device from Stevens et al. [50]

high speed cameras tend to have several common attributes. The frame rates are generally measured in the *kHz* range, with exposure times on the order of microseconds. Because of this, camera resolution is typically low compared to standard contemporary cameras. However, due to the high frame rate, gigabytes of raw footage per second of testing can be generated.

When considering high frequency events such as an RDE detonation, several criteria must be addressed. If one is concerned with observing a DW at multiple points within the same cycle, the frame rate must exceed the DW frequency by a suitable margin to see the desired evolution; this is essentially the Nyquist criterion. Additionally, the exposure time must be kept short to minimize blur for the fast-moving flow features such as DWs. However, the exposure time must be sufficient for the camera to collect enough photons to resolve the features within the flow. This time will depend on the intensity of the radiation over the observed frequency range.

For combustion environments, it would be ideal to directly observe the flame. A material with high transmittance is often used as a window for the combustion envi-

ronment, which will introduce minimal transmission losses and some lensing effects. A high melting temperature is also desired to increase service life. Due to the high temperature gradients and rapid temperature fluctuations, a low coefficient of thermal expansion is desired to minimize thermal stresses within the window, which will also increase service life.

Common window materials include fused quartz (SiO_2) or sapphire (Al_2O_3). These materials are often expensive, particularly when additional processing such as shaping and polishing are required. They are also brittle, fracturing easily unless properly secured. By contrast, materials such as polycarbonate, which is also known by its trade names Merlon, Makrolon, and Lexan, are much more flexible and better able to withstand high vibration, making them resistant to fracture and less sensitive to their mounting mechanism. The material and its processing is also much less expensive. This can be a consideration when designing a window for a predefined geometry that does not lend itself to redesign for a window made from traditional window materials, or for cost considerations. For these reasons, polycarbonate windows have been used as a window material to observe DWs [56, 57, 58], though with greatly reduced lifespan due to melting, burning, and erosion of the material. The burning of the material also produces additional chemical reactions, which could potentially affect the combustion chemistry and produce additional combustion features other than those being studied. The choice of material depends on the duration of the test, the temperature at the window, cost, and the nature of the radiation.

While all of these materials have high transmittance in the visual portion of the electromagnetic spectrum (400-700 nm)[59] and are therefore suitable for studies using chemiluminescence in the visible portion of the spectrum, they are not necessarily transparent in other parts of the spectrum. This is relevant to studies involving the use of OH* chemiluminescence. OH* is produced during combustion of both hydrogen

and hydrocarbon fuels with O_2 through various elementary chemical reactions, and exists for a brief period before being consumed by other elementary reactions, which makes it a useful indicator for the location in which chemical reactions are occurring [7]. OH* chemiluminescence relies on observation of radiation in the near-ultraviolet portion of the spectrum, with the band centered on 307.8 nm where OH* is known to emit radiation [60, 61, 62]. Radiation emitted from the combustion source is filtered with a band pass filter corresponding to the radiation emitted from OH*, then processed by the camera, which records the intensity of the radiation.

Because OH* is produced almost exclusively in the chemical reaction zone, this procedure allows visualization of the flame front itself, without interference from radiation being emitted by other sources or reactions. Because of the dependence of OH* chemiluminescence on radiation in a non-visible band of the spectrum, the window material choices become constrained for this application; specifically, high quality fused quartz/silica and sapphire are suitable [63], lower grade quartz and glass may or may not be suitable depending on manufacturing impurities, and polycarbonate is nearly opaque in the OH* radiation emission band as shown in Figure 37. For this reason, polycarbonate windows are not suitable for OH* chemiluminescence imaging.

2.4.3   Flow Metering.

Flow metering for compressible gases can be accomplished with a variety of Venturi tube devices. An example of such a device is the sonic nozzle [55]. Figure 38 shows a cross section profile sketch for a sonic nozzle. The device is mechanically simple, consisting of an orifice of known area with an aerodynamic profile to reduce losses. From isentropic flow theory, flow in the nozzle is accelerated to the sonic condition

53
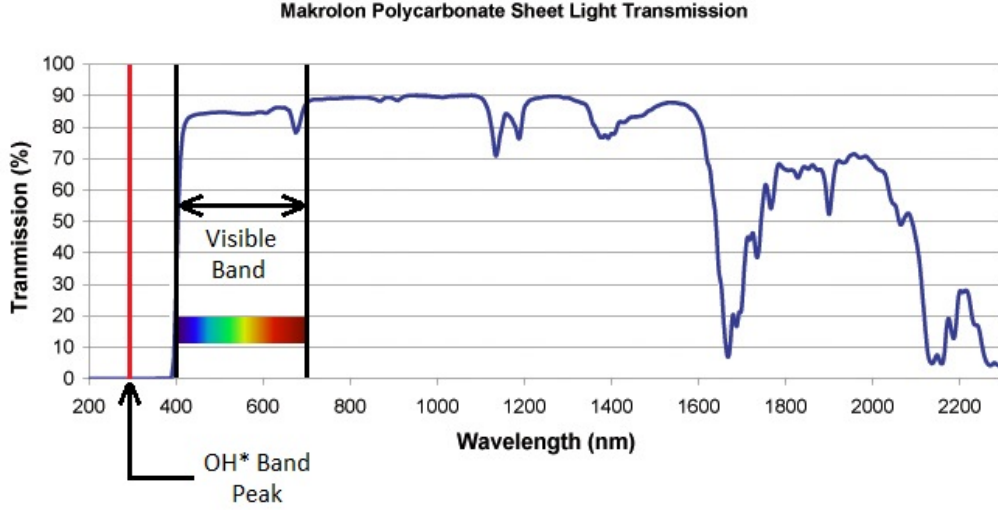
Figure 37. Spectral transmission for an example polycarbonate sheet. Note the transmission is high in the visible band and much of the near infrared spectrum, but is nearly opaque in the ultraviolet spectrum. Adapted from [64] with the addition of the Visible Band marker, OH* Band Peak indicators, and for formatting.

at the nozzle's throat, and the mass flow rate can then be estimated as

$$\dot{m} = C_D \frac{P_0 A^*}{\sqrt{T_0}} \sqrt{\frac{\gamma}{R} \left(\frac{2}{\gamma + 1} \right)^{\frac{\gamma+1}{\gamma-1}}} \tag{22}$$

provided the pressure critical pressure ratio is satisfied

$$\left(\frac{P}{P_0} \right)_{critical} = \left(\frac{2}{\gamma + 1} \right)^{\frac{\gamma}{\gamma-1}} \tag{23}$$

Thus, the mass flow rate can be estimated from the stagnation pressure (P_0), and stagnation temperature (T_0), the sonic nozzle's throat area (A^*), the working fluid's ratio of specific heats (γ), and the working fluid's specific gas constant (R). The discharge coefficient (C_D), is a term that accounts for viscous losses where $C_D = 1$ for the ideal case of no losses, and varies from $0 < C_D < 1$ for real nozzles. Yin et al. [65] found that the discharge coefficient varies between 0.90 and 0.98 for a number of small diameter (millimeter scale) sonic nozzles. The maximum C_D occurs

at $r/d = 2$, which corresponds to an optimization between aerodynamic smoothness and boundary layer growth. Szaniszlo [66] found that for a number of sonic nozzles operating at a Reynolds number, Re, of $10^5 < Re < 10^7$, the discharge coefficient was bounded by $0.984 < C_D < 0.995$, which is very close to one. These data also show a transition from laminar to turbulent flow at approximately $Re = 10^6$. At Re higher than this value, the flow remains turbulent, but the C_D increases monotonically towards one, as the flow begins to better approximate inviscid flow at high Re.
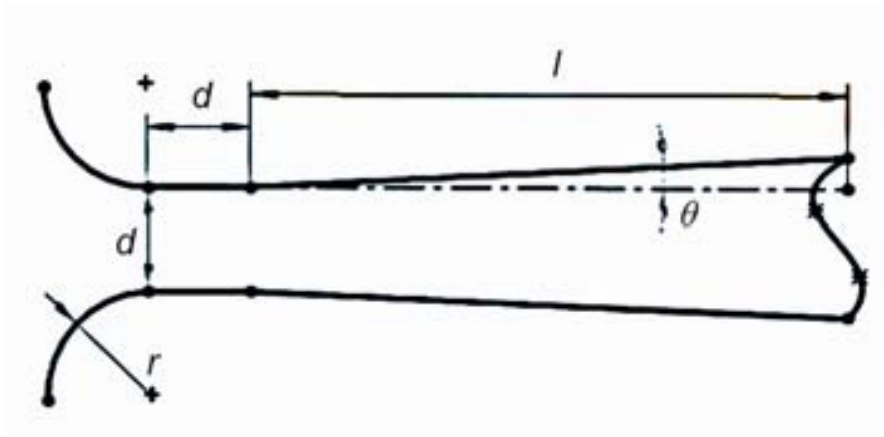
Figure 38. Cross sectional profile of a Sonic Nozzle [65]

2.5 Design Considerations

Due to their operating conditions, RDEs warrant special consideration for some of their design features. The extreme temperatures create a challenging environment for most materials necessitating cooling or managed operation, as discussed in Section 2.5.1. Due to the fuels used and the high detonation frequency, the design of the fuel injection system can have an effect on performance as discussed in Section 2.5.2. While the design of these features is not the focus of the current research, they affect the test device in question and represent challenges to future, operational designs.

2.5.1 Thermal Management.

Given the extreme temperatures present in a detonation environment, thermal management must be a consideration for any RDE design [3]. For reference, for an $H_2 - air$ detonation at $P_1 = 1.0132 Bar, T_1 = 288.15K$ the NASA CEA program predicts a post-detonation environment with $P_2 = 16.342 Bar, T_2 = 2942.44K$. While partial pre-burning effects and other losses will reduce these values, they remain elevated above the melting temperatures for most engineering materials. For reference, the melting point is 1670 K for AISI 304 Stainless Steel, 1665-1728 K for Nickel and its common alloys, and 1953 K for Titanium [67].

Several methods of managing these elevated temperatures are available and in common use in gas turbine engines which may be applicable to RDE cooling. An overview of these is shown in Figure 39. The film cooling and full coverage film cooling schemes both introduce further challenges into RDE design. By introducing air, the oxidizer, as a coolant into the detonation channel, the reaction chemistry is changed. Additionally, due to the PGC operating cycle in the detonation channel, much like the reactant flow the cooling flow may stop as the DW passes. This necessitates either increasing the coolant rate to compensate for the intermittency, or adding another compressor stage specifically for the coolant flow, similar to what has been done with PDEs [68]. Therefore, the convection cooling or impingement cooling schemes both appear more desirable. However, the rate at which coolant must be introduced to make these cooling schemes viable may be prohibitive. If a liquid fuel is used, it may be possible to use the liquid fuel as the coolant for the convection or impingement cooling schemes [68, 3, 69]. An alternative approach may be the introduction of ablative materials similar to those used on hypersonic aircraft heat shields [70]. However, this would necessarily produce a device with a finite operational life without significant overhaul. While all of these schemes present technical challenges

for integration with an RDE, for an operationally viable design a suitable thermal management scheme must be developed.

(a) Convection cooling.
(c) Film cooling.
(b) Impingement cooling.
(d) Full-coverage film cooling.
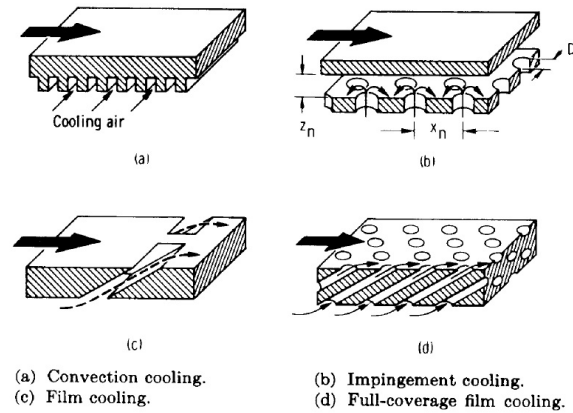
Figure 39. Cooling schemes commonly employed for turbines. Adapted from Glassman et al. [71] by removal of transpiration cooling scheme.

For research devices such as the one considered in this research these considerations may be simplified. For tests where the device will reach thermal equilibrium a separate water cooling system may be utilized. This would rely on running a cooling flow of water in channels around the hot areas of the detonation channel. Depending on the thickness of the material and the thermal conductivity, as well as the flow rate of the water, a temperature gradient will be supported between the channel mean temperature and the material surface temperature. If this temperature is kept sufficiently low, the material will not suffer damage. While the weight of such a water cooling scheme may be prohibitive on an operational system, weight is typically a low priority for ground testing.

Water cooling has been used for testing by Theuerkauf [72], Theuerkauf et al. [73, 74], Hatgus et al. [69], and many others [3]. For short duration tests, one can rely on the heat capacity and conduction of the test article itself to provide protection by conducting heat from the material surface to lower temperature regions of the device. This becomes an unsteady conduction problem to a first approximation. Provided the device has sufficient mass to absorb the thermal energy transfered to it from

57

the detonation, and sufficient time is allowed between runs to allow the device to reduce its temperature low enough for additional tests, the thermal damage to the test article's material can be greatly reduced relative to what the temperature limits of the material suggest. This method has been widely used by Huff [41], Huff et al. [34, 44], initial testing for Theuerkauf et al. [73], and many others, and is the thermal managment scheme used in the present work.

2.5.2 Injector Nozzles for Gaseous Fuels.

A number of reactant injection schemes are possible for RDEs. The purpose of the injectors is to introduce the reactants into the detonation channel. To maximize thermodynamic cycle efficiency, the total pressure loss resulting from injection should be minimized. For non-premixed reactants, the injection scheme also seeks to mix the oxidizer and the fuel to permit combustion. Due to the short interval between reactant injection and DW passage it is critical that the RDE's injection scheme is capable of rapidly mixing the reactants.

Duvall et al. [75] surveyed a number of common injection schemes including the Pintle, Jet In Crossflow (JIC), and Semi-Impinging Jet (SIJ) injector schemes shown in Figure 40. For the RDE considered, the Pintle injector experienced the lowest pressure loss, and the SIJ injector experienced the greatest pressure loss. The JIC injector configuration is one of the simplest architectures for fuel injection schemes, and is used in the present research. Sonic fuel injection is typically desired for jet in crossflow operation. The presence of a sonic jet in cross flow has been heavily investigated both in general and with specific application to fuel injection in SCRAMJET engines [76, 77, 78, 79, 80, 81]. Sonic fuel injectors are designed to penetrate into the air stream and generate turbulence, mixing the reactants. In supersonic crossflow, a bow shock forms in front of the jet, slowing the flow and increasing residence time.

Viscous interactions at the wall cause multiple recirculation zones at the jet's base, which can act as flame holders. Furthermore, the horseshoe vortex that forms at the jet/crossflow interface assists in mixing of reactants. Genin and Menon note that the flow structure is unsteady due to turbulent interactions [76]. Furthermore, the Mach number (M) and jet to free-stream momentum ratio, (J) defined as

$$J = (\rho u^2)_{jet}/(\rho u^2)_\infty \tag{24}$$

can affect the size of the recirculation zones and jet penetration. Specifically, increasing freestream M decreased the size of the recirculation zones, but had minimal impact on jet penetration. Increasing J resulted in an increase of both the recirculation pocket size and jet penetration. The authors chose no metric to compare jet penetration depth or recirculation zone size between cases.
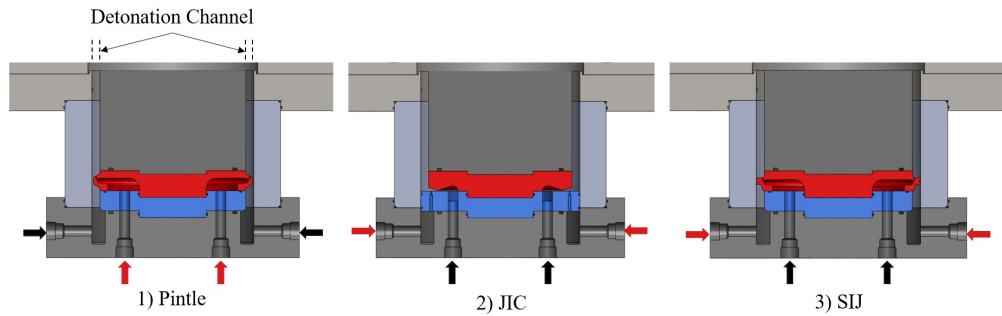
Figure 40. RDE injector types. From Duvall et al. [75].

Seiner et al. note that the jet in cross flow scheme has substantial pressure loss associated with it, which can significantly hinder efficiency [77]. The fuel injection within an RDE encounters significant temporal unsteadiness, and thus specific details of these jets as studied for nominally steady flows such as those encountered in SCRAMJETs are suspect. Additionally, the cross flow in an RDE will not be supersonic in the fuel injection region, so pressure losses may be less prohibitive in this
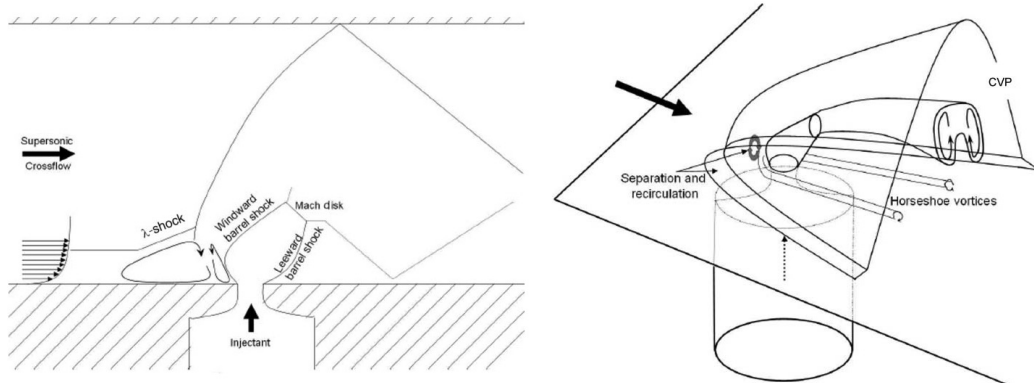
Figure 41. Structure of the interaction of a sonic jet in supersonic crossflow. Modified from Genin and Menon [76].

application.

Compression/expansion ramps, shown in Figure 42 are another passive fuel injection scheme commonly investigated for fuel injection in SCRAMJET engines [77]. This injection scheme is designed specifically to reduce pressure losses while permitting turbulence generation near the fuel injectors. While slightly more complex to produce, this may be a viable injection scheme in RDEs as well.
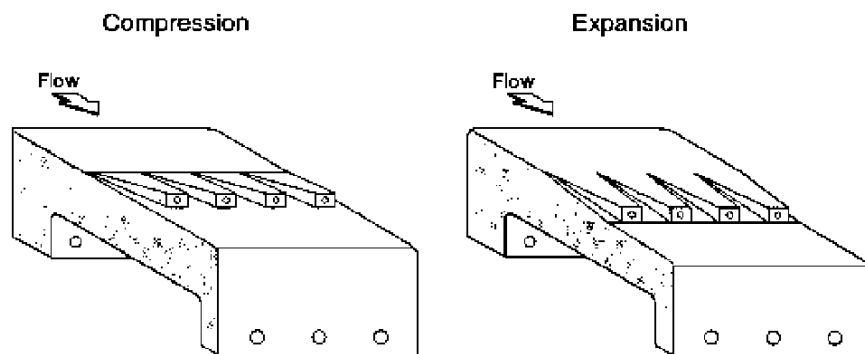
Figure 42. Schematic of parallel injection of fuel with air. From Seiner et al. [77].

The effect of the fuel and oxidizer injector spacing has been shown to be significant by Fujii et al. [82]. Select results from a 2D numerical simulation are shown in Figure 43. These calculations were performed with an unwrapped channel, modeled with periodic boundaries. The total injector area was kept constant for all cases, with the number of injectors (N) varied over a fixed length. The results for premixed

60

reactants with $N = 25$ and $N = 125$ are similar, with nearly all reactants being consumed by the DW, leaving no more than trace quantities of fuel. Non-premixed reactants at $N = 125$ shows a similar behavior, but non-premixed reactants at $N = 25$ shows a markedly different DW front, and comparatively large quantities of unburned fuels downstream of the DW front. The unburned fuel does not release heat at the detonation front, and is therefore less effective at driving the detonation. This is reflected in the DW speeds achieved.
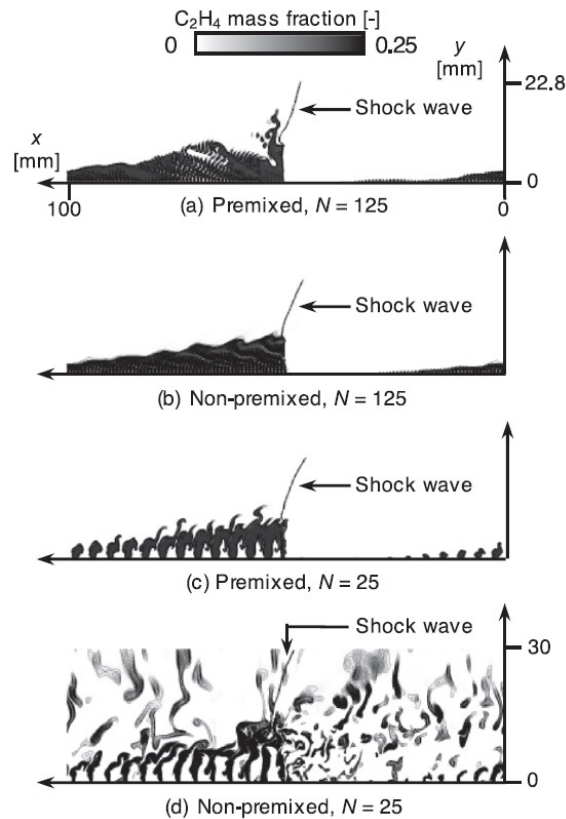
Figure 43. Effect of injector spacing on DW structure. From Fujii et al. [82].

Table 2 shows the effect of the number of holes (N) on the DW speed for both premixed and non-premixed detonations for the geometry examined by Fujii et al. [82]. The hole sizes were adjusted to maintain a constant injection area for all cases. The premixed cases all produce a v_D near $(v_D)_{CJ}$. For non-premixed reactants, the $N = 125$ case produced $v_D = (v_D)_{CJ}$, but the $N = 25$ case produced only $v_D =$

61

Table 2. Effect of injector spacing on v_D for Stoichiometric $C_2H_4+3O_2$; $(v_D)_{CJ} = 2377m/s$ for initial conditions of $P = 101kPa, T = 293K$ Data from Fujii et al. [82]

Mixture Type	N	v_D	$v_d/(v_D)_{CJ}$
Premixed	500	2382	1.00
Premixed	125	2372	1.00
Premixed	100	2374	1.00
Premixed	50	2363	0.99
Premixed	25	2490	1.05
Premixed	10	2498	1.05
Non-Premixed	125	2377	1.00
Non-Premixed	25	1999	0.84

$0.84(v_D)_{CJ}$. The discrepancy between the result of the premixed and non-premixed v_D at $N = 25$, and the discrepancy between the result of the non-premixed v_D at different values of N, suggests a strong link between mixing time and detonation velocity. Whereas the premixed detonations encountered little variance, as the reactants were already well mixed, the reactants in the non-premixed cases had not mixed well resulting in a less detonable mixture. While the applicability of the numbers in this specific study cannot be directly correlated to the design of other devices, this does suggest that the designer of an RDE should be cognizant of the effect injector spacing can have in non-premixed RDEs.

Experimental results from a premixed RDE by Andrus et al. [83] were not able to replicate the results shown for premixed RDEs, with wave speeds of approximately half the CJ speed. However, it was noted that deflagration combustion occurred in the channel for the mixture prior to arrival of the DW. A study using CEA where fuel was partially preburned and then detonated was conducted by Andrus et al., which indicated that preburning of the reactants had a significant impact on the DW velocity compared to the same mixture with no preburning. For instance, with 20% of the reactant preburned the DW velocity was reduced by approximately 10% at an initial temperature of $300K$. Therefore, the issue may be less related to injector

effects than to other effects not modeled in the CFD results from Fujii et al. [82]. This is a significant limitation in the current state of the art of detonation CFD, as Andrus et al. [83] showed in a survey of experimental and CFD computed detonations shown in Figure 44. It is notable that the CFD computed wave speeds tend to exceed the experimentally determined normalized wave speeds for both premixed and non-premixed experimental cases. Additionally, the non-premixed RDE experiments produced higher normalized wave speeds than the premixed RDE was able to achieve, which may be accounted for by the presence of more extensive preburning. Therefore, while the overall trends indicated in the nozzle CFD examination of nozzle spacing by Fujii et al. [82] may be representative of real system behavior, the specific values presented are likely unrealistic.
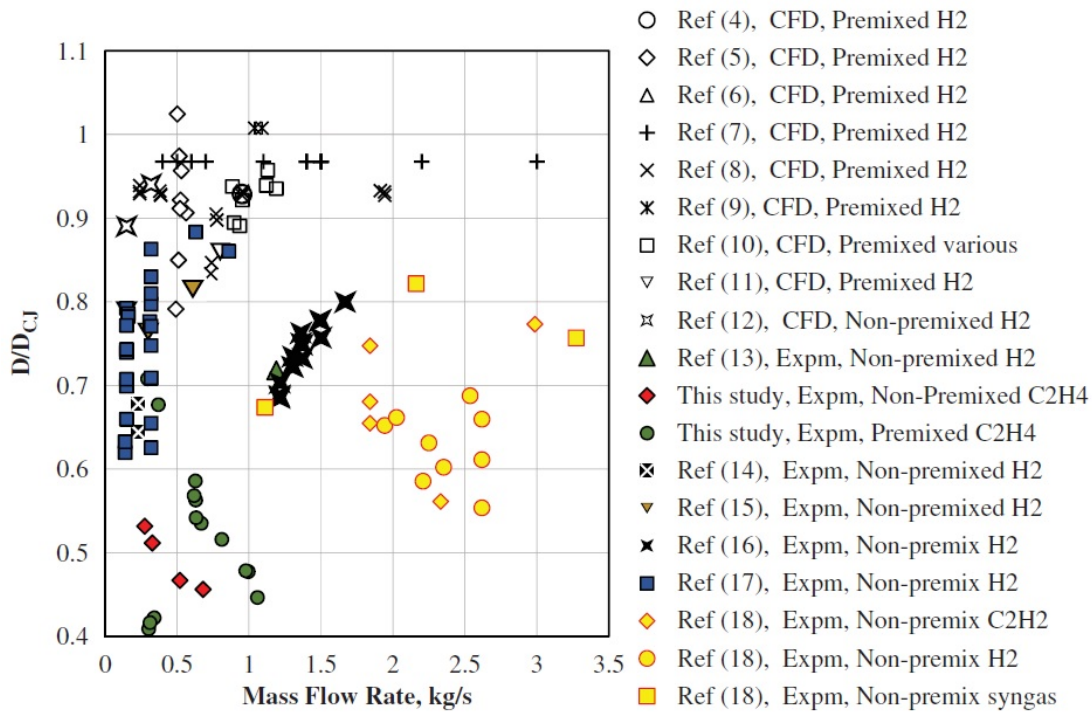
Figure 44. Comparison of DW speeds. From Andrus et al. [83].

2.6 Auxiliary Power Units

Auxiliary Power Units (APUs) are gas turbine engines connected to an electrical generator, and are designed to provide power for uses other than propulsion. Early APUs were typically comprised of a radial compressor, combustor, and radial inflow turbine, and provided power required to start the main engine with limited available electrical power [84]. Contemporary APUs have a multitude of architectures with axial or radial turbines, single or two stage turbomachinery, and fixed or variable geometry [85], and are commonly used on aircraft for a variety of applications, including main engine start, ground electrical power and environmental control, and emergency in flight power or emergency in flight main engine restart[84, 86]. Commercial aircraft APUs are often designed to provide power on the ground, with the main engines providing power in flight. The ability of an APU to start the aircraft independent of Aerospace Ground Equipment (AGE) such as start carts is especially important for military aircraft as it increases self sufficiency [86].

The desired utilization of an APU will introduce specific operational requirements and characteristics of the APU. Essentially all APUs used on flight vehicles are designed to maximize power density and minimize Specific Fuel Consumption (SFC), with low cost and maintenance requirements desired as well [85]. However, increasing the pressure ratio and therefore maximum temperature to achieve greater efficiency generally requires more mechanical complexity, resulting in greater cost and lower reliability [84]. For short-life systems such as missiles or for in-flight emergency power, rapid startup/response and high reliability APUs are desired [87, 88]. Restrictions on pressure fluctuations, maximum pressure and temperature, particulate debris, and other flow conditioning are typical for APUs used in engine startup applications, and a maximum temperature requirement in particular may significantly restrict thermodynamic efficiency of the device [84, 86, 87]. APUs that start and shut down

frequently, such as those used for ground operations on commercial aircraft, require high thermal load cycle life [84, 87]. For APUs designed to operate during flight the ability of the APU to be used at flight pressures and temperatures is also a critical design consideration. While some exceptions do exist, particularly for rockets and missiles, most APUs are designed for operation on the aircraft's primary fuel to simplify design considerations and supply logistics [84]. The designed usage of the APU will also dictate the ratio of pneumatic to electrical power provided/available. APUs commonly operate at pressure ratios of 4-10 with a Turbine Inlet Temperature (TIT) of $1300 - 1650K$ $(1900 - 2500°F)$ [85].

2.6.1 Turbomachinery.

Turbomachinery are rotating aerodynamics components designed to add power to or extract power from a working fluid. Turbines are turbomachinery used to extract power from a flow. Turbines are generally accompanied by Inlet Guide Vanes (IGVs) to condition the flow for maximum power extraction, and may also be accompanied by Exit Guide Vanes (EGVs) to increase efficiency.

A turbine operating at steady state experiences a change in angular momentum of [30]

$$\tau_O = \frac{\dot{m}}{g_c}(r_i v_i - r_e v_e) \tag{25}$$

The output power from the turbine is

$$\dot{W}_t = \omega \tau_O \tag{26}$$

or alternatively

$$\dot{W}_t = \frac{\dot{m}\omega}{g_c}(r_i v_i - r_e v_e) \tag{27}$$

which is the Euler turbine equation. Furthermore, from the first law of thermody-

namics, the power can be related to the thermodynamic states before and after the turbine with

$$\dot{W}_t = \dot{m}(h_{t,i} - h_{t,e}) \tag{28}$$

If the flow of products into the IGVs is perfectly aligned with the primary flow direction, i.e. radial for a RRDE, then the direction of propagation of the DW is inconsequential. However, if the flow enters the IGV ring at an angle, it is expected that the direction of propagation would make some difference based on the difference in change in angular momentum. For this reason, it is desirable to know if a difference exists in the flow direction at the IGV based on direction of propagation. If this does indeed result in a difference in performance, then controlling the direction of propagation would be desired. Unfortunately, the direction of propagation is essentially random without special procedures [3].

2.7 Summary

This chapter began with Sections 2.1 and 2.2, which provided an overview of the basic chemistry and fundamentals of detonations, providing the basis for detonation combustion. Integration of this chemistry with a specific combustion architectures was explored in Section 2.3, with an emphasis on detonation propulsion schemes. Section 2.4 provided a review of the methods used for measurement in a high frequency detonation environment, and the challenges associated with their usage. Section 2.5 provided further discussion on challenging design issues in development of an RDE. The chapter is concluded with a discussion of APUs in Section 2.6, which are a technology believed to be suitable for RRDE integration.

As discussed in Section 2.3.3.2 the location of the DW in a RRDE is currently unknown. The primary focus of this investigation is to gain insight into the behavior of the flow within the detonation channel, to include the location of the DW.

66

Sections 2.3.3.2 and 2.6.1 discuss the uncertainty in the effect of DW propagation with turbomachinery integration and performance. A secondary goal of the current research is to investigate this effect, providing a foundation for further development of operational RRDE systems.

III. Experimental Setup

The present research strives to achieve multiple research objectives, including flowfield visualization within the detonation channel, the effect of wave direction on turbine integration, and operation with simple gaseous hydrocarbon fuels. The research RRDE device is the same RRDE used by Huff et al., described in Section 3.1. Deviations to this configuration used to investigate the flowfield within the detonation channel are discussed in Section 3.2. Similarly, changes to the baseline configuration to investigate the effect of wave direction on turbine performance are discussed in Section 3.3. The configuration changes necessary to operate the research device on gaseous hydrocarbon fuels are outlined in Section 3.4.

3.1 Baseline Device Configurations

To distinguish the modifications of the present work from the initial device configuration, the original baseline configuration is described. The baseline RRDE is first discussed in Section 3.1.1. The facilities utilized to perform tests and collect data are described in Section 3.1.2.

3.1.1 Baseline RRDE.

This research utilized the RRDE hardware first developed by Huff et al. [41, 44, 34, 35]. The baseline device is shown in Figure 45 as an exploded diagram, and photographically in Figure 46. As described by Huff et al. it consisted of a Top Plate, Throat Ring, Channel Plate, Air Distribution Ring, Fuel Ring, Spacer Ring, Baseplate, Fuel Mounting Plate, and a Nozzle. The Baseplate serves as the chassis, and is in turn bolted to the thrust stand (not shown) to secure the device during testing. The Baseplate accepts the other various major components and assemblies.

68

The Fuel Mounting Ring is secured to the Baseplate and has twelve ports to accept fuel lines. The Nozzle is secured to the Baseplate, and serves as an aerodynamic surface. The Fuel Ring is mounted on the opposite side of the base plate, and has numerous small diameter holes to inject fuel into the device. Bolts installed in the Top Plate also pass through holes in the Spacer Ring into threaded holes in the Baseplate, securing these components together. The Spacer Ring accepts the high pressure air lines, and also serves to position the Top Plate at the correct position relative to the Base Plate. The Top Plate serves as the chassis for a sub-assembly of the Top Plate, Throat Ring, and Channel Plate, and also has a threaded port to accept pressure measurement instrumentation. The Throat Ring serves as an aerodynamic surface, with shims installed to vary the offset of this component from the Top Plate. The Channel Plate is secured coaxially with the Throat Ring and shims to the Top Plate. The Channel Plate serves as an aerodynamic surface, and also has several ports to accept pressure measurement instrumentation. This Top Plate sub-assembly is secured to the Spacer Ring as described above, locating the Air Distribution Ring and captivating it into position. The Air Distribution Ring itself provides a more azimuthally uniform air flow distribution to the Throat Ring by breaking up the airflow from the ten high pressure 3/4" DIA air lines installed in the spacer ring to fifty-five 0.375" DIA holes in the Air Distribution ring.

When assembled, these components provide an architecture to accept air and fuel lines, and route these reactants through passages and channels. A cross section of this flow path can be seen in Figure 47. The high pressure air is injected into the device through the Spacer Ring, distributed through the Air Distribution Ring, and fed into the Air Plenum, where it is compressed and ideally choked at the Throat at radius r_t, which is formed by the Throat Ring and the Fuel Ring. Similarly, high pressure fuel is injected through the Fuel Mounting Ring, passing into a distribution channel
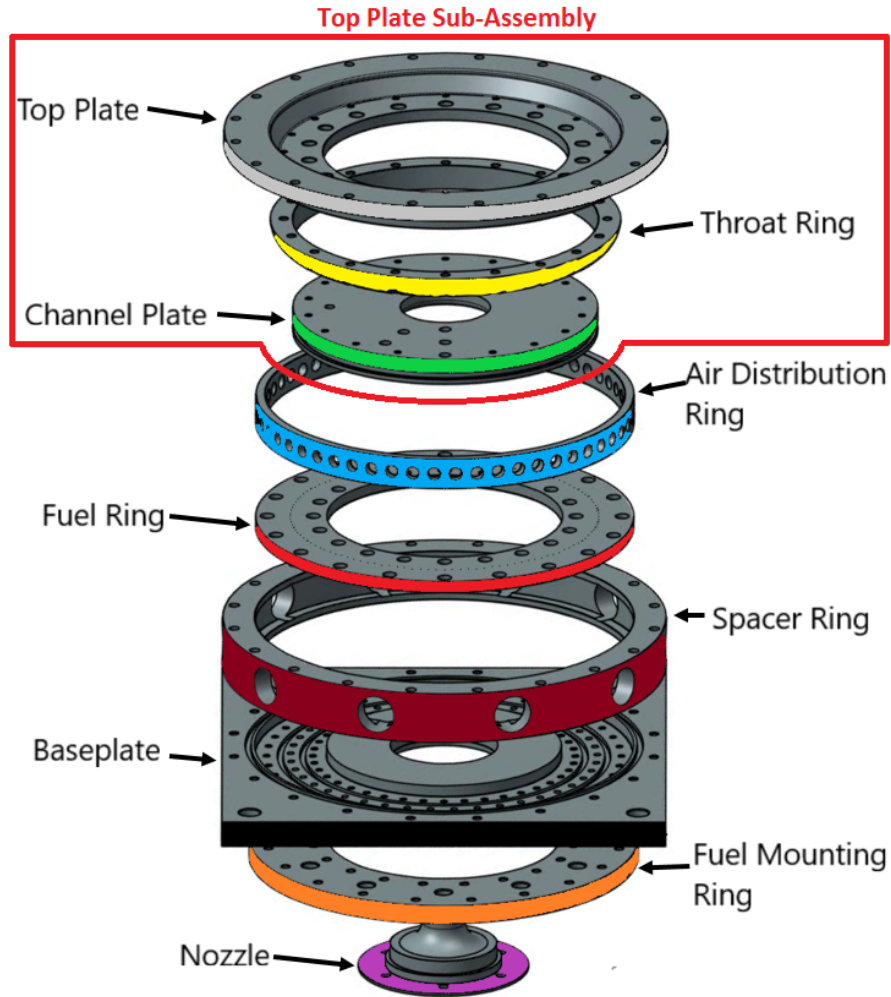
Figure 45. RRDE assembly major components. Modified from Huff [41].

in the Baseplate, and injected through the Fuel Ring at the Throat perpendicular to the airflow, forming a jet in cross flow injection system. The fuel and air mix as they propagate into the Detonation Channel, which is designed to have a constant cross section area radially until at least the Nozzle. The backward facing step formed by the Throat Ring both promotes mixing of the reactants and allows pressure reflections from the Detonation Wave (DW) which aid in DW propagation. The Detonation Channel is formed by the Fuel Ring and Base Plate on the lower surface, and the Channel Plate on the upper surface. These mixed reactants are consumed by a DW as they travel radially inward through the Detonation Channel. Following heat

70

(a) Front   (b) Back
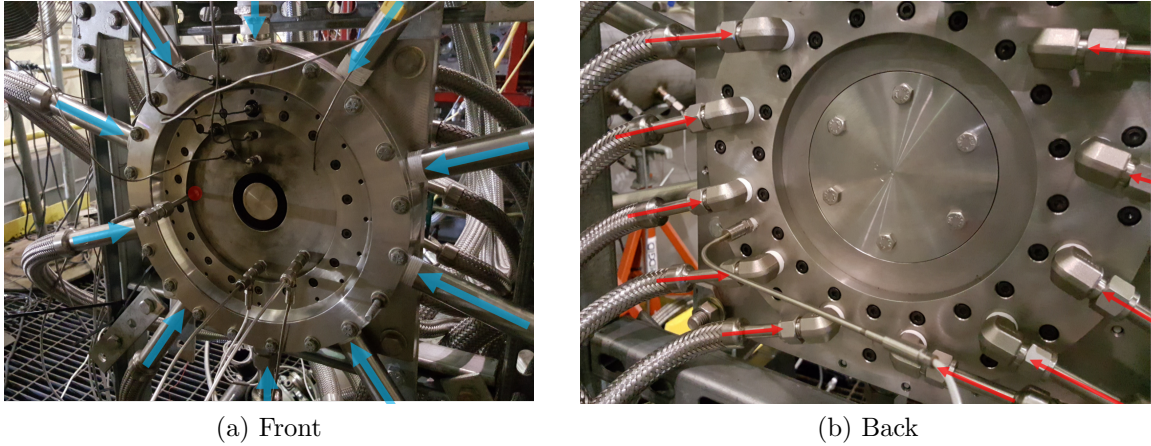
Figure 46. The original pure combustor baseline configuration. Blue arrows indicate air lines. Red arrows indicate fuel lines. The red dot indicates the predet port.

release the products propagate into the Nozzle, where they are turned axially by the Nozzle and inner radius of the Channel Plate and exit the device. Depending on the geometry of the installed Nozzle, the cross sectional area may vary through the Nozzle to provide back pressure. The detonation channel itself is intended to provide confinement of the detonation, which controls expansion of the products and aids the propagation of the DW.

This device is highly modular, allowing the user to independently change the Channel Plate, Nozzle, and Throat Ring height (with shims), which changes the channel area (A_c), exit area(A_n), and throat area (A_t), respectively. For a given channel height, the nondimensional throat area ratio (AR_t) and nozzle area ratio (AR_n) can be defined as follows:

$$AR_t = \frac{A_t}{A_c} \tag{29}$$

$$AR_n = \frac{A_n}{A_c} \tag{30}$$

The response of the baseline device to variations in A_c, AR_t, and AR_n has been documented in the previous work [41]. Throat channel heights (h_c) of 3.5, 4.0, and 4.5 mm, defined as the channel height at r_t, have been investigated. $A_c = 2\pi r_t h_c$,

71
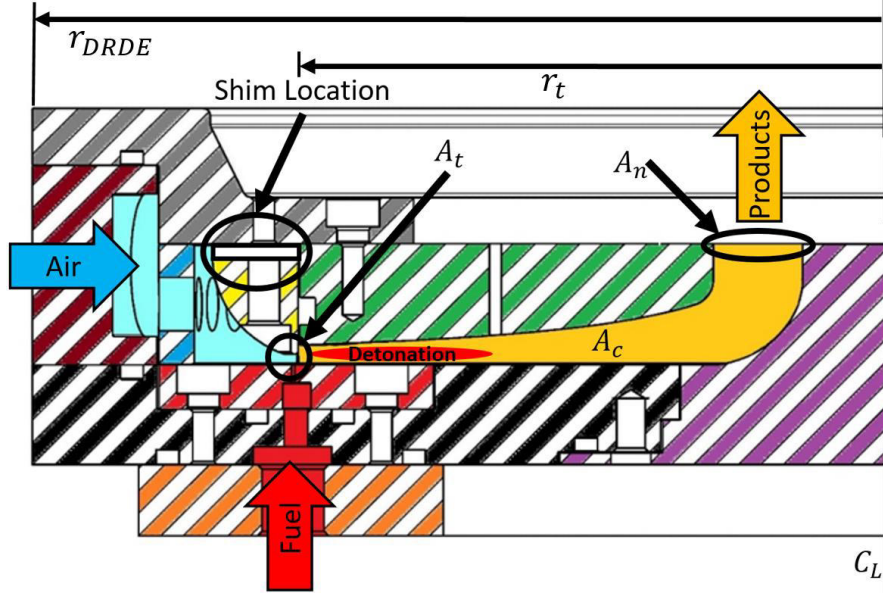
Figure 47. Cross section of the original pure combustor baseline configuration. From Huff [34]

and because r_t is fixed, the value of A_c is uniquely determined by h_c. AR_n values between 0.5 and 1 were investigated at $AR_t = 0.2$. The number and size of the fuel injection holes may also be varied by changing the Fuel Ring, as could the air injection scheme by manufacturing new air distribution components, though this has not been attempted to date. With a fixed geometry Nozzle installed, regardless of area ratio the device may be considered to be in a "pure combustor" configuration as shown in Figures 46 and 47; the primary purpose of which is to examine the detonation characteristics within the channel. Such characteristics include the response of v_D, N_D, r_D, etc. to changes in A_c, AR_t, AR_n, ϕ, $\dot{m}''$, fuel, etc. While the device does produce thrust in this configuration it is not optimized for this purpose.

Omega pressure transducers (Ref Table 3) and thermocouples (Ref Table 4), as well as Kulite high frequency pressure probes (Ref Table 5), were used to collect data from the RRDE itself. Figure 48(a) identifies the locations of the Omega pressure transducer CTAP ports in green, ITPs with Kulites in blue, and the Omega thermocouple in yellow. The location of the Kulite installed in the fuel plenum is indicated

in Figure 48(b).

The high speed pressure transducer shown in Figure 48(b) was installed in the fuel plenum prior to the current research to measure the pressure fluctuations following passage of a DW, but has not been used until the present research. As discussed in Section 2.3.3, flow reversal occurs following the passage of the DW due to the pressure increase. This pressure transducer will allow further investigation and quantification of this effect within the fuel plenum itself.

Table 3. Omega pressure transducers for Baseline Pure Combustor RRDE.

Location	Model	P Range	Uncertainty	Serial #	Measurement
-	-	kPa(PSIA)	kPa(PSIA)	-	Device
Channel Plate, R1=9.53 (cm)	PX429-250A5V	0-1700(0-250)	±1.4(0.2)	463871	CTAP
Channel Plate, R2=8.26 (cm)	PX429-250A5V	0-1700(0-250)	±1.4(0.2)	461789	CTAP
Channel Plate, R3=6.99 (cm)	PX429-250A5V	0-1700(0-250)	±1.4(0.2)	461766	CTAP
Channel Plate, R4=5.71 (cm)	PX429-250A5V	0-1700(0-250)	±1.4(0.2)	424889	CTAP
Channel Plate, R5=4.45 (cm)	PX429-250A5V	0-1700(0-250)	±1.4(0.2)	463884	CTAP
Air Plenum, AP	PX429-150A5V	0-1000(0-150)	±0.82(0.12)	423725	CTAP

Table 4. Omega thermocouples for Baseline Pure Combustor RRDE.

Location	Model	T_{max}	Uncertainty	Measurement
-	-	(K)	(K)	Device
Channel Plate Exterior	KMQXL-062U-6 (K-type)	1608	±0.0075T	Direct

Table 5. Kulite high speed pressure transducers for Baseline Pure Combustor RRDE.

Location	Model	P Range	Bandwidth	Serial #	Measurement
-	-	kPa(PSIA)	(-3dB)	-	Device
Channel Plate, K1=6.99(cm)	ETL-4-GTS-190-1000A	0-6900(0-1000)	50Hz-150KHz	N/A	ITP
Channel Plate, K2=6.99(cm)	ETL-4-GTS-190-1000A	0-6900(0-1000)	50Hz-150KHz	N/A	ITP
Fuel Plenum	ETL-4-GTS-190-1000A	0-6900(0-1000)	50Hz-150KHz	7832-10-168	Direct

The Nozzle may be replaced with a Garrett GT3582R turbocharger, which the research device was designed to interface with by Huff et al. [41, 34], as shown in Figure 24. In this configuration, a special channel top plate is installed with mounting provisions for a set of fixed blade 23.5°, 32.0°, or 39.0° turning angle IGVs, which condition the flow for entry into the radial inflow turbine. The variations in turning

73

(a) Front   (b) Back
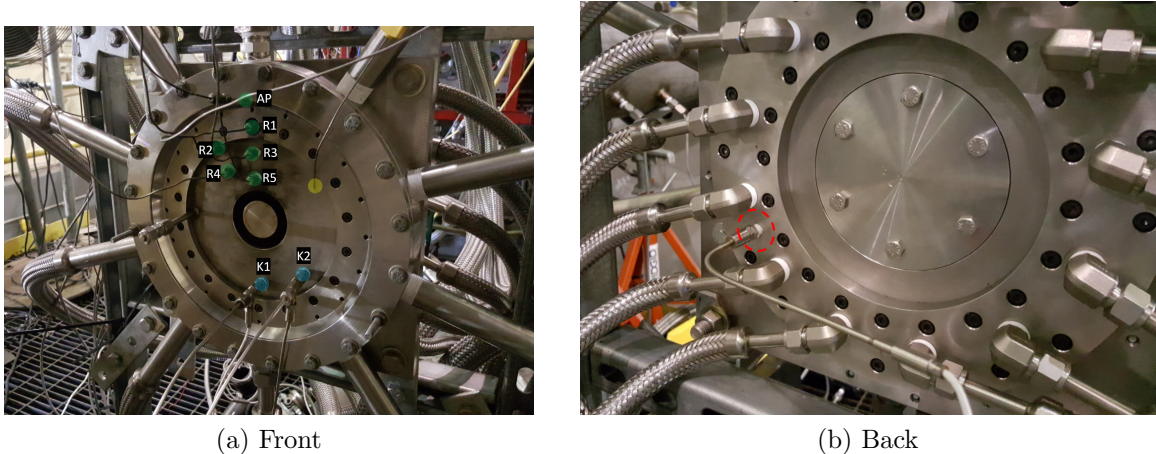
Figure 48.   The original pure combustor baseline configuration's instrumentation. Front: Green dots indicate CTAP ports. Blue dots indicate ITP ports. The yellow dot indicates the thermocouple location. Back: The high speed Kulite pressure transducer's location is indicated with a dotted circle.

angle permit differing tangential flow velocity to more closely match the turbine tip speed. The compressor of the turbocharger is only used to determine output power for the device and does not pump fuel or oxidizer used for combustion. With the turbocharger, modified top plate, and a NGV ring installed the device was considered to be in a "turbo" configuration.

Prior to the present research, two of the high pressure air flexlines were also replaced with an alternative style of air line following damage to the previously installed flexlines unrelated to operation of the RRDE. This change is expected to have minimal impact on operation.

3.1.2 Test Facilities.

To support the operation of the device, test facilities that support safe operation of the detonating test article, provide the reactants at the desired pressures and flow rate, and are set up to receive and store the measurement data were required. The Detonation Engine Research Facility (DERF) located in D-Bay on Wright Patterson Air Force Base (WPAFB) was utilized to satisfy these requirements.

74
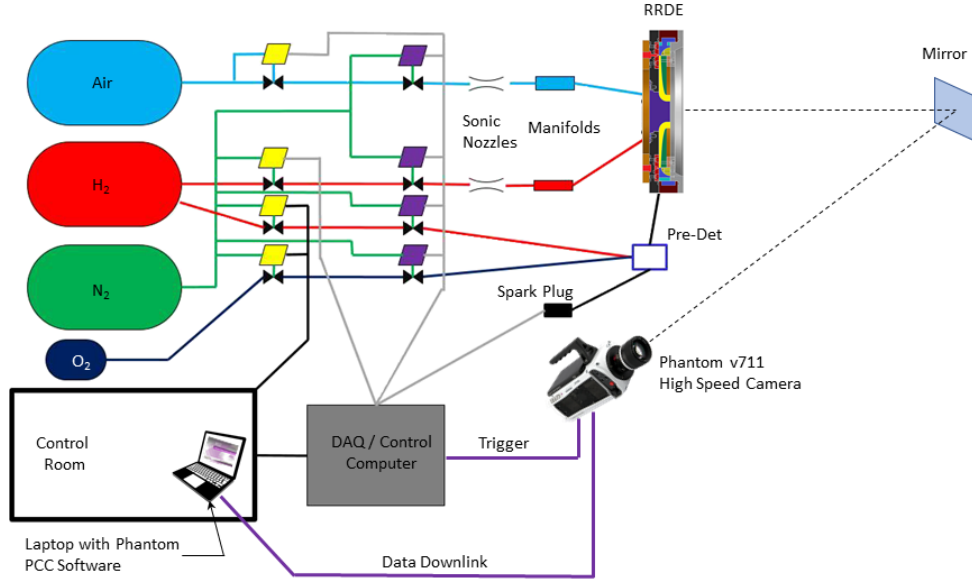
Figure 49. Test facility setup, adapted from Huff et al. [34].

The test facilities setup is described here, and in further detail by Huff [41]. For all configurations, the gaseous fuel and oxidizer used in testing were pressurized and stored in high pressure reservoirs as shown in Figure 49. These reactants are routed into the facility through pipes and tubing, then regulated down to a suitable working pressure for the distribution system. The reactants are then further regulated in pressure to achieve the desired mass flow rate set by the user before every experiment via the digital flow control computer. Prior to entering the research device, the reactants pass through sonic nozzles of a known diameter (Ref. Table 6), with the pressure and temperature measured upstream of the sonic nozzle with pressure transducers (Ref. Table 7) and thermocouples (Ref. Table 8) respectively as shown in Figure 50 to determine the mass flow rate of the reactants via Equation 22.

Table 6. FlowMaxx Sonic Nozzles used with the Baseline RRDE facilities.

System	Model	$D_2, mm(in)$	Serial #
Air	SN32-SA-0315	8.001 (0.315)	980-1
Fuel	SN16-SA-089	2.261 (0.089)	922-2

75
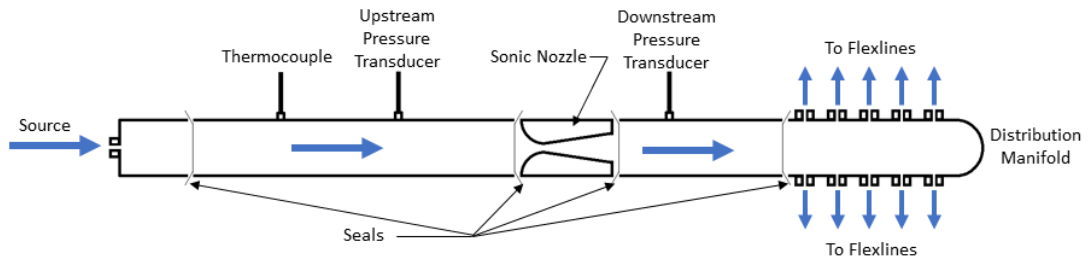
(a) Sketch of generic mass flow measurement device
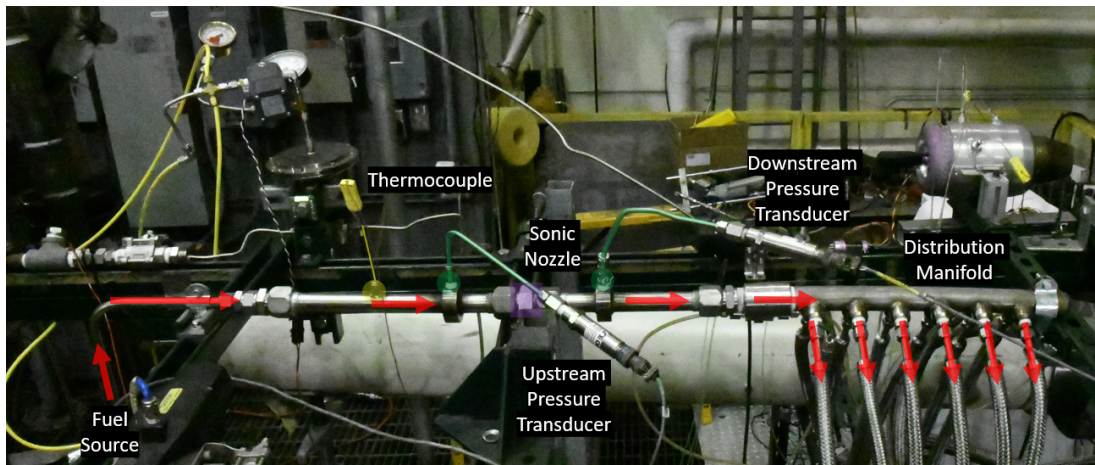
(b) Fuel System
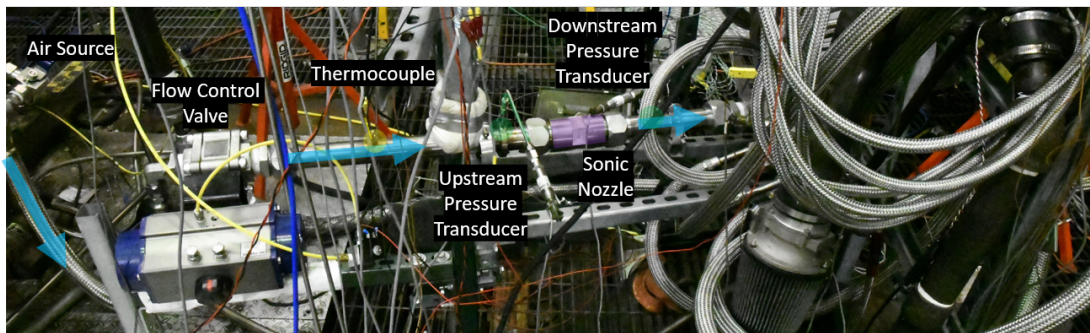
(c) Air System

Figure 50. Gaseous reactant measurement and distribution systems.

Location	Model	P Range	Uncertainty	Serial #	Measurement
-	-	kPa (PSIA)	kPa (PSIA)	-	Device
Fuel Sonic Nozzle Upstream	PX429-3.5KA5V	0-24100(0-3500)	±19(2.8)	466402	Direct
Fuel Sonic Nozzle Downstream	PX429-2.5KA5V	0-17200(0-2500)	±14(2.0)	450124	Direct
Air Sonic Nozzle Upstream	PX429-2.5KA5V	0-17200(0-2500)	±14(2.0)	463399	Direct
Air Sonic Nozzle Downstream	PX429-1.0KA5V	0-6900(0-1000)	±6(0.8)	443599	Direct

Table 8. Omega thermocouples for Baseline RRDE facilities.

Location	Model	T_{max}	Uncertainty	Measurement
-	-	(K)	(K)	Device
Air Sonic Nozzle Upstream	KMQSS-125U-6 (K-type)	1608	±0.0075T	Direct
Fuel Sonic Nozzle Upstream	KMQSS-125U-6 (K-type)	1608	±0.0075T	Direct

The pressure is also measured with a pressure transducer downstream of the sonic nozzle (Ref. Table 7) to confirm choked flow via Equation 23. Following the sonic nozzle, the reactants enter the distribution manifold, which routes the reactants to the research device through the metallic flex lines at the back (fuel) and outer radius (oxidizer) of the device, as shown in Figure 46.

Note that as configured the pressure transducers and thermocouples indicated in Figure 50 measure the static pressure and temperature of the flow. This is true for both the oxidizer and fuel measurement systems. However, as will be discussed shortly the quantities P_0 and T_0 are required for mass flow calculations. For the geometry used in the flow measurement system, the ratio of the cross section area at the location of the pressure and temperature measurement to the throat area is $\frac{A}{A^*} = 30.9$ for the air measurement system and $\frac{A}{A^*} = 84.9$ for the fuel measurement system. Using the area-Mach number relation from quasi-1D isentropic flow theory,

$$\left(\frac{A}{A^*}\right)^2 = \frac{1}{M^2}\left[\frac{2}{\gamma+1}\left(1+\frac{\gamma-1}{2}M^2\right)\right]^{\frac{\gamma+1}{\gamma-1}} \tag{31}$$

and solving for M it was found that $M = 0.0188$ for air and $M = 0.0068$ for fuel in

the measurement section. Then, from 1-D isentropic flow theory using

$$\frac{T_0}{T} = 1 + \frac{\gamma - 1}{2}M^2 \tag{32}$$

and

$$\frac{P_0}{P} = \left(\frac{T_0}{T}\right)^{\frac{\gamma}{\gamma-1}} \tag{33}$$

the solution of these equations shows that for air $\frac{T_0}{T} = 1.0001$ and $\frac{P_0}{P} = 1.0002$, and for the fuel system $\frac{T_0}{T} \approx 1$ and $\frac{P_0}{P} \approx 1$. Thus, the static pressures and temperatures measured are essentially the same as the total pressures and temperatures at the Mach numbers experienced for the geometry used in these systems. Therefore, these quantities were taken to be the total quantities in calculations.

The signals from all transducers and thermocouples were received by a National Instruments Data Acquisition (DAQ) computer. A custom Laboratory Virtual Instrument Engineering Workbench (LabVIEW) program was used to control reactant flow, operate the predet, and record all transducer signals. The LabVIEW program also provided preliminary results for $\dot{m}_{air}$, $\dot{m}_{fuel}$, and ϕ based on time averaged $\dot{m}$ through the sonic nozzles from the time the predet is fired until the time the fuel is shut off, and f via an FFT power spectrum function from the high speed pressure transducers.

Error of derived quantities such as $\dot{m}$, $\dot{m}''$, and ϕ was estimated using Moffat's method of partial derivatives [89]

$$\delta R = \left\{\sum_{i=1}^{N}\left(\frac{\partial R}{\partial X_i}\delta X_i\right)^2\right\}^{\frac{1}{2}} \tag{34}$$

In this way, both the error of the variables, δX_i, and the sensitivity of the function to this error, $\frac{\partial R}{\partial X_i}$, is accounted for in the error estimate of derived quantities.

For example, consider Equation 22 for $\dot{m}$ under choked flow conditions. P_0 and T_0 are measured in the experiment with uncertainties δP_0 and δT_0. C_D has a fixed value assumed to be 0.99, and A^* is precisely known; therefore these two variables are considered to be without error for the purpose of this error estimate. The gas properties $\gamma = 1.4$ for both air and H_2 gas, and $R = 288.2 \; \frac{J}{kg-K}$ for air and $R = 4124.3 \; \frac{J}{kg-K}$ for H_2 gas, are also considered to be precisely known. Taking the partial derivative with respect to P_0 and T_0,

$$\frac{\partial \dot{m}}{\partial P_0} = \frac{C_D A^*}{\sqrt{T_0}} \sqrt{\frac{\gamma}{R} \left(\frac{2}{\gamma + 1} \right)^{\frac{\gamma+1}{\gamma-1}}} \tag{35}$$

$$\frac{\partial \dot{m}}{\partial T_0} = \frac{-C_D P_0 A^*}{2 T_0^{\frac{3}{2}}} \sqrt{\frac{\gamma}{R} \left(\frac{2}{\gamma + 1} \right)^{\frac{\gamma+1}{\gamma-1}}} \tag{36}$$

With the known error in the measured quantities, δP_0 and δT_0 (Ref. Tables 7 and 8), the error in the derived quantity $\dot{m}$, $\delta \dot{m}$, is then estimated to be

$$\delta \dot{m} = \sqrt{ \left(\frac{\partial \dot{m}}{\partial P_0} \delta P_0 \right)^2 + \left(\frac{\partial \dot{m}}{\partial T_0} \delta T_0 \right)^2 } \tag{37}$$

which varies from test to test depending on the temperature of the reactants and the total pressure required to achieve the target mass flow rate.

To initiate a detonation, a pre-detonator, or pre-det, was used. The pre-det operates with the same H_2 fuel used to operate the RRDE, with gaseous O_2 used for the oxidizer. The flow of these reactants was regulated by the control computer, which allows flow of these reactants into the pre-det for a brief period once the fire signal is received. After the $H_2 - O_2$ reactants are injected into the pre-det, the control computer sends a second trigger signal to the spark plug, which initiates combustion within the pre-det, where the reactants undergo DDT and are routed into the detonation channel to initiate DDT in the RRDE's detonation channel. The

location of the pre-det port is highlighted in red in Figure 46. The pre-det can be fired without reactants flowing in the RRDE and frequently was for operational checkout. For testing the RRDE's reactants were brought to a steady mass flow rate prior to firing the pre-det.

For cases where a high speed photography system was to be used, the control computer also sent the trigger signal to the high speed camera to initiate recording, which is initiated immediately following the trigger signal. The duration of the recording is set by the user prior to testing through the Phantom PCC software package on a separate laptop in the control room. Following recording, the imagery is transmitted to the control laptop for review and further processing. Details on the usage of this camera specific to the present testing are discussed in Section 3.2.

3.2   Flowfield Visualization

Observation of the flowfield within the research device is the primary objective of the present research; specifically, observation of the DW radial location (r_D) was desired. Determination of r_D in an RRDE is non-trivial due to the absence of a constraint restricting the DW to a specific radius or small range of radii, as is the case in axial RDEs. Additionally, due to the geometry of the original RRDE, direct observation of the DW was not possible. Huff [41] was able to observe the reflection of the DW's chemiluminescence off of the nozzle or turbine, but this shows the angular location of the wave only. Determination of a more precise DW location enables a better calculation for the DW velocity (v_D). Visual interrogation of the flowfield to identify detonation features was desired to reduce ambiguity in identifying features. To do this, the top plate was replaced with a window of the same contour.

3.2.1 Window Material Choice.

Selection of a window material involved multiple tradeoffs between technical performance/suitability, cost, and manufacturing/delivery time. As discussed in Section 2.4.2, OH* chemiluminescence is commonly used in combustion studies to determine the exact location of the combustion chemical reactions. This can provide results that are easier to interpret, and can be taken with high speed cameras designed for this application. For this reason, OH* chemiluminescence was considered as an imaging technique for the present research. However, OH* chemiluminescence requires a material that is transparent in the 307.8nm range of the electromagnetic spectrum. This limits material choices to materials such as high grade fused quartz or sapphire. However, manufacturing large parts such as the channel top plate from these materials is expensive both because of the cost of the material itself and the cost of the specialized precision grinding manufacturing techniques required to shape it to a specified profile. Additionally, both of these materials are brittle and require specialized mounting fixtures to avoid fracture in high vibration environments, which would necessitate further modifications to the test device. An alternative would be to manufacture a small window in the channel top plate, designed to accept a smaller, standard size window, eliminating the specialized manufacturing and the bulk of the material cost. However, this would restrict the radial and angular viewing area, modify the flow boundary with the gap at the window-metal interface, and require manufacture of an additional specialized channel top plate to house the window.

In contrast, clear polycarbonate is opaque at the 307.8nm wavelength, precluding the use of OH* chemiluminescence, but is transparent to radiation in the visible spectrum. The polycarbonate material itself is relatively low in cost, and can be shaped to a specified profile using lower cost machining techniques. The polycarbonate top plate itself was manufactured with drilled and tapped holes designed to accept the

same style fastener used to install the original metallic channel top plate, resulting in minimal design change. Despite the presence of these holes and the high vibration environment, the polycarbonate material is not brittle and did not fracture during testing. The decision to use polycarbonate was made primarily because of cost considerations, material was available on-hand, the entire channel top plate could readily be made transparent for maximum visibility, and it was sufficient to complete the research objective when coupled with standard high speed photography.

3.2.2 Polycarbonate Window Setup.

To interrogate the flowfield for the present research, the pure combustor configuration of the research device was utilized. The DW itself was observed by replacing the channel top plate with a $12.2mm$ thick clear Makrolon polycarbonate sheet that was machined with the profile of the $4.5mm$ channel top plate to serve as a window, as shown in Figure 51. Because the original channel top plate was thicker than the polycarbonate, a metallic spacer ring was also manufactured to offset the transparent top plate by this difference in thickness such that a $4.5mm$ channel height was achieved. This reduction in thickness means there was a difference in the channel's profile in the vicinity of the nozzle exit; specifically, the profile does not exist on the channel plate side for the thickness of the metallic spacer ring; this profile deviation is indicated by dotted lines in Figure 51(b).

After machining, the polycarbonate channel top plate was semitransparent due to typical machining imperfections; however, the location of objects in close proximity to the surface was easily discernible. Because of the small channel height, and because of the radiative intensity of the DW's chemiluminescence, the location of a light source within the channel was readily apparent. Figure 52(a) shows the machined polycarbonate channel top plates prior to installation with the letter "A" and various
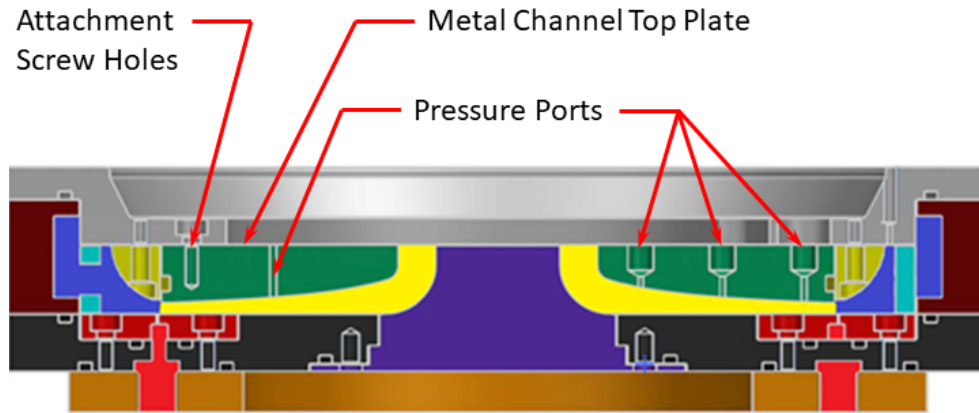
(a) Baseline metal channel top plate
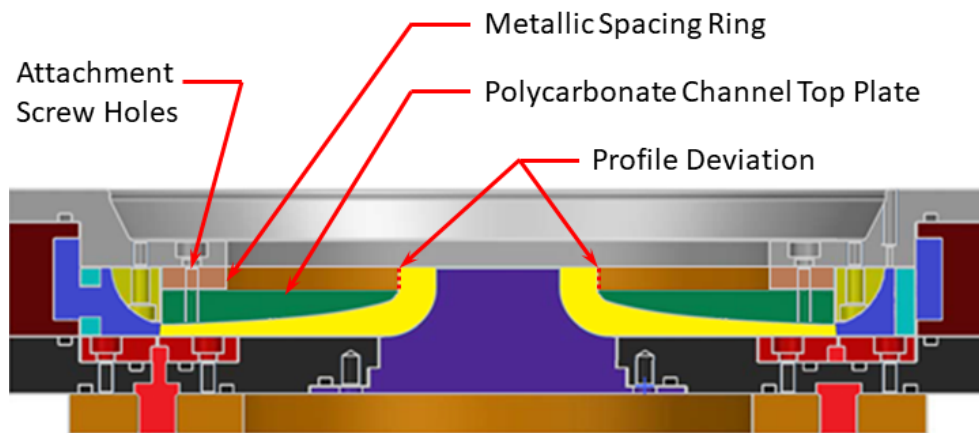
(b) Transparent polycarbonate channel top plate with metallic spacing ring installed

Figure 51. Cross sections of the Baseline configuration (a) and the polycarbonate channel top plate configuration (b). Baseline configuration cross section courtesy of Riley Huff, AFRL/RQTC

lines printed on the paper underneath. The image near the outer edge is easily distinguishable, but begins to blur near the inner edge as the curvature and space between the paper and the surface increases due to the contour. Based on this and other visual assessments, the plates' optical qualities were deemed sufficient for use in testing. The plate on the right is near identical, and has the metal spacer ring located in the position it was installed in. Figure 52(b) shows transparent channel top plate installed on the research device, with the spacer ring visible as the light metallic ring adjacent to the polycarbonate window.

83
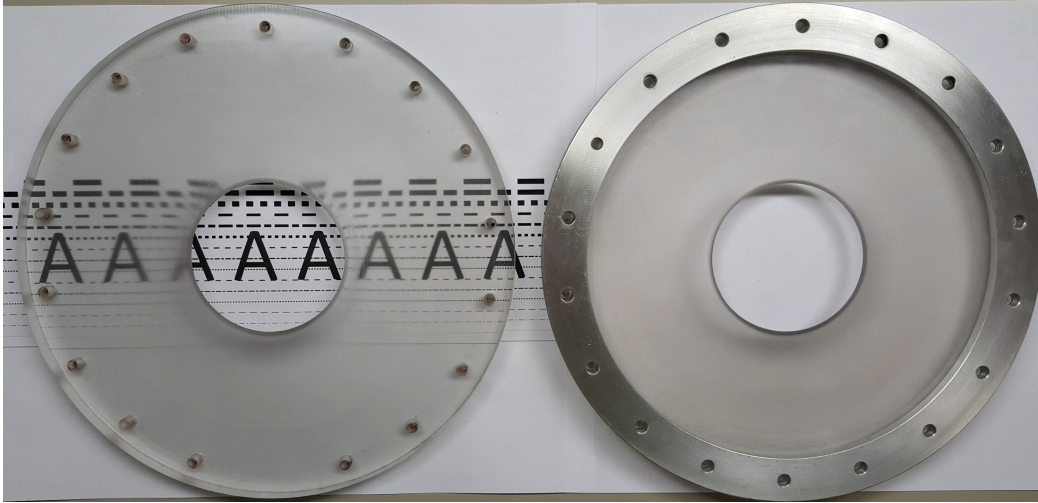
(a) Prior to installation
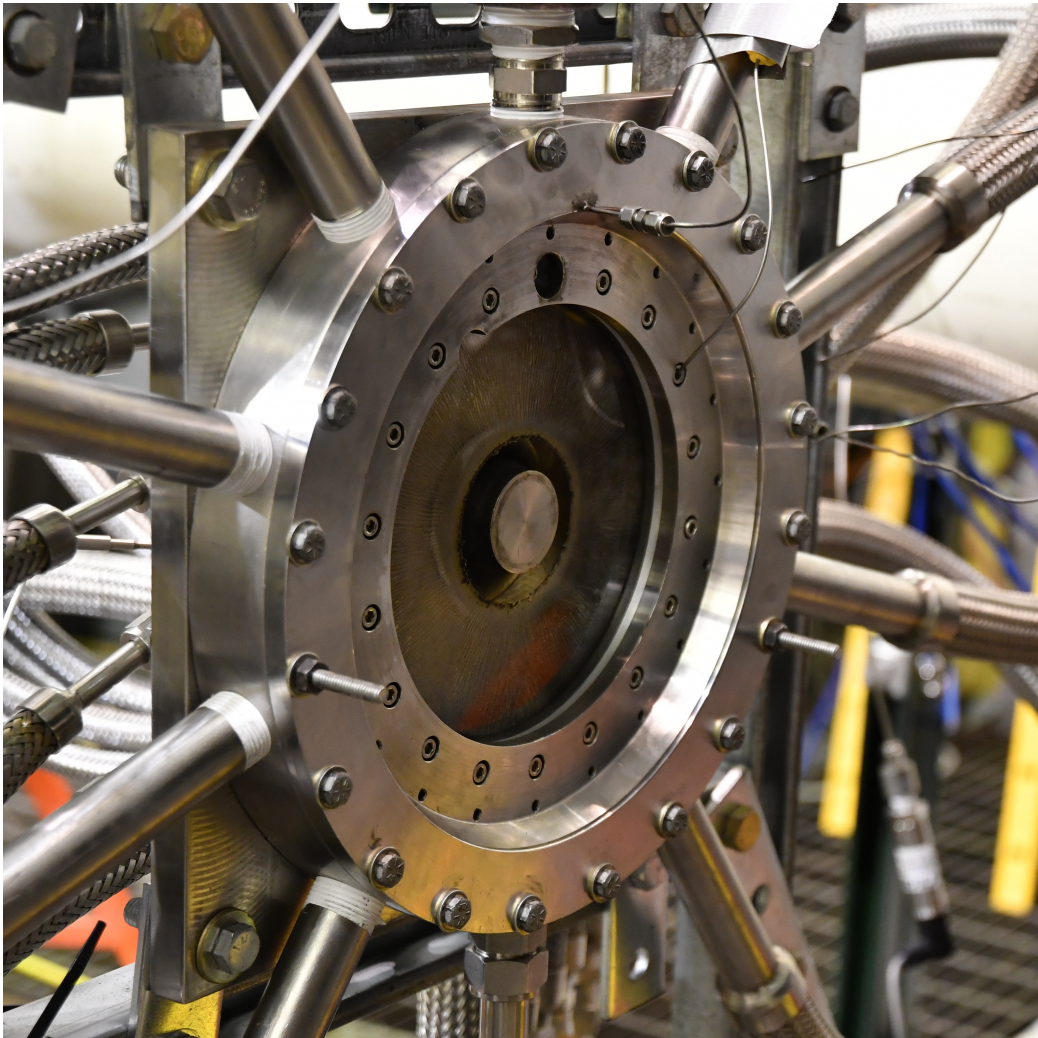
(b) Installed

Figure 52. Machined polycarbonate channel top plates.

The polycarbonate channel top plate allows imaging of chemiluminescence within the channel at all stages of the experiment as shown in Figure 53. Image a shows the test device immediately prior to ignition. Images b and c show the test device immediately after ignition. In Image c the streaks shown in the exhaust plume are from melted or fragmented burning polycarbonate being expelled from the test device. Image d shows the test device after ignition startup and Image e shows the test device after the fuel was cut off, as the flame is being extinguished.
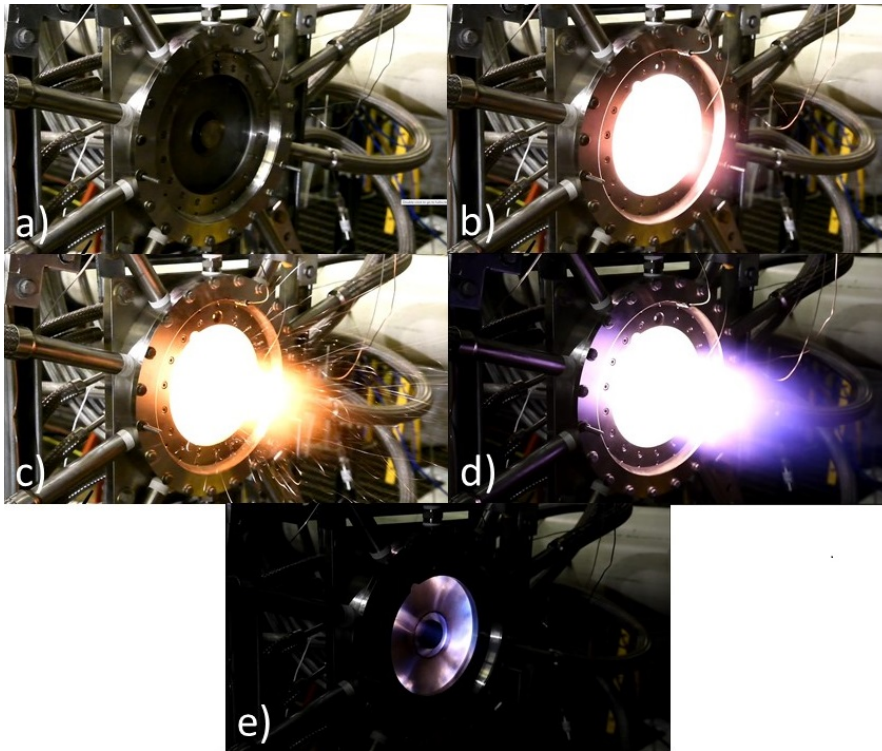
Figure 53. A test run with the transparent polycarbonate top plate installed.

From previous experiments, the operational frequency of the device was known to be in the kHz range. For this reason, high speed photography was chosen to observe the radial location of the DW within the channel. A Phantom v711 camera was used with a maximum framerate of 7,530 fps at a resolution of $1280x800$ pixels to 680,000 fps at $128x8$ pixels, and $> 7Gpx/s$ throughput [90]. For the present research, imagery was recorded at a resolution of $304x304$ or $512x512$ pixels, with a frame rate of 25,000

fps and an exposure time between 0.294-39 μs to capture the DWs.

Figure 54 shows the high speed camera's setup. The camera was connected to a laptop with Phantom Camera Control (PCC) software installed, which was used to control the camera's resolution, frame rate, and exposure time. The PCC software was also used to view and save the collected imagery and has some video editing capability. A trigger source was also connected to the camera, which was used to initiate recording. The DAQ (not shown) served as the trigger source and initiated the recording sequence immediately prior to ignition. The camera viewed the RDE's reflection off a mirror positioned in the RRDE's exhaust in order to protect the camera from the heat and potential debris expelled during combustion.
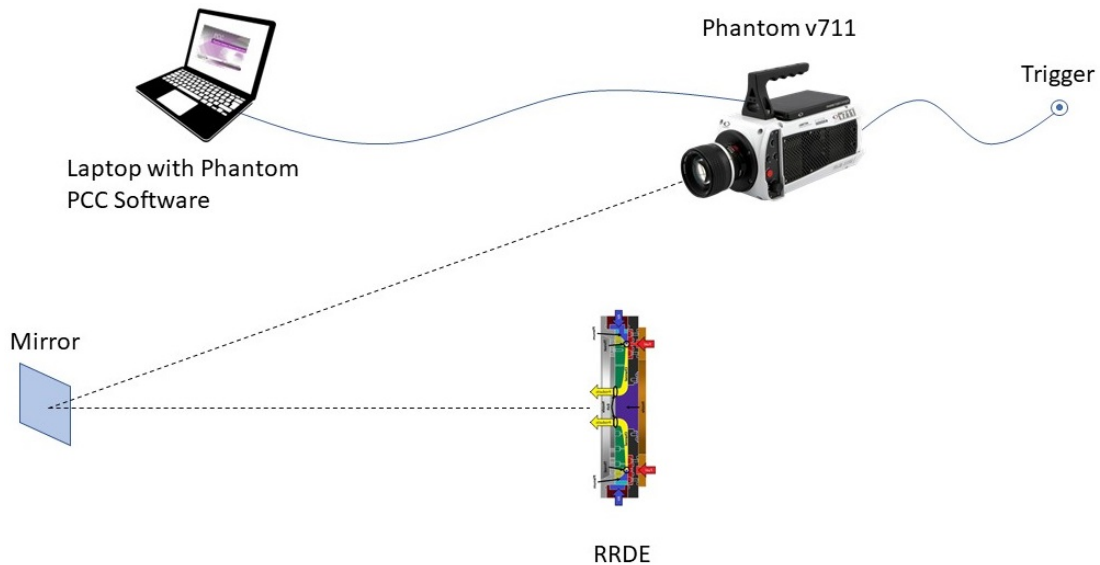
Figure 54. The polycarbonate channel testing Phantom high speed camera setup.

The instrumentation for the RRDE itself was reduced from the instrumentation used by the baseline RRDE, as the polycarbonate channel plate did not have pressure ports available. Of the Omega pressure transducers listed in Table 3, only the one located in the air plenum was installed. The Omega thermocouple from Table 4 remained in place, as it simply rested on the Channel Plate's outer surface. Of the Kulite high frequency pressure probes listed in Table 5, only the fuel plenum pressure

transducer was installed. Of the remaining instrumentation, the locations remained unchanged from those shown in Figure 48.

3.2.3   Wave Number and Frequency Determination.

Calculation of the DW speed (v_D) per Equation 20 required determination of the frequency (f_D), DW radius (r_D), and number of DWs (N_D). N_D was determined by viewing the high speed imagery. The frequency was determined by taking the FFT of the pressure transducer signal from the high speed Kulite pressure transducer installed in the fuel plenum and examining the peak frequencies of the resultant power spectrum, and its variation in time was examined with a spectrogram of the signal.

Figure 55 shows a sample signal from the Kulite high speed pressure transducer installed in the fuel plenum. The signal was relatively flat from $4.9 - 5.0s$, at which point the magnitude began to increase due to detonation initiation. The signal then experienced high frequency oscillations of increased magnitude, corresponding to the passage of a DW. The frequency of these oscillations therefore corresponded to the DW frequency.

The power spectrum of this signal was obtained with an FFT in MATLAB, shown in Figure 56. In this case the FFT's power spectrum shows two distinct bands of increased magnitude. For each of these bands, the largest peak was chosen as the dominant wave pass frequency. For the sample case shown, analysis of the high speed camera footage reveals that this case was an unsteady transition case, which alternates between one and two DWs. From this FFT, it was inferred that the 2552 Hz band corresponds to the one DW case, whereas the 4324 Hz band corresponds to the two DW case. For cases that were stable at either 1 or 2 waves, a second peak may not appear, or may correspond to a harmonic. In general any number of modes may occur, which will each contribute frequency content to the power spectrum.
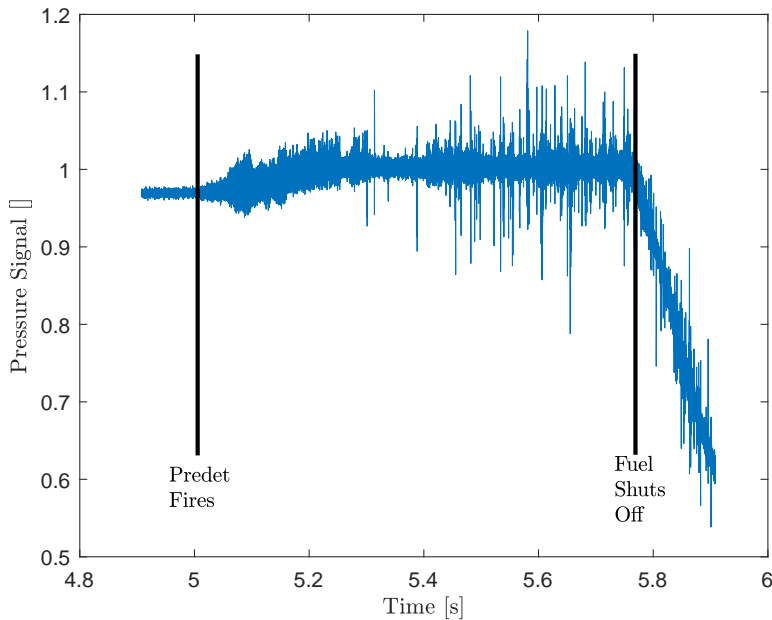
Figure 55. Example fuel plenum Kulite pressure signal.

While the power spectrum is a useful tool, it contains no information on the time history of the signal. Thus, while peaks are present for both one and two wave operation, it is impossible to determine when these occurred from an FFT, or any transient behavior. Because the data were observed to vary temporally in both the pressure signal and the imaging, a spectrogram was utilized to better understand the transient wave behavior. Figure 57 shows an example spectrogram for a transitional case. Unlike the FFT, the spectrogram gives the frequency distribution of the signal as it varies in time. In this example, the frequency bands at $4.3kHz$ and $8.6kHz$ from $150 - 250ms$ corresponds to an $N_D = 2$ mode and its harmonic, whereas the frequency band at $2.6kHz$ from $250 - 1000ms$ corresponds to an $N_D = 1$ mode. The narrowness of the $4.3kHz$ frequency band shows that there was little frequency variation when operating in this mode, whereas the more diffuse $2.6kHz$ frequency band shows a larger variation in operating frequency. This is reflected in the band widths in Figure 56. The spectrogram also shows the $3.8kHz$ content occurs at the
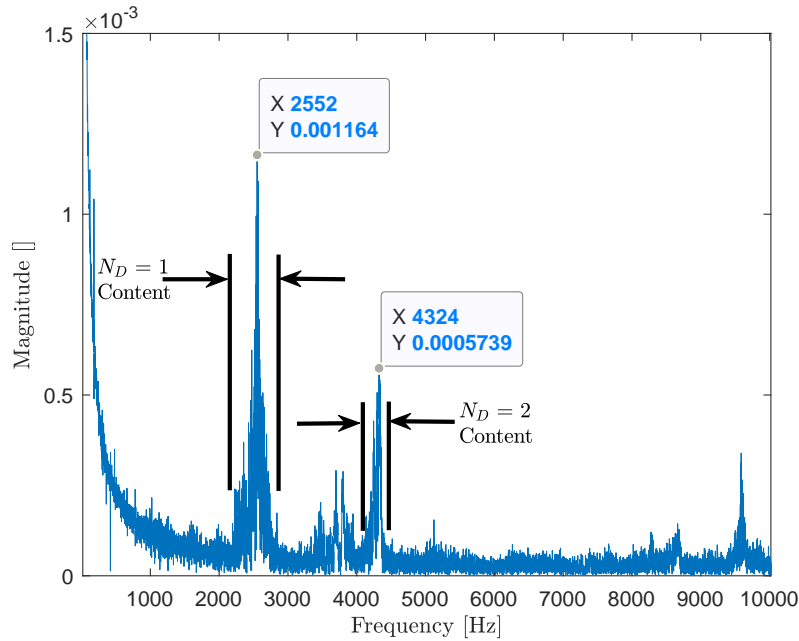
Figure 56. Example FFT power spectrum of the fuel plenum Kulite pressure signal in Figure 55.

end of the run, and is likely a transient phenomenon related to engine shutdown.

Since the FFT power spectrum in Figure 56 was taken for the entire duration of the experiment, it has signal components from the entire run duration, which is composed of different modes including startup, $N_D = 2$ operation, $N_D = 1$ operation, shutdown, and transients between $N_D = 2$ and $N_D = 1$ operation. The power spectrum can be enhanced for a specific mode by using only the data for the timeframe in which that mode persists, as was done for $N_D = 1$ and $N_D = 2$ operation shown in Figure 58. As compared to Figure 56, Figure 58(a) shows that for the $N_D = 1$ operation FFT power spectrum there is a large magnitude signal in the $2.5kHz$ range corresponding to $N_D = 1$, the peak in the $4.3kHz$ range corresponding to $N_D = 2$ operation has been eliminated, and some of the lower magnitude features have also been eliminated. Conversely, Figure 58(b) shows a large magnitude signal in the $4.3kHz$ range whereas the $2500Hz$ band is greatly reduced and lower magnitude features are virtually eliminated. A second band in the $8.6kHz$ range appears to be
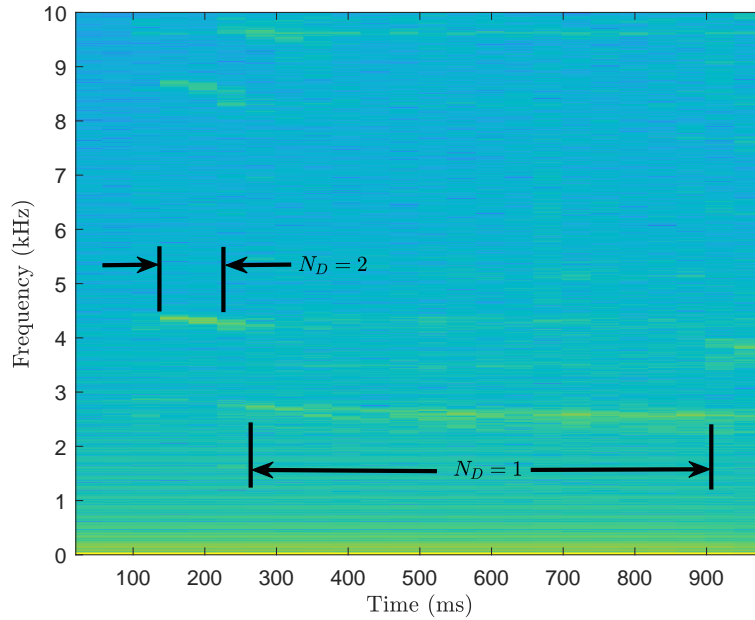
Figure 57. Example spectrogram of the fuel plenum Kulite pressure signal in Figure 55.

a harmonic of the $4.3kHz$ range signal.

With these refined FFT power spectrums, these signals can be analyzed to determine operational frequency statistics for the experiment in the modes of interest. Figure 59 shows the error analysis process for the wave frequency data. As shown in Figure 58 the FFT data gives the distribution of the power spectrum in the vicinity of the dominant frequencies. There is also low magnitude noise in the signal that is not strongly correlated to the DW frequency, which is undesirable. The process begins by restricting the domain of the FFT data to the vicinity of the DW's dominant frequency, as shown in a for $N_D = 1$ and b for $N_D = 2$. This eliminates interference from other modes and the low frequency peaks. Frequencies with a power spectrum magnitude of less than 20% of the dominant frequencies were considered to be noise, and were filtered by setting their magnitude to zero. The mean frequency was then

(a) $N_D = 1$ Reduced Time   (b) $N_D = 2$ Reduced Time
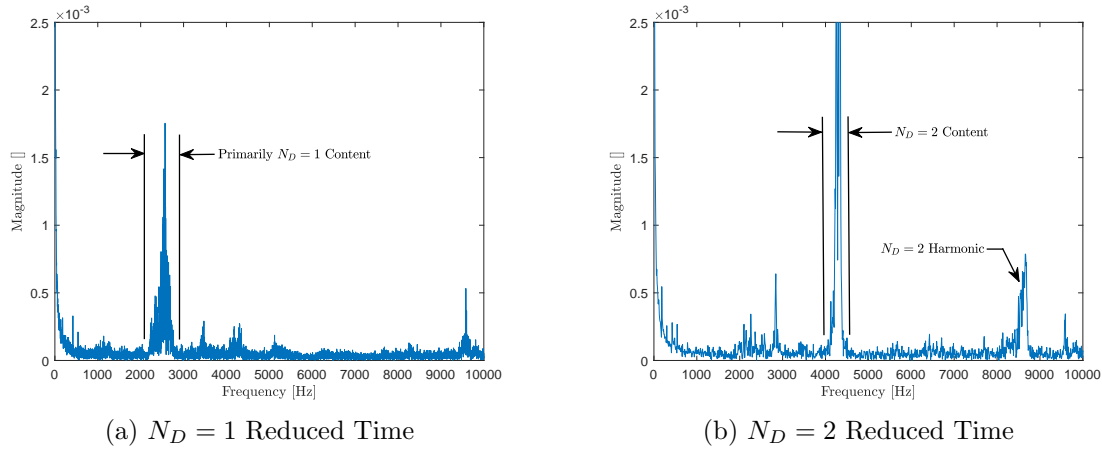
Figure 58. FFT Power Spectrums for the fuel plenum Kulite pressure signal for the time ranges corresponding to (a) $N_D = 1$ **and** (b) $N_D = 2$, **as indicated in Figure 57.**

obtained for this filtered data by evaluating the expression

$$\mu_{f_D} = \frac{\sum f_{D,filtered} P}{\sum P} \tag{38}$$

The Cumulative Distribution Function (CDF) of the distribution was then determined. The CDF was then used to estimate the frequencies corresponding to $\pm 2\sigma$ of the median value ($CDF = 0.5 \pm 0.477$) to determine the bounds of the frequency range.

3.2.4   Radius Estimation - Manual Estimation Method.

With the frequency and mode identified, to calculate v_D only the radius at which the detonation propagates, r_D, is still required. As a fist attempt to estimate r_D, and to serve as a check for other methods, r_D was first estimated manually by directly observing the high speed photography.

Determination of the r_D is considerably more complicated than the wave number or frequency, requiring significant user input and judgment. The DWs were first observed qualitatively to determine the number of waves, and whether or not the

91
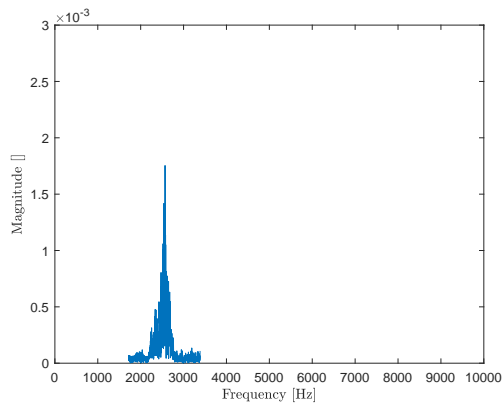
(a) $N_D = 1$ Reduced Range
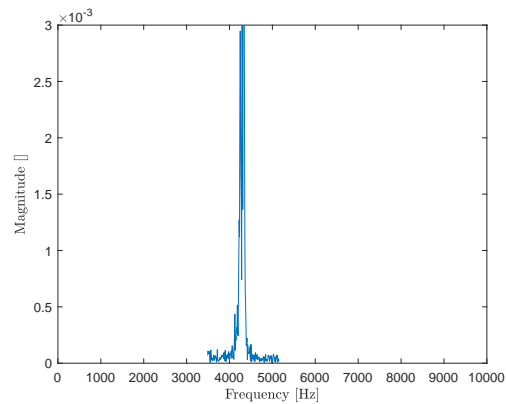
(b) $N_D = 2$ Reduced Range
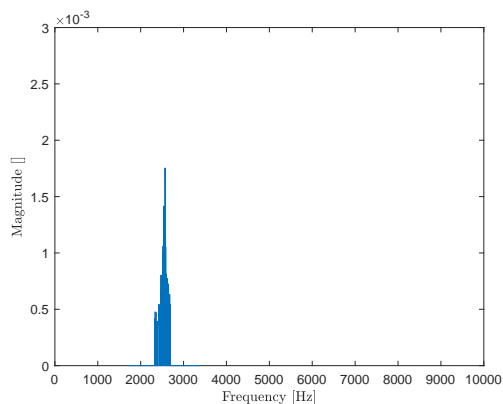
(c) $N_D = 1$ Filtered Power Spectrum
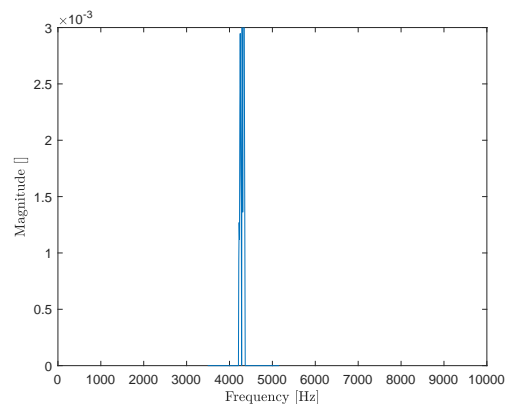
(d) $N_D = 2$ Filtered Power Spectrum
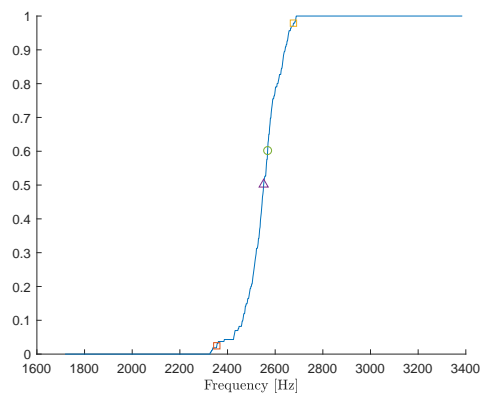
(e) $N_D = 1$ Power Spectrum CDF
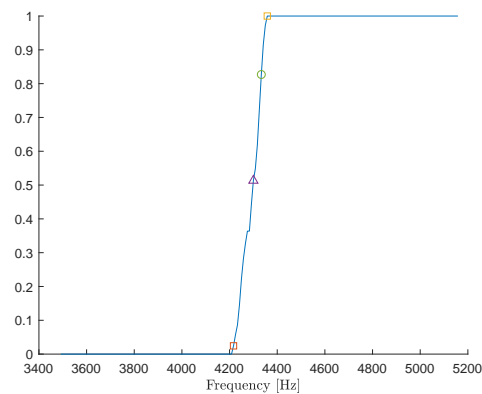
(f) $N_D = 2$ Power Spectrum CDF

Figure 59. Example evaluation process of the frequency error. Left: $N_D = 1$; Right: $N_D = 2$. *a-b* shows the reduced range of the FFT power spectrums shown in Figure 58, centered on the dominant (largest peak) wave frequency. *c-d* shows the filtered data, with noise eliminated. *e-f* shows the CDF generated from the restricted, filtered data and the median value (triangles), dominant frequency (circles), and $\pm 2\sigma$ of the median value (squares) indicated.

92

wave number transitioned after the ignition period. If transition did not occur, the DW was observed over multiple cycles to determine the wave behavior. For many of the cases, the DW structure changed from cycle to cycle. Following this observation procedure, an image was selected that was representative of the average behavior of the DW. For transitional cases, this procedure was modified by selecting images corresponding to the typical behavior for each wave number in a similar manner.

Following selection of a representative image, a transparent overlay with graduated increments was placed on the image and scaled using features visible in the image such that the numbered graduated increments correspond to distances in *cm*. This overlay was then translated and rotated such that the overlay's 0 was located at the center and extends to the DW. Typical examples are shown in Figure 60, which shows the images selected for various cases with overlay. The location of the DW was then estimated based on intensity and DW features visible in the image. For instance, in Figure 60 for the 1 wave case the high intensity region was located at a radius of 4.5 *cm*, whereas for the 2 wave case the high intensity regions were at a radius of 6.5 *cm*.

Figure 61 shows a sample image with most of the features of interest called out. This image was selected as an example because of the visible features which are typical for the captured imagery, although in general not all features were necessarily visible in any given image. Both the outer nozzle edge and outer edge of the viewing area are of a known radius, and were used to scale the image. The inner edge of the polycarbonate window was also visible in many images. While the inner edge of the polycarbonate window was of a known diameter as manufactured, this diameter increased as the experiment proceeded, and thus was not used for scaling. The DW and its expansion region was visible as a region of high intensity chemiluminescence. The direction of travel is indicated by the thick arrows. Secondary burning was also present away from either DW. Secondary burning in the region under the pressure
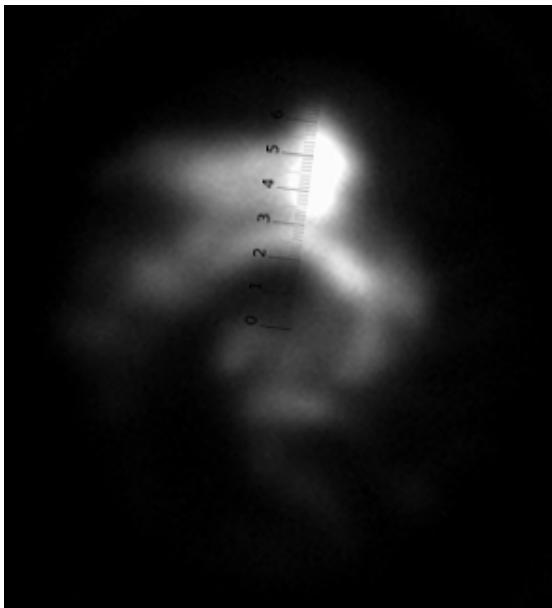
(a) $N_D = 1$ Image
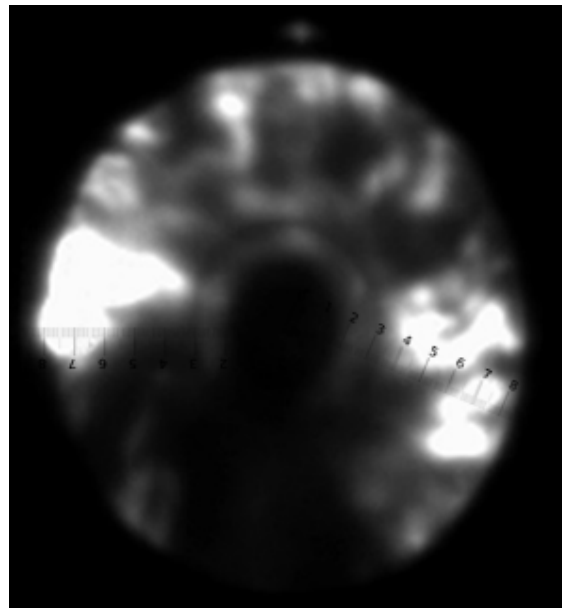
(b) $N_D = 2$ Image
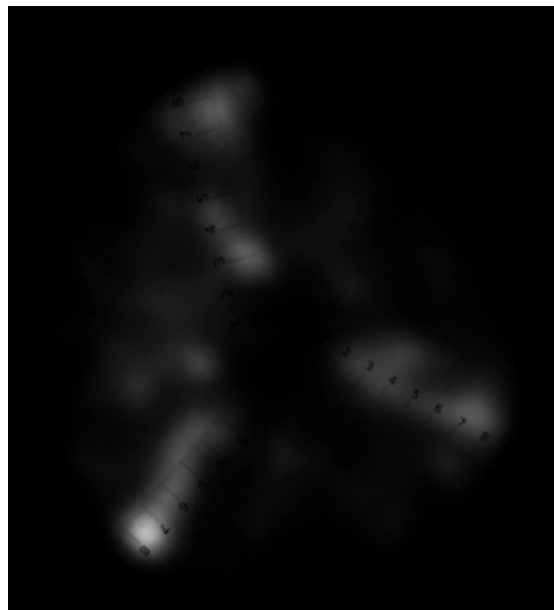
(c) $N_D = 3$ Image

Figure 60. Example DW radial locations with scaled graduated increments superimposed.

port cutout is also visible, indicated by the bright spot at the 12 o'clock position outside the outer edge of the viewing area. While not easily distinguishable in this image, the chemiluminescence from the DW can reflect off the nozzle in some cases, producing a bright spot on the nozzle, which should not be confused with combustion at the inner radius.
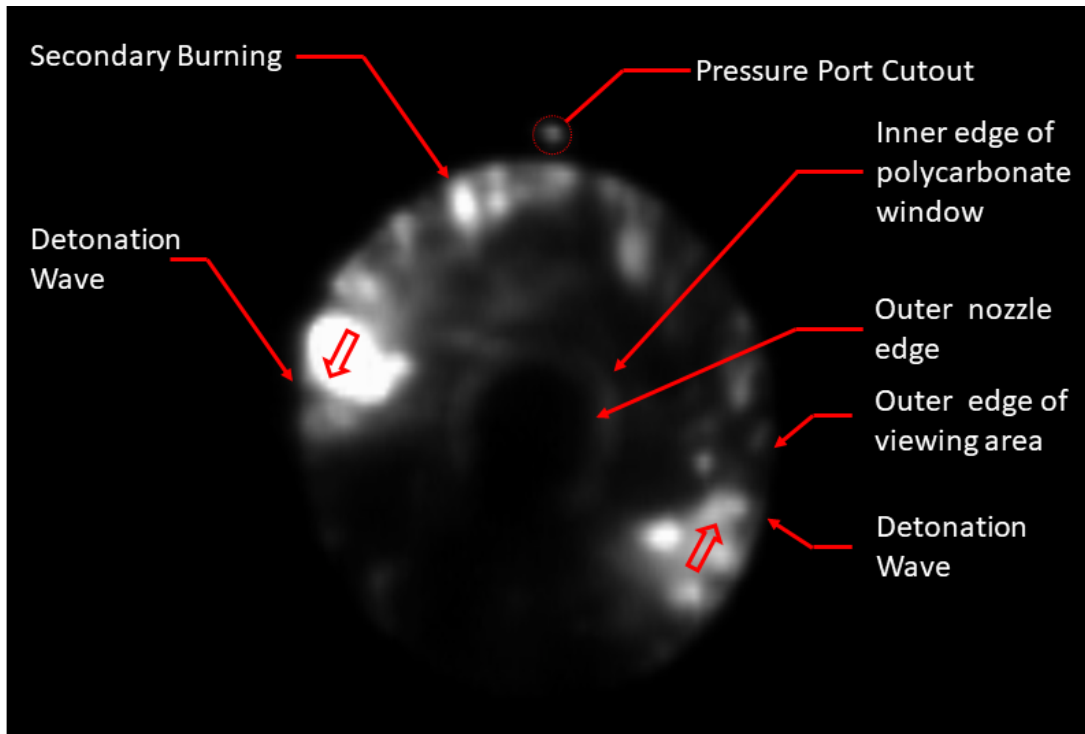
Figure 61. Example view with features of interest called out.

3.2.5 Radius Estimation - Peak Intensity Method.

While the manual estimation method produced good general trends, it was labor intensive, had a small sample size, and was susceptible to human error. A more automated, repeatable procedure was desired to produce scientific data. To this end estimation of r_D was also accomplished by tracking the peak intensity visible in the viewing window using MATLAB.

The procedure began by reading the video file into MATLAB. With user input, the

95

image was cropped to a smaller size such that the entire viewing window was visible. The center of the viewing area was then determined with user input, corresponding to the center of the nozzle. Due to being viewed at an angle the viewing area was skewed such that the nominally circular viewing window appears elliptical in the recording; to compensate for this effect the equation of an ellipse sized to correspond to the outer edge of the viewing area was determined, which was centered on the nozzle. The high speed imagery was then played back to confirm the center end edges were properly aligned, and adjusted as needed. With user setup complete, the entire video file may then be analyzed without further user input.

For each pixel, the value may vary in integer values from 0 (black) to 255 (white), with higher values indicating greater photon counts by the high speed camera. Presuming that the maximum intensity was correlated to the location of a DW, the indexed location of the maximum intensity location $[x_{D,e}, y_{D,e}]$ can then be determined for the image array.
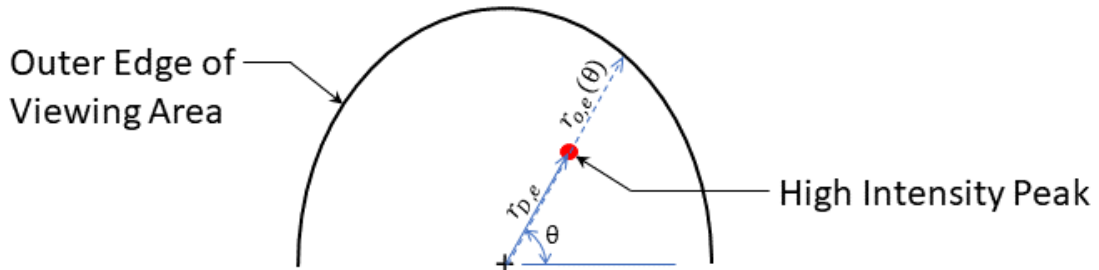
Figure 62. Radial scaling of an point in an elliptical domain.

This maximum intensity location was scaled within the ellipse to estimate its corrected radial location, as shown in Figure 62. The parametric equation of the ellipse representing the outer edge of the viewing area takes the form

$$x_{o,e} = a_1 cos(\theta)$$
$$y_{o,e} = a_2 sin(\theta)$$

(39)

96

where $[a_1, a_2]$ are the axes of the ellipse. The radius of the high intensity point $[x_{D,e}, y_{D,e}]$ in the elliptical frame can then be estimated as

$$r_{D,e} = \sqrt{(x_{D,e} - x_{center})^2 + (y_{D,e} - y_{center})^2} \tag{40}$$

and θ can be determined with MATLAB's four-quadrant inverse tangent function, $atan2((y_{D,e} - y_{center}), (x_{D,e} - x_{center}))$. With θ, Equation 39 can be evaluated, and the outer radius of the ellipse at θ can be calculated as

$$r_{o,e} = \sqrt{(x_{o,e})^2 + (y_{o,e})^2} \tag{41}$$

The fractional distance of the point is then

$$r' = r_{D,e}/r_{o,e} \tag{42}$$

with which the known viewing area outer radius can be multiplied to determine the corrected radial location of the point within the channel,

$$r_D = r' r_o \tag{43}$$

The location of the maximum intensity can thus be mapped to a radius for each time step, and was tracked for every frame.

Figure 63(a) shows the automated detection of the maximum intensity in a single frame with proper function, with the scaling ellipses shown. Figure 63(b) shows an error in the tracking system, where a reflection off the nozzle was detected instead of a DW. Figure 63(c) shows the points detected in the first $\approx 300ms$ of an analyzed video with primarily $N_D = 2$ operation, corresponding to ≈ 7500 frames. The high concentration of points towards the outer edge of the viewing area is characteristic

97

of a DW with little radial location dispersion. The concentration of points near the center was due to reflection from the nozzle, and was especially pronounced inside the radius of the polycarbonate window inner radius where transmission losses from the polycarbonate material do not occur; conversely, immediately outside the polycarbonate window inner radius the polycarbonate window is at its maximum angle relative to the camera, minimizing transmission and causing a reduction in hits. A single point at the 12 o'clock position outside the ellipse was from the pressure port cutout. False returns from debris ejected from the RRDE are visible outside the ellipse at the 2 o'clock position. In the top left corner is a point corresponding to 0 intensity, which is an error caused by the image array having the same value everywhere (most likely a black image), resulting in the MATLAB program returning the index of the first row and column as the maximum intensity location.

Figure 63(d) shows all results of this process as a function of time. There was a distinct transition from ignition to $N_D = 2$ operation to $N_D = 1$ operation, and then a more gradual transition to shutdown transients. The $N_D = 2$ operation band was much more narrow than the $N_D = 1$ operation band. Figure 63(e) shows the spectrogram of the data in Figure 63(d), and shows distinct bands for the $N_D = 1$ and $N_D = 2$ bands. Note that again the $N_D = 1$ band was both more diffuse than the $N_D = 2$ band, and a larger magnitude, indicating that the frequency varies more and the magnitude of the fluctuations was higher.

Figures 63(f) and 63(g) show data for $N_D = 2$ and $N_D = 1$, respectively. These data were filtered from the data in Figure 63(d) by restricting the data examined. First, the range of the data was restricted to the times corresponding to the N_D to be considered. Data outside of the viewing window outer radius were then eliminated from consideration, with the assumption that these corresponded primarily to false hits such as the 0 intensity error, debris, or exhaust plume flash. Data inside the

(a) Maximum intensity tracking, proper function

(b) Tracking error, spoofed by reflection off of nozzle

(c) Hit plot for the first 300 ms of operation

(d) Radial location vs time

(e) Radial location spectrogram

(f) $N_D = 2$ filtered radial locations

(g) $N_D = 1$ filtered radial locations
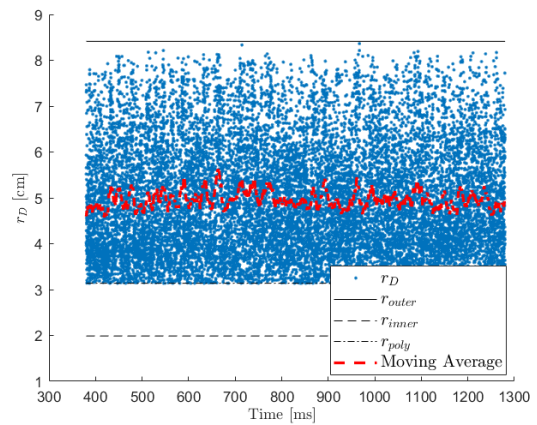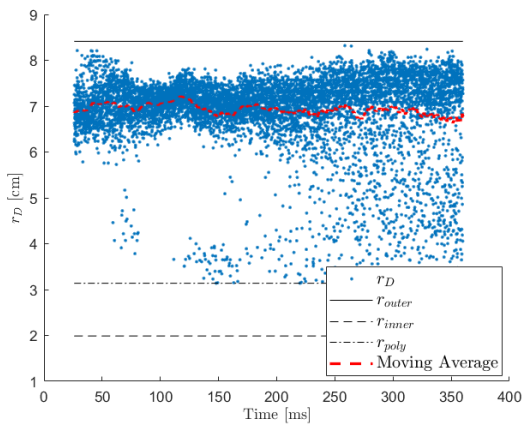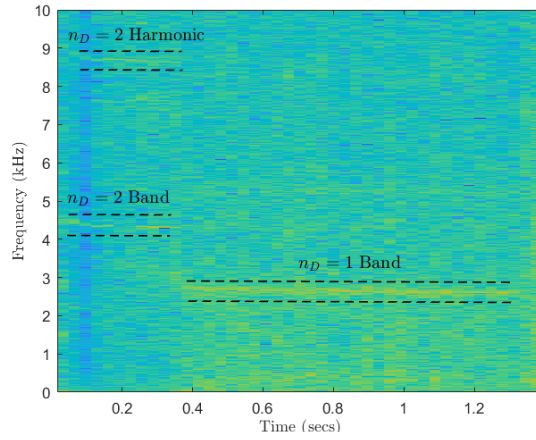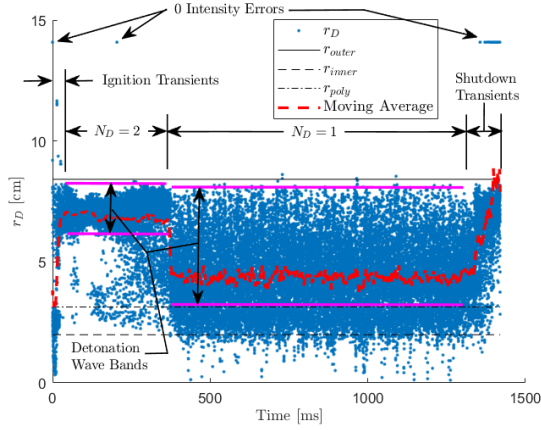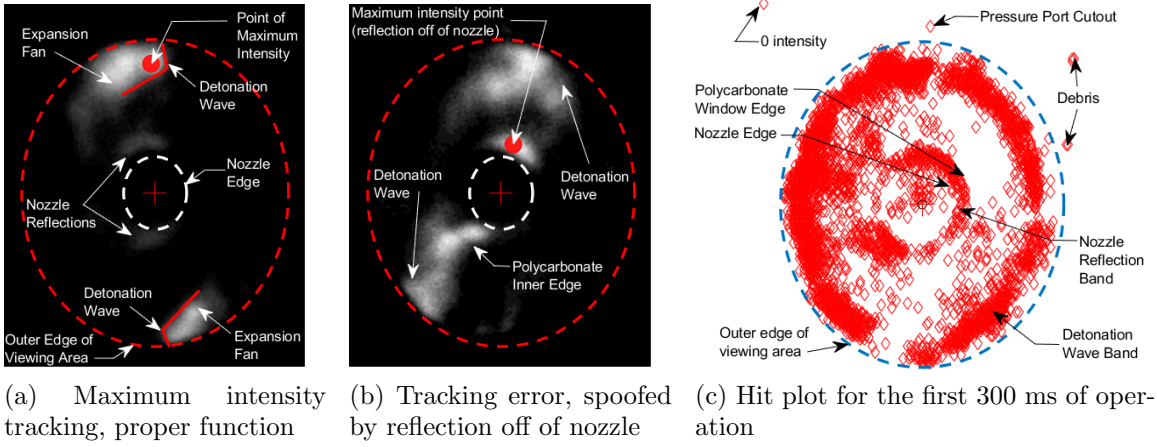
Figure 63. Semi-automated process for detonation radius estimation

99
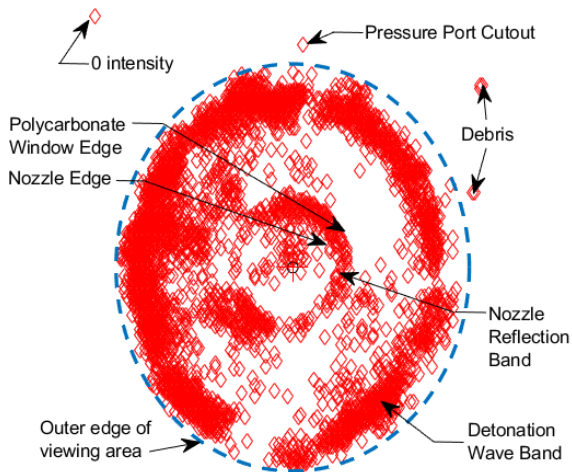
(a) Hit plot for the first 300 ms of operation
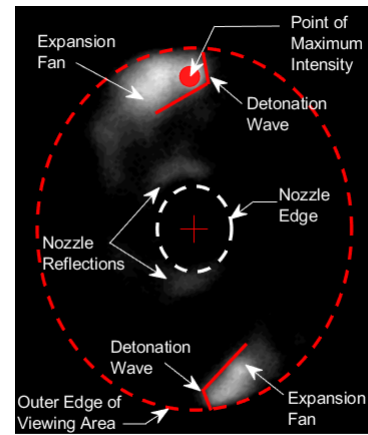
(b) Maximum intensity tracking, proper function
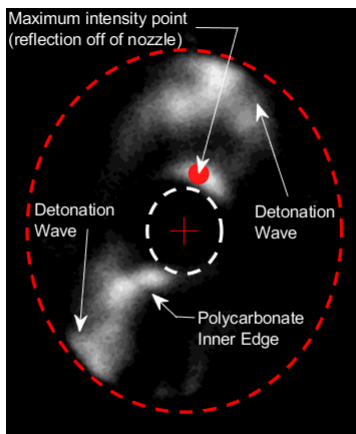
(c) Tracking error, spoofed by reflection off of nozzle
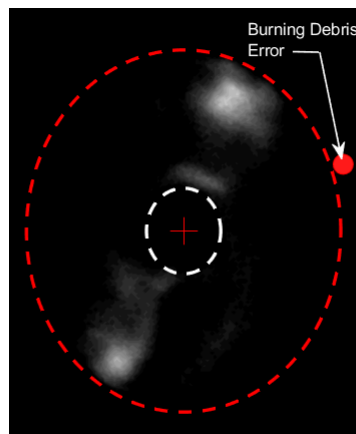
(d) Tracking error, spoofed by burning debris
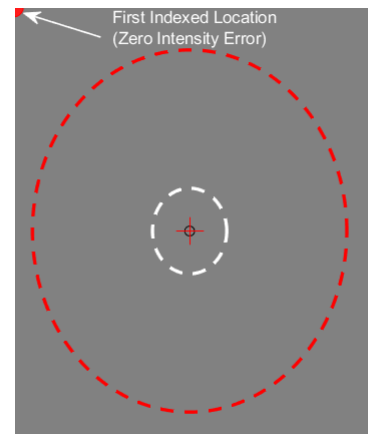
(e) Tracking error, spoofed by uniform 0 intensity

Figure 64. Common tracking errors encountered in the detonation radius estimation process.

inner radius of the polycarbonate window were also rejected, with the assumption that few if any DWs should exist in the nozzle, and that these returns were caused by reflections off of the nozzle or the exhaust plume. The moving average was then recalculated and plotted as shown for this filtered data.

Systematic elimination of remaining errors within the remaining data was not attempted. Potential sources of error may include reflection off of the channel, deflagrative burning, and possibly other unknown sources. This is the suspected source of the hits with $r_D = 5.5cm$ in Figure 63(f) based on observation of the video footage, but a generalized procedure to eliminate these errors was not identified. While these errors may also exist in the data in Figure 63(g), the DW was also observed to change location frequently with $N_D = 1$ operation, indicating that the dispersive behavior was unlikely an error and more likely a reflection of the actual variation.

Using the restricted, filtered data as shown in Figures 63(f) and 63(g), the mean (μ_{r_D}), standard deviation (σ_{r_D}), and median $(\widetilde{r_D})$ of the data set was taken. The μ_{r_D} and $\widetilde{r_D}$ are reported for these data, and $2\sigma_{r_D}$ was reported as the natural variation of the data. The error of μ_{r_D} was estimated by taking the moving average of the data with a window of ±100 datapoints of the data point under consideration at a given time. With a $25,000 fps$ frame rate and a wave frequency of $2kHz$, this corresponds to ≈ 25 cycles considered for the moving average. The σ for these moving averages was then calculated, and the 2σ value of the moving average values was reported as the uncertainty in the average value, which was used in calculations.

Though this method produced results which generally agreed with the observed behavior, there are several sources of error in this measurement. The black and white image was stored with each pixel having an unsigned 8 bit value. Because the range of values an unsigned 8 bit data point can have is an integer between 0 and 255, the data for the entire picture must have values exclusively in this range. For a 304x304

101

pixel picture, the uniqueness of a maximum intensity point is not guaranteed, however MATLAB will return only the first indexed value in an array if multiple maxima are present. This becomes especially problematic when the image is oversaturated with a large percentage of the image reading the maximum possible value, as the problem is not easily identified or filtered. This is also problematic when there is a uniform 0 intensity in the image, as the first indexed pixel is returned, corresponding to the top left of the image. This error is less problematic, as this location is outside of the viewing area of the polycarbonate channel and is readily identifiable as an error. Flaming debris exiting the channel, thought to be burning polycarbonate pieces, was observed as the maximum intensity point, and occasionally propagated outside the outer radius of the viewing area as well. To eliminate the errors due to anomalies outside of the viewing area, these data were filtered out for analysis.

It was also observed that separating peak intensities resulting from detonation, deflagration, and reflections was problematic, with detonations being the desired feature. The influence of deflagrative returns was minimized by choosing time segments with minimal deflagration to evaluate. Reflections corresponding to false returns were primarily observed to be from the nozzle, between the nozzle's edge and the inner edge of the polycarbonate channel plate where transmission losses were minimized, as shown in Figure 63(b). This nozzle reflection band is shown in Figure 63(c). These false returns from nozzle reflections were eliminated by filtering out all data from within the inner radius of the polycarbonate channel plate. More difficult to systematically eliminate were reflections of the DW chemiluminescence off of the channel between the inner edge of the polycarbonate window and the outer edge of the viewing area. Observation confirmed that many of the data points with $r_D < 6$ in Figure 63(f) were in fact reflections, with the darker band near $r_D = 7$ corresponding to maximum intensity near the DW. However a repeatable, systematic, generalized

procedure to eliminate these errors from the data set was not identified. These errant data points were therefore left as a known source of error, and account for a portion of the measurement's reported error. It was hypothesized after the experiments were conducted that using a black, non-reflective paint on the channel's visible surfaces would have reduced these errors.

Finally, there are three errors which remain unquantified but may prove to have a bias effect on the measurement. Due to the variation in polycarbonate's curvature and thickness, the transmissivity losses vary radially. The thicker polycarbonate at the outer radius reduces transmission, although this is expected to be a minor effect. Curvature of the plate also affects transmissivity, and is especially pronounced at the inner edge of the polycarbonate top plate, where the curvature is maximized. There is a notable gap in returns at this location as shown in Figure 63(c) and (d), followed by a sharp increase in transmission inside this radius due to reflections from the nozzle and low transmissivity losses of the air as discussed previously. Because the DW primarily operated in low curvature areas and the transmission losses due to thickness variations is minimal in this region, this is not expected to have a significant impact on the results. A second potential source of measurement bias comes from the assumption that the maximum intensity corresponds to the DW location, when in fact the maximum intensity from a DW was observed to occur behind the DW in its expansion region. Because the expansion region generally extends towards the nozzle, this may introduce a measurement bias resulting in an r_D lower than the actual value. The third potential source of bias error, and potentially the most important depending on mode, is that the viewing area is confined to the area visible through the polycarbonate window. However, when operating near the outer radius such as the DWs shown in Figure 63(a) the entire DW may not be visible, as the outer $2.1cm$ of the channel is not visible through this window. This will in effect

bias the measurement again resulting in an r_D lower than the actual value. Again, a systematic, generalized method for eliminating these errors could not be identified, although the manual estimation method discussed in Section 3.2.4 allows for such user interpretation.

3.2.6   Radius Estimation - Other Methods Considered.

The estimation of r_D using a time integrated approach was considered and attempted. This method proceeded similar to the Peak Intensity method, but instead of tracking a single location, the entire array was considered. As before, each frame was cropped and converted to an array in MATLAB, with each location in the array having a value between 0 (black) and 255 (white). An integration array was then initialized the same size as the image arrays with a uniform value of zero. Starting from a beginning index to a final index, the values for each location in the array were added to the integration array for each frame, with the hope that clear, distinct bands corresponding to the high intensity DW would become apparent when plotted as a contour plot, with the largest magnitude contours corresponding to the radii where DWs were propagating. In practice, this failed to produce distinct bands in general due to secondary burning, and was artificially skewed towards the center due to the fact that the burning products moved towards the center. The peak intensity method was used instead as it produced more reliable results that were more readily interpreted.

The use of more sophisticated digital image processing techniques was also considered. This would have included machine learning similar to facial recognition technology, but with the program tuned to detect the DW and its features instead. However, due to the complexities of data filtering, this method was not further pursued. Specific challenges included several of the videos are heavily saturated towards

the end of the test sequence, transitional cases exist where different numbers of DWs exist depending on time, a general procedure to identify features which the image can be scaled to, and the fact that due to movement of the RRDE, mirror, and/or camera the location of the center of the device in the frame may change over the duration of the run. Additionally, the DW shapes were often irregular, further compounding the challenge.

3.2.7 Corrected Wave Speeds.

With better estimates of the r_D and f_D of DWs in the channel, a better DW speed estimate was determined with Equation 20, repeated here

$$v_D = 2\pi r_D \left(\frac{f_D}{N_D} \right)$$

Using Moffat's method of partial derivatives [89] the error was estimated by first taking the partial derivatives of this function

$$\frac{\partial v_D}{\partial r_D} = 2\pi \left(\frac{f_D}{N_D} \right) \tag{44}$$

$$\frac{\partial v_D}{\partial f_D} = 2\pi r_D \left(\frac{1}{N_D} \right) \tag{45}$$

The error in v_D can then be estimated to be

$$\delta v_D = \sqrt{\left(\frac{\partial v_D}{\partial r_D} \delta r_D \right)^2 + \left(\frac{\partial v_D}{\partial f_D} \delta f_D \right)^2} \tag{46}$$

The value of δv_D depends on the uncertainty in the frequency of the frequency measurement and the uncertainty of the radius measurement. In general both of these uncertainties may vary significantly from case to case, and resulted in δv_D $\mathcal{O}(20 - 150 m/s)$.

3.3 Wave Direction Effects on Turbine Integration Configuration

Previous efforts have shown the efficiency of the turbine was lower than anticipated when integrated with the RRDE. While many potential loss sources exist, including non-optimized components and gaps between the turbine and its housing, the uncontrolled expansion of the post-turbine exhaust was one of the simplest to correct without extensive redesign and re-manufacturing of components. Huff designed a flow straightening device which could be mounted to the exhaust port of the turbine, controlling the expansion of products. The device consists of a length of pipe with flanges on either end used to secure it to the RRDE as shown in Figure 65. Restrictive plates can also optionally be installed at the exit plane flange to provide back pressure by reducing the exit diameter, as shown in Figure 65(b). The turbine exit area ratio, the ratio of the straightener exit area to the turbine exit area, was defined as $AR_e = \frac{A_{exit}}{A_{turbine}}$. A ball valve was located at the exit of the compressor to allow back pressure via restriction of the compressor flow exit area in a similar fashion. Two Kiel probes are installed in the device to measure total pressure. Huff used this device for further research in improving the turbine efficiency of the RRDE, and this device was also installed for all turbo configuration tests conducted in the present research, which was conducted in tandem with Huff's experiments [42].

A ball valve was located at the exit of the compressor to allow back pressure via restriction of the compressor flow exit area in a similar fashion. By turning the ball valve to a specified angle, or Compressor Ball Valve Angle (CBVA), the flow area is restricted as shown in Figure 66.

3.3.1 Turbo Instrumentation.

A variety of instrumentation was used, including pressure transducers, thermocouples, an RPM sensors, and a mass air flow (MAF) device. Omega pressure transducers

106

(a) Sketch	(b) Installed
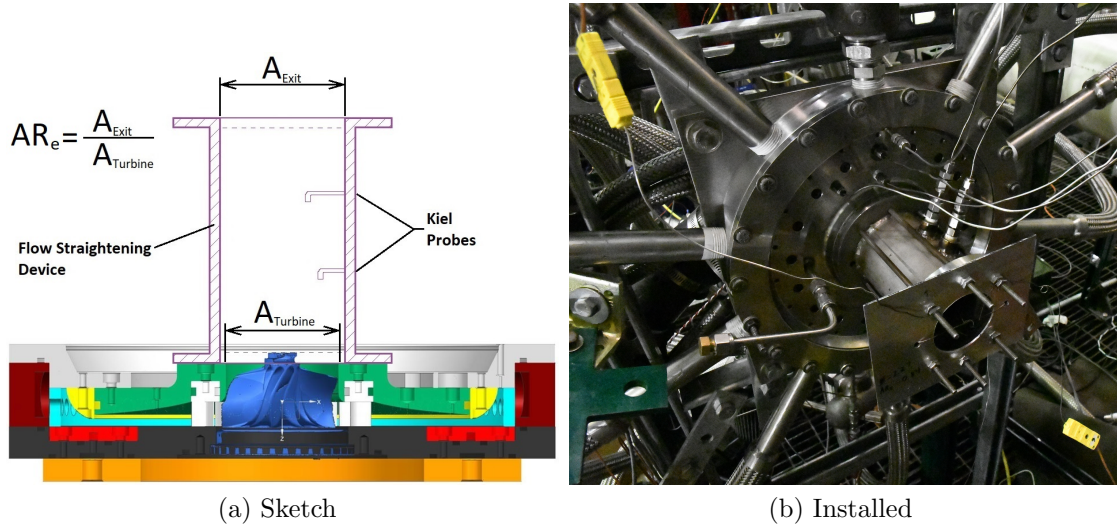
Figure 65. (a)Turbo configuration with Flow Straightening Device shown. Image modified from that provided courtesy of R. Huff, AFRL/RQTC by addition of the flow straightening device. (b) Installed hardware used in the present work.

(Ref Table 9) and thermocouples (Ref Table 10), as well as Kulite high frequency pressure probes (Ref Table 11), were used to collect data from the RRDE itself. Figure 67(a) identifies the locations of the Omega pressure transducer CTAP ports in green and the Omega thermocouple, in yellow. The S1 and S2 pressure probes were installed for the present research, as were thermocouples TC1-3 at the flow straightener exit. The location of the Kulite ITPs is obscured in this image but is the same location as shown in Figure 48(a). The location of the Kulite installed in the fuel plenum was unchanged from the baseline configuration indicated in Figure 48(b). Figure 67(b) identifies the locations of the Omega pressure transducer ports in green and the Omega thermocouple in blue. The location of the MAF device at the inlet and the ball valve at the exit is also shown.

3.3.2   Wave Direction Determination.

Simple determination of wave direction was first accomplished by examining the phase lag of the pressure traces from the high speed ITP devices. The pressure
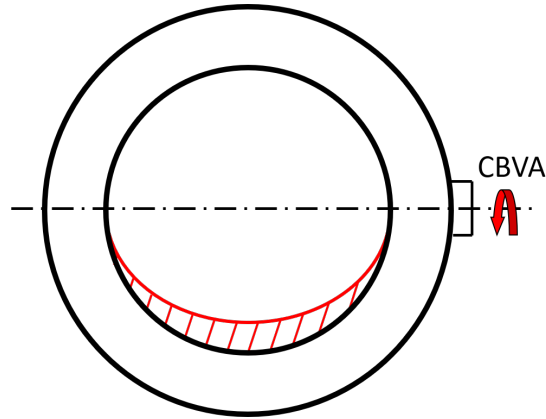
Figure 66. Compressor Area Ratio sketch
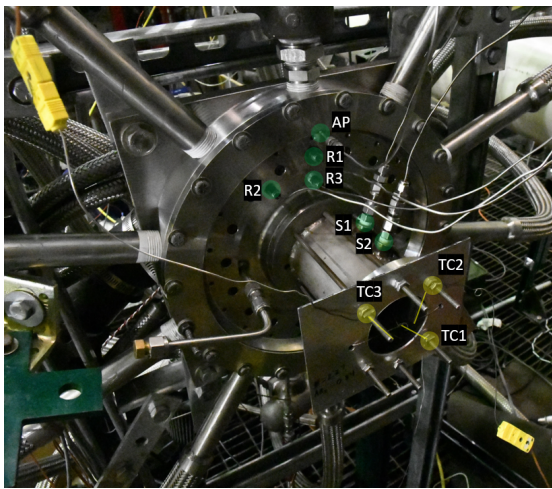
(a) Turbine side instrumentation
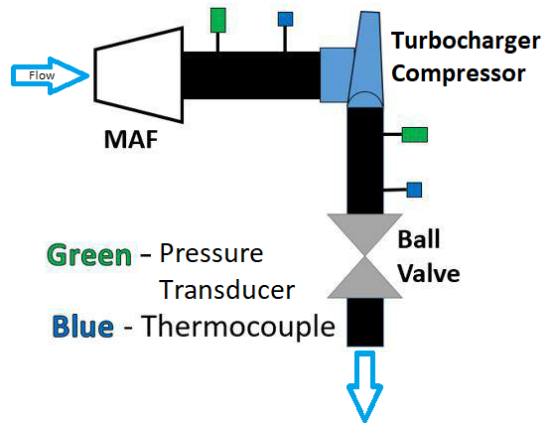
(b) Compressor side instrumentation. Modified from [44].

Figure 67. Instrumentation connected to the turbo configuration RRDE.

ports were located at an offset from one another, $\theta_p = 45°$. The apparent phase lag between signals was expected to be $\phi_p = N_D \theta_p$ for a rotating detonation. However, the magnitude of the phase lag must be less than 180° or the wave propagation direction will be indeterminate. Therefore, this method may only work if there is high confidence that $N_D \leq 3$ for this geometry, with $\phi_p = 45°$ corresponding to a $N_D = 1$ mode, $\phi_p = 90°$ corresponding to a $N_D = 2$ mode, and $\phi_p = 135°$ corresponding to a $N_D = 3$ mode. $\phi_p = 180°$ corresponds to a $N_D = 4$ mode, but the direction of travel is indeterminate. Based on previous experiments, $N_D \leq 3$ for the operating range

Table 9. Omega pressure transducers

Location	Model	P Range	Uncertainty	Serial #	Measurement
-	-	kPa(PSIA)	kPa(PSIA)	-	Device
Channel Plate, R1=9.53 (cm)	PX429-250A5V	0-1720(0-250)	±1.4(0.20)	463871	CTAP
Channel Plate, R2=8.26 (cm)	PX429-250A5V	0-1720(0-250)	±1.4(0.20)	461789	CTAP
Channel Plate, R3=6.99 (cm)	PX429-250A5V	0-1720(0-250)	±1.4(0.20)	461766	CTAP
Turbine Exit, S1	PX429-250A5V	0-1720(0-250)	±1.4(0.20)	424889	CTAP w/Kiel Probe
Turbine Exit, S2	PX429-250A5V	0-1720(0-250)	±1.4(0.20)	463884	CTAP w/Kiel Probe
Air Plenum, AP	PX429-150A5V	0-1030(0-150)	±0.8(0.12)	423225	CTAP
Turbo Compressor Inlet	PX329-030A5V	0-210(0-30)	±0.2(0.03)	114141052	Direct
Turbo Compressor Exit	PX429-150A5V	0-1030(0-150)	±0.8(0.12)	431097	Direct

Table 10. Omega thermocouples

Location	Model	T_{max}	Uncertainty	Measurement
-	-	(K)	(K)	Device
Turbo Turbine Exit 1, TC1	KMQXL-020U-12 (K-type)	1608	±0.0075T	Direct
Turbo Turbine Exit 2, TC2	KMQXL-040U-12 (K-type)	1608	±0.0075T	Direct
Turbo Turbine Exit 3, TC3	KMQXL-040U-12 (K-type)	1608	±0.0075T	Direct
Turbo Compressor Inlet	K-type	1608	±0.0075T	Direct
Turbo Compressor Exit	K-type	1608	±0.0075T	Direct

considered, so this geometric configuration was expected to be sufficient.

For example, consider Figure 68. In Figure 68(a) the waves are rounded and 180° out of phase. The rounded shape of these waves suggests these are acoustic waves, not detonations. The reason for the 180° phase angle difference is unknown, but likely indicates a non-rotating mode, and a propagation direction cannot be determined. In Figure 68(b) the waves are steeper, suggesting a detonation mode. The phase angle between the two waves is approximately 90°, suggesting an $N_D = 2$ mode. Finally, the K1 (blue) signal trails the K2 (red) signal, indicating clockwise detonation propagation.

A more advanced analysis was accomplished using MATLAB's Magnitude-Squared Coherence (mscohere) and Cross Power Spectral Density (cpsd) functions, which correlates two discrete signals with a uniform sample rate. The Magnitude-Squared Coherence function identifies frequencies where the two signals are strongly correlated, with values near 1.0 indicating strong coherence. The Cross Power Spectral
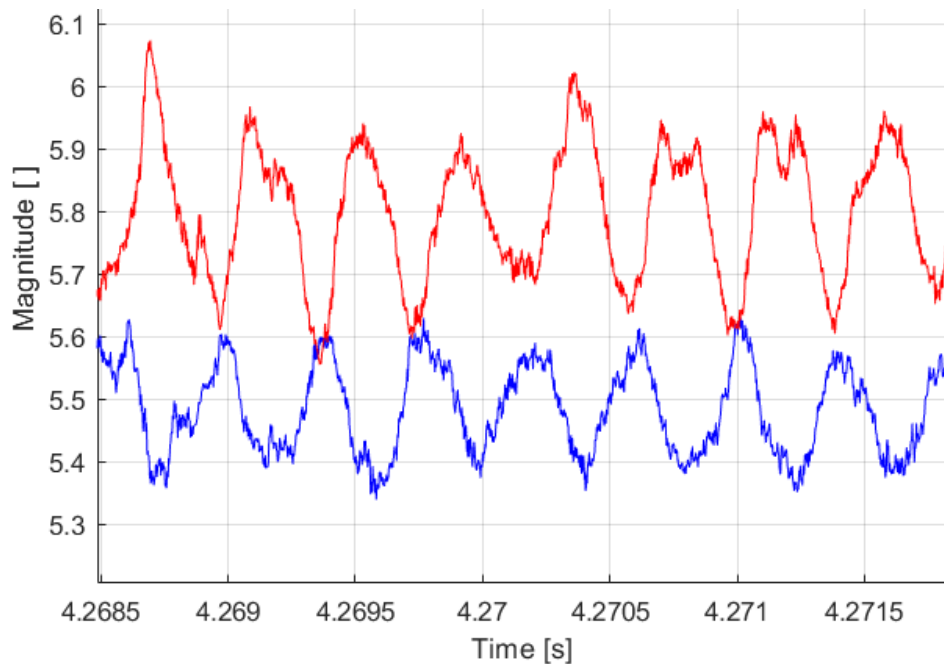
(a) Accoustic Waves
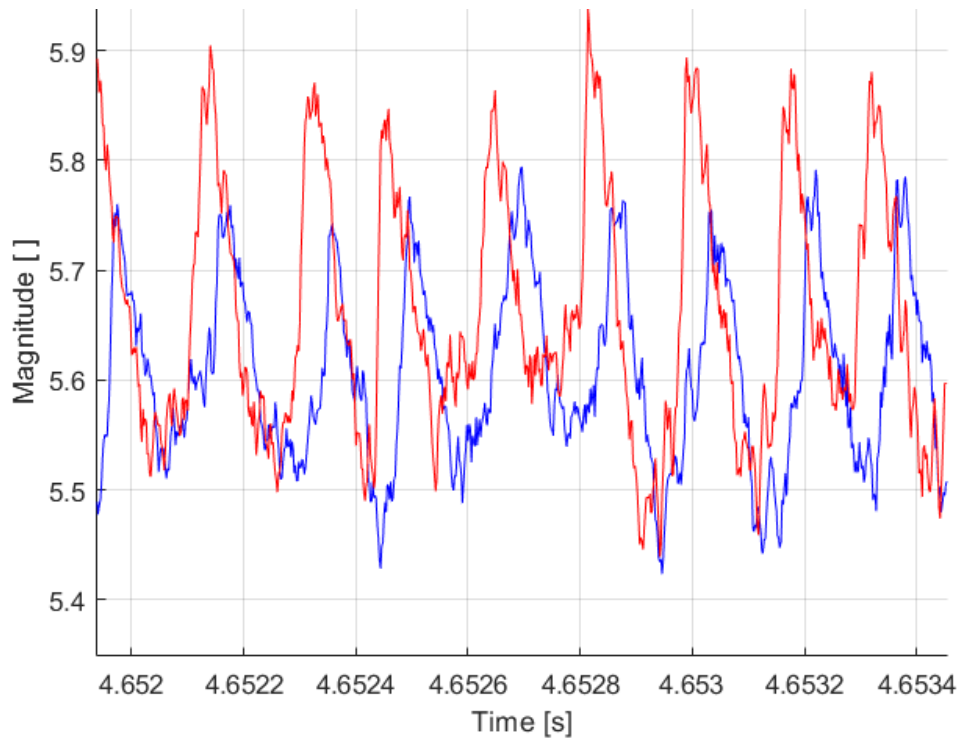
(b) $N_D = 2$ DWs

Figure 68. **Wave propagation determination from K1 (blue) and K2 (red) pressure signals.**

110

Table 11. Kulite high speed pressure transducers

Location	Model	P Range kPa(PSIA)	Serial #	Measurement Device
-	-	-	-	
Channel Plate, K1=6.99(cm)	XTEH-10L-190SM-1000A	0-6900(0-1000)	8414-7-426	ITP
Channel Plate, K2=6.99(cm)	XTEH-10L-190SM-1000A	0-6900(0-1000)	8414-7-428	ITP

Table 12. FlowMaxx Sonic Nozzles

System	Model	$D_2, mm(in)$	Serial #
Air	SN32-SA-0315	8.001 (0.315)	392-3
Fuel	SN16-SA-089	2.261 (0.089)	922-2

Density function identifies the phase angle between the signals at a given frequency. Due to the noisy appearance of the Magnitude-Squared Coherence diagram, the FFT of one of the signals was also taken to aid in determining frequencies of interest.

For example, consider the test in Figure 69. The FFT power spectrum identifies regions of interest in the $2.4kHz$ and $5.8kHz$ ranges. Examining the Magnitude Squared Coherence diagram, the value near these frequencies is near 1.0, indicating strong coherence at these frequencies. The Cross Spectrum Phase diagram has four horizontal lines both above and below the zero line, corresponding to the idealized phase angles for N_D=1, 2, 3, and 4 for both clockwise (positive) and counterclockwise (negative) propagation. For the $2.4kHz$ band, the Cross Spectrum Phase diagram crosses from the top of the range on the left to the bottom on the right of the line. This is indicative of a $\pm\pi$ rad / $\pm180°$ phase angle, which agrees with earlier observation for the acoustic waves. For the $5.8kHz$ band, the phase angle is near the $\frac{\pi}{2}$ rad / $90°$ line, corresponding to a $N_D = 2$ clockwise propagation, again in agreement with earlier observations.

Because the signals in general may have a temporal dependence, a procedure to evaluate the phase angle variation in time was desired, similar to a how a spectrogram shows frequency variation in time using a series of short time FFTs. A similar function for phase angles could not be found; therefore, a custom function was created. The

111
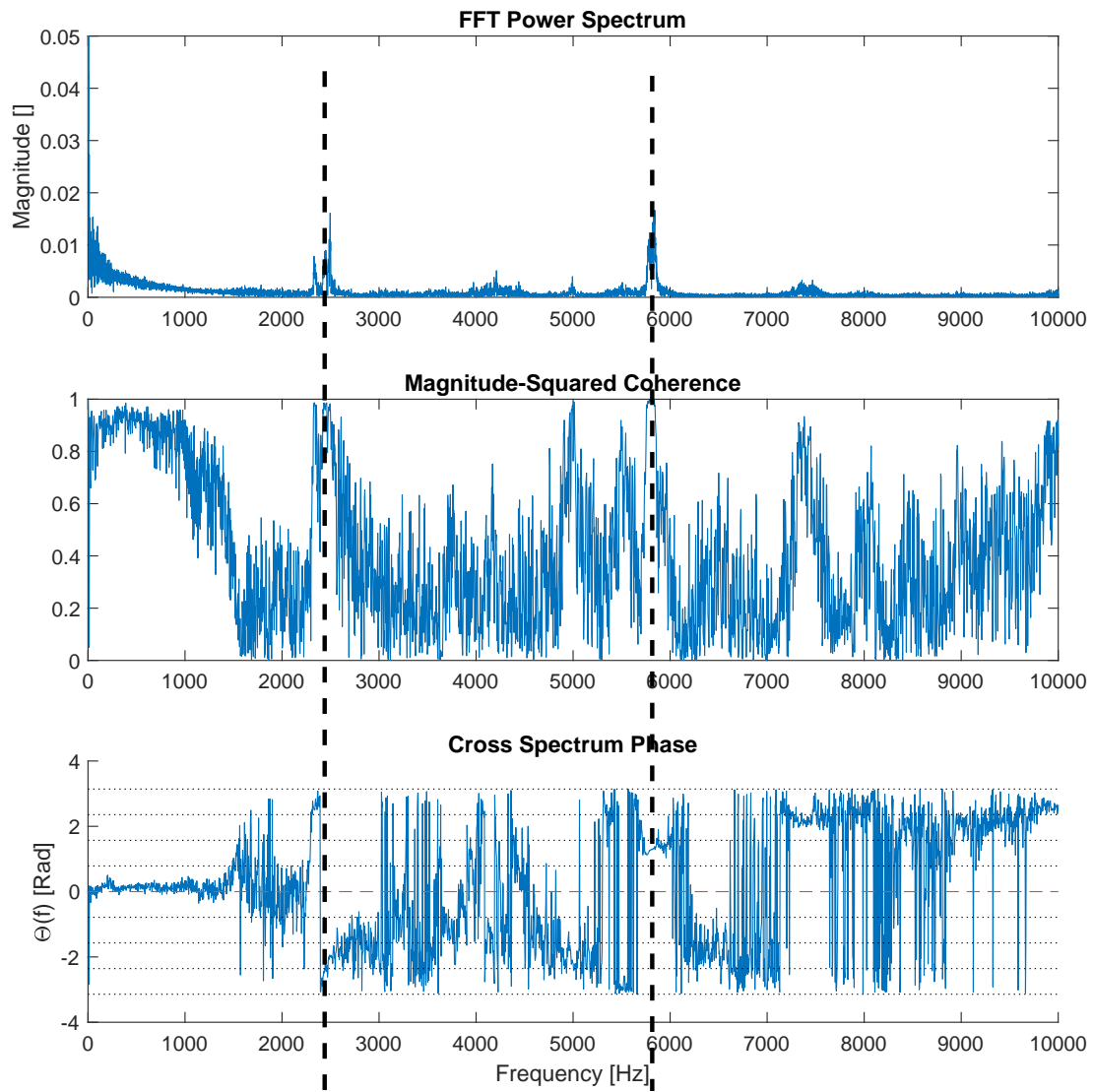
Figure 69. Wave propagation determination from K1 (blue) and K2 (red) pressure signals.

procedure begins by creating a spectrogram of one of the signals, which aids the user in determining frequencies of interest as a function of time. This is shown in Figure 70. In this example, there is a transition approximately half way through the run, with an operating frequency of $f_D \approx 5.8kHz$.

A short-time Magnitude-Squared Coherence contour plot was then generated, which is a series of Magnitude-Squared Coherence diagrams for short time segments, colored by the Magnitude Squared Coherence similar to a spectrogram. There is a band in the $5.8kHz$ range similar to the band in the spectrogram, indicating that both signals have frequency content in this frequency range. A value of near 1.0 indicates strong coherence between the two signals.

Having identified that there is coherence in the signals at a frequency, the phase angle variation as a function of time is desired. In a similar process to the short-time Magnitude-Squared Coherence contour plot, a short-time Cross Power Spectral Diagram contour plot was generated by evaluating the Cross Power Spectral Diagram for short time segments, colored by the phase angle. The phase angle is only usefully interpreted at times where there is strong signal coherence. Evaluating the phase angle from the short-time Magnitude-Squared Coherence contour plot at the same time and frequency identified from the short-time Magnitude-Squared Coherence contour plot gives the phase angle for that time and frequency, as shown in Figure 70. In this case, evaluating the signal in the vicinity of $0.65s$ the maximum coherence was found at $5.8kHz$, and the phase angle between the signals was found to be $73.3°$, which is close to the $90°$ phase angle expected for $N_D = 2$ clockwise DW propagation.

3.3.2.1 Procedure Validation.

Given that this wave phase angle determination procedure has not been used before to the author's knowledge, validation of the procedure was required. To validate
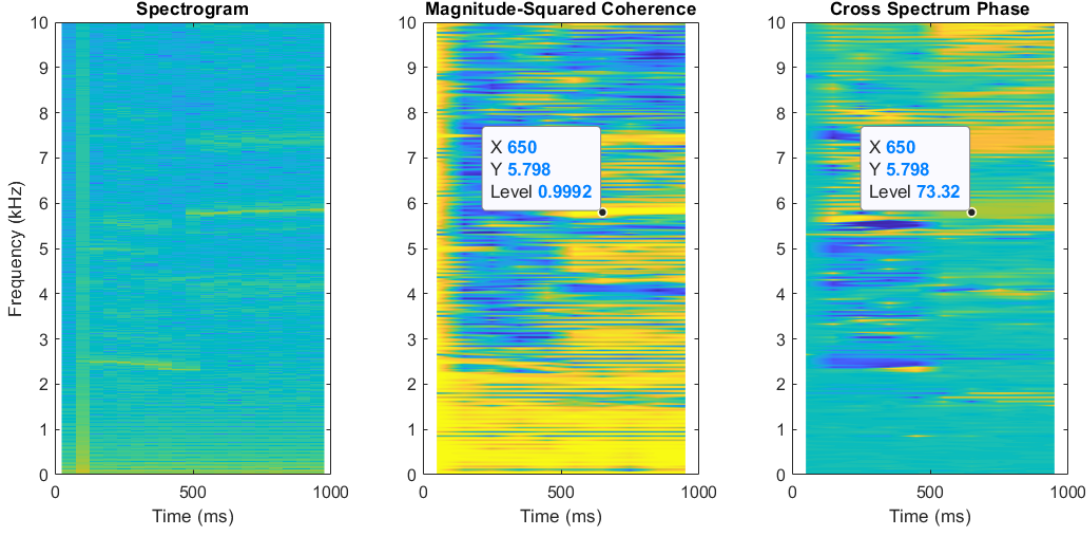
Figure 70. Phase angle determination process.

the process, a test case was evaluated with known parameters. Two discrete signals with a sampling frequency of $500kHz$ were generated corresponding to sawtooth waves with a 135° phase angle difference, which approximate DW pressure signals for $N_D = 3$ with an apparent wave pass frequency of $5.5kHz$. Equation 47 was used to generate the sawtooth wave, truncated to the first ten terms.

$$y(t)_{sawtooth} = \frac{2A}{\pi} \sum_{k=1}^{\infty} (-1)^k \frac{sin(2\pi kft)}{k} \tag{47}$$

To more realistically simulate the observed data, noise was randomly added to the signals with a Gaussian distribution and a standard deviation of 0.1. A segment of this signal is shown in Figure 71(a).

The spectrogram of one of these signals was taken, as shown in Figure 71(b). This showed frequency content in the $5.5kHz$ range as indicated by the distinct yellow line. The Magnitude-Squared Coherence Diagram also shows coherence in the $5.5kHz$ band, indicating this frequency is shared by both signals. The maximum value is nearly 1.0, indicating strong coherence. Evaluating the Cross Spectrum Phase at the same time and frequency shows a phase angle of $134.9° \approx 135°$, characteristic of $N_D =$

114
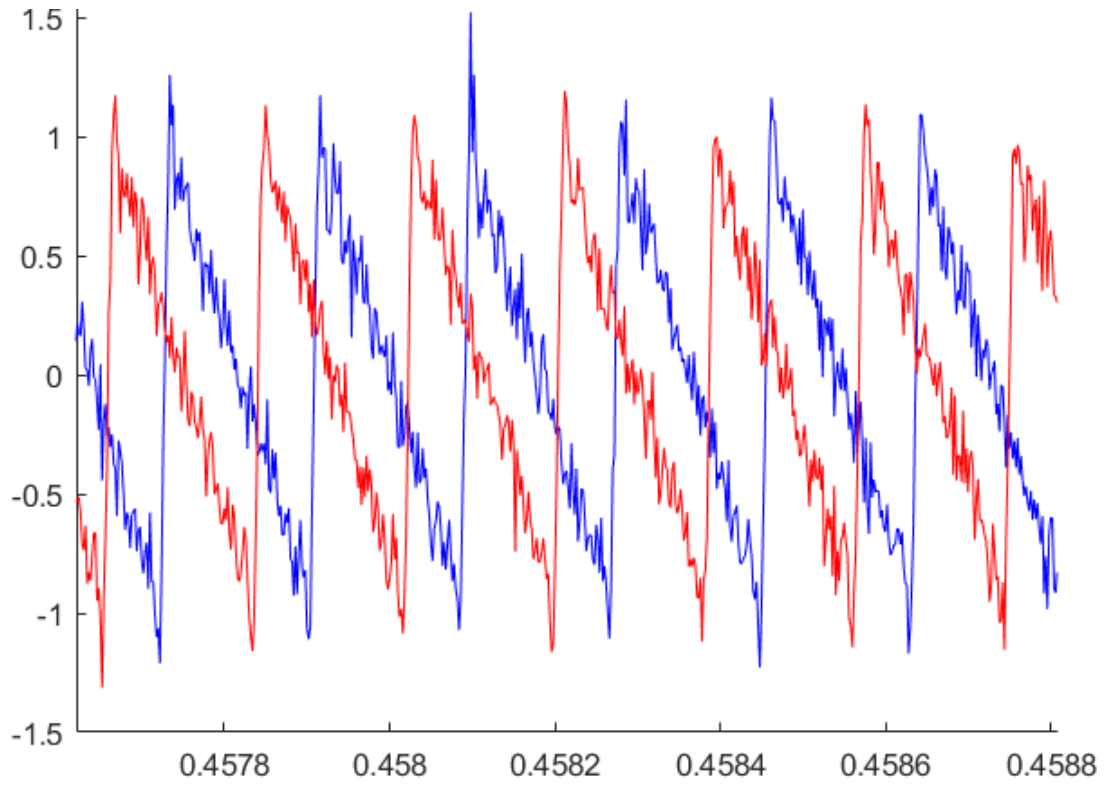
(a) Noisy Sawtooth Wave
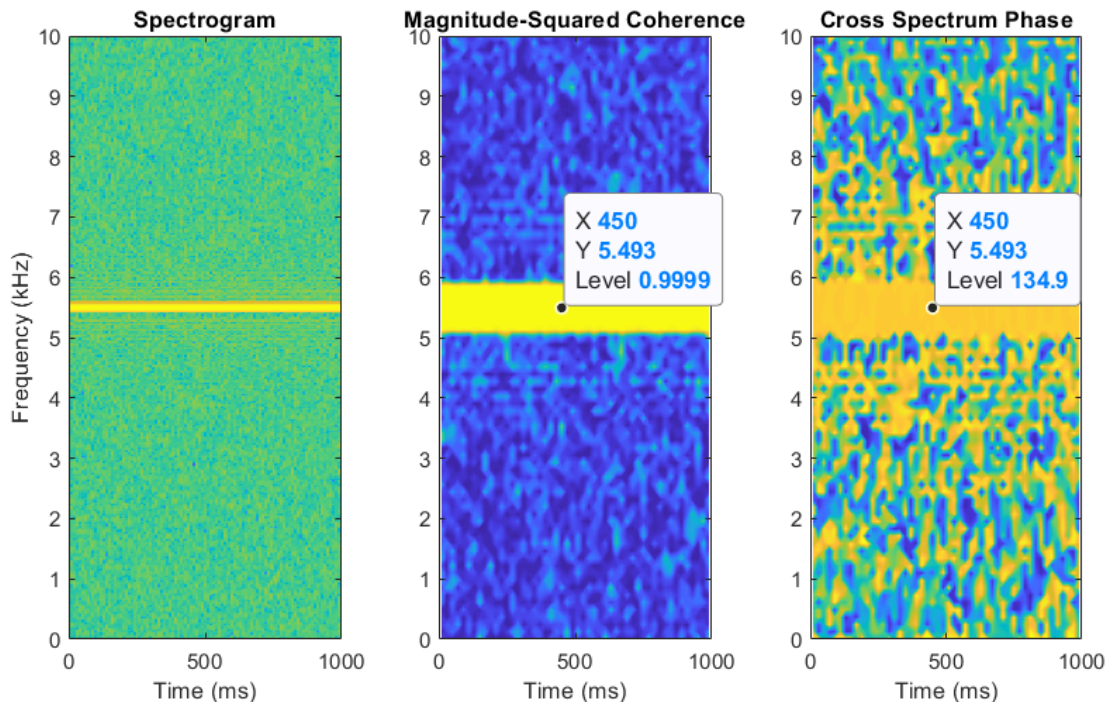
(b) Phase angle determination process

Figure 71. Verification process for phase angle determination.

115

3 operation with clockwise (red → blue) propagation. Given that the determined characteristics match the characteristics of the generated signal, the procedure was considered validated.

3.3.3 Performance Comparison.

For a performance comparison of the device operating with differing DW propagation directions, suitable performance metrics were required for comparison. The primary metric chosen to compare performance was device output power. A suitable test point was chosen corresponding to operation within the compressor's design point, that produced DWs with a clearly determined propagation direction.

Because the device had an established compressor operating map from the manufacturer, estimation of the device efficiency was readily accomplished. The compressor operating map has efficiency islands corresponding to isocontours of η_c. Determination η_c was accomplished by calculating the compressor pressure ratio (π_c) and corrected compressor mass flow rate ($\dot{m}_{c,c}$). The compressor pressure ratio was estimated by measuring the static pressure and temperature upstream and downstream of the compressor which were corrected to total pressures and temperatures with isentropic flow relations. $\dot{m}$ was known from the MAF sensor at the compressor inlet. With the known values for static P and T known upstream and downstream, the static ρ value was calculated. From continuity, $v = \frac{\dot{m}}{\rho A}$, with the value of A known from measurements of the flow path geometry at the upstream and downstream measurement locations. The speed of sound at the location was determined from $a = \sqrt{\gamma R T}$, and the local value of M was then calculated as $M = v/a$. With the local value of M known at a given location upstream and downstream of the compressor, the values

of P_t and T_t at those locations were determined with the isentropic flow relations,

$$T_t = T \left(1 + \frac{\gamma - 1}{2} M^2 \right) \tag{48}$$

$$P_t = P \left(1 + \frac{\gamma - 1}{2} M^2 \right)^{\frac{\gamma}{\gamma - 1}} \tag{49}$$

The ratio of the upstream and downstream P_t was taken, resulting in

$$\pi_c = \frac{P_{t,e}}{P_{t,i}} \tag{50}$$

The corrected mass flow rate was calculated with the corrected total pressure, $\delta_i = \frac{P_{t,i}}{P_{ref}}$ and corrected total temperature, $\theta_i = \frac{T_{t,i}}{T_{ref}}$, where $P_{ref} = 1atm$ and $T_{ref} = 300K$, with

$$\dot{m}_{c,c} = \frac{\dot{m}_c \sqrt{\theta_i}}{\delta_i} \tag{51}$$

A corrected rotational speed was also calculated as

$$N_{c,c} = \frac{N_c}{\sqrt{\theta_i}} \tag{52}$$

With values for $\dot{m}_{c,c}$ and π_c the compressor's efficiency was read directly from the manufacturer's efficiency map, shown in Figure 72.

From the Euler Pump Equation,

$$\dot{W} = \dot{m}(h_{t,e} - h_{t,i}) \tag{53}$$

Assuming a constant value for c_p in the compressor, this becomes

$$\dot{W} = \dot{m}c_p(T_{t,e} - T_{t,i}) \tag{54}$$

117
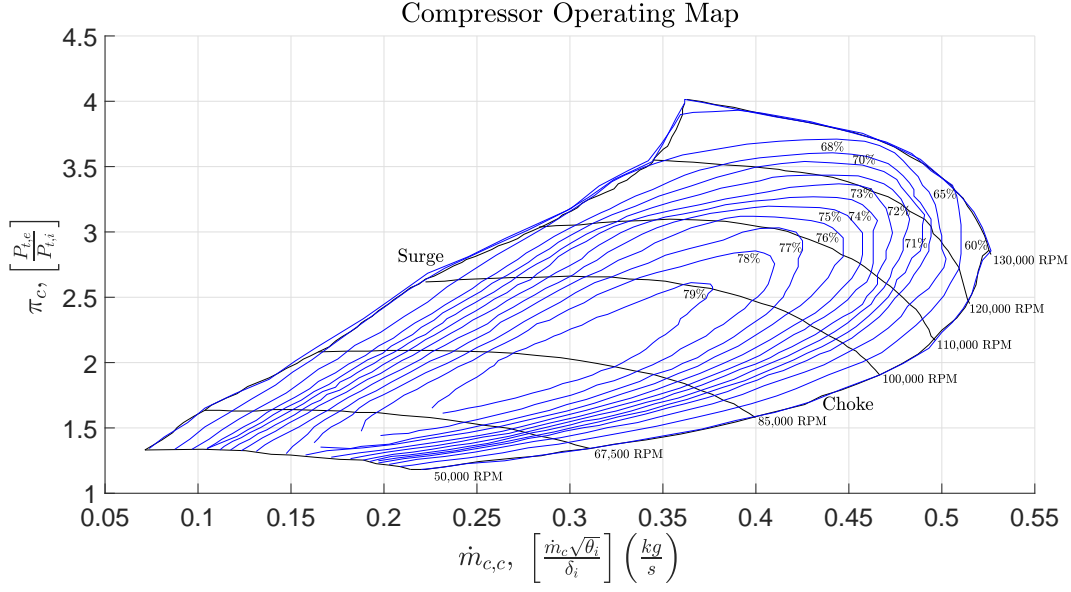
Figure 72. Compressor operating map, digitized and adapted from [91]
.

From the compressor stage efficiency for a calorically perfect gas,

$$\eta_c = \frac{\pi_c^{\frac{\gamma-1}{\gamma}} - 1}{\tau_c - 1} \tag{55}$$

the compressor power relationship becomes

$$\dot{W} = \frac{\dot{m} c_p T_{t,i}}{\eta_c} \left(\pi_c^{\frac{\gamma-1}{\gamma}} - 1 \right) \tag{56}$$

Thus, the compressor's output power was determined.

3.4 Gaseous Hydrocarbon Operation Configuration

In addition to testing with $H_2 - Air$, operation of the RRDE with gaseous $C_2H_4 - Air$ reactants was desired to begin the transition towards operation with a logistically supportable liquid hydrocarbon fuel. The baseline pure combustor configuration was utilized for this effort. Only the fuel was changed for this test, and because both H_2

118

and C_2H_4 are gaseous fuels, the change in support infrastructure was minimal.

The primary difference in this configuration as compared to the baseline configuration is that the ducting connecting the fuel system to a H_2 storage tank was instead connected to a C_2H_4 storage tank. Due to the pressures at which the gaseous fuel was stored, as it was regulated to a lower pressure in the fuel line the expansion of the gas lowered its temperature. Because of the phase transition behavior of C_2H_4 this risked producing a multi-phase flow with some of the fuel transitioning back to a fluid, or reduced reactivity. To account for this, the fuel lines were opened before the experiment and allowed to warm to near room temperature prior to testing.

The mass flow rate control system required adjustment of γ and R to match those of the corresponding test fuel, and changing of the sonic nozzle diameter would have been required if another sonic nozzle was used. Following testing, the analysis for $\dot{m}''$ and ϕ proceeded in the same manner as that of H_2 in Section 3.1, again with appropriate modification of the fuel's gas properties.

3.5 Summary

The chapter began with a discussion of the baseline RRDE and its associated test facilities in Section 3.1. Modifications to the baseline RRDE and facilities to achieve flowfield visualization and procedures to estimate r_D were discussed in Section 3.2. Visual access to the detonation channel required a transparent material, for which polycarbonate was chosen as described in Section 3.2.1. The metallic channel plate was then replaced with a new channel plate manufactured from transparent polycarbonate, as described in Section 3.2.2. Testing with the transparent polycarbonate top plate was then conducted with the wave pass frequency and wave number determined as described in Section 3.2.3, and r_D was estimated manually as described in Section 3.2.4 and via an automated procedure based on peak intensity in Section 3.2.5, with

other potential methods discussed in Section 3.2.6. With a known N_D, f_D, and r_D the methodology to calculate an improved v_D was described in Section 3.2.7.

Following testing with the transparent channel plates, the radial inflow turbocharger was installed to explore DW propagation direction effects on the turbomachinery as described in 3.3. Changes to the instrumentation required were described in Section 3.3.1. Three generalized procedures were then described which permit the determination of wave direction within the channel, assuming a rotating DW, including visual examination of the phase lag between pressure traces, use of a FFT power spectrum, Magnitude-Squared Coherence, and Cross spectrum Phase diagram for examination of an entire test run, and a short-time variant of these functions displayed as a contour plot for time-dependent examination of the wave direction. Finally, a discussion on the facilities modifications required for operation with alternative gaseous hydrocarbon fuels were discussed in Section 3.4.

IV. Results and Discussion

The results of the present research are provided in this chapter. Section 4.1 presents the experimental flowfield visualization results conducted to understand the location and velocity of the detonation wave within the RRDE channel. Section 4.2 examines the response of the RRDE's power generation to wave direction, turbine back pressure, and compressor back pressure. Finally, Section 4.3 discusses preliminary attempts to operate the RRDE with gaseous hydrocarbon fuels.

4.1 Flowfield Visualization

Utilizing the polycarbonate channel plate windows, flow visualization testing was conducted as described in Section 3.2 with $H_2 - Air$ reactants at varying values of $\dot{m}''$ and ϕ. The detonation waves were captured by high speed photography by viewing the window through a mirror, and detonation frequency was primarily determined by the pressure fluctuations recorded by a high speed pressure transducer. Test conditions were selected to match those of previous testing performed by Huff [41] for reference. Fewer test points were conducted than in the previous research due to the limited life of the channel top plates, as discussed in Section 4.1.2. The operating conditions of this testing and the modes observed are summarized in Table 13. $\dot{m}''$ values varied from 35-170 $\frac{kg}{m^2-s}$ and ϕ values varied from 0.5-0.9. These experiments had a similar operability to that found by Huff [41] as shown in Figure 73, though the present research found a transition region where both one and two wave operation occurred in the vicinity of the line drawn between one wave and two wave operation by Huff. The mode persistence behavior for several cases is demonstrated in Appendix A.

Figure 73 (b) shows that multiple modes were observed for a given operating condition in many cases. This is because in these cases multiple modes were observed

in a given test, ostensibly conducted at a constant operating condition. The temporal variation of the observed modes may be due to several factors. Following ignition the response of the fuel and air injectors and lines downstream of the sonic nozzles to the pressure rise caused by ignition may be transient, resulting in a variation in the mass flux and equivalence ratio within the channel before the system recovers to quasi-steady operation. The fuel and air injectors are of dissimilar type and size, the lines supplying them are different in quantity, length, and diameter, and the pressures of the reactants within the lines to achieve the required flow rates and the gas properties of the reactants themselves are dissimilar, so the fuel and oxidizer systems need not have the same response characteristics following ignition, to include recovery time.

The thermal response of the system may also play a role, as the heat transfer characteristics on startup are transient and may affect the system response. At ignition the wall temperature is lower and more readily facilitates heat transfer, but as the detonation channel walls increase in temperature throughout the run and the device itself heats up the heat transfer rate through the walls would decrease. Section 4.1.2 describes how the test conditions changed over the course of the run due to a change in both channel geometry and reactant mixture composition due to the melting and burning of the polycarbonate material. This may also in part explain the mode transition, as the melting rate of the polycarbonate channel plate is expected to increase as its temperature increases, increasing the rate at which the chemically reactive polycarbonate and its derivative species are released into the detonation channel. Alternatively, the RRDE may naturally oscillate between possible modes due to instability. Further study is required to better understand this transition phenomenon.

Figure 74 shows a side by side comparison of one and two wave modes. Note the difference in operating radius and DW shape. The one wave case shown here was near the nozzle exit, whereas the two wave case is near the outer edge. Trailing the

122

Table 13. Operating map for flow visualization testing with $H_2 - Air$ reactants using the Pure Combustor configuration. Nominal parameters: Channel Height=$4.5mm$, $AR_t = 0.2$, $AR_n = 0.6$. Asterisk (*) indicates a possible non-detonation mode

Test	Date	Case	h_c (mm)	AR_t	AR_n	$\dot{m}''(\frac{kg}{m^2s})$	ϕ	$v_{D,CJ}(\frac{m}{s})$	N_D
1	22082018	15.44.01	4.7	0.19	0.60	77.3 ± 16.3	$.64 \pm .01$	1710	$1, 2$
2	23082018	11.43.37	4.6	0.19	0.59	78.0 ± 13.3	$.90 \pm .01$	1880	1
3	24082018	08.05.28	4.9	0.18	0.59	76.2 ± 12.3	$.89 \pm .01$	1870	1
4	24082018	08.13.34	5.2	0.17	0.58	72.9 ± 11.2	$.73 \pm .01$	1780	$1, 2*$
5	24082018	08.37.22	5.4	0.17	0.58	164 ± 23.7	$.50 \pm .01$	1590	$2, 3*$
6	24082018	08.50.29	5.7	0.16	0.57	159 ± 21.9	$.52 \pm .01$	1610	$3*$
7	24082018	09.01.13	6.0	0.15	0.57	40.0 ± 5.4	$.71 \pm .01$	1760	$1,2$
8	24082018	09.08.52	6.3	0.14	0.57	38.7 ± 5.0	$.76 \pm .01$	1800	$1,2$
9	24082018	09.12.58	6.5	0.14	0.57	37.1 ± 4.6	$.80 \pm .01$	1820	$1,2$
10	24082018	09.21.46	6.8	0.13	0.57	35.9 ± 4.3	$.85 \pm .01$	1850	$1,2$
11	22012019	12.08.51	5.5	0.16	0.57	171.2 ± 110.8	$.77 \pm .01$	1800	1
12	22012019	13.21.49	7.8	0.12	0.56	124.2 ± 57.9	$.71 \pm .01$	1770	2
13	22012019	15.43.53	9.9	0.09	0.56	97.4 ± 35.5	$.68 \pm .01$	1740	2
14	25012019	11.22.45	4.9	0.18	0.59	48.5 ± 15.3	$.53 \pm .01$	1620	2
15	25012019	11.44.34	5.7	0.16	0.58	42.6 ± 11.6	$.63 \pm .01$	1700	2
16	25012019	11.59.26	6.4	0.14	0.57	53.9 ± 12.9	$.51 \pm .01$	1600	2
17	25012019	12.11.49	7.2	0.13	0.57	48.1 ± 10.3	$.60 \pm .01$	1680	2

(a) Huff
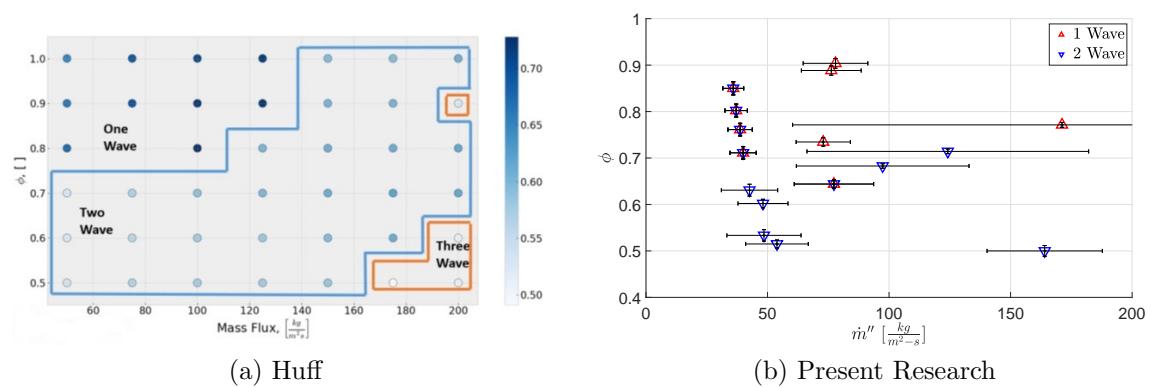
(b) Present Research

Figure 73. Comparison of the operability map from (a) Huff [41] with dots colored by $\frac{v_D}{v_{D,CJ}}$ and (b) the operational mode observed in the present research with error bars shown. $AR_n = 0.6(nominal)$.

(a) $N_D = 1$ example from Test 3.

(b) $N_D = 2$ example from Test 1.
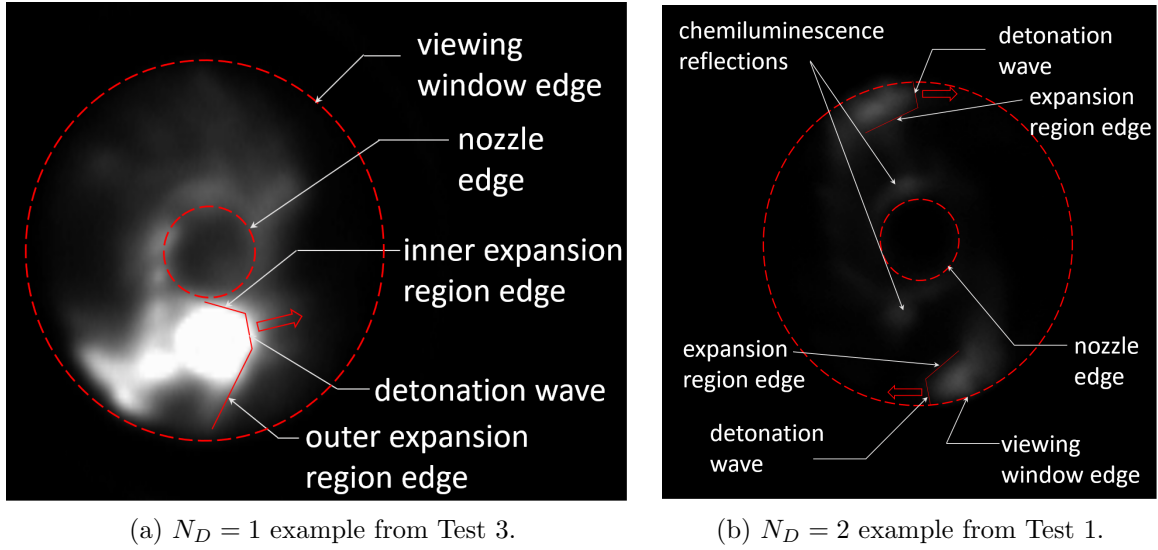
Figure 74. Comparison of an $N_D = 1$ and an $N_D = 2$ case.

DW front, a region of high chemiluminescence in the expansion waves was observed, corresponding to high temperature radiating products. For the two wave case, the expansion region curved upward due to the radial flow of the gases. Chemiluminescent reflection were also observed on the nozzle.

Initial analysis revealed several trends. When the RRDE was operating in a one wave mode the DW tended to shift to a radial location near the inner radius, as shown in Figures 75(a) and (b). These DWs tended to have a less regular shape, and significant radial shift from one cycle to the next was possible. Since these DWs propagated away from the wall, the DW was unconstrained by physical barriers in either radial direction, reducing confinement. Because of this, there were expansion waves on either side of the DW, both upstream and downstream. This behavior is sketched in Figure 76(a). Figure 75(c) shows a two wave case near the outer edge but not attached to it. This DW was observed to be unsteady, with one wave nearly catching up to the other, then decaying in speed, producing an oscillating angle between the DWs. Figure 75(d) shows a one wave DW near the outer radius, confined or nearly confined by the outer edge, which was an anomaly among the

124

one-wave cases. This may be due to the $\dot{m}''$ in Case 11 being considerably higher (Ref. Table 13). Two wave cases near the outer radius are shown in Figure 75(e) and (f). These DWs were steady, at $\approx 180°$ angles relative to one another. Due to propagation near the outer radius, these DWs were partially confined on their outer edge by the backward facing step of the throat ring, as sketched in Figure 76(b). While the progression of Figure 75 shows that $\bar{r}_D$ tends to depend on the operating mode, with one wave modes typically near the inner radius and two wave modes typically near the outer radius, there was some overlap in the radius at which the modes occurred.

The one wave cases propagating away from the outer edge were observed to have a degree of unsteadiness. As shown in Figure 77 for Test 3, the shape of the detonation wave was susceptible to variation within a given cycle. The radial location was also susceptible to variation. While the root cause of these phenomena is uncertain, they may be related to the lack of confinement permitting instability of the DW.

When operating in a one wave mode, intermittent transition to a two wave counter-rotating mode was also observed as shown for Test 3 in Figure 78. Following an instability the one wave detonation shown propagating counterclockwise in Frames a and b bifurcates in Frame c. Two waves then propagate around either side of the nozzle, reflecting as they intersect on opposite sides of the channel. This is a two wave mode and may be a detonation, but is not a conventional rotating detonation mode. This mode eventually transitioned back to a one wave rotating mode, which could re-initiate in either azimuthal direction. The exact instability that caused this mode is unknown, but as it was seen exclusively in one wave operation propagating away from the outer edge, the lack of confinement on the outer edge may be a factor. Alternatively, this may be caused by ingestion of an especially large pocket of product gases which had recirculated back to this radial location disrupting the wave prop-
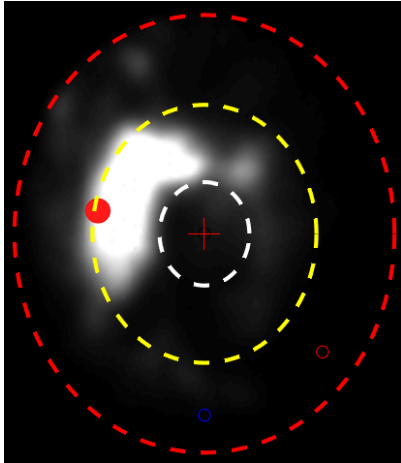
(a) Test 1, $N_D = 1$, $\bar{r}_D = 4.96cm$.
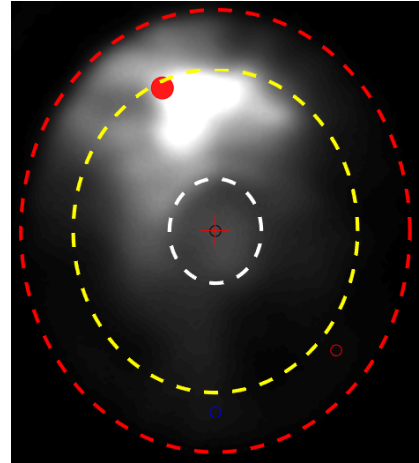
(b) Test 2, $N_D = 1$, $\bar{r}_D = 6.15cm$.
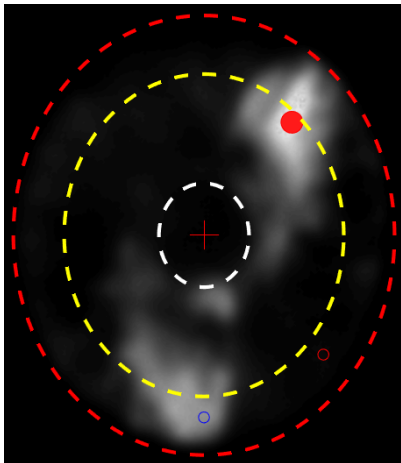
(c) Test 13, $N_D = 2$, $\bar{r}_D = 6.17cm$.
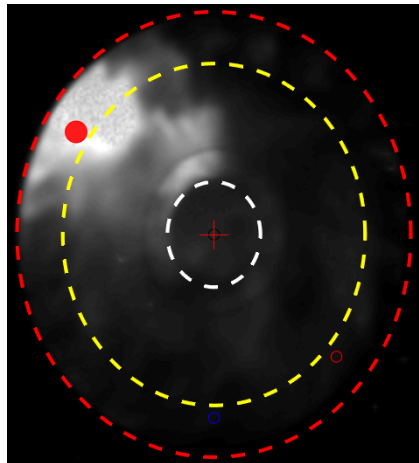
(d) Test 11, $N_D = 1$, $\bar{r}_D = 6.46cm$.
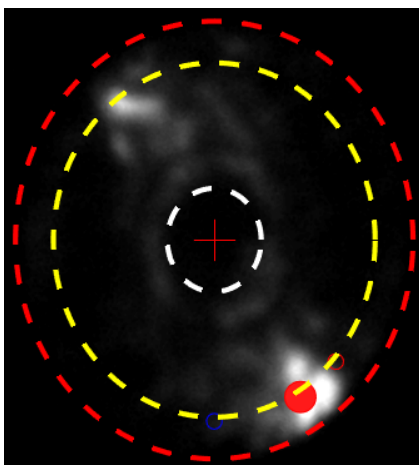
(e) Test 17, $N_D = 2$, $\bar{r}_D = 6.81cm$.
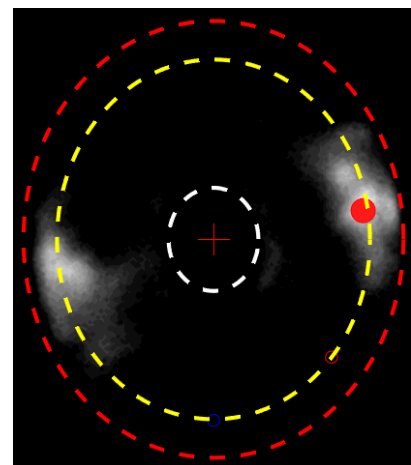
(f) Test 1, $N_D = 2$, $\bar{r}_D = 6.93cm$.

Figure 75. Comparison of $\bar{r}_D$ for various cases, indicated by yellow dotted lines. Presented in order of increasing $\bar{r}_D$.

126

(a) Propagation of DW away from wall.

(b) Propagation of DW near wall.
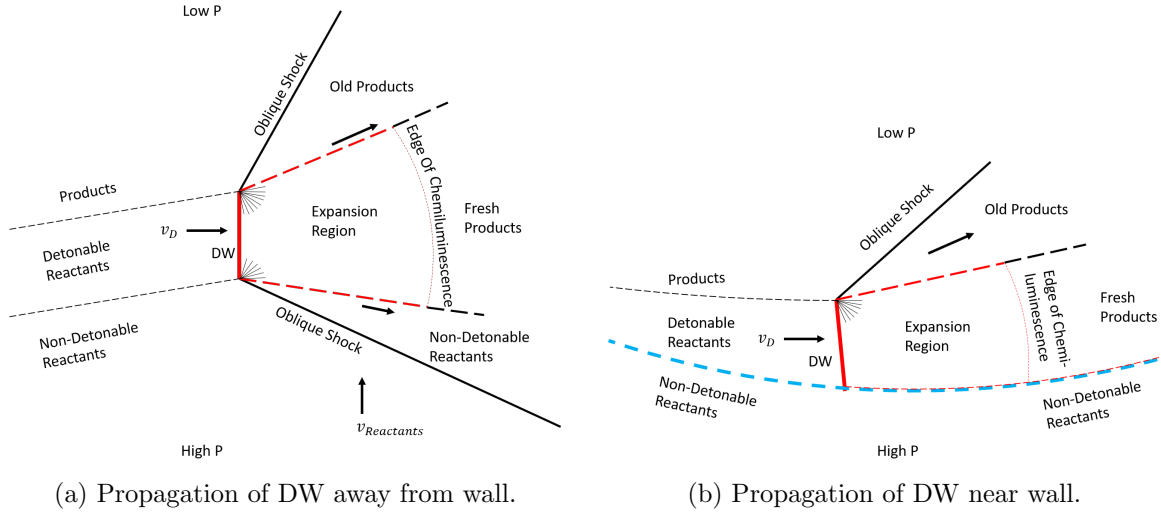
Figure 76. Sketch of (a) a geometrically unconstrained DW and (b) a geometrically constrained DW propagating within an RRDE detonation channel; the throat ring is in the direction of high pressure, and the nozzle is in the direction of low pressure.

agation. Transition between the one wave rotating and two wave counter-rotating modes took between less than one cycle up to several cycles, typically less than ten.

One notable outlier to the trend of one wave detonations near the inner radius was observed in Test 11. As shown in Figures 75 and 79 this one wave detonation propagates near the outer radius of the channel. Test 11 occurred at a high $\dot{m}''$ and moderate ϕ (Ref. Table 13). This mode existed for the first 1/20th second of the test, after which it degenerated into a clapping mode similar to that shown in Figure 78. A more complete discussion on the persistence of the modes in Test 11 can be found in Appendix A, Figure 115.

Conversely, when the RRDE operated in a two wave rotating mode the DW tended to shift to a radial location of $6.75cm$, near the outer radius. Figure 80 shows the evolution of a stable two wave case from Test 1 for one period in parts *a-l*. The DW traverses the outer radius of the channel. While minor fluctuations in intensity and shape exist, the wedge shape of the chemiluminescent expansion wave aft of the detonation is readily identifiable for both waves. These DWs exhibited a more regular shape, with little radial variation.

127
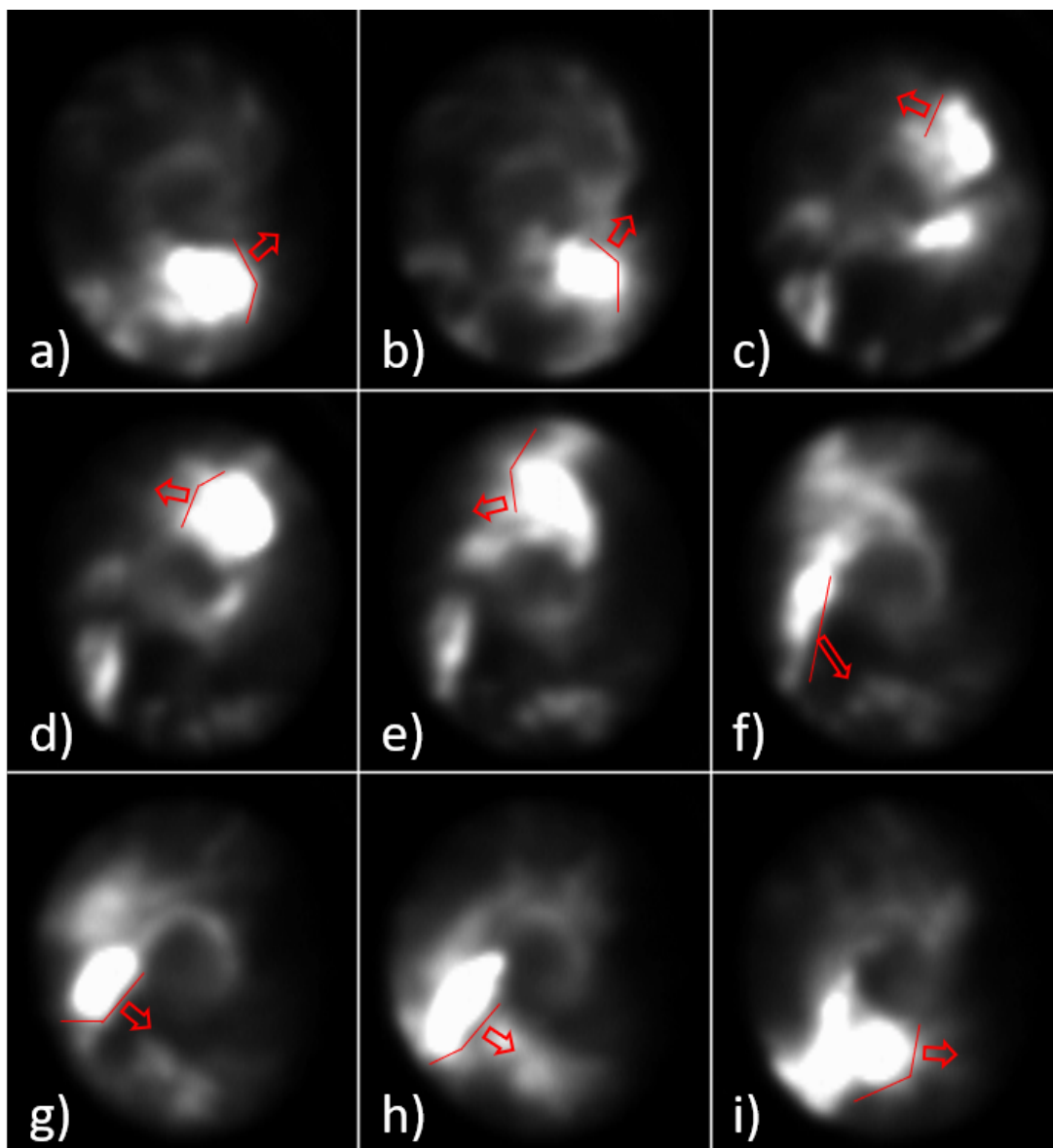
Figure 77. Typical one wave detonation evolution within the RRDE channel for Test 3 over one period with counterclockwise DW progression. Images taken at $80\mu s$ intervals.
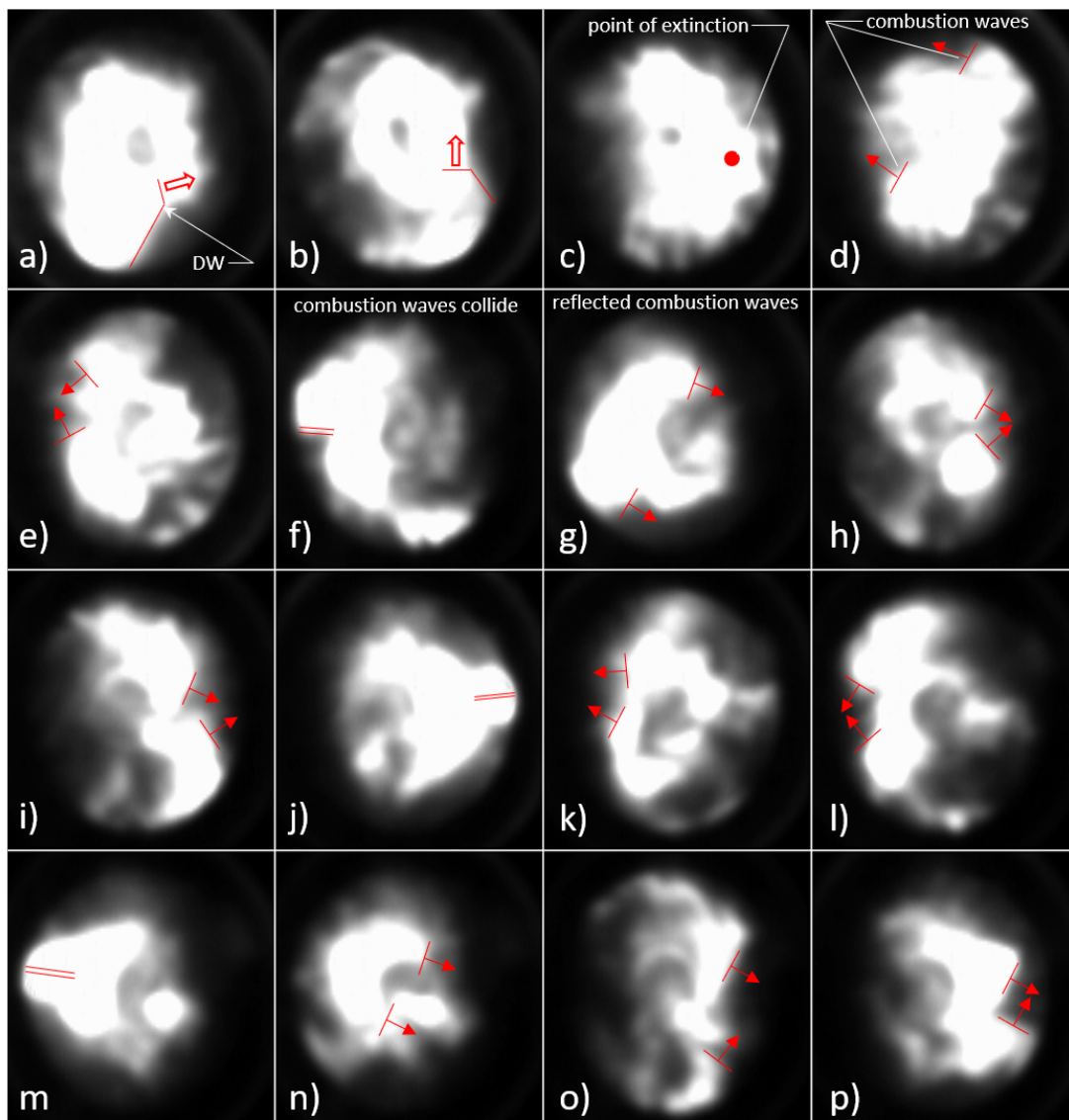
Figure 78. Breakdown of a one wave detonation into two counter-propagating DWs for Test 3. Images taken at $120\mu s$ intervals.
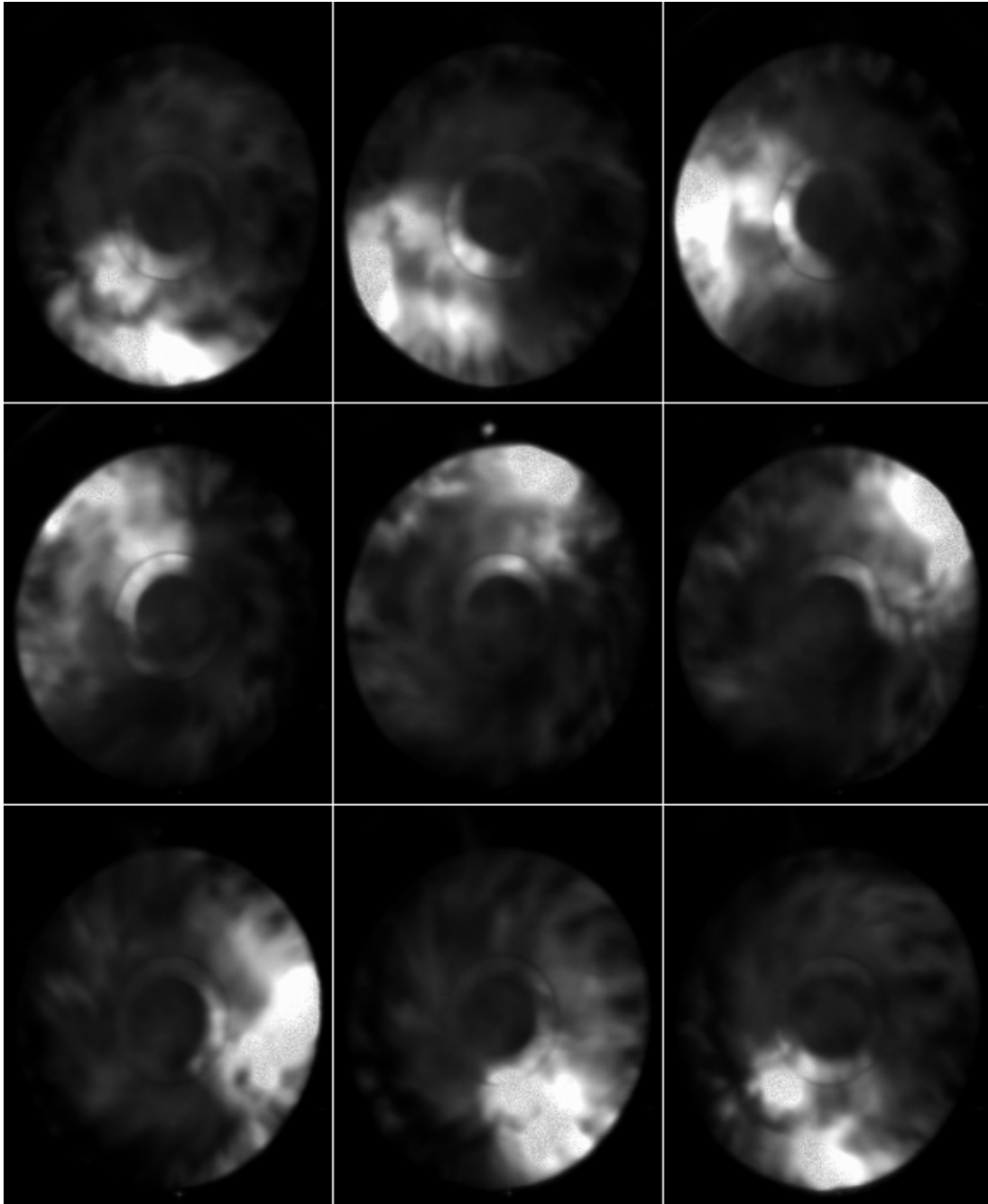
Figure 79. One wave detonation evolution within the RRDE channel for Test 11 over one period with clockwise DW progression. Images taken at $40\mu s$ intervals.
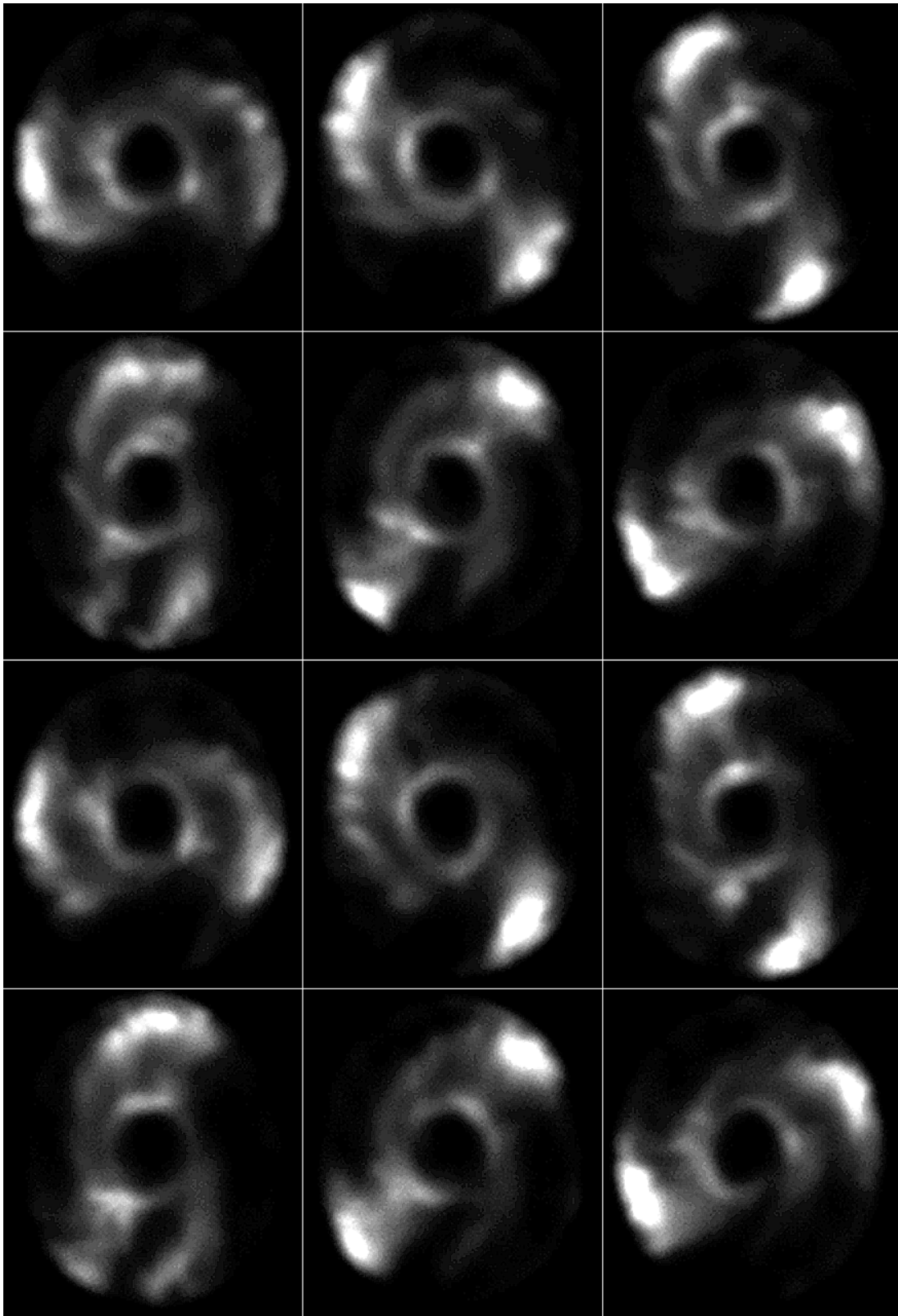
Figure 80. Two wave detonation evolution within the RRDE channel for Test 1 over one period with clockwise progression. Images taken at $40\mu s$ intervals with a $39\mu s$ exposure.

Unstable propagation of rotating two wave detonations was observed as well. A mode was observed in Test 13 with the DWs that were not at opposite sides of the channel, but were rather oscillating about the 180° angle. This is shown in Figure 81, with two DWs labeled a and b, and the angle between them indicated by colored lines. Green lines indicate images where wave a trails wave b, whereas yellow lines indicate images where wave b trails wave a. This mode was observed over at least several dozen cycles, before the DW transitioned to an unstable one wave mode, and was preceded by a stable two wave mode.

An instability in the flow in Test 12 lead to a four counter-rotating wave clapping mode as shown in Figure 82. This mode followed a two wave rotating mode at startup, persisted for $\approx 0.2s$, then transitioned back to a two wave detonation. Based on this behavior, this mode appears to be analogous to the two counter-rotating waves of the clapping mode frequently observed in one wave cases.

In Test 6 a stable three node mode was observed. Figure 83 shows the evolution of this case for one period in parts a-j. This behavior is sketched in Figure 84. The mode is comprised of counter-rotating sets of combustion waves. These waves periodically intersected creating regions of high intensity chemiluminescence which appear similar to DWs. This mode was observed to be stable, persisting for the duration of the experiment after initial ignition transients. The locations of the intersections were also stable, with little variation. A similar three node mode was observed in Test 5 as well.

Considering the behavior of the three counter-rotating modes observed, these modes appear to be related to the nominally rotating modes. The two counter-rotating wave mode was observed in nominally one rotating wave operation. The four counter-rotating wave mode was observed in a nominally two rotating wave operation regime. Three wave operation was not observed in the present work, but the
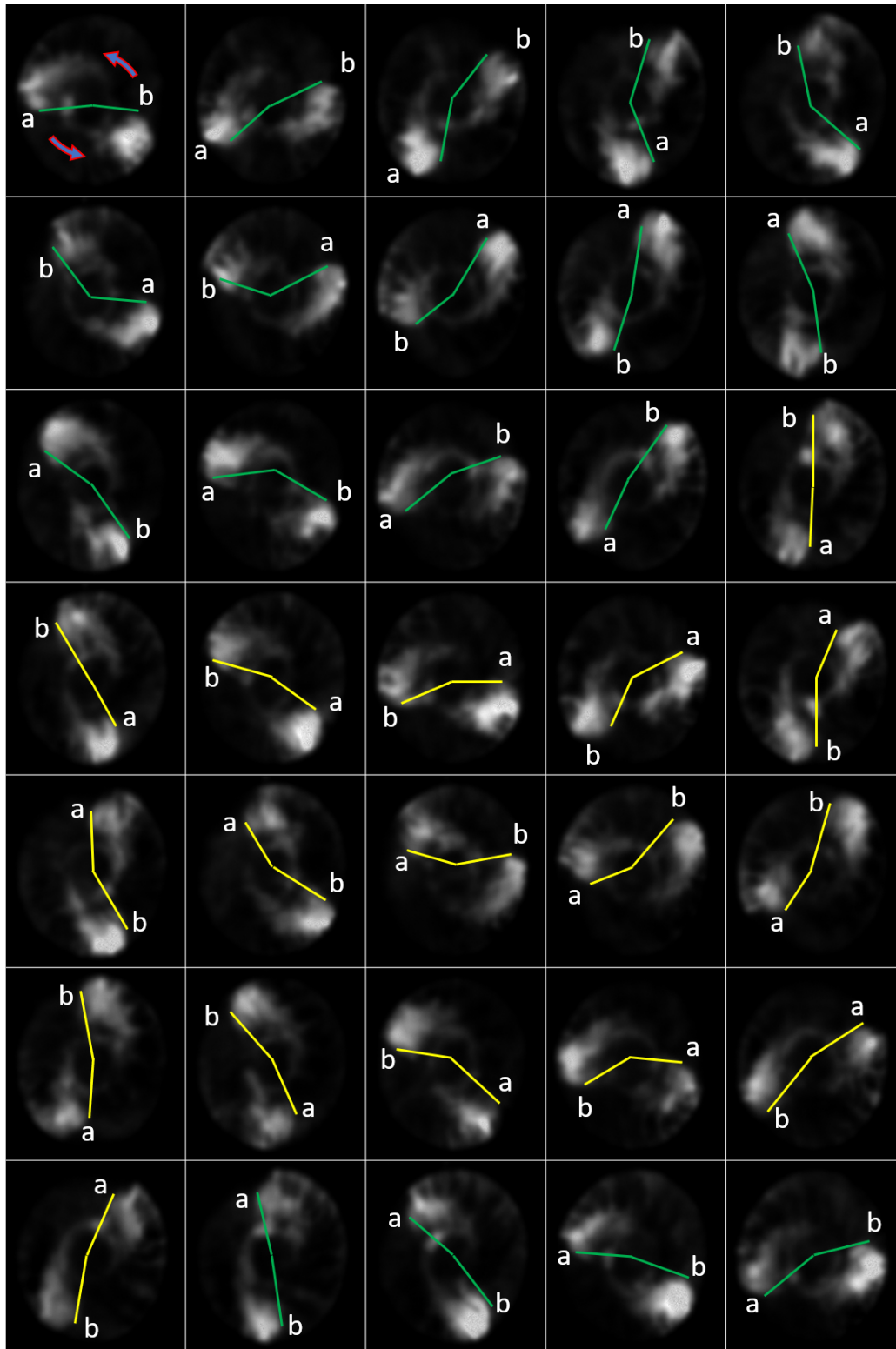
Figure 81. Unstable two wave detonation evolution within the RRDE channel for Test 13 with counterclockwise progression. Images taken at $40\mu s$ intervals with a $0.294\mu s$ exposure.
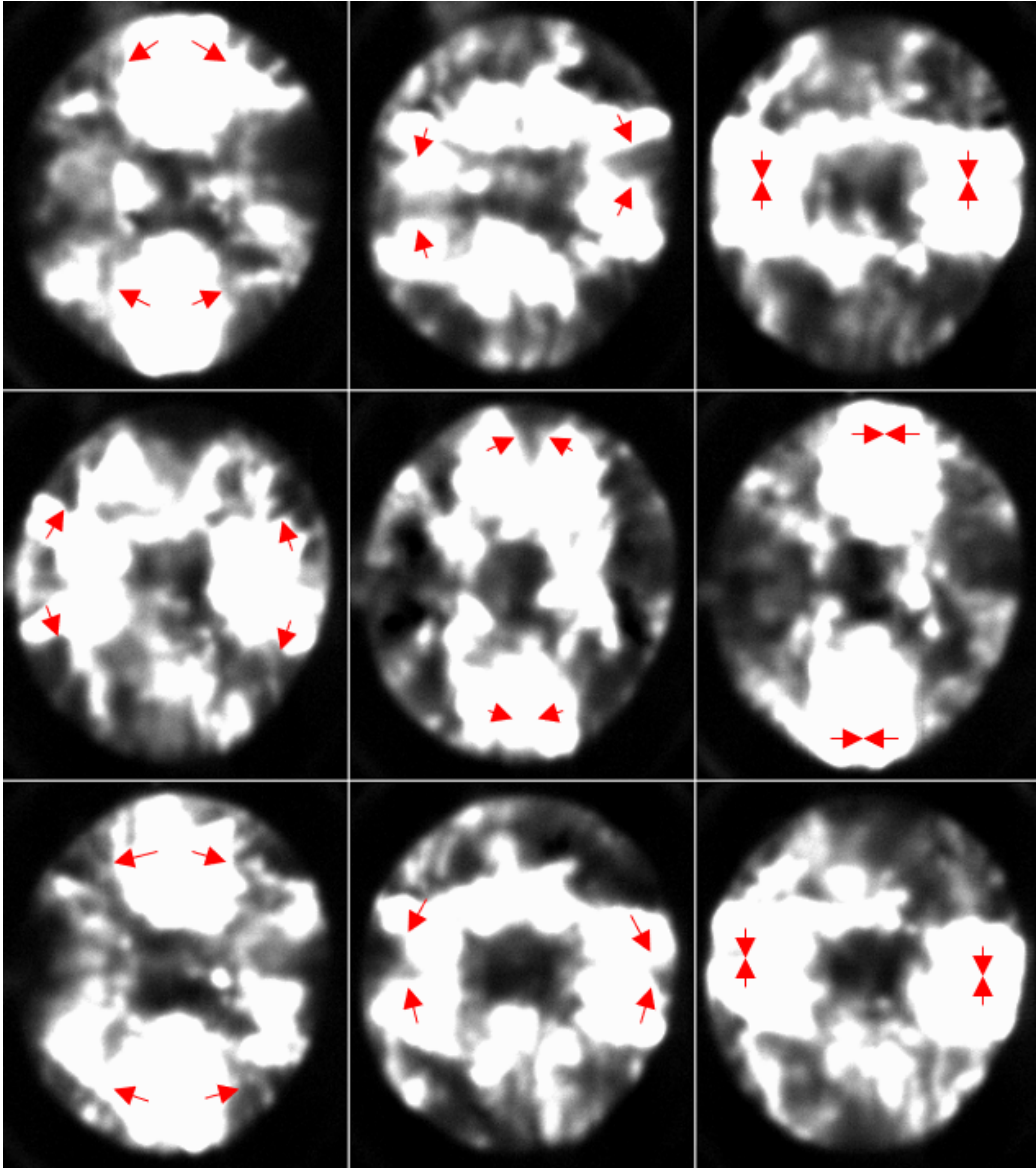
Figure 82. Four wave clapping mode from Test 12. Images taken at $40\mu s$ intervals with a $1\mu s$ exposure.
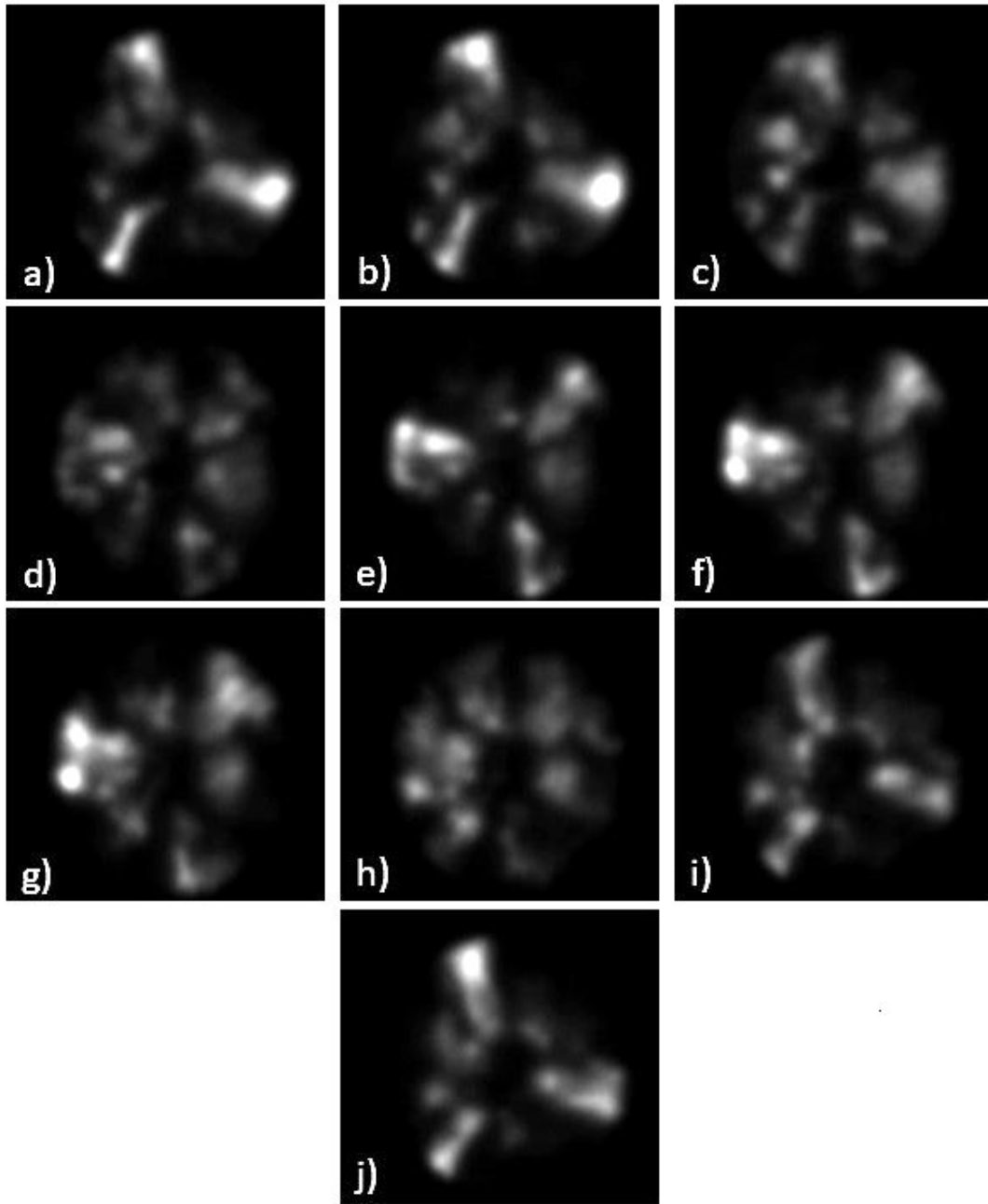
Figure 83. Three node mode evolution within the RRDE channel for Test 6 over 1 period. Images taken at $40\mu s$ intervals with a $1\mu s$ exposure.
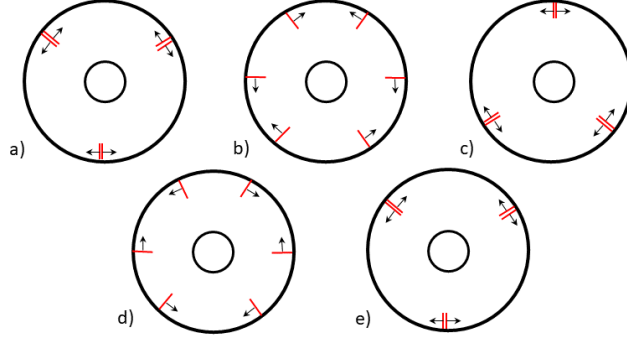
Figure 84. Three node mode notional sketch with combustion wave location and direction of propagation indicated. One period shown.

three node mode comprised of six counter-rotating waves was observed in an operating regime where three rotating wave operation occurred in previous work by Huff [41]. Thus, the number of counter-rotating waves in these modes appear to be related to the rotating mode with half as many waves. For both the two counter-rotating wave mode and four counter-rotating wave mode cases it was observed that a set of waves propagating in one direction became more powerful than the set of waves propagating in the opposite direction, and re-initiated a rotating mode with one or two waves, respectively.

The radius at which the DWs propagate varies as shown in Figure 85. Two wave detonations occurred at $\bar{r}_D > 6.0cm$, whereas one wave detonations occurred at $4.5cm < \bar{r}_D < 7.0cm$. The value of r_D did not have a strong dependence $\dot{m}''$, but did appear to increase slightly on average as $\dot{m}''$ increased. For one wave operation,

$$r_D = 0.01073\dot{m}'' + 4.766; R^2 = 0.6133 \tag{57}$$

whereas for two wave operation,

$$r_D = 0.00488\dot{m}'' + 6.366; R^2 = 0.2202 \tag{58}$$

136

Table 14. Radial location, frequency, and wave speed results. $\bar{v}_D$ **calculated from the Peak Intensity** $\bar{r}_D$ **value.**

Test	ϕ	$\dot{m}''\frac{kg}{m^2-s}$	N_D	$\bar{f}_D(+/-)$ Hz	Manual $\bar{r}_D$ cm	Peak Intensity $\bar{r}_D$ cm	r'_D cm	$\bar{v}_D(+/-)$ m/s	$\frac{\bar{v}_D}{v_{D,CJ}}(+/-)$
1	$.64 \pm .01$	77.3 ± 16.3	1	2531 (215/304)	4.5	4.96 ± 0.36	2.38	788 (86/108)	.46 (.05/.06)
			2	4335 (25/25)	7.5	6.93 ± 0.22	1.66	944 (31/31)	.55 (.02/.02)
2	$.90 \pm .01$	78.0 ± 13.3	1	2581 (189/331)	5.5	6.15 ± 0.34	2.62	998 (91/139)	.53 (.05/.07)
3	$.89 \pm .01$	76.2 ± 12.3	1	2575 (192/338)	5.5	6.03 ± 0.50	2.69	976 (109/152)	.52 (.06/.08)
4	$.73 \pm .01$	72.9 ± 11.2	1	2557 (173/311)	5.0	$5.69 \pm 0.48*$	2.62*	914 (98/135)*	.51 (.06/.08)
			2a	4305 (77/79)	4.0	$5.69 \pm 0.48*$	2.62*	769 (66/66)*	.43 (.04/.04)
5	$.50 \pm .01$	164.0 ± 23.7	2	4410 (310/150)	7.0	7.81 ± 0.12	1.04	1082 (79/41)	.68 (.05/.03)
			3a	5584 (67/68)	7.5	7.61 ± 0.16	1.13	890 (22/22)	.56 (.01/.01)
6	$.52 \pm .01$	158.8 ± 21.9	3a	5662 (16/23)	8.0	7.26 ± 0.44	1.34	861 (53/53)	.53 (.03/.03)
7	$.71 \pm .01$	40.0 ± 5.4	1	2557 (151/316)	6.0	5.20 ± 0.51	2.00	835 (94/129)	.47 (.05/.07)
			2	4185 (140/125)	7.0	6.59 ± 0.32	2.17	866 (52/50)	.49 (.03/.03)
8	$.76 \pm .01$	38.7 ± 5.0	1	2549 (118/298)	5.0	4.97 ± 0.27	1.58	797 (56/101)	.44 (.03/.06)
			2	4301 (49/110)	7.5	6.27 ± 0.13	2.05	847 (20/28)	.47 (.01/.02)
9	$.80 \pm .01$	37.1 ± 4.6	1	2550 (127/195)	4.5	4.93 ± 0.27	1.52	790 (58/73)	.43 (.03/.04)
			2	4296 (62/80)	6.5	6.69 ± 0.39	1.90	902 (54/55)	.50 (.03/.03)
10	$.85 \pm .01$	35.9 ± 4.3	1	2533 (92/185)	5.5	5.23 ± 0.32	2.00	832 (58/78)	.45 (.03/.04)
			2	4304 (71/88)	7.0	6.33 ± 0.85	1.94	856 (115/116)	.46 (.06/.06)
11	$.77 \pm .01$	171.2 ± 110.8	1	3075 (33/32)	N/A	6.46 ± 0.33	2.48	1248 (65/65)	.69 (.04/.04)
12	$.71 \pm .01$	124.2 ± 57.9	2	4897 (161/130)	N/A	6.29 ± 0.12	2.07	968 (37/32)	.55 (.02/.02)
13	$.68 \pm .01$	97.4 ± 35.5	2	4525 (25/25)	N/A	6.17 ± 0.21	1.31	877 (30/30)	.50 (.02/.02)
14	$.53 \pm .01$	48.5 ± 15.3	2	4079 (19/43)	N/A	6.59 ± 0.65	2.79	845 (83/84)	.52 (.05/.05)
15	$.63 \pm .01$	42.6 ± 11.6	2	4202 (55/68)	N/A	6.87 ± 0.34	2.29	906 (46/47)	.53 (.03/.03)
16	$.51 \pm .01$	53.9 ± 12.9	2	4212 (35/39)	N/A	6.99 ± 0.23	1.62	925 (31/31)	.58 (.02/.02)
17	$.60 \pm .01$	48.1 ± 10.3	2	4346 (166/130)	N/A	6.81 ± 0.24	1.66	929 (48/43)	.55 (.03/.03)

The R^2 values indicate the correlation was weak for two wave operation, but fair for one wave operation. In general, the one-wave cases propagated near the inner radius of the device, near the nozzle. For the one wave operation, $r_{D,ave} \approx 5.5cm$. Conversely, for two wave operation the DW moved radially outward, with $r_{D,ave} \approx 6.8cm$. The value of ϕ also appeared to impact r_D, with $\bar{r}_D$ increasing with ϕ for one wave operation, and decreasing with ϕ for two wave operation. For one wave operation,

$$r_D = 3.343\phi + 2.889; R^2 = 0.2376 \tag{59}$$

whereas for two wave operation,

$$r_D = -2.703\phi + 8.485; R^2 = 0.4624 \tag{60}$$

The R^2 value for both of these curve fits indicates weak correlation, although the correlation is better for the two wave operation.

Huff [41] used a fixed radius of $7.0cm$ in his calculations of v_D. Given that the $r_D \approx 5.5cm$ operating in a one wave mode, the calculations presented overestimated the detonation velocity for one wave cases. The v_D for the $N_D = 2$ cases would have been only slightly overestimated, as $r_{D,ave} \approx 6.8cm$ for two wave cases. Therefore, a proposed correction factor of $\frac{5.5}{7} \approx 0.78$ is suggested for the $N_D = 1$ cases presented in Huff. Applying this correction factor to the Huff's $N_D = 1$ cases in Figure 73, all of the Huff's DWs experienced a detonation velocity near $\frac{v_D}{v_{D,CJ}} \approx 0.5$.

Figure 86 shows the calculated v_D values normalized by $v_{D,CJ}$ for the present research, as calculated with the estimated peak intensity mean radius and Kulite pressure transducer frequency. With two exceptions, these values are all $\frac{v_D}{v_{D,CJ}} \approx 0.5 \pm 0.1$, which is in line with Huff's data with the correction factor applied. For the two exceptional cases with $\frac{v_D}{v_{D,CJ}} \approx 0.7$, the $\dot{m}''$ was considerably higher than the other cases. Figure 86 (a) indicates that $\frac{v_D}{v_{D,CJ}}$ increases slightly with ϕ for one wave operation,

$$\frac{v_D}{v_{D,CJ}} = 0.1198\phi + 0.4074; R^2 = 0.0163 \tag{61}$$

although the R^2 value is such that this correlation is nearly useless. For two wave operation $\frac{v_D}{v_{D,CJ}}$ tended to decrease with ϕ,

$$\frac{v_D}{v_{D,CJ}} = -0.4036\phi + 0.7986; R^2 = 0.6122 \tag{62}$$

with the R^2 value indicating fair correlation. Figure 86 (b) shows that for both one wave

$$\frac{v_D}{v_{D,CJ}} = 0.001793\dot{m}'' + 0.3765; R^2 = 0.9164 \tag{63}$$

138
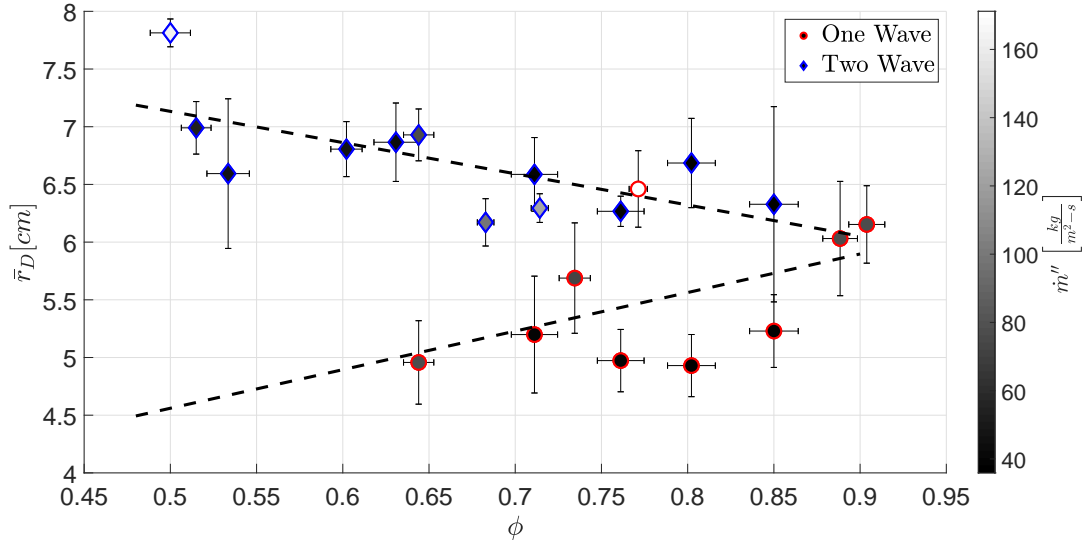
(a) Detonation Radius vs Equivalence Ratio
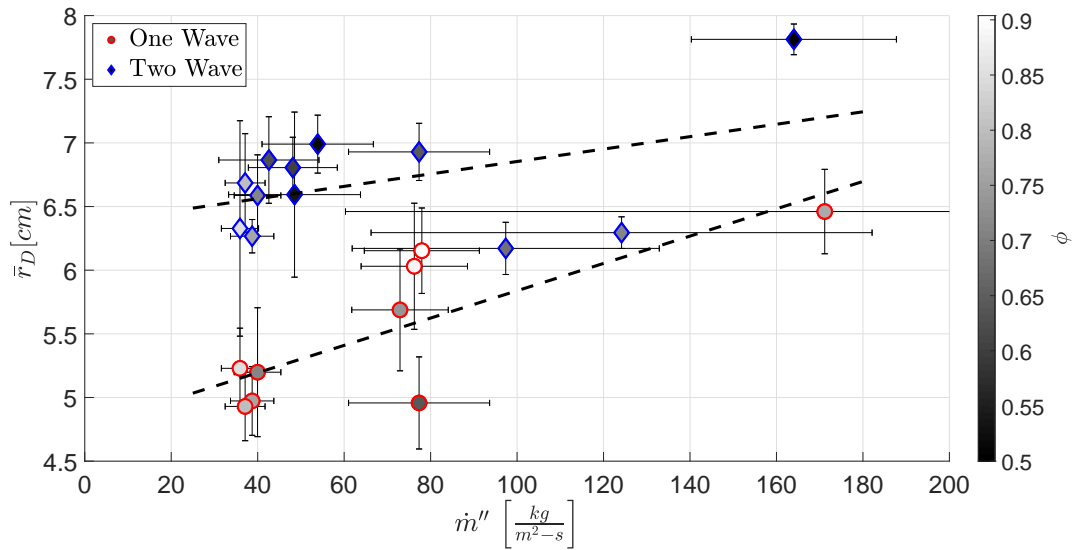
(b) Detonation Radius vs Mass Flux

Figure 85. DW radius vs (*a*) equivalence ratio and (*b*) mass flux for the RRDE with $H_2 - Air$ **reactants.**

and two wave

$$\frac{v_D}{v_{D,CJ}} = 0.001072\dot{m}'' + 0.4592; R^2 = 0.5744 \tag{64}$$

operation, $\frac{v_D}{v_{D,CJ}}$ tended to increase with $\dot{m}''$, with strong correlation for one wave operation and fair correlation for two wave operation.

Figure 87 shows the normalized detonation velocity as a function of detonation radius. The data appear to show an increase in $\frac{v_D}{V_{D,CJ}}$ as a function of $\bar{r}_D$ for both one wave,

$$\frac{v_D}{v_{D,CJ}} = 0.1207\bar{r}_D - 0.1638; R^2 = 0.7793 \tag{65}$$

and two wave

$$\frac{v_D}{v_{D,CJ}} = 0.1132\bar{r}_D - 0.2263; R^2 = 0.7618 \tag{66}$$

operation with the R^2 value indicating good correlation for both. The trend lines for the one and two wave operation again show that the two wave cases tend to propagate at a larger radius.

Taken together, Figures 86 and 87 strongly suggest that dilution of the reactants with products is occurring. As discussed in Appendix B, as dilution of the reactants with products increases, the value of v_D decreases. Additionally, for $\phi > 0.5$ as T_1 increased, v_D decreased, with this effect being more pronounced as ϕ increased. Inferring that the degree of mixing of reactants and products increases as the distance the reactants traverse in the channel increases, then the degree of mixing, and hence value of n increases with r_D.

The velocity deficit may have also been influenced as a function of radius by parasitic secondary combustion in the reactant mixture and lateral relief. Secondary combustion in the reactant mixture ahead of the DW is visible in the one wave cases, which may be in part due to the longer distance the reactants must travel to reach the DW radius. Previous research by Andrus et al. [83] demonstrated computationally
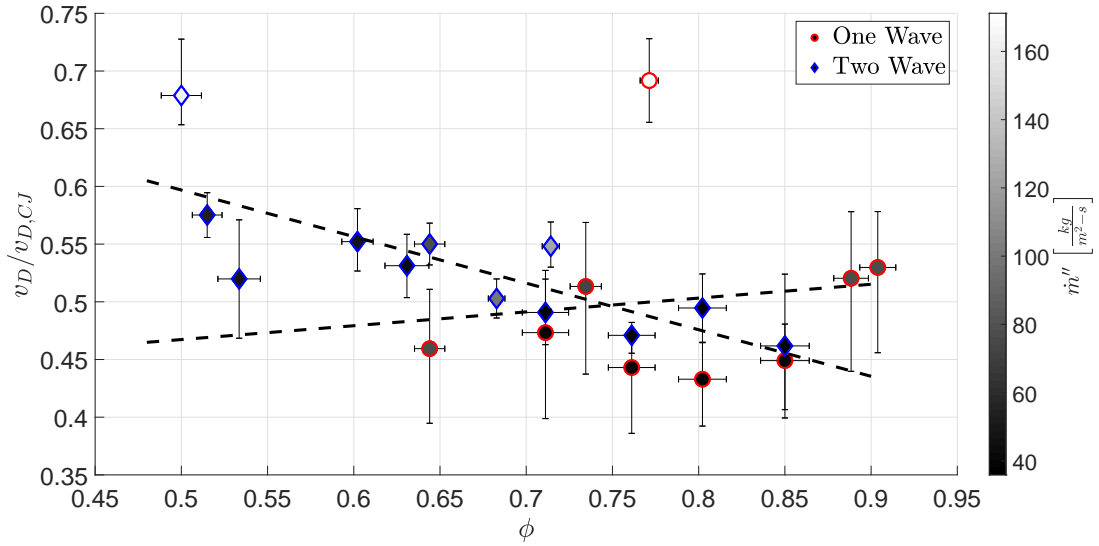
(a) DW normalized velocity vs equivalence ratio
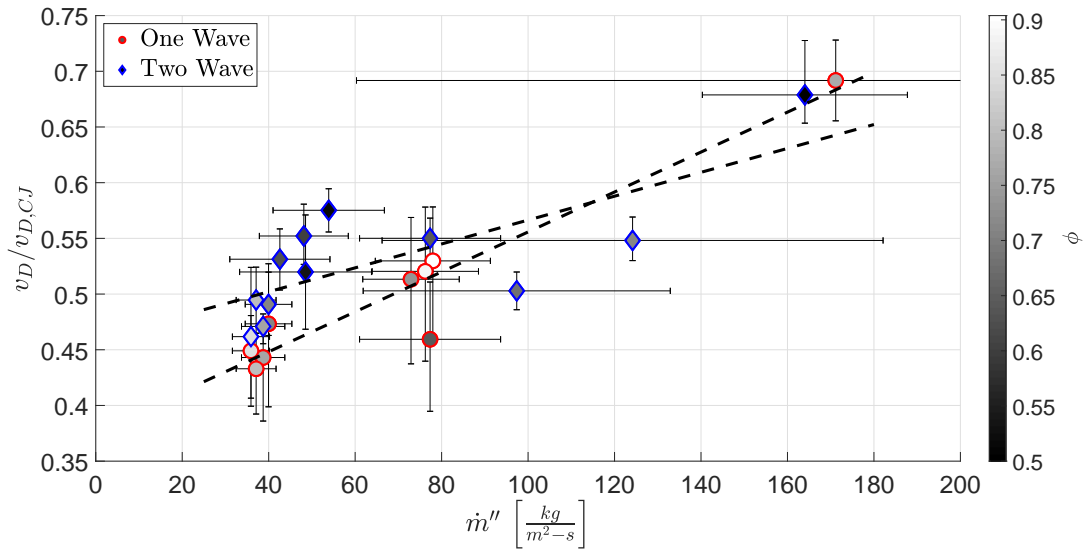
(b) DW normalized velocity vs mass flux

Figure 86. DW normalized velocity vs (a) equivalence ratio and (b) mass flux for the RRDE with $H_2 - Air$ reactants.
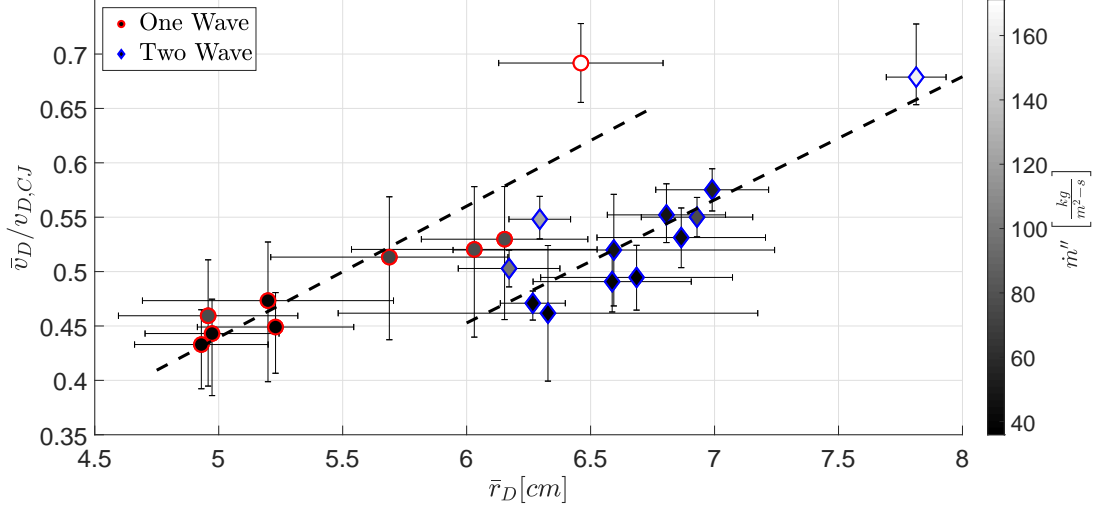
Figure 87. DW normalized velocity vs detonation radius for the RRDE with $H_2 - Air$ reactants.

that secondary combustion may significantly reduce the wave speed, $\mathcal{O}(10\%)$ for a 20% pre-burned mixture. Research by Cho et al. [92] indicated that lateral relief of a DW can affect the wave speed significantly as well, experimentally demonstrating between $\frac{\bar{v}_D}{v_{D,CJ}} \approx 95\%$ in a thin channel without lateral relief and $\frac{\bar{v}_D}{v_{D,CJ}} \approx 72 - 88\%$ with lateral relief on one side in an $H_2 - Air$ detonation. For detonations near the center of the channel, this effect is exacerbated as there is lateral relief on either side of the DW front, whereas for DW propagation near the outer edge the degree of confinement is increased, with lateral relief primarily on one side of the DW.

4.1.1 Optical Frequency Measurement.

The calculation to determine wave speed requires the DW number, wave pass frequency, and detonation radius. Focusing on the frequency measurement techniques, typical frequency measurements were conducted by tracking the pressure and taking an FFT to determine the frequency of the fluctuations. For testing with the baseline RRDE ITPs were used to determine wave frequency and direction. The ITPs were located on the channel plate at the same radial distance, and offset from each other by

45°. The approximate location of these measurements is indicated by circles labeled K1 (Blue) and K2 (Red) in Figure 88. For testing with the polycarbonate channel plates, the pressure transducer was located in the fuel plenum, which proved capable of detecting the pressure fluctuations. To investigate whether a similar frequency measurement could be made non-intrusively with optical access, tracking the luminous intensity at the K1 and K2 locations was attempted.

Section 3.2.5 describes how the luminous intensity for each pixel in a frame is captured by the high speed camera. As shown in Figure 88 the intensity traces for $N_D = 1$ cases produced a 45° phase lag, and $N_D = 2$ cases produced a 90° phase lag, as expected. Intensity traces from Case 6 with a three node acoustic mode displayed a 180° phase lag. The high speed photographic intensity offered less resolution than the Kulite pressure measurements due to the lower sampling rate, however.

Taking the FFT of this intensity signal proved to be a viable method to determine f_D for some cases. For example, the FFT of the fuel plenum pressure signal in Test 1 for $N_D = 2$ gave $\bar{f}_D = 4335 \pm 25\ Hz$, whereas the FFT of the optical intensity signal peaked at $4319\ Hz$ for the K1 position and $4316\ Hz$ for the K2 position as shown in Figure 89, which was within the margin of error of the pressure signal's determined value. Similarly, the FFT of the pressure signal in Test 1 for $N_D = 1$ gave $\bar{f}_D = 2531(+215/-304)\ Hz$, whereas the FFT of the optical intensity signal peaked at $2664\ Hz$ for the K1 position and $2658\ Hz$ for the K2 position, again within the margin of error of the pressure signal's determined value. This in effect demonstrates a non-intrusive method for determining wave frequency assuming optical access.

As shown in Figure 89, tracking optical intensity at the K1 and K2 locations worked well for Tests 1,2,6, and 11-17. However, for most of the remaining cases the frequency was estimated as half of the pressure transducer signal frequency. There are numerous reasons why this may be the case. Considering luminous intensity of

143
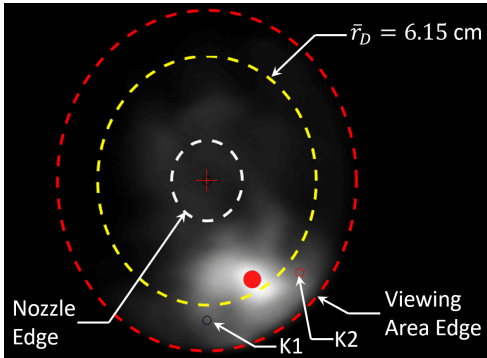
(a) Test 2,$N_D = 1$ operation.
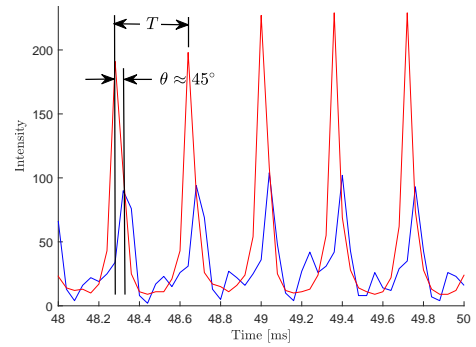
(b) Intensity traces at the the ITP locations from Test 2 for $N_D = 1$ operation.
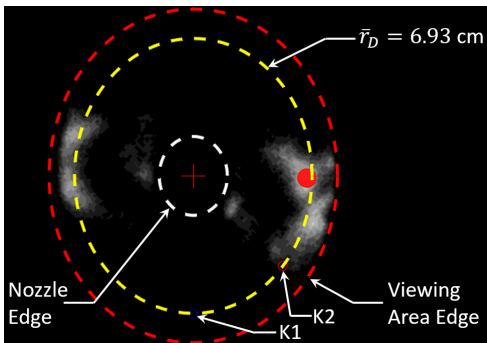
(c) Test 1, $N_D = 2$ operation.
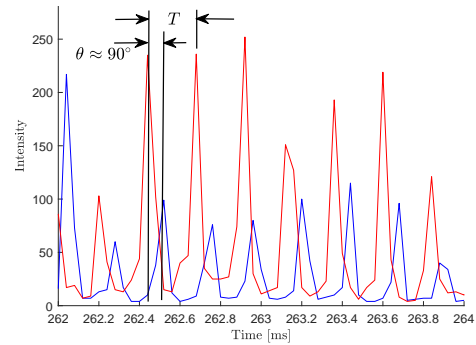
(d) Intensity traces at the the ITP locations from Test 1 for $N_D = 2$ operation.
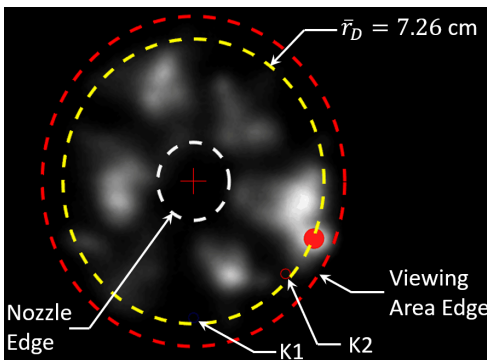
(e) Test 6, three node acoustic operation.
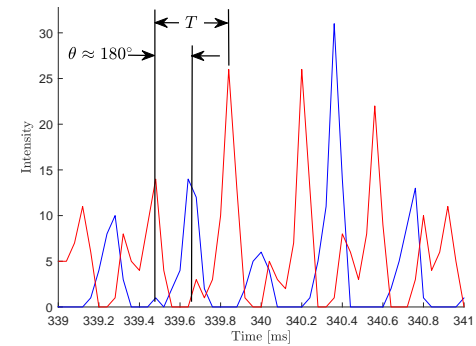
(f) Intensity traces at the the ITP locations from Test 6 for three node acoustic operation.

Figure 88. Comparison of intensity traces at the K1 and K2 locations from high speed photography for various operational modes.

144
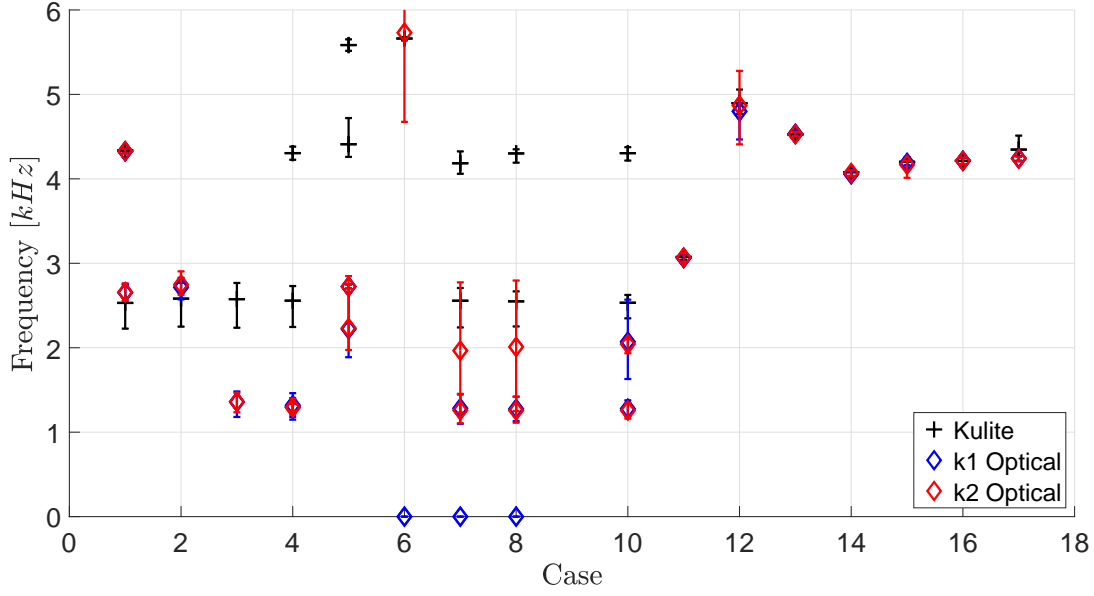
Figure 89. Comparison of the wave pass frequency as determined by the Kulite pressure transducer and optically tracking luminous intensity at the K1 and K2 locations.

the DW, underexposed cases where the high speed camera shutter was not open long enough to collect chemiluminescence from the DW at the tracked location allow these tracked locations to miss DWs as they pass, and overexposed cases clip the signal. Additionally, if the detonation wave is not aligned with the tracked location, the signal from the wave will not be received. By contrast, pressure signals propagate throughout the flowfield, and the signal can be received even if the pressure source is not well aligned with the pressure port. This highlights the fact that pressure transducer measurements are more reliable and easier to collect and interpret. However, by definition introduction of a pressure port is an intrusive measurement technique, and with proper photography settings the optical intensity tracking method offers a potential non-intrusive method to measure frequency.

4.1.2 Polycarbonate visualization considerations.

While the polycarbonate material was sufficient to observe chemiluminescence and estimate r_D, it proved to be a less than ideal material. As noted previously,

145

polycarbonate precluded the use of OH* chemiluminescence photography. Unlike previous tests involving metal construction of the detonation channel, testing with polycarbonate channel plates resulted in variation of the detonation channel geometry. The target parameters for the test were Channel Height=4.5mm, $AR_t = 0.2$, and $AR_n = 0.6$. However, as shown in Table 13 these parameters all varied from test to test, which was a direct consequence of melting, burning, and erosion of the channel plate shown in Figure 90. This was because the melting and burning point of polycarbonate was far below the DW's temperature, ensuring the polycarbonate melted and burned as the test proceeded. Heavy black lines on the table indicate where the channel plate was replaced between tests.

The material loss had three primary effects on the experiment. First, the loss of polycarbonate material altered the channel geometry, which in turn altered the conditions of the test. For example, the channel height for Tests 1 and 2 began at 4.5 mm, increasing to 6.9 mm by the end of Test 10. Similarly, the nozzle exit outer radius increased from 3.1 cm at the beginning of Tests 1 and 2 to 3.5 cm by the end of Test 10. The attained AR_t therefore varied from 0.2 at the beginning of Test 1 to 0.13 upon completion of Test 10. Similarly, the value of AR_n varied from 0.6 to 0.57. The variance in AR_n is smaller than for AR_t because both A_c and A_n increased as testing proceeded, whereas A_t remained constant. The change in A_c resulted in a large error in the $\dot{m}''$ calculations, especially at high $\dot{m}''$ and ϕ where the rate of erosion was increased. Second, the burning of material released additional radiation which obscured the DW, and at sufficiently long run times the DW became indistinguishable from this surface burning. Third, the burning of the polycarbonate also resulted in additional heat release and chemical species being introduced to the flow.

Preliminary calculations have shown that burning of the polycarbonate material

itself has the potential to considerably alter the chemistry of the reactant mixture, which may in part explain the variance from Huff's results. Considering the channel plate to be made entirely from $C_{16}H_{14}O_3$, with a molecular weight of 254.3 $\frac{g}{mol}$ and a density of 1.2 $\frac{g}{cm^3}$, then the stoichiometrically balanced chemical equation that results for combustion in air is $C_{16}H_{14}O_3 + 18O_2 + 67.68N_2 \rightarrow 16CO_2 + 7H_2O + 67.68N_2$. Then $\left(\frac{F}{A}\right)_{stoich} = 0.103$, indicating that the polycarbonate material requires a significant amount of O_2 for combustion. Modeling the polycarbonate loss as constant for the entire face, the rate at which polycarbonate is introduced into the flow over the duration of the run is then

$$\dot{m}_{polycarbonate} \approx \frac{\Delta h_c \pi (r_{outer}^2 - r_{inner}^2)\rho_{polycarbonate}}{\Delta t} \tag{67}$$

The effective equivalence ratio of just the polycarbonate burning with air is then

$$\phi_{polycarbonate} = \frac{\dot{m}_{polycarbonate}}{\dot{m}_{air}\left(\frac{F}{A}\right)_{stoich,polycarbonate}} \tag{68}$$

Considering the flow rate data and material loss rate for Tests 1-17, this produced $\phi_{polycarbonate} \approx 0.5 \pm 0.1$. It is highly unlikely that the flow within the RRDE actually fully experienced this effective fuel rate increase. The polycarbonate must transition from solid to liquid, then liquid to gas, and given that the phase transition from liquid to gas takes time, much of the liquefied polycarbonate was likely exhausted into the test cell before it could burn within the channel and affect the chemistry, whereas the gaseous H_2 fuel was readily detonable upon mixing with air. While the precise impact of the essentially ablative channel plate on the chemistry within the channel cannot be calculated to a high degree of confidence, the $\phi_{polycarbonate}$ values experienced indicate it may not be negligible.

Given that the heat transfer within the RRDE is transient due to the short run

times, the channel plate erosion rate was also likely transient, with less erosion at the start of the run and more at the end. This may be the cause of the modal transition behavior experienced in the present research that was not observed by Huff (Reference Appendix A).

In addition to the demonstrated and potential effects on the test conditions, the melted polycarbonate can migrate to other areas such as the fuel injectors, potentially obstructing fuel flow. After Tests 1-10 with the polycarbonate channel top plates installed, the RRDE required intensive removal of the melted polycarbonate before reassembly could be accomplished. Figure 90(a) shows an untested polycarbonate window and a polycarbonate window after one test (Test 1). Dark, burnt polycarbonate was visible around the inner radius at the exhaust, as well as the outer radius where the polycarbonate contacted metal RRDE components. Material has visibly and measurably melted, eroded, and/or burned on the surface.

Figures 90(b) and (c) show the base plate and fuel ring following Tests 11-13. Buildup of polycarbonate soot was evident in the vicinity of the fuel injector holes, which are at the throat. Buildup of soot extended upstream of the throat, indicating back flow of products through the throat. Soot accumulation appeared to be reduced in the vicinity of the inboard row of fastener holes securing the Fuel Ring, indicating an interaction at these locations. Soot accumulation occurred sporadically on the Base Plate. Figures 90(d) and (e) show the Top Plate sub-assembly, also following Tests 11-13. The exit area was visibly enlarged due to significant erosion of the polycarbonate material. No fasteners are installed as they all blew out during Test 13 due to the pressures within the channel and the thickness reduction of the polycarbonate material the fasteners were threaded into. Significant melting has occurred around the fastener holes and the outer edge of the plate, with a significant gap at the throat. Soot is visible in the throat ring upstream of the throat, again indicating flow reversal
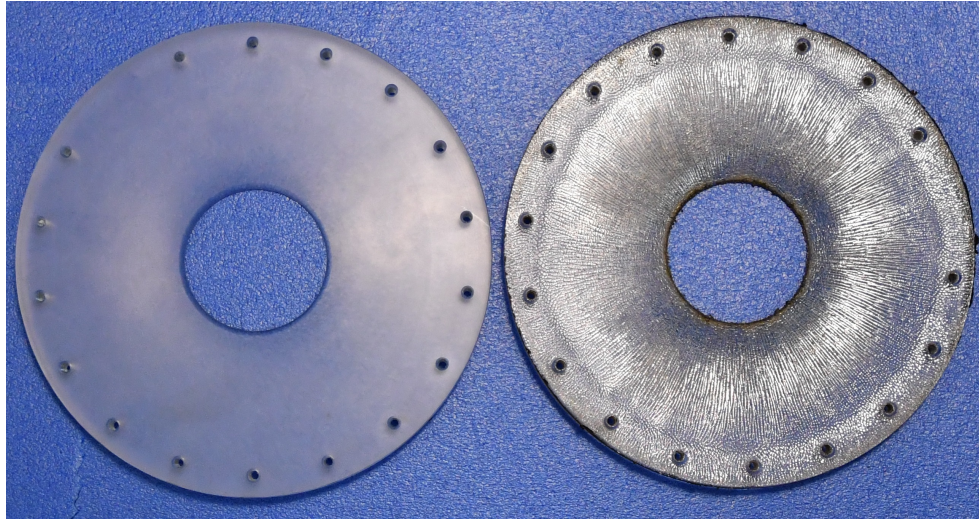
(a) Untested polycarbonate window (left) and a polycarbonate window after one test (right).
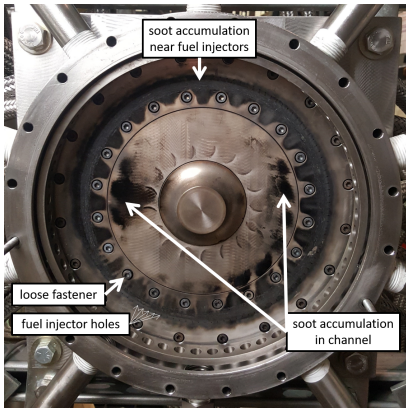
(b) Base Plate
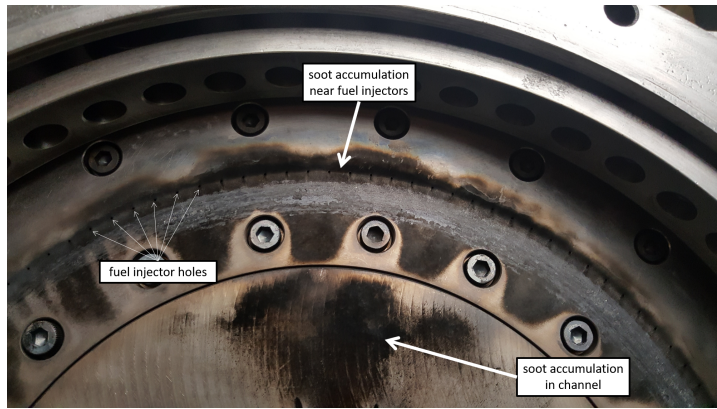
(c) Base Plate closeup
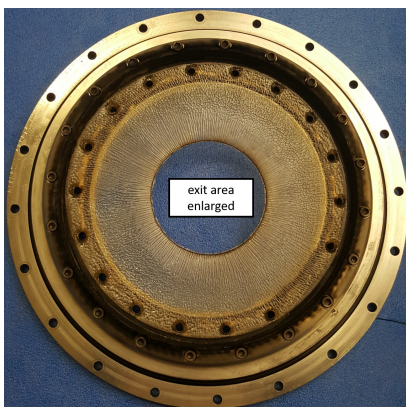
(d) Top Plate sub-assembly
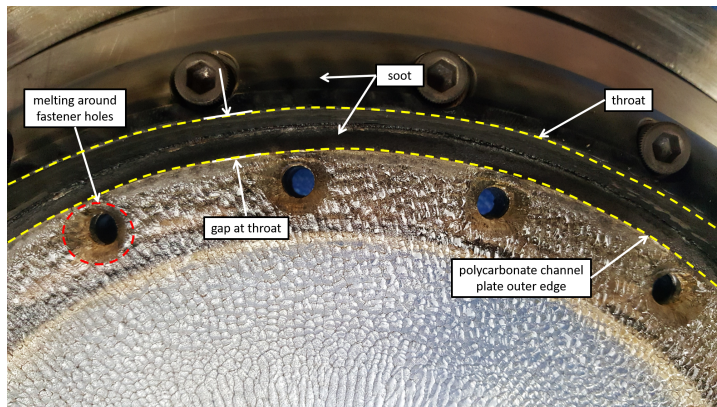
(e) Top Plate sub-assembly closeup

Figure 90. Images of polycarbonate window and accumulation of soot on the test article.

occurred.

4.2 Turbocharger Integration

Following examination of the DW location in the pure combustor configuration the RRDE was reconfigured into its turbo configuration for further testing. Specific test objectives included examining the response of the RRDE to the addition of a flow straightening device, back pressure to the turbine, and back pressure to the compressor. Additionally, the effect of wave propagation direction on the output power was explored. All testing performed in the present work was conducted with the 39° NGV ring installed, and $AR_t = 0.2$.

4.2.1 Flow straightener and back pressure effects.

The effect of the flow straightening device and back pressure was examined first. A total of seventy-one tests were conducted with and without the flow straightening device, and at varying degrees of turbine and compressor back pressure. The flow straightening device consisted of a cylindrical pipe collar slightly larger in diameter than the turbine exit, which was secured to the RRDE at the turbine exit as shown in Figure 65. This produced a turbine exit area ratio of straightener exit area to turbine exit area of $AR_e = 1.14$ (slightly expanded). Two orifice plates were also manufactured with a diameter less than the turbine exit and installed at the exhaust of the flow straightening collar, resulting in $AR_e = 0.84$ or $AR_e = 0.65$. The flow restriction caused by the orifice plates increased the back pressure on the turbine. Similarly, a ball valve at the exit of the compressor could be turned to different angles to create an area restriction for the compressor as shown in Figure 66, again increasing back pressure. Table 15 shows the test conditions and resulting data for all tests conducted. To clarify a point regarding the test numbering scheme, test
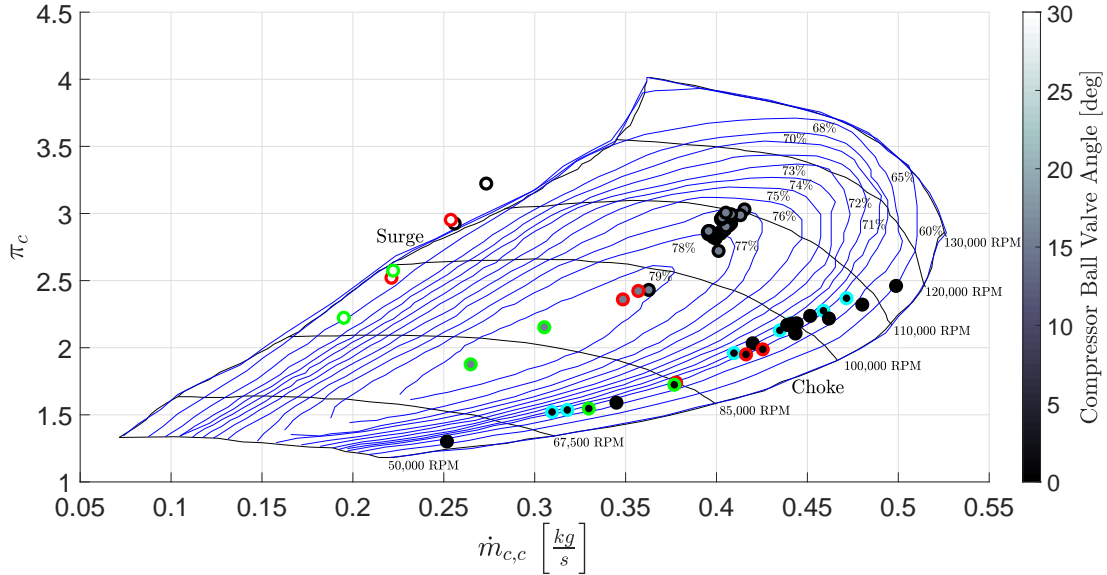
Figure 91. Test points on the compressor operating map with efficiency islands shown.

numbers appearing in Section 4.2 are specific to the turbocharger integration testing only, and are entirely unrelated to the test numbers used in previous discussions of the polycarbonate channel plate visualization testing.

The compressor operating map for the tests conducted is shown in Figure 91. In this figure, the symbol edge color corresponds to the turbine exit condition, with cyan representing no flow straightening collar or back pressure plate, black representing the flow straightening collar with no back pressure plate, red representing the $AR_e = 0.84$ back pressure plate, and green representing the $AR_e = 0.65$ back pressure plate. The center color corresponds to the compressor exit condition, specifically the Compressor Ball Valve Angle (CBVA) for these tests, with black representing a 0° CBVA (fully open), gray representing the 15° CBVA and white representing the 30° CBVA, corresponding to compressor exit area ratios of approximately 1.0, 0.8, and 0.5, respectively.

The CBVA strongly correlated to the operating condition of the compressor. A CBVAs of 0° resulting in operation near the choke line for all exit conditions. A CBVAs of 15° resulted in operation near the peak efficiency operating line for all exit

Table 15. Turbine Integration Test Data

Test	Date	AR_e	CBVA (deg)	$\dot{m}''_t \frac{kg}{m^2-s}$	ϕ	N_D	$\bar{f}_D(+/-)$ Hz	π_c	$\dot{m}_{c,c} \frac{kg}{s}$	RPM x1000	$\dot{W}_{shaft}$ kW	η_{th}	$\dot{W}_{shaft}/\dot{m}_t \frac{kW}{kg/s}$
1	20181109	1.00	0	52.0±3.7	0.539±0.013	N/A	2389(7/6)	1.5	0.31	73	16.5±0.5	0.038±0.003	72
2	20181109	1.00	0	52.1±3.7	0.581±0.013	N/A	2421(19/11)	1.5	0.32	74	17.3±0.6	0.037±0.002	75
3	20181109	1.00	0	76.5±4.9	0.509±0.009	N/A	2384(5/3)	2.0	0.41	92	35.7±0.9	0.059±0.003	105
4	20181109	1.00	0	76.6±4.9	0.592±0.010	N/A	5807(37/38)	2.1	0.43	98	43.0±1.0	0.061±0.003	127
5	20181109	1.00	0	102.8±6.3	0.507±0.007	N/A	2370(11/9)	2.3	0.46	104	50.4±1.2	0.062±0.002	111
6	20181109	1.00	0	103.3±6.3	0.590±0.007	N/A	2426(18/17)	2.4	0.47	108	56.2±1.3	0.059±0.002	123
7	20181109	1.00	0	78.8±5.0	0.599±0.009	N/A	5819(37/38)	2.2	0.44	100	45.1±1.1	0.061±0.003	129
8	20181109	1.14	0	79.6±5.1	0.604±0.009	N/A	5822(37/30)	2.2	0.44	100	46.1±1.1	0.061±0.003	131
9	20181109	1.14	0	79.3±5.1	0.659±0.010	N/A	5920(29/38)	2.2	0.45	102	48.7±1.1	0.060±0.002	139
10	20181109	1.14	0	80.3±5.1	0.584±0.009	N/A	5770(57/58)	2.2	0.44	N/A	44.9±1.1	0.061±0.003	126
11	20181109	1.14	0	80.3±5.1	0.573±0.009	N/A	5735(60/40)	2.2	0.44	99	44.5±1.1	0.062±0.003	125
12	20181109	1.14	0	79.9±5.1	0.516±0.009	N/A	5585(127/95)	2.0	0.42	95	38.8±1.0	0.060±0.003	110
13	20181109	1.14	0	80.5±5.1	0.582±0.009	N/A	5771(46/44)	2.2	0.44	100	45.0±1.1	0.062±0.003	126
14	20181109	1.14	15	78.2±5.0	0.605±0.009	N/A	5850(42/40)	2.7	0.40	103	50.0±0.7	0.068±0.003	144
15	20181109	1.14	15	78.6±5.0	N/A	N/A	2322(13/8)	2.4	0.36	96	38.8±0.6	0.065±0.003	112
16	20181109	0.84	15	82.6±5.2	0.521±0.008	N/A	2210(150/393)	2.4	0.35	94	36.0±0.5	0.054±0.002	98
17	20181109	0.84	15	76.3±4.9	0.588±0.010	N/A	5764(52/33)	2.4	0.36	95	38.1±0.6	0.054±0.002	113
18	20181109	0.65	15	77.0±4.9	0.580±0.009	N/A	5794(59/47)	2.2	0.31	88	27.8±0.4	0.040±0.002	81
19	20181109	0.65	15	77.5±5.0	0.502±0.009	N/A	2179(42/144)	1.9	0.26	79	19.3±0.3	0.032±0.001	56
20	20181109	0.65	30	77.2±5.0	0.504±0.009	N/A	2143(147/289)	2.2	0.19	88	22.6±0.4	0.037±0.002	66
21	20181109	0.65	30	77.7±5.0	0.600±0.010	N/A	5783(33/27)	2.6	0.22	96	31.0±0.5	0.043±0.002	90
22	20181109	0.84	30	77.4±5.0	0.603±0.010	N/A	5782(36/27)	3.0	0.25	105	46.6±0.7	0.064±0.002	136
23	20181109	0.84	30	77.5±5.0	N/A	N/A	2303(18/7)	2.5	0.22	96	30.2±0.5	0.051±0.002	88
24	20181109	1.14	30	76.9±4.9	0.527±0.009	N/A	2359(26/491)	2.9	0.26	106	46.6±0.7	0.074±0.003	137
25	20181109	1.14	30	77.4±5.0	0.590±0.010	N/A	5816(47/53)	3.2	0.27	110	54.9±0.8	0.077±0.003	160
26	20181109	0.84	0	76.9±4.9	0.651±0.010	N/A	5916(28/25)	2.0	0.43	95	39.8±1.1	0.051±0.002	117
27	20181109	0.84	0	77.5±5.0	0.501±0.009	N/A	2326(2/2)	1.7	0.38	85	27.8±0.9	0.046±0.003	81
28	20181109	0.84	0	77.8±5.0	0.590±0.010	N/A	5783(32/36)	2.0	0.42	93	36.4±1.0	0.051±0.002	106
29	20181109	0.65	0	77.5±5.0	N/A	N/A	2207(7/9)	1.5	0.33	76	18.8±0.7	0.031±0.002	55
30	20181109	0.65	0	77.7±5.0	0.599±0.010	N/A	5789(62/59)	1.7	0.38	85	27.2±0.9	0.038±0.002	79
31	20181217	1.14	0	77.4±4.5	0.604±0.004	N/A	5740(45/35)	2.1	0.44	99	45.2±1.2	0.062±0.002	132
32	20181217	1.14	0	77.2±4.5	0.607±0.004	N/A	5762(77/51)	2.1	0.44	100	45.4±1.2	0.062±0.002	133
33	20181217	1.14	0	87.5±5.1	0.601±0.004	N/A	5755(41/34)	2.2	0.46	105	50.6±1.3	0.062±0.002	131
34	20181217	1.14	0	104.0±6.0	0.607±0.003	N/A	2401(25/13)	2.3	0.48	110	58.5±1.6	0.059±0.002	127
35	20181217	1.14	0	103.7±6.0	0.642±0.004	N/A	5830(65/32)	2.5	0.50	117	71.3±1.9	0.069±0.002	155
36	20181217	1.14	0	37.1±2.2	0.663±0.005	N/A	2433(13/45)	1.3	0.25	60	8.9±0.4	0.023±0.001	54
37	20181217	1.14	0	53.5±3.1	0.591±0.004	N/A	2420(32/15)	1.6	0.34	78	21.1±0.7	0.043±0.002	89
38	20181220	1.14	15	77.5 ± 4.5	0.605 ± 0.004	3	5827(93/95)	2.9	0.40	105	53.1 ± 0.7	0.073 ± 0.001	155
39	20181220	1.14	15	77.6 ± 4.5	0.607 ± 0.004	3	5867(86/88)	2.9	0.40	106	53.6 ± 0.7	0.073 ± 0.001	156
40	20181220	1.14	15	77.9 ± 4.5	0.610 ± 0.004	3	5902(84/89)	2.9	0.40	106	54.2 ± 0.7	0.073 ± 0.001	157
41	20181220	1.14	15	77.9 ± 4.5	0.611 ± 0.004	3	5922(84/95)	2.9	0.40	106	54.2 ± 0.7	0.073 ± 0.001	157
42	20181220	1.14	15	77.9 ± 4.5	0.615 ± 0.004	3	5936(90/90)	2.9	0.40	107	54.5 ± 0.7	0.073 ± 0.001	158
43	20181220	1.14	15	78.0 ± 4.5	0.617 ± 0.004	3	5954(84/87)	2.9	0.41	107	55.2 ± 0.8	0.074 ± 0.001	160
44	20181220	1.14	15	78.1 ± 4.5	0.621 ± 0.004	3	5973(83/92)	2.9	0.41	107	55.3 ± 0.8	0.073 ± 0.001	160
45	20181220	1.14	15	78.1 ± 4.5	0.623 ± 0.004	3	5986(113/93)	2.9	0.41	107	55.9 ± 0.8	0.074 ± 0.001	162
46	20181220	1.14	15	78.1 ± 4.5	0.625 ± 0.004	3	6000(80/93)	2.9	0.41	107	55.8 ± 0.8	0.073 ± 0.001	161
47	20181220	1.14	15	78.2 ± 4.5	0.627 ± 0.004	3	6013(82/94)	2.9	0.41	108	55.4 ± 0.8	0.073 ± 0.001	160
48	20181220	1.14	15	78.5 ± 4.5	0.685 ± 0.004	3	6115(98/89)	3.0	0.42	110	58.7 ± 0.8	0.070 ± 0.001	169
49	20181220	1.14	15	78.5 ± 4.5	0.585 ± 0.004	3	5904(69/80)	2.9	0.40	107	54.3 ± 0.7	0.076 ± 0.001	156
50	20181220	1.14	15	78.7 ± 4.6	0.601 ± 0.004	3	5958(82/88)	2.9	0.41	108	54.6 ± 0.7	0.074 ± 0.001	157
51	20181220	1.14	15	78.7 ± 4.6	0.660 ± 0.004	3	6071(103/96)	3.0	0.41	109	57.6 ± 0.8	0.071 ± 0.001	166
52	20190115	1.14	15	77.5 ± 4.5	0.591 ± 0.004	3	5790(77/107)	2.8	0.40	N/A	51.4 ± 0.7	0.072 ± 0.001	150
53	20190115	1.14	15	77.4 ± 4.5	0.593 ± 0.004	3	5809(89/92)	2.8	0.40	N/A	51.3 ± 0.7	0.072 ± 0.001	150
54	20190115	1.14	15	77.3 ± 4.5	0.593 ± 0.004	3	5834(93/91)	2.8	0.40	N/A	51.5 ± 0.7	0.072 ± 0.001	150
55	20190115	1.14	15	77.3 ± 4.5	0.593 ± 0.004	3	5862(88/106)	2.9	0.40	N/A	52.4 ± 0.7	0.073 ± 0.001	153
56	20190115	1.14	15	77.3 ± 4.5	0.593 ± 0.004	3	5875(88/171)	2.9	0.40	N/A	52.3 ± 0.7	0.073 ± 0.001	153
57	20190115	1.14	15	77.2 ± 4.5	0.593 ± 0.004	3	5875(88/171)	2.9	0.40	N/A	52.3 ± 0.7	0.073 ± 0.001	153
58	20190115	1.14	15	77.1 ± 4.5	0.593 ± 0.004	3	5906(67/173)	2.9	0.40	N/A	52.8 ± 0.7	0.074 ± 0.001	155
59	20190115	1.14	15	77.1 ± 4.5	0.593 ± 0.004	3	5912(54/172)	2.9	0.40	N/A	52.7 ± 0.7	0.074 ± 0.001	154
60	20190115	1.14	15	77.0 ± 4.5	0.597 ± 0.004	3	5916(76/175)	2.9	0.40	N/A	52.6 ± 0.7	0.073 ± 0.001	154
61	20190115	1.14	15	77.0 ± 4.5	0.597 ± 0.004	3	5919(65/176)	2.9	0.40	N/A	52.7 ± 0.7	0.074 ± 0.001	155
62	20190115	1.14	15	77.1 ± 4.5	0.698 ± 0.004	3	6068(130/131)	3.0	0.40	N/A	55.5 ± 0.7	0.066 ± 0.001	163
63	20190115	1.14	15	77.1 ± 4.5	0.697 ± 0.004	3	6055(132/135)	3.0	0.40	N/A	55.3 ± 0.7	0.066 ± 0.001	162
64	20190115	1.14	15	77.0 ± 4.5	0.700 ± 0.004	3	6078(108/117)	3.0	0.40	N/A	55.1 ± 0.7	0.066 ± 0.001	162
65	20190115	1.14	15	76.6 ± 4.4	0.703 ± 0.004	3	6089(115/135)	3.0	0.41	N/A	56.4 ± 0.7	0.067 ± 0.001	166
66	20190115	1.14	15	76.9 ± 4.5	0.703 ± 0.004	3	6100(121/127)	3.0	0.41	N/A	56.4 ± 0.7	0.067 ± 0.001	167
67	20190115	1.14	15	76.3 ± 4.4	0.706 ± 0.004	3	6100(121/127)	3.0	0.41	N/A	56.4 ± 0.7	0.067 ± 0.001	167
68	20190115	1.14	15	76.8 ± 4.4	0.704 ± 0.004	3	6110(112/131)	3.0	0.40	N/A	54.8 ± 0.7	0.065 ± 0.001	161
69	20190115	1.14	15	76.3 ± 4.4	0.712 ± 0.004	3	6138(113/142)	3.0	0.41	N/A	56.8 ± 0.7	0.067 ± 0.001	168
70	20190115	1.14	15	76.8 ± 4.4	0.719 ± 0.004	3	6156(111/149)	3.0	0.40	N/A	55.0 ± 0.7	0.064 ± 0.001	162
71	20190115	1.14	15	76.8 ± 4.4	0.720 ± 0.004	3	6164(112/156)	3.0	0.41	N/A	56.0 ± 0.7	0.065 ± 0.001	165
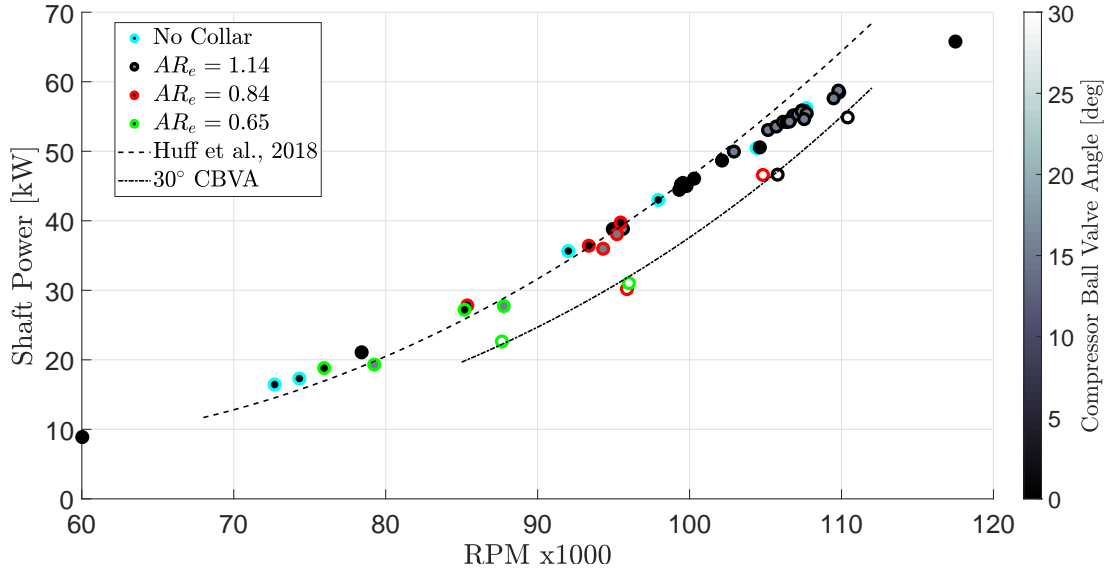
Figure 92. Shaft power as a function of the rotor angular speed in RPM.

conditions tested. Operation along this line allows peak transfer of power from the turbine to the compressor. A CBVAs of 30° resulted in operation near or in some cases past the surge line. Operating in this regime risks permanent damage to the turbocharger due to aerodynamic interactions within the compressor, and exceeding the surge line should be avoided where possible.

Examining the shaft power produced as a function of the rotational speed, there was a clear trend for all data of increasing power with increasing rotational speed as expected, shown in Figure 92. These data experienced similar behavior to that observed by Huff et al. [44] in similar testing on this RRDE conducted without a flow straightening collar, or compressor or turbine back pressure. The trendline from Huff's testing is shown in Figure 92 over the range of rotor speeds considered in the previous work, which correlates well for the CBVA data at 0° and 15° for all turbine exit conditions in the present work. However, for all turbine exit conditions considered the data for a CBVA of 30° resulted in lower shaft power for a given rotor speed.

In general the output power was expected to increase proportional to the rate

at which chemical potential energy is being introduced to the combustor. Defining input energy rate $= \dot{m}''\phi(A_{channel}LHV_{H2}(F/A)_{Stoich,H2})$ Figure 93 shows that as the input energy rate increases, the shaft power tends to increase as well. Isocontours for η_{th} , defined as the ratio of the shaft power to the input energy rate, are shown for reference. This figure shows that both the compressor and turbine exit conditions influence the output shaft power for a given input energy rate. These data show the shaft power increases as the CBVA increases and decreases at the turbine back pressure increases. It was previously hypothesized that the flow straightening collar would increase output power by controlling expansion of the post-turbine products. These data show that there is a negligible effect on operation with the addition of the flow straightening collar with no back pressure plate installed as compared to operation without the collar entirely. Figure 94 makes this comparison more obvious by only showing the cases with no collar or the collar with no turbine back pressure plates, and a CBVA of 0°. The data both with and without the flow straightening collar follow the same trend line. To maximize power without risking damage from surge to the compressor, operation at a CBVA of 15° with no turbine back pressure plate is advisable.

Figure 93 also shows that η_{th} is very low; $\eta_{th} < 0.08$ for all tests. There are a number of reasons that this may be the case. Measurements of the flow within the flow straightening collar revealed very high temperatures post-turbine, indicating the turbine is not effectively extracting this thermal energy from the flow. A swirl component also appears to be present post-turbine, as the two Kiel probes installed to measure post-turbine total pressure gave varying results based on their axial position and angle of installation. Figure 95 shows the pressure readings from the instrumentation for the detonation channel and turbine exit flow paths. The S1 and S2 Kiel probe locations are indicated as TurbExit1 (purple) and TurbExit2 (green), respec-
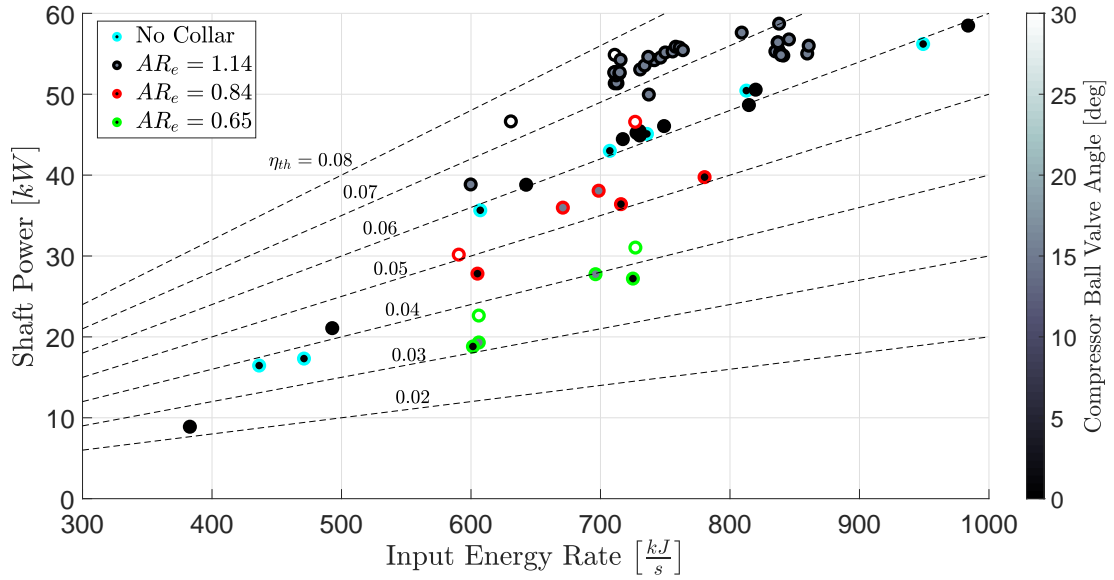
154

Figure 93. Shaft power as a function of the input energy rate with thermal efficiency lines indicated.

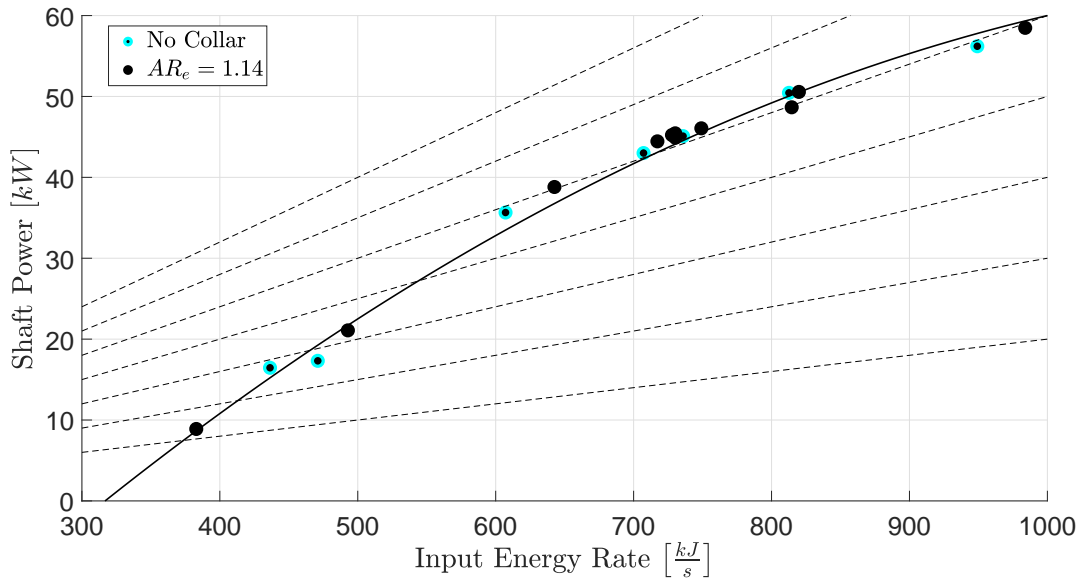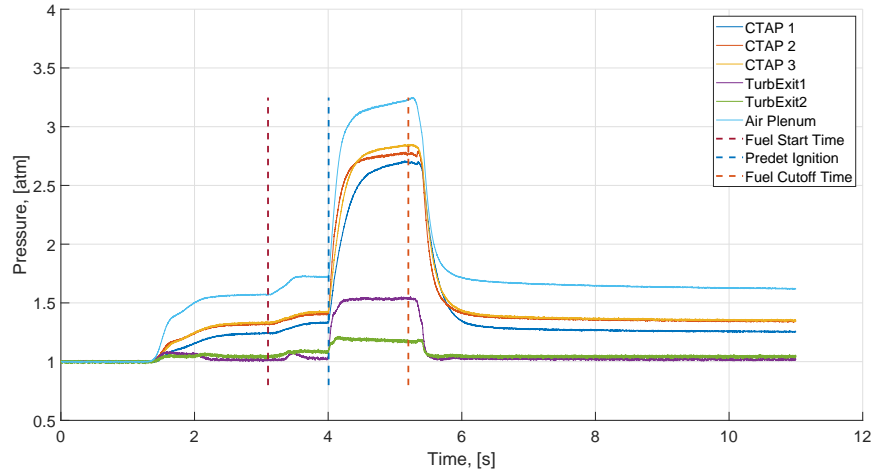**Figure 94.** Shaft power as a function of the input energy rate with thermal efficiency lines indicated. 0° CBVA, no turbine back pressure plates. Best fit line: $\dot{W}_{Shaft} = -50 + 0.18\dot{E}_{Input} - 7 \cdot 10^{-5}\dot{E}_{Input}^2$.

155

tively. The S1 and S2 pressure traces for Test 14 show that the pressures are above atmospheric, but at different magnitudes. The pressure traces for Tests 51 and 71 show both the S1 and S2 pressures are sub-atmospheric, which is non-physical. Both probes were intact following Tests 14 and 51. The S1 Kiel probe was confirmed to be destroyed at the end of Test 71, and the S2 Kiel probe was damaged and missing its shroud. Regardless of the probe condition, it was possible to measure sub-atmospheric pressures with the Kiel probes, which appears to be due to a swirl component causing suction at the probe orifice.

Turbine tip losses are also likely excessive due to the construction of the RRDE. As shown in Figure 96 there are gaps between the turbine blade tips and the RRDE's turbine housing. These gaps produce losses, and due to manufacturing tolerances in the RRDE these gaps are large to minimize rubbing of the blades on the housing. For comparison, the gap between the turbine blades and their housing was found to be $0.70mm$, whereas the gap between the compressor blades and their housing, which were designed and manufactured by Garrett and not modified for this or previous testing, was found to be between $0.20mm$ and $0.34mm$. The IGV blades were also designed without prior knowledge of the actual flow conditions within the RRDE, so there is undoubtedly significant room for optimization of the blade design to minimize losses.

Specifically considering the data collected to determine the response of the RRDE to changes in the CBVA and AR_e, which was all collected on the same day, trends are indicated in Figure 97. The trend line for the baseline device with a CBVA of 0° and either no collar or the collar with no restriction plate is shown for reference. The dashed arrow shows the trend that as AR_e increases, corresponding to lower turbine back pressure, the shaft power increased. Additionally, as the CBVA increased, corresponding to increased compressor back pressure, the shaft power increased for all

(a) Test 14
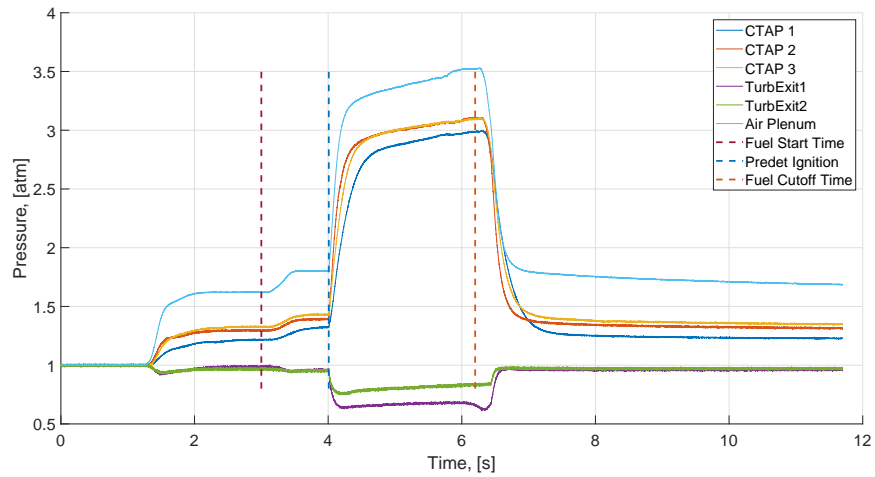
(b) Test 51
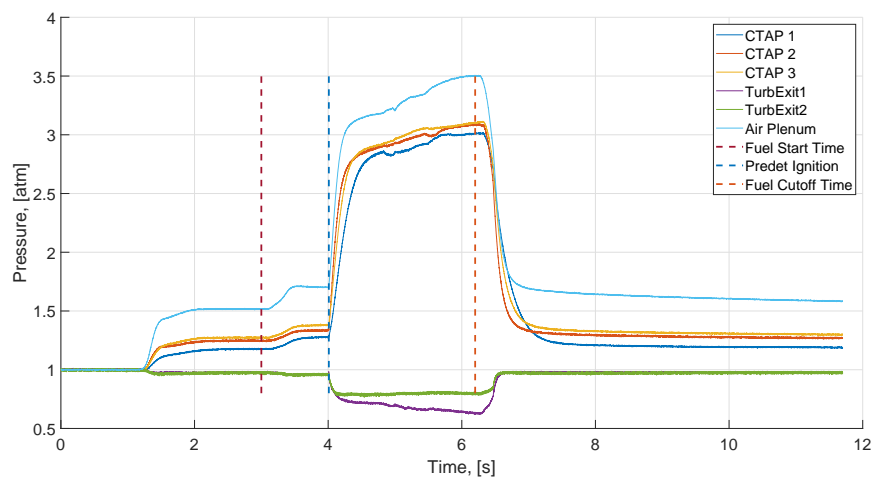
(c) Test 71

Figure 95. Example Pressure Readings.

157
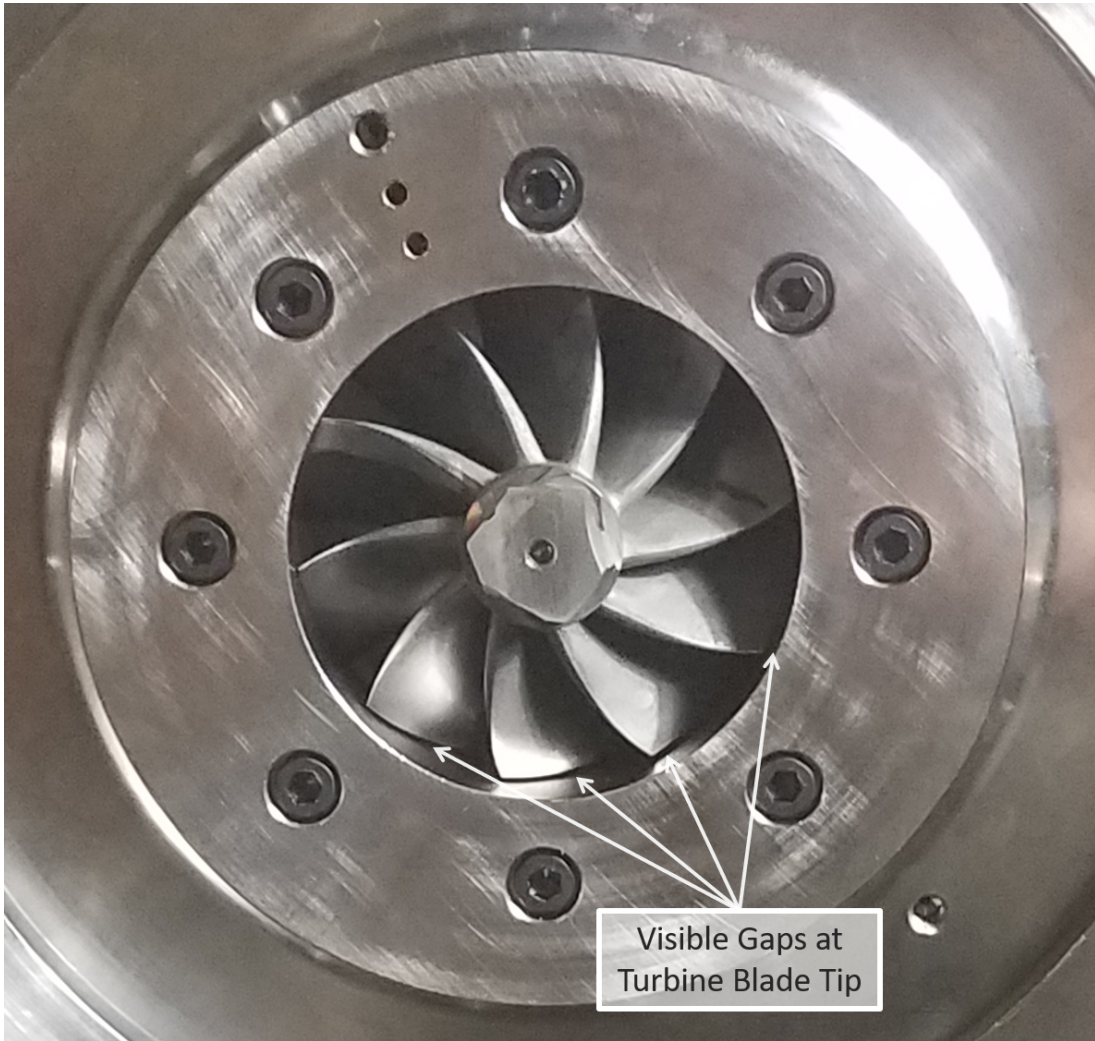
Figure 96. Gaps between the turbine blade tip and the RRDE turbine housing.
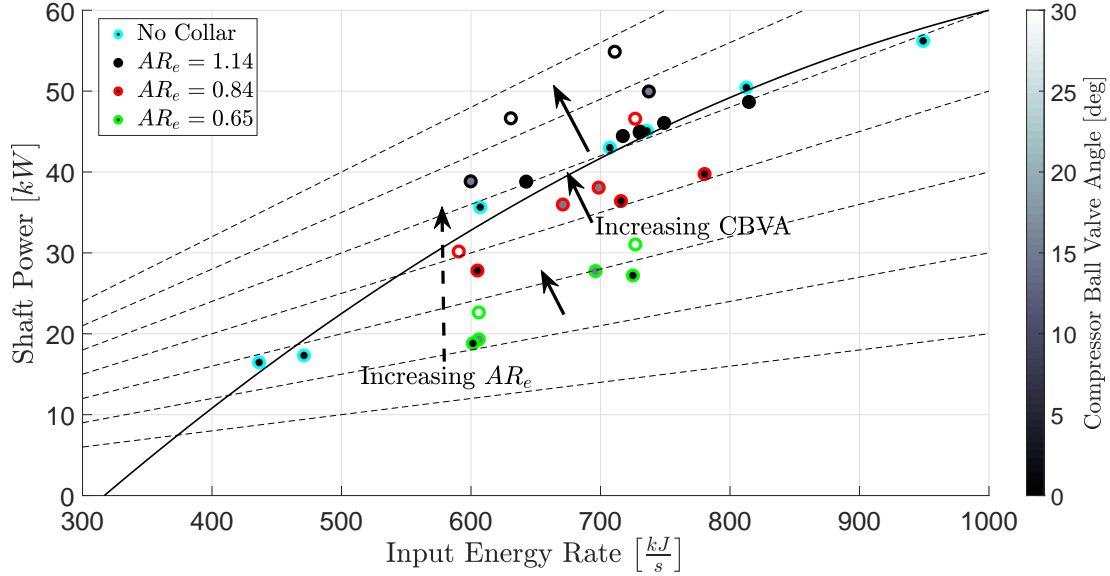
Figure 97. **Variation of shaft power as a function of the input energy rate, CBVA, and** AR_e **with thermal efficiency lines indicated.** **Solid line:** $\dot{W}_{Shaft} = -50 + 0.18\dot{E}_{Input} - 7 \cdot 10^{-5}\dot{E}_{Input}^2$**.**

AR_e conditions considered.

4.2.2   Repeatability.

As all testing on the RRDE to date has focused on examining the response of the RRDE to changes in various parameters few tests had been conducted at similar conditions to establish repeatability. To examine the repeatability of the RRDE thirty-five of the tests conducted (Tests 14 and 38-71) that were in a similar configuration over a narrow range of mass fluxes and equivalence ratios were considered. The turbocharger was installed with the 39° turning angle IGV blade ring. The flow straightening device was installed with no back pressure plate producing $AR_e = 1.14$, and the CBVA was set to 15°. Based on previous testing, the RRDE's target test point was $\dot{m}'' = 78\frac{kg}{m^2-s}$ through the detonation channel at $\phi \approx 0.6 - 0.7$. This test point was selected as it produced a DW as opposed to an acoustic mode, and produced a readily identifiable DW direction. Due to drift in the controller, the mass

fluxes and equivalence ratios varied from test to test as shown in Table 15, leading to some dispersion in the test conditions.

Figures 98 and 99 show the results of this repeatability testing. The mass flux was held nearly constant at $\dot{m}'' \approx 77.5 \frac{kg}{m^2-s}$, and the equivalence ratio varied over the range $0.58 < \phi < 0.72$. All data fell within $\pm 2.75 \ kW$ of the best fit line for compressor power, and $\pm 150 \ Hz$ for the wave pass frequency which is $\approx \pm 5\%$ for both.

The data were collected on three different dates spaced approximately one month apart apiece, indicated by the color of the marker's edge. No clear trends are present, although the 20 December 2018 tests appear to have had a marginally higher output power overall. This could have been due to a variance in environmental conditions such as barometric pressure, temperature, or humidity that were not controlled for. This trend is not present in the frequency data.

4.2.3 Wave Direction Effects on Turbine Integration.

To examine the effects of DW propagation direction on turbine power extraction, preliminary analysis of the effect of wave direction on turbocharger power was conducted with three test points at similar operating conditions, specifically Tests 47, 48, and 51 from the repeatability analysis testing discussed in Section 4.2.2. As shown in Table 15, all three of these cases produced has $\dot{m}'' \approx 78.3$, with $0.625 \leq \phi \leq 0.685$. Examples of the wave direction determination process used for these three tests are shown in Figures 100, 101, and 102. The wave direction can be estimated by viewing the pressure traces directly as shown in part (a) of these figures. For K1 (blue) traces leading K2 (red) traces, the wave direction is counterclockwise, whereas K2 traces leading K1 traces indicate clockwise wave direction. The phase angle between these waves can also be used to estimate the number of waves. For rotating detonation
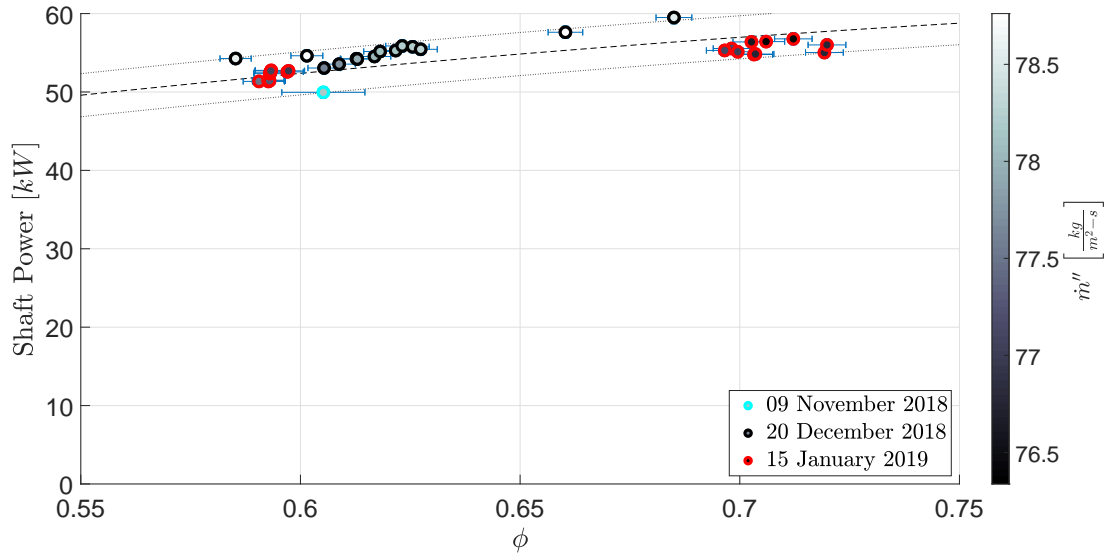
(a) Absolute Scale
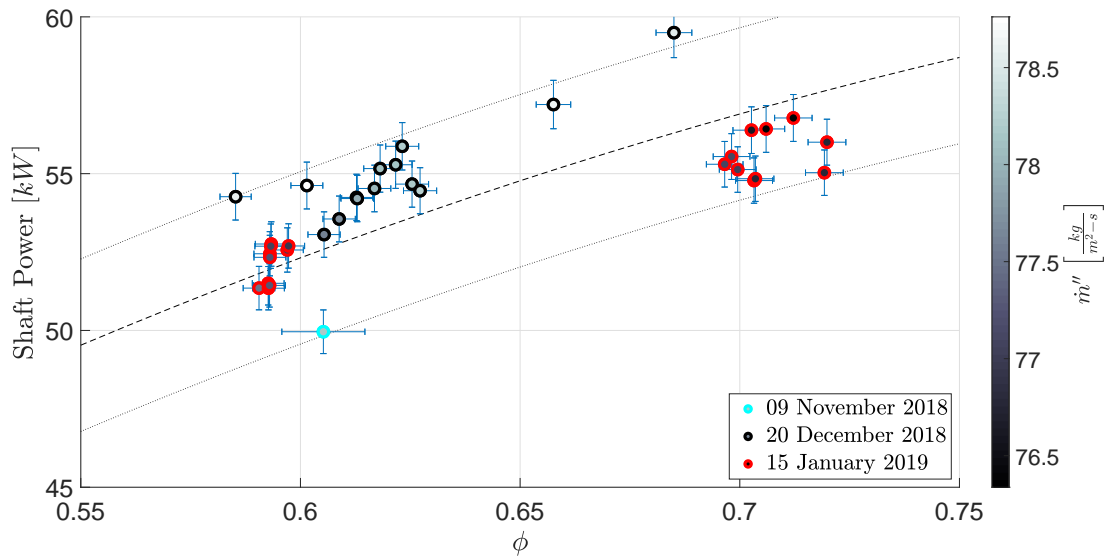
(b) Closeup

Figure 98. Shaft power as a function of equivalence ratio colored by mass flux. Best fit line: $\dot{W}_{Input} = 62.8010 - 65.5368\,(\phi - 1)^2$
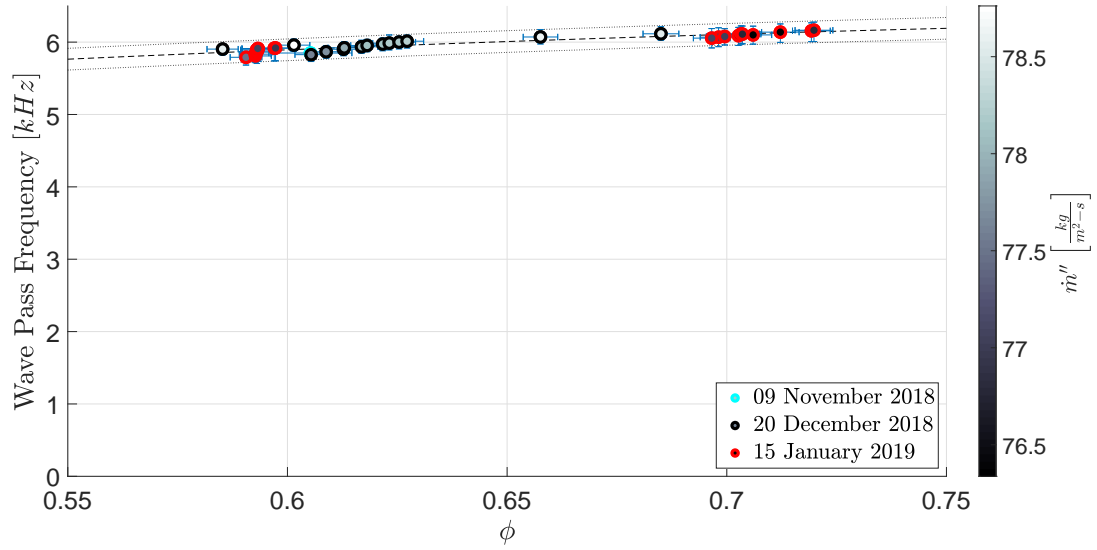
(a) Absolute Scale
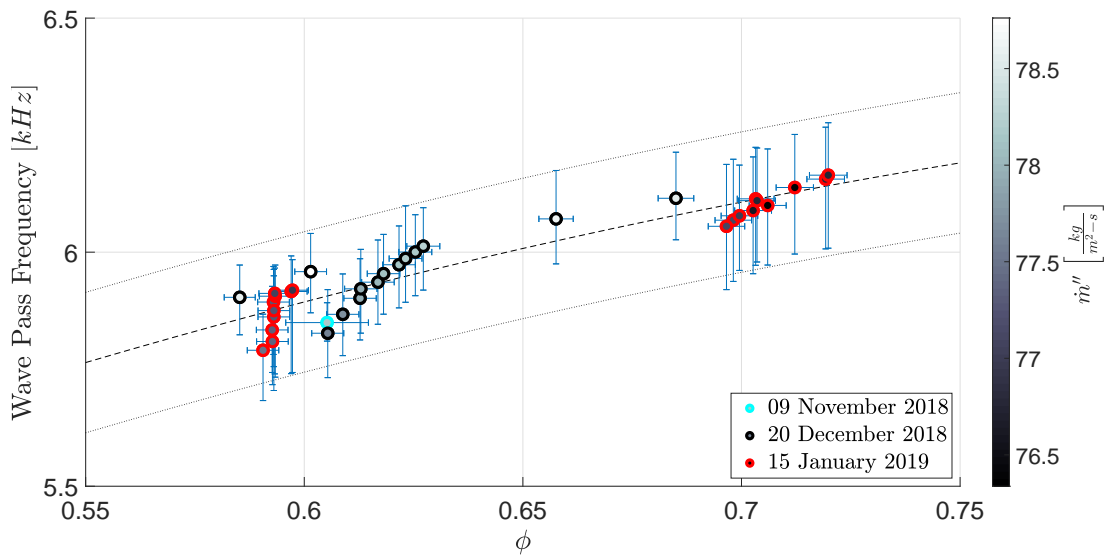
(b) Closeup

Figure 99. Frequency as a function of equivalence ratio colored by mass flux. Best fit line: $f_{ave} = 6381.2 - 3046.8\,(\phi - 1)^2$

waves, the apparent wave phase angle (θ) is $\theta = \theta' N_D$., where $\theta' = 45°$ is the angle between the pressure ports, and N_D is the wave number. For the $\theta' = 45°$ this method requires confidence that one, two, or three wave operation is occurring, producing $\theta = 45°$, 90°, or 135° phase angles, respectively. In this case, all three pressure trace sets show $\theta \approx 135°$, indicating three wave operation.

The exact reason that three wave operation occurred is not well understood. The wave number of detonations with the turbine installed has not been previously reported due in part to the difficulty in determining this quantity. However, the wave pass frequencies were near $6.0kHz$ as shown in Table 15, which was consistent with the wave pass frequency previously observed for three wave operation in the pure combustor configuration (Ref. Huff [41], Figure 63b). Huff's testing also showed that the RRDE operating maps for $\dot{m}''$ and ϕ vary based on the channel height and AR_n. Therefore, while the operability of the RRDE in the turbocharger configuration was markedly different than the operability observed in the combustor configuration, it should not necessarily be expected to behave identically. The presence of the turbocharger added back pressure in a different way than the nozzles used in the flow visualization testing. The presence of the IGV blades also restricts the inner radius at which a detonation may occur, which could force the DW radially outward and lead to a larger wave number.

While this primitive method of visually comparing the pressure traces as shown in part (a) Figures 100, 101, and 102 was effective, the wave direction and phase angle can be more precisely determined with the FFT, Magnitude-Squared Coherence, and Cross Spectrum Phase diagrams, as shown in part (b) of Figures 100, 101, and 102. Read from top to bottom of part (b), the FFT peaks indicate frequencies of interest from a single pressure transducer, which can be used to guide the user's analysis. Considering the peak frequencies identified by the FFT, the Magnitude-Squared
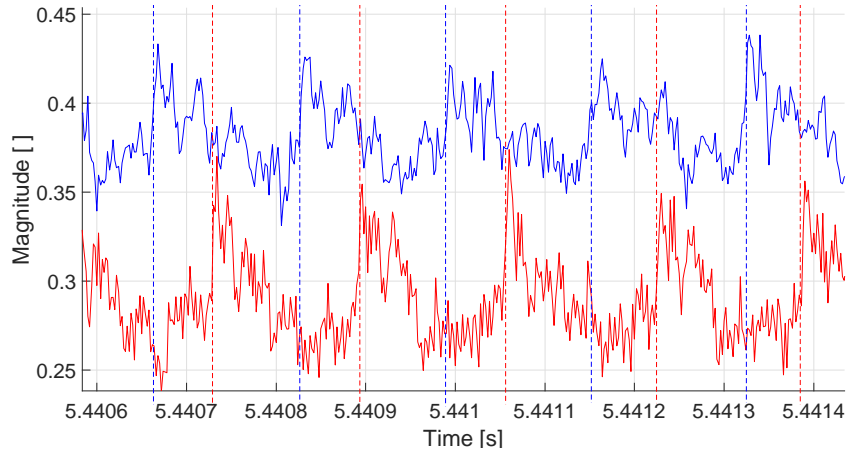
(a) Pressure trace closeup
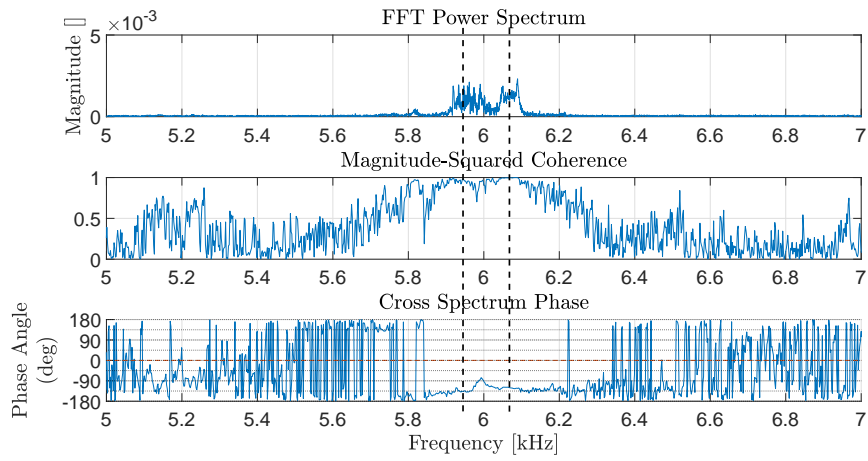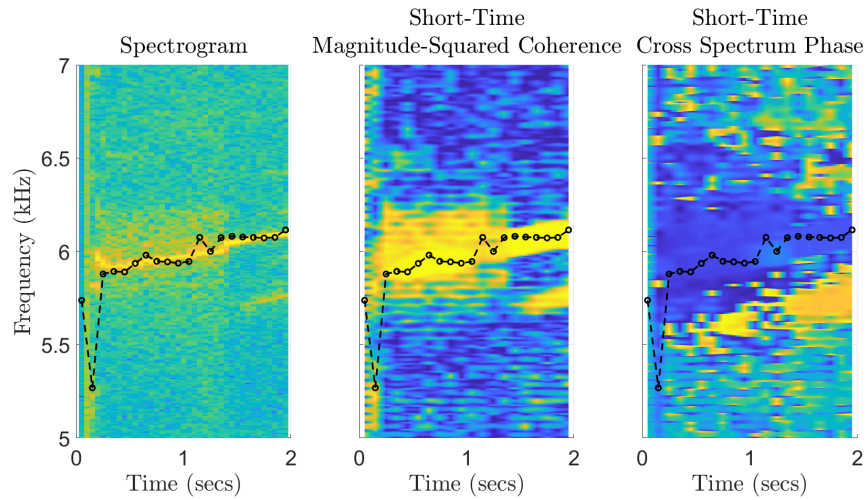
(b) Entire Run

(c) Short Time

Figure 100. Test 47 Propagation Direction Determination (Counterclockwise).

164
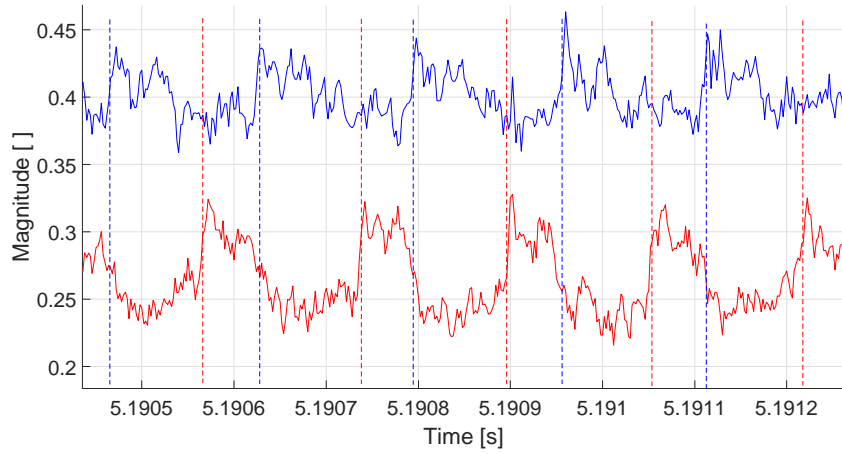
(a) Pressure trace closeup

(b) Entire Run

(c) Short Time

Figure 101. Test 48 Propagation Direction Determination (Clockwise).
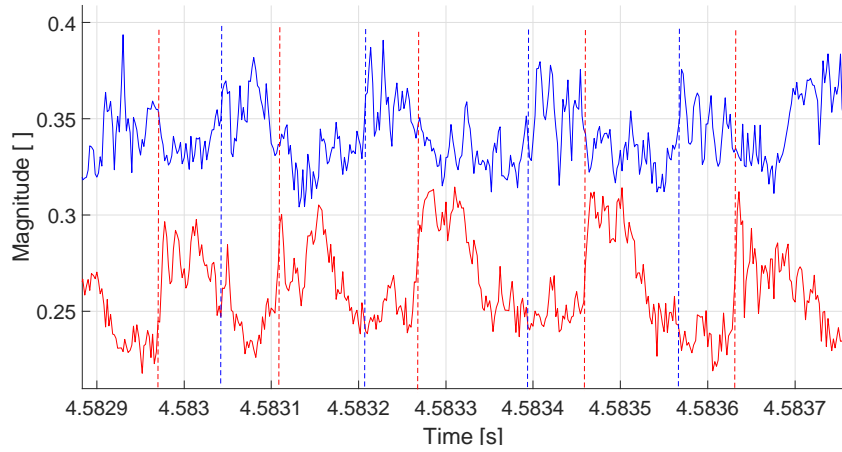
(a) Pressure trace closeup
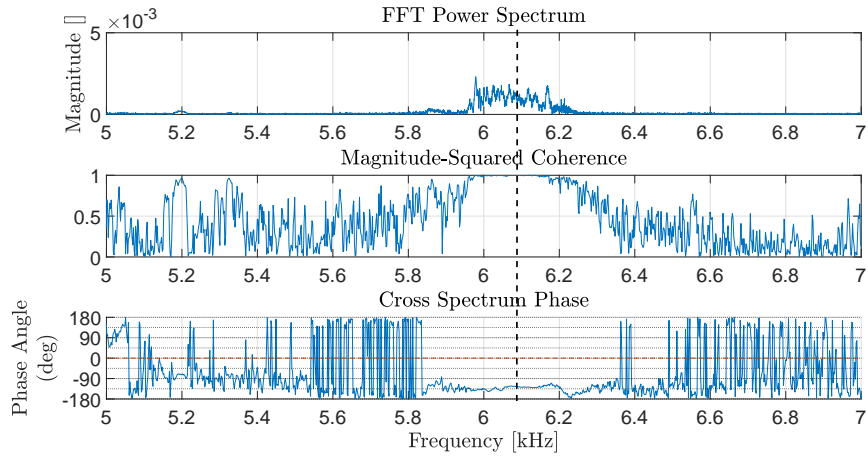
(b) Entire Run
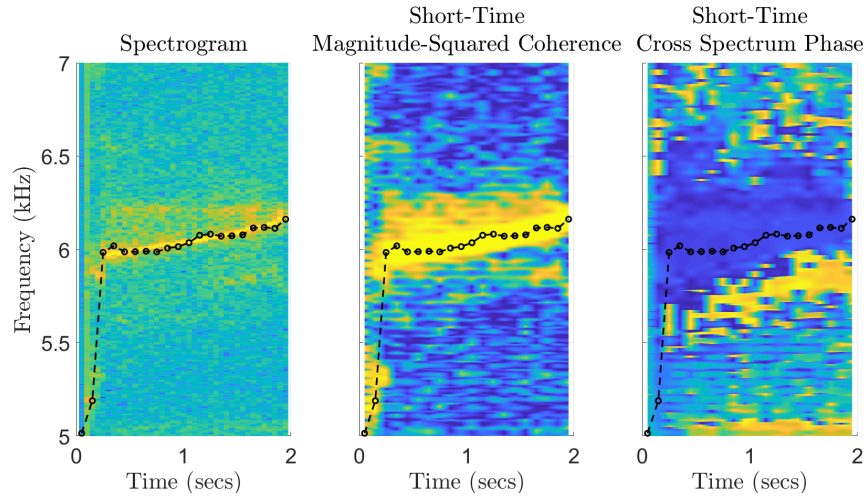
(c) Short Time

Figure 102. Test 51 Propagation Direction Determination (Counterclockwise).

166

Coherence plot is near 1.0 where both signals have frequency content peaks at the frequencies. Then reading the Cross Spectrum Phase diagram gives the phase angle between the signals, with positive angles indicating clockwise propagation and negative phase angles indicating counterclockwise propagation. Dotted lines indicating the wave number are indicated on these plots. For these tests, the FFT peaks near 6.1 kHz with a Magnitude Squared Coherence magnitude near 1.0 at this frequency. For Tests 47 and 51, the Cross Spectrum Phase diagram indicates counterclockwise propagation in a three wave mode. For Tests 48, the Cross Spectrum Phase diagram indicates clockwise propagation in a three wave mode.

Magnitude-Squared Coherence and Cross Spectrum Phase diagram analysis is more exact than simple comparison of the pressure trace phase difference, but gives no indication of any variation with time that these signals may have. For this reason, a short-time formulation of these functions was used. Whereas the spectrogram is a short-time series of FFTs, a similar formulation was developed to take short-time Magnitude-Squared Coherence and short-time Cross Spectrum Phase as shown in part (c) of Figures 100, 101, and 102. This is directly analogous to the process shown in part (b) of Figures 100, 101, and 102, but for short time periods, allowing time dependent variation to be displayed. For the present work, $0.1s$ time increments were used, resulting in twenty segments considered for the $2.0s$ of high speed data in the tests considered here.

As before, the spectrogram was used as a guide to identify frequencies of interest, with yellow bands indicating peaks in frequency content. Finding these bands on the short–time Magnitude-Squared Coherence diagram and then finding which frequency (y axis) has a coherence nearest 1.0 for each time (x axis) results in the lines of frequency vs time indicated by open circles and dashed lines in part (c) of Figures 100, 101, and 102, which closely match the peak frequencies indicated by their respective
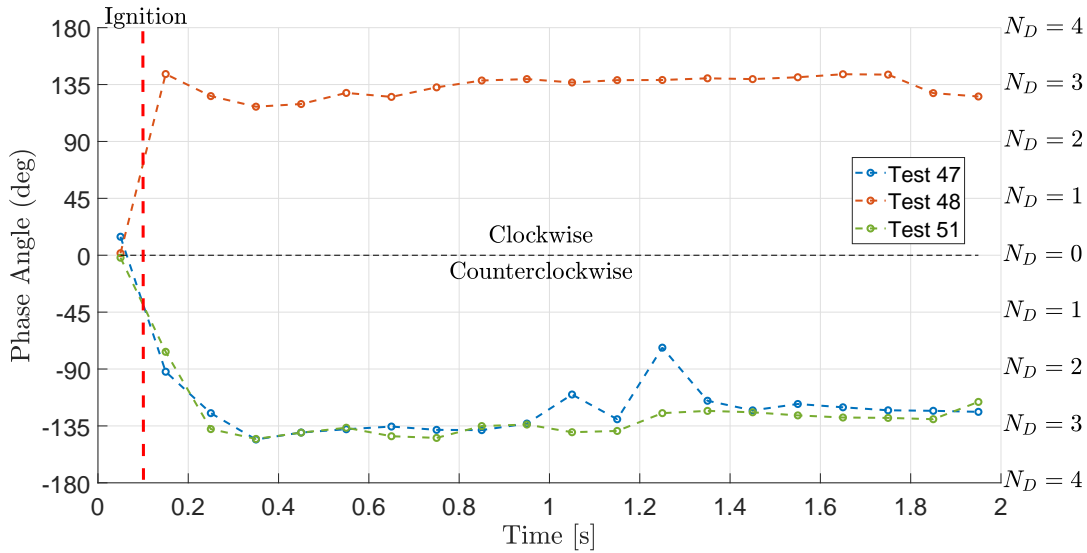
Figure 103. Phase Angles vs Time for Tests 47, 48, and 51.

spectrograms, as expected. Note that on the short–time Magnitude-Squared Coherence diagram dark blue indicates a value near 0.0, and bright yellow indicates a value near 1.0; i.e. a high degree of coherence between the signals.

Then the value of the short–time Cross Spectrum Phase diagram for each time at the maximum coherence frequency (the locations of the open circles) gives the phase angle in degrees as a function of time, with negative values indicating counterclockwise propagation and positive values indicating clockwise propagation. For the short–time Cross Spectrum Phase diagrams shown here, bright yellow indicated a +180 degree phase angle, whereas dark blue indicated a -180 degree phase angle. Extracting the phase angle for each time segment at the maximum coherence frequency resulted in the phase angle as a function of time, shown for Tests 47, 48, and 51 in Figure 103. Note that the first data point was for each of these tests was from pressure transducer data taken before ignition, resulting in a near zero phase angle typical of pulsing or steady operation. Similarly, the second data point contains both transient ignition and some pre-ignition content, and may be unreliable.

As found with the previous analysis techniques, Test 51 shows a phase angle

near $-135°$ indicating three wave counterclockwise propagation for the duration of the run, whereas Test 48 shows a phase angle near $+135°$ indicating three wave clockwise propagation for the duration of the run. Tests 47 shows a phase angle near $-135°$ indicating three wave counterclockwise propagation for the majority of the run, but temporarily shifts to a phase angle near -70 degrees $\approx 1.25s$ into the run. The spectrogram indicates some kind of transition phenomenon may have occurred at this time as the dispersion in frequency content abruptly decreased, though the exact nature of the transition is unclear as three wave counterclockwise operation is indicated both before and after the transition point.

To compare the performance with variation in wave direction, compressor power was chosen as the primary figure of merit. If the DW direction has a significant effect on turbine performance, this effect should manifest as a variation in compressor power, as the compressor is decoupled from the dynamics within the detonation channel except for the shaft power and shaft speed provided to it by the turbine.

Figure 104 shows a total of three data points with clockwise and counterclockwise data represented, and the best fit line and $\pm 5\%$ bounds from the repeatability data set considered in Section 4.2.2, of which these data points are a subset. All three data points were collected on the same date. These data show the shaft power and wave pass frequency varied with ϕ to the same degree as the bulk of the data set considered in Section 4.2.2, of which these data points are a subset.

Given that detonation cases from this data set were identified for both clockwise and counter-clockwise propagation, the lack of separate trend lines indicating divergent compressor power or wave pass frequency based on detonation propagation direction suggests that this parameter does not strongly affect performance. This may indicate that the flow direction at the entrance to the IGV ring was near-radial, or that the IGVs were able to turn the products effectively.
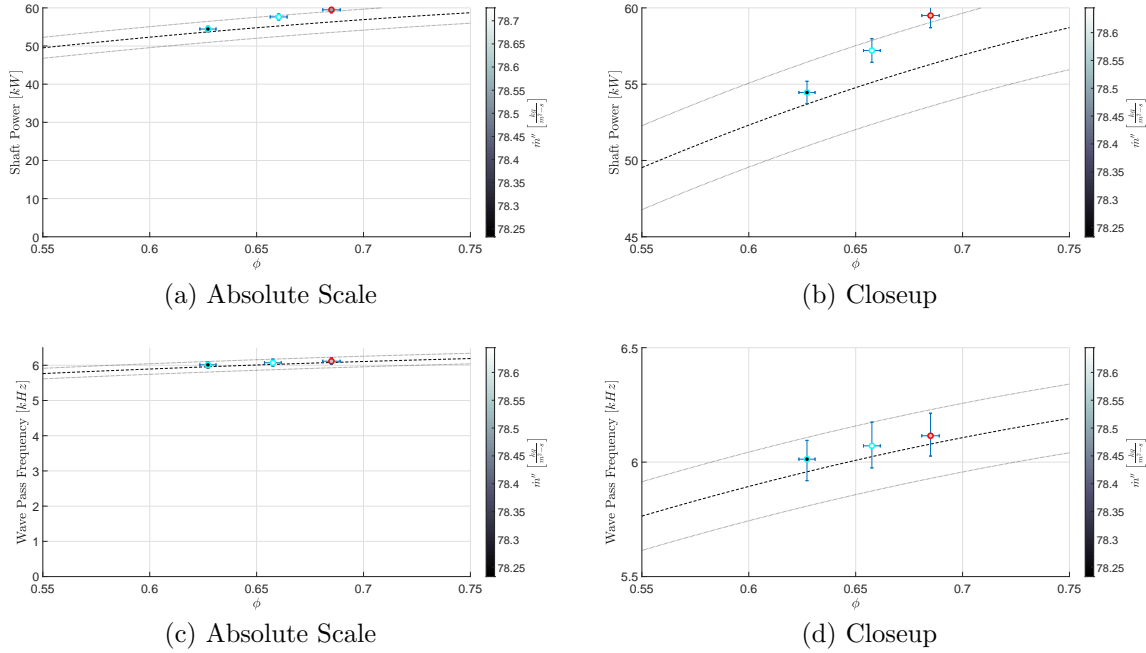
Figure 104. Comparison of shaft power (upper) and wave pass frequency (lower) as a function of equivalence ratio from Tests 47, 48, and 51 for counterclockwise (cyan) and clockwise (red) data.

The lack of power variation based on wave direction indicates that wave direction need not be controlled when integrating an RRDE with a radial inflow turbine. This simplifies the design process and design considerations.

4.2.4 Turbomachinery Damage.

Significant damage to the turbomachinery and ancillary hot flow hardware was observed upon teardown after testing. The turbine was damaged at the beginning of the present work from previous testing but the damage has been exacerbated over the course of subsequent testing.

As shown in Figure 105 there are numerous nicks at the inlet of the radial inflow turbine on each of the blades. This damage decreases turbine efficiency, can potentially lead to cracks resulting in blade failure, and introduces dynamic balance issues which could damage the bearings with subsequent loading cycles. The bearings

170
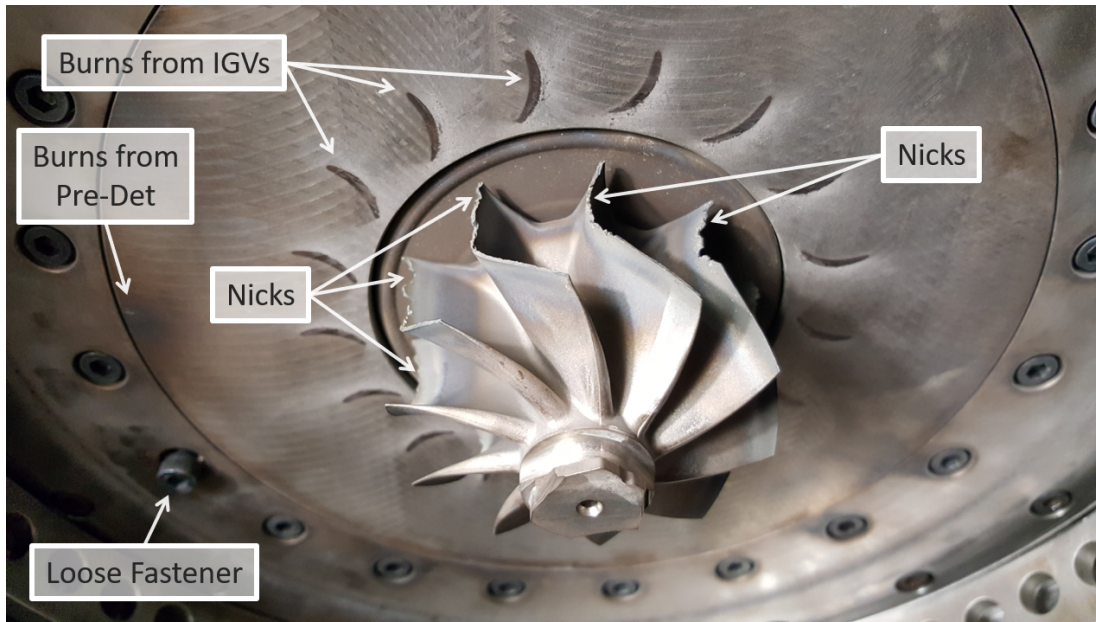
Figure 105. Damage to the radial inflow turbine observed after testing.

remained freely rotating at the end of the present work, however. Burn marks from the IGV blades in contact with the opposing side of the detonation channel are also visible. A loose fastener was observed in the detonation channel, which is a potential concern for turbine integration. Should one of these fasteners back out into the detonation channel and propagate through the IGV ring into the turbine while operating at 100,000+ RPM this would likely cause catastrophic turbine blade damage.

Damage to the IGV blades was also observed as shown in Figures 106 and 107. There is heavy surface oxidation on the suction side of the IGVs, as well as pits, gouging and dents. This damage was particularly evident on the trailing edge of the IGV blades, where the blade thickness is at a minimum. It is believed that the pits, gouges, and dents were caused by debris such as the fractured turbine blade pieces, being flung by the turbine blade into the suction side of the IGVs, which face the turbine blades. This debris can bounce back and forth between the IGV blades and turbine multiple times until it is sufficiently fragmented to accelerate with the exhaust flow fast enough to depart the turbine. The susceptibility of radial inflow turbines

171
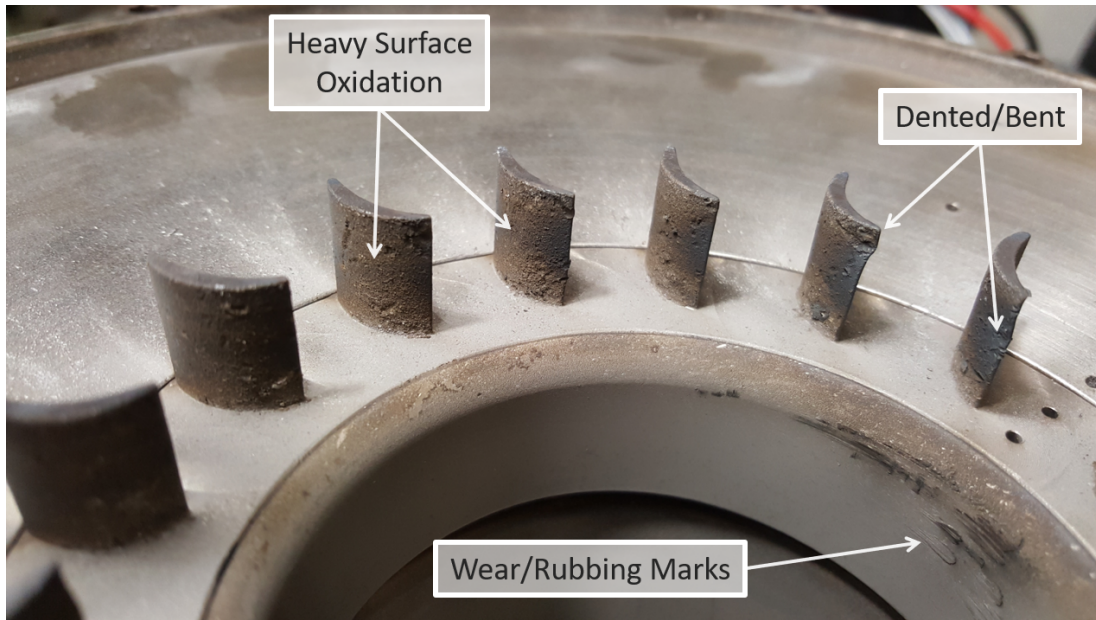
Figure 106. Damage to the IGV blades on the suction side facing the turbine.

to this damage mode is described in Chapter 9 of Wilson and Korakianitis [93]. The surface oxidation on the pressure side of the IGVs appears to be less intense than that on the suction side. The IGV blades are most susceptible to thermal damage because they are thin structures exposed directly to the detonation flow field on both sides, and are not actively cooled, whereas the comparatively thick metal the rest of the RRDE detonation channel is made from is only exposed to hot flow on one side and has significantly more mass to store thermal energy.

Exposure to the exhaust also caused damage to the diagnostic instrumentation described in Section 3.3.1 as shown in Figure 108. This image shows the flow straightening device from the perspective of the turbine blades looking out to the exit. The IGVs are blurry but visible in the foreground, and the thermocouples are visible at the exit. Both the S1 and S2 Kiel probes sustained extensive damage. The S1 Kiel probe, which was closest to the turbine, burned off leaving a portion of the shank extending into the flow. This would function as a poor static temperature measurement device at this point. The shroud of the S2 Kiel probe burned off as well. While

172
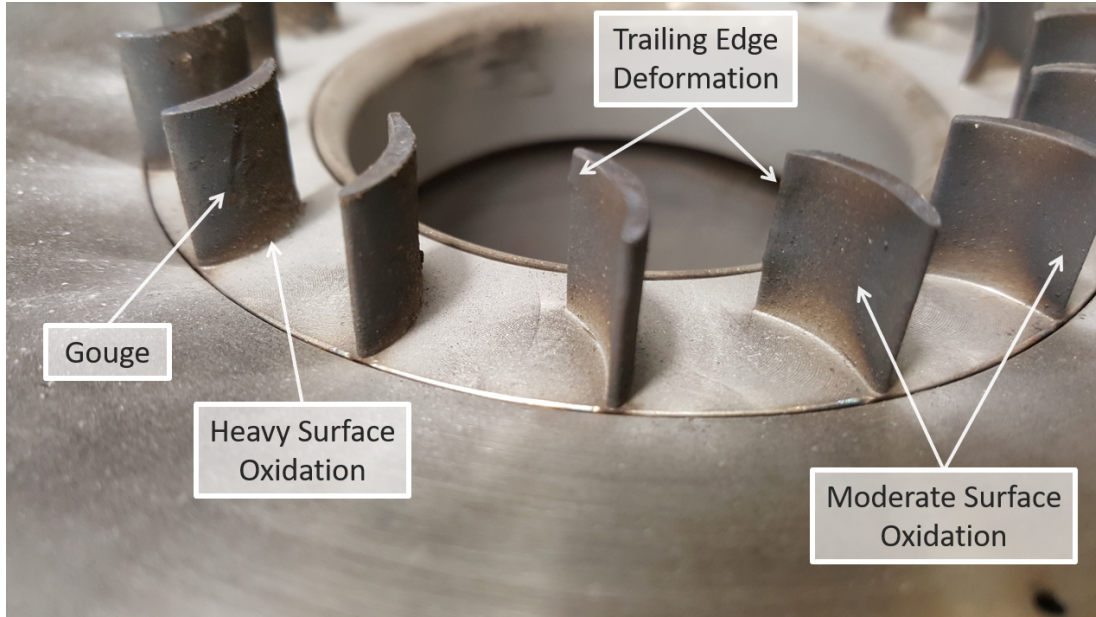
Figure 107. Damage to the IGV blades on the suction side (left) and pressure side (right).

the total pressure probe opening remained intact and could thus still function as a total pressure measurement device, it would have been more sensitive to angle of attack variations after the shroud separated. Note that as these probes were connected to their pressure transducers via CTAP devices, the pressure transducers themselves remained protected.

4.3 Gaseous Hydrocarbon Operation

In order to investigate the operability of the RRDE using an alternative hydrocarbon fuel, C_2H_4, the RRDE was operated as specified in Section 3.4. All tests were conducted with the pure combustor configuration, with $AR_t = 0.2$, $AR_n = 0.6$, and the 4.5 mm height channel plate, based on previous experience with $H_2 - Air$ in this configuration. The equivalence ratios were within the range $0.5 < \phi < 1.25$, with mass fluxes in the $50 < \dot{m}'' < 220$ range, as shown in Figure 109

The RRDE failed to detonate with the $C_2H_4 - Air$ mixture at all test points
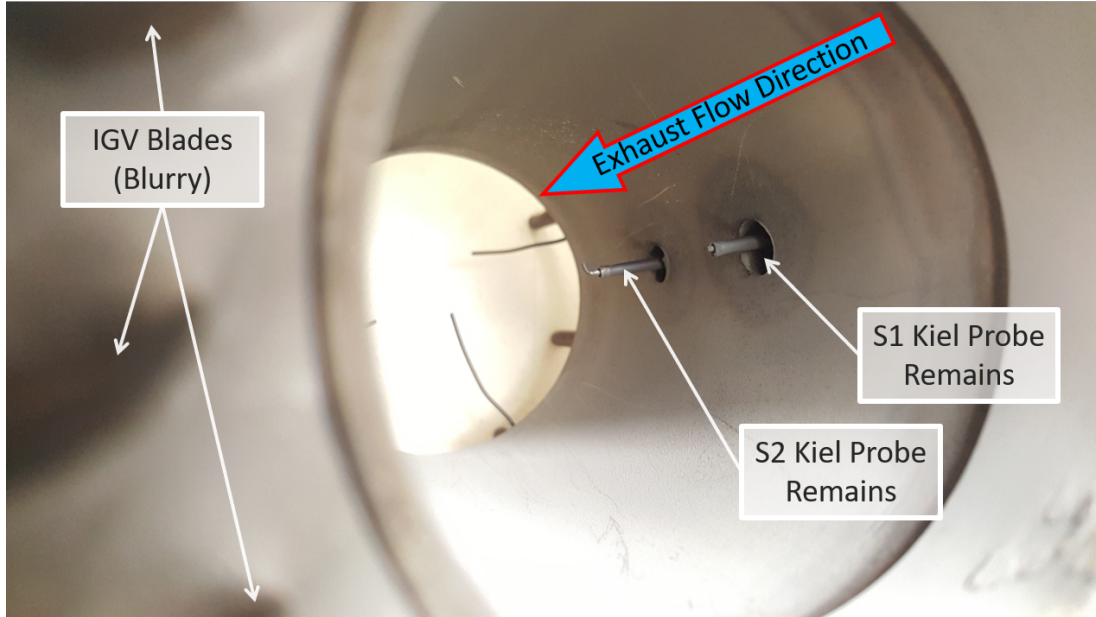
Figure 108. Damage to the instrumentation within the flow straightening section.

considered. The specific reason for this failure to detonate is unknown at this time. Given that $C_2H_4 - Air$ does not necessarily have the same operability range as $H_2 - Air$, this may simply indicate that testing was not occurring in an operable regime. Increasing the mass flux and therefore pressure by increasing flow rates or decreasing channel height may provide more beneficial conditions capable of supporting DWs.

4.4   Summary

Flow visualization was utilized to understand the first objective of this study. Namely, whether radial variation of the detonation wave was occurring based on mode, which could account for a previous observations such as increased apparent wave speed for two wave cases. Examination of flow features was also desired to the extent possible with the broadband chemiluminescence visualization technique used.

Several modes were observed, including one and two wave rotating detonations, two and four wave counter-rotating clapping modes, as well as a three node mode which may in fact be a six wave counter-rotating mode. One wave rotating modes

174
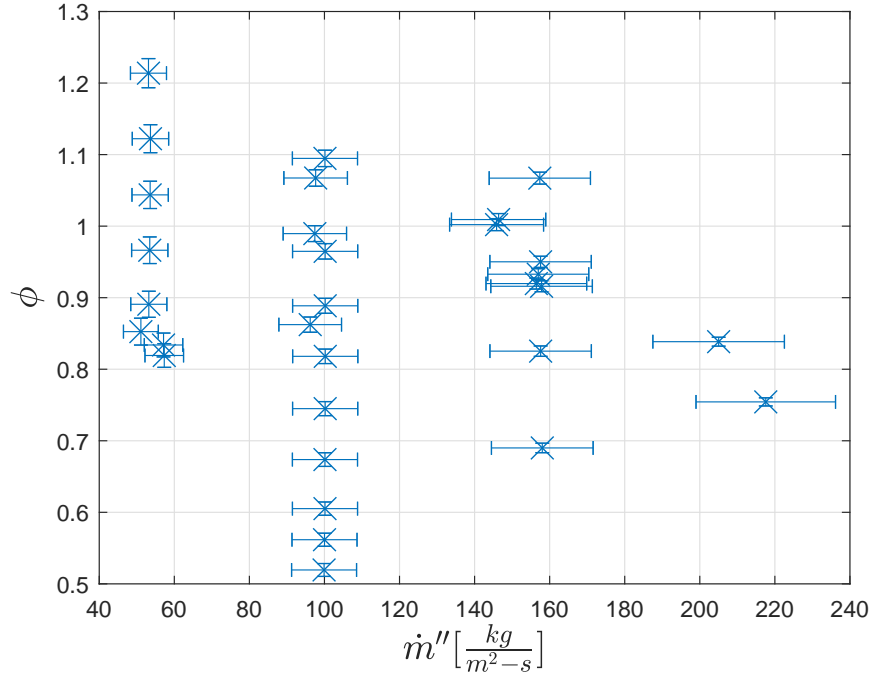
Figure 109. Map of attempted detonation test points using $C_2H_4 - Air$ reactants with error bars indicated. No test resulted in successful detonation.

tended to propagate closer to the inner radius with two wave rotating modes nearer the outer radius, although exceptions for both cases existed. In general the two wave counter-rotating mode appeared to be related to one rotating mode operation, the four counter-rotating wave mode appeared to be related to the two rotating wave mode, and the three node mode appeared in the regime where three wave rotating mode was previously observed suggesting they may be related.

The normalized mean detonation velocity, $\frac{\bar{v}_D}{v_D CJ}$, was observed to increase as the mean detonation radius, $\bar{r}_D$, increased. There are a number of reasons this may be the case, including increased confinement providing pressure reflections capable of driving the detonation off of the throat ring, decreased mixing of products and reactants, and decreased parasitic combustion. While the RRDE operated at low $\bar{r}_D$, this result suggests design efforts should focus on an operating point that will provide operation as near the outer radius as possible.

175

The addition of polycarbonate into the detonation resulted in a significant amount of reactive material being added into the flowfield, with polycarbonate equivalence ratios of $\phi_{polycarbonate} \approx 0.5$. The impact this had on the detonation is unknown, although the effect may not be as severe as the equivalence ratio alone would suggest. Hydrogen is more reactive and was more likely to oxidize first before the hydrocarbon polycarbonate. In addition, the erosion of polycarbonate modified the channel plate geometry, altering the test conditions both between and within tests, resulting in significant error in $\dot{m}''$ calculations.

Investigation of the power generation characteristics of the RRDE integrated with a turbocharger was a second objective of the present research. Investigation of the power generation response to a post-turbine flow straightening device and turbine and/or compressor back pressure was desired. Additionally, the effect of wave direction on the output power and the repeatability in general of the output power was desired.

Initial testing was conducted both with and without a flow straightening collar installed to examine the effects of controlling the post-turbine expansion of the products. This flow straightening device had no discernible impact on performance; neither helping nor hurting by itself. However, the flow straightening collar served as an attachment point for instrumentation and flow restriction devices and was left installed for subsequent testing.

Further testing examined the response of the RRDE to the addition of back pressure, which was accomplished by changing the exit area of the turbine via restrictive plates and the compressor by a ball valve. Increasing turbine back pressure was shown to decrease shaft power, whereas increasing compressor back pressure increased shaft power. However, increasing the compressor back pressure with a CBVA of 30° put the compressor in an operating condition near or over the surge line, risking hardware

176

damage.

Preliminary evidence indicates the DW direction had no clear impact on performance. This may imply the flow direction is near-radial at the IGV ring. While more work is required to prove that DW propagation direction does not affect performance with turbomachinery installed, if this is indeed the case it may greatly simplify design considerations.

Investigation of hydrocarbon fuels with the RRDE was a third objective of the present research, though it was not covered extensively due to time considerations. Specifically, the operability map of the RRDE with gaseous hydrocarbon fuels as a function of mass flux, equivalence ratio, and geometric configuration was desired.

The RRDE did not detonate for any of the test conditions examined using ethylene fuel. However, the testing represented a narrow band of test conditions, with only one combination of channel plate height, AR_t, and AR_n examined, and the only fuel injection ring installed, which was designed for H_2 injection; only ϕ and $\dot{m}''$ were varied. It is possible that the operability range of ethylene is dissimilar to $H_2 - Air$, and that another combination of parameters would work, potentially including a different fuel injector plate with injectors optimized for C_2H_4 injection at the flow rates of interest. Time constraints prohibited full exploration of the trade space in the present work, and the lack of initial success should not be construed as an indication that C_2H_4 operation in the test device is not viable.

V. Conclusion

With the ever-increasing demand for aircraft electrical power to operate systems such as Directed Energy (DE) weapons, sensor arrays, and electronic warfare suites, the electrical output demands on aircraft are outpacing the abilities of their engine's electrical power generation capabilities. Many electrical systems require high output for a brief duration on short notice, which these engines are not well suited to provide. While the initial power may be provided by batteries, rapidly recharging these systems is critical for subsequent operation. The Radial Rotating Detonation Engine (RRDE) is being researched as a technology capable of providing the high power density and rapid response required to provide the high output power on demand with short notice. Due to the radial flow path of the RRDE, it can be made into a very compact power source when integrated with a radial inflow turbine. This compact form factor is beneficial for an aircraft of any size, but is critical for smaller tactical aircraft where available space for systems is at a premium.

5.1 Objectives

The present work investigates several remaining questions regarding the operation of an RRDE. The first objective was to examine the nature of the detonation wave within the channel. Previous work had indicated that the detonation wave was not located at a constant radius, though this hypothesis was not able to be confirmed due to the construction of the device. This was thought to be due to the radial degree of freedom that the planar channel configuration allows. The ability of the detonation wave to change its operational radius has implications for design of both the RRDE detonation channel itself, as well as integration of components with the RRDE. Direct observation of the DWs was required to avoid ambiguity in interpretation.

The second objective was to investigate the interaction of the RRDE with a radial inflow turbine. Specifically, the response of the RRDE's power output to the addition of a post-turbine flow straightening device and to the addition of compressor and turbine back pressure was required to better understand how the RRDE could be integrated into an operational power production system. As part of this objective, preliminary investigation of the effects of wave direction on power production was desired, as well as the repeatability of the RRDE's power output.

A tertiary objective was to conduct a preliminary investigation into operation with gaseous hydrocarbon fuels in lieu of gaseous hydrogen, which was previously the only fuel used in the research device. Hydrogen is generally considered to be more readily detonable than most hydrocarbon fuels. However, its low storage density under standard conditions, lack of logistical support, as well as safety concerns related to storage and ease of flammability, preclude the use of hydrogen on most aircraft. Development of the RRDE to operate on the logistically supportable, safer, and denser hydrocarbon fuels is required for their practical use, and demonstrating operability of the RRDE with gaseous hydrocarbons would be a step in this direction.

5.2   Methodology

Facilities at AFRL/RQTC's Detonation Engine Research Facility (DERF), located in D-Bay on WPAFB, were configured to conduct the present research. Flow visualization was conducted with $H_2 - Air$ reactants using high speed photography to capture the DW's chemiluminescence. The metal channel plate was replaced with one manufactured from visually transparent polycarbonate to permit viewing of the DW within the channel. A high speed pressure transducer measured pressure fluctuations in the fuel plenum correlated to passage of the detonation wave. The high speed camera footage was processed by tracking the maximum intensity frame by frame,

which was converted into a radial location and averaged over the duration in which the mode persisted. With the frequency measurement from the pressure transducer and the radius measurement from the high speed photography, a detonation wave speed was determined and compared to the theoretical Chapman–Jouguet (CJ) wave speed for the reactant mixture. In this way, the operating mode, radius, and wave speed were determined for each case.

Testing with the radial inflow turbocharger was initially conducted without a flow straightening collar or back pressure to the turbine or compressor for baseline performance evaluation. The flow straightening device was then installed and tested, followed by testing with turbine and compressor exit area restrictions to increase the turbine and compressor back pressure, respectively. The compressor's output power was determined for each case based on the pressure ratio generated by the compressor and its mass flow rate, which was then converted to shaft power produced by the turbine using the manufacturer's operating map. Two high speed pressure transducers were installed in the channel at a 45° offset angle relative to each other to determine the wave direction within the channel, with the phase angle between the pressure traces used to establish wave direction.

Preliminary testing with gaseous Ethylene (C_2H_4) was conducted in the baseline combustor configuration with a metal channel plate. Specifically, the $4.5mm$ height channel plate was installed with the $AR_n = 0.6$ nozzle and $AR_t = 0.2$. While the RRDE was instrumented with all of the pressure and temperature transducers of the baseline RRDE that operated with H_2, the primary emphasis of this study was to determine where ignition was possible. The only change from the baseline RRDE configuration was to change the fuel supply source to an Ethylene bottle. Neither of the reactants were actively heated.

5.3 Results

Testing with the polycarbonate channel plate revealed several operating modes in the RRDE. One wave and two rotating wave operation modes were observed, as expected. However, two wave and four wave counter-rotating clapping modes were also observed, as well as a three node acoustic mode. Operation in a one wave mode was frequently unsteady, transitioning to the two counter-rotating wave clapping mode. Additionally, unsteadiness in the two wave rotating mode was observed resulting in oscillation of the two waves phase angle in one case, and temporary transition to a four wave counter-rotating mode in another. One wave modes tended to propagate around the inner radius of the RRDE, whereas two wave modes tended to move radially outward.

For both one and two wave modes, as $\bar{r}_D$ increased, $\frac{\bar{v}_D}{v_{D,CJ}}$ increased. This indicates detonative operation at the maximum $\bar{r}_D$ is desirable. This also suggests that a combination of products recirculated back into the reactant mixture and parasitic combustion is responsible for this degradation in wave speed, both of which will occur to a greater extent the longer the distance the reactants must propagate through the channel to reach the DW radius. While operation was similar to that observed in previous work, the modes observed while operating with the polycarbonate channel installed differed. This may be due in part to the introduction of polycarbonate into the flowfield, which was shown to have the potential to significantly alter the combustion chemistry.

Turbocharger testing revealed that the flow straightening collar had a negligible impact on performance compared to the baseline device without the collar. This indicates expansion of the products post-turbine does not significantly impact the turbine performance. Adding back pressure to the turbine uniformly lowered performance. Conversely, adding back pressure to the compressor tended to increase output power.

For CBVA of 0°, 15°, and 30°, the shaft power increased with CBVA. However, the CBVA also affected where the compressor was operating on its operating map. A 0° CBVA resulted in operation near the choke line, a 15° CBVA produced operation near the peak efficiency operating line, and a 30° CBVA resulted in operation near or exceeding the choke line. Repeatability analysis showed power production within $\pm 5\%$ at similar operating conditions. Preliminary analysis also indicated wave direction had little or no impact on output power at the conditions tested. This could indicate that the flow direction at the IGV blade ring entrance is near radial. Because the reactants are injected radially with no azimuthal component, conservation of angular momentum dictates that on average the angular momentum of the flow should sum to zero, resulting in radial flow on average. However, local variations in flow velocity could have existed due to proximity to the detonation wave.

Preliminary testing with gaseous hydrocarbon fuels ($C_2H_4 - Air$) was unsuccessful in initiating either a detonation or acoustic burning over the entire range of operating conditions considered, with $40 < \dot{m}'' < 220$ and $0.5 < \phi < 1.25$, $h_c = 4.5\ mm$, $AR_t = 0.2$, and $AR_e = 0.6$. While detonation was not successfully initiated, the test conditions were selected based on the successful configuration and operating range of $H_2 - Air$, and an alternative configuration may be more successful for different fuels. Increasing the mass flux or either of the reactant initial temperatures may also be required to initiate detonation.

5.4 Recommendations for Future Work

In the near term, investigating the conditions under which initiating a detonation within the RRDE using gaseous hydrocarbon fuels and air is possible should be a research priority.

While the fact that the detonation wave changes its radial position based on op-

erating condition has been confirmed, due to excessive introduction of polycarbonate into the flowfield there is some uncertainty as to the specific behavior of the flowfield under normal operating conditions. This uncertainty could be mitigated by testing with a non-reactive window material such as quartz or sapphire. This would also allow the use of flow diagnostics such as OH^* chemiluminescence, enabling a more refined analysis of the location and structure of the detonation wave. The present work indicates that a larger operating radius ($\bar{r}_D$) resulted in a higher wave speed, indicating better detonation performance. It may be possible to force the DW to a larger radius by designing a converging channel, increasing performance. This could be accomplished by simply making a flat channel plate, which would naturally converge as the radius decreased along the radially inward flow path. Should this geometry prove viable, this would also allow manufacturing of a quartz or sapphire window at greatly reduced cost, as a planar window is much less expensive to manufacture than one with a compound curve, such as the one used in the present work. Thus, these potential methods could prove mutually beneficial. A flat plate design could also offer the added benefit of simple adjustment of h_c by shims, as compared to the present baseline device which required a new channel plate manufactured to achieve every channel height of interest while maintaining a constant A_c along the radius.

For continued research in turbocharger testing, the IGV blade ring has not yet been optimized, and the turbine used in research to date is similarly not designed for this particular application. Analysis by Huff et al. [42] demonstrated that a large percentage of available energy within the flow is being rejected as heat, significantly damaging the overall efficiency of the test device. A redesign of the turbomachinery components with the benefit of a better understanding of the operating environment may lead to significant improvements in thermal efficiency. Similarly, replacing the compressor side, which was only used to determine the shaft power and would not be

used in a bleed air turbine concept, with an electrical generator would be beneficial in determining the operating characteristics of such a system.

Development of a turbine operating map would also assist in diagnosing where improvements could be made. While the manufacturer provided a turbine operating map, the geometry of the turbine enclosure was entirely modified to accommodate the detonation channel and the performance in general cannot be expected to match. While measurements from the Kiel probes to measure total pressure directly produced unreliable data, preliminary analysis by Huff et al. [42] showed a dramatically different turbine operating map in the new configuration. By instrumenting the device with more reliable CTAP probes and correcting these properties back to their total quantities a more accurate turbine operating map could be obtained. Analysis by Paxson and Kaemming [94] demonstrated that turbine efficiency is maximized near its design point, and without an accurate turbine operating map the new maximum efficiency pressure ratio is unclear. Such analysis could drive the design of a more refined post-turbine nozzle than the crude orifice plates used in the present research, matching the pressure ratio to the maximum efficiency pressure ratio for the turbine and increasing overall power extraction performance.

Due to the material choice of stainless steel and the lack of active cooling, run times were constrained to short duration only, $\mathcal{O}(s)$, relying on the mass of the RRDE to absorb thermal energy and keep the hot section surfaces below their melting point for these short durations. Investigation of alternative materials or cooling schemes is required to enable prolonged operation of the RRDE. Finally, variation of the radial channel size of the RRDE is required to assess the scalability of this radial flow configuration. Both the effects on wave behavior and power generation potential should be examined.

184

5.5 Summary

The present work has demonstrated that continued research and development of the RRDE has resulted in both a better understanding of the operation of the device via flowfield visualization, and an increase in power generation by increasing back pressure on the compressor. As promising as the initial results have been, analysis shows that even greater performance could be achieved with further component optimization or a second design iteration. The RRDE has shown great potential to serve as a bleed air turbine APU with high power density. With further development this technology could offer a potential solution to the emergent rapid response, high power generation requirements of select airborne electronic systems.

Appendix A. Mode Persistence

The operational mode of the RRDE was observed to vary over the duration of the test for most tests. This could be a change from one quasi-steady mode to another, high frequency variation between modes, or transition between identifiable modes and transient operation with no discernible pattern. This appendix provides a visual way to demonstrate the persistence of modes experienced for various tests to provide the reader with a better appreciation for the transient operating behavior observed over the course of hours of high speed video footage. The operating conditions for these tests are described in Table 13. The spectrogram for the test, which is a series of short-time FFTs placed sequentially and displayed as a contour plot, is provided to show the variation in frequency between the modes.

Figure 110 shows the modes observed in Test 1 from the polycarbonate channel plate testing. A two wave mode persists for $\approx 0.4s$, after which it evolves into a combination of one rotating wave and two wave clapping modes for $\approx 0.9s$, after which the fuel was shut off. Previous testing by Huff [41] showed only two wave operation at this operating condition. The exact reason for this deviation is unknown, but as discussed in Section 4.1.2 burning of the polycarbonate may be affecting the operating condition.

Figure 111 shows the modes observed in Test 2. Steady one wave operation persisted for $\approx 0.1s$, followed by a combination of one rotating wave and two wave clapping for the remainder of the test. Previous testing by Huff [41] showed only one wave operation at this operating condition.

Figure 112 shows the modes observed in Test 5. This test experienced two rotating wave operation for the first $\approx 0.1s$, followed by an unsteady transition period of $\approx 0.2s$ and a three node non-rotating mode for the remainder of the test. Previous testing by Huff [41] showed this test was on the border of the two and three wave rotating
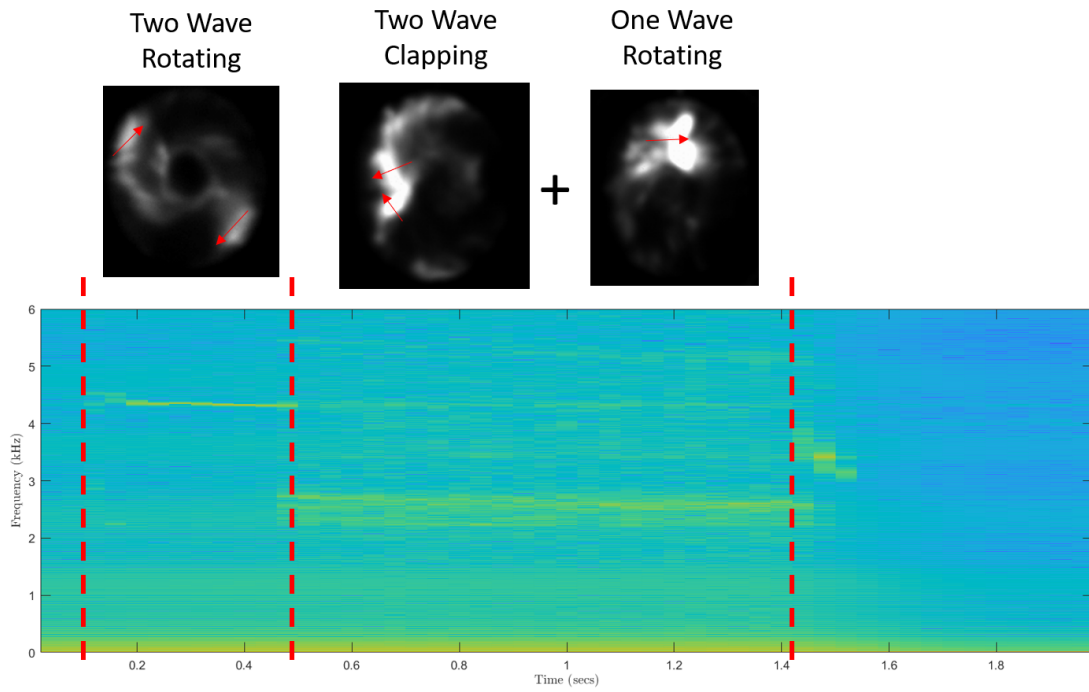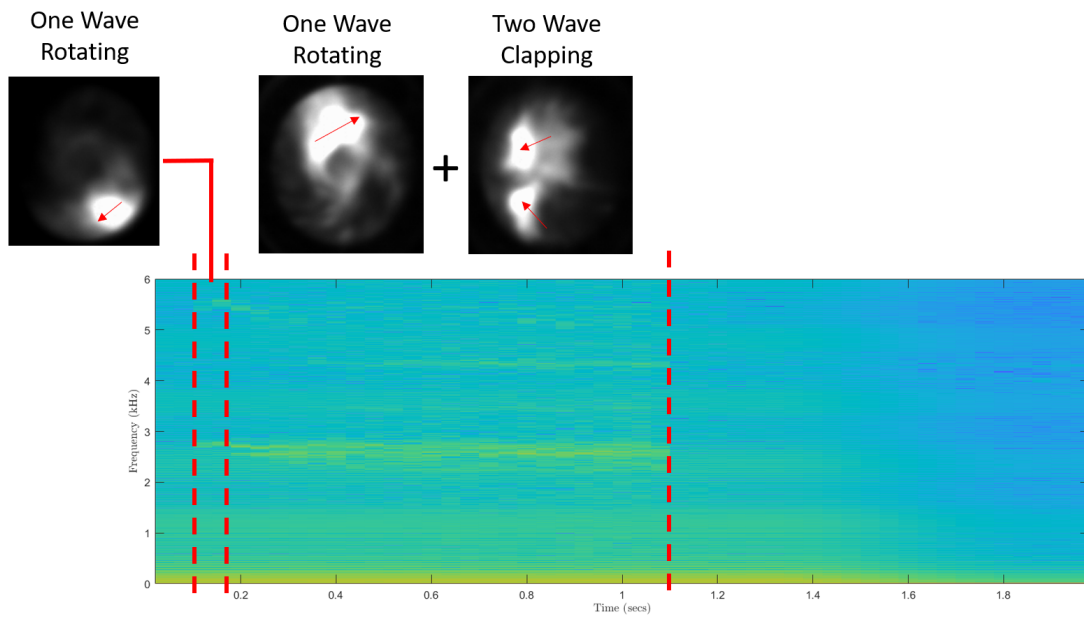
186

Figure 110. Test 1 Mode Persistence

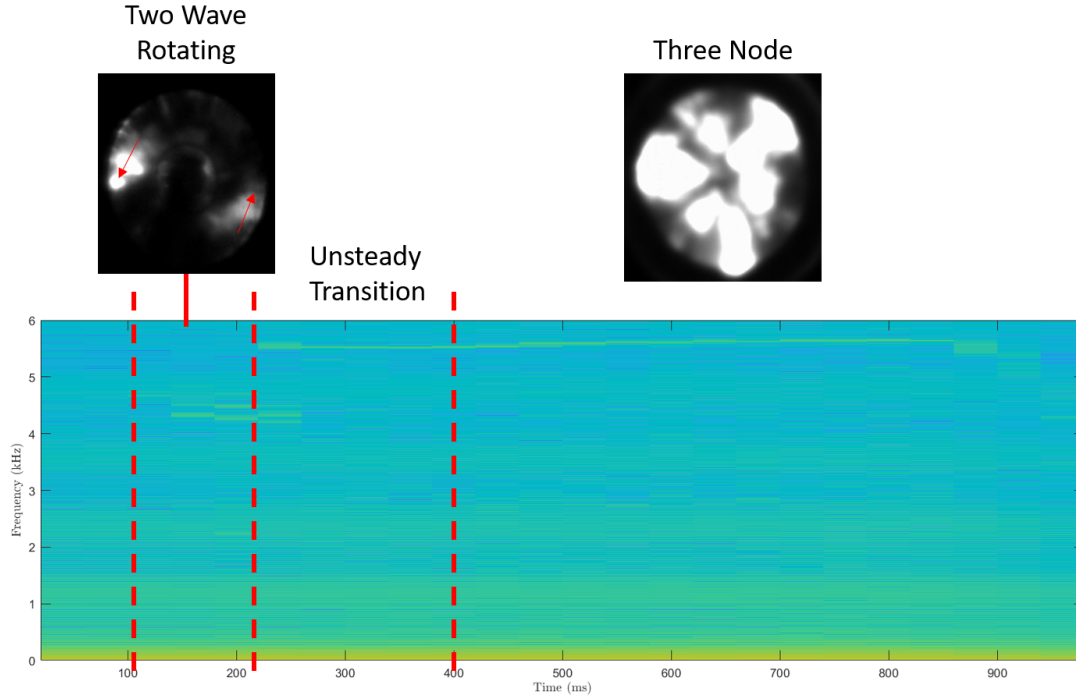**Figure 111. Test 2 Mode Persistence**

187

Figure 112. Test 5 Mode Persistence

modes for this operating condition.

Figure 113 shows the modes observed in Test 6. Test 6 experienced the non-rotating three node mode for the entire duration of the test. Previous testing by Huff [41] showed this test was on the border of the two and three wave rotating modes for this operating condition.

Figure 114 shows the modes observed in Test 10. Test 10 experienced two rotating wave operation for the first $\approx 0.1s$, after which it transitioned to a one wave rotating mode for the remainder of the test. Previous testing by Huff [41] was not conducted at a $\dot{m}''$ this low, but suggests one wave operation would be expected based on the equivalence ratio and general trend of low $\dot{m}''$ and high ϕ producing one wave operation (Ref. Figure 73).

Figure 115 shows the modes observed in Test 11. Test 11 experienced a one wave rotating detonation mode for the first $\approx 0.05s$ of the test, after which it degenerated into a two wave clapping mode for the remainder of the test. Previous testing by Huff
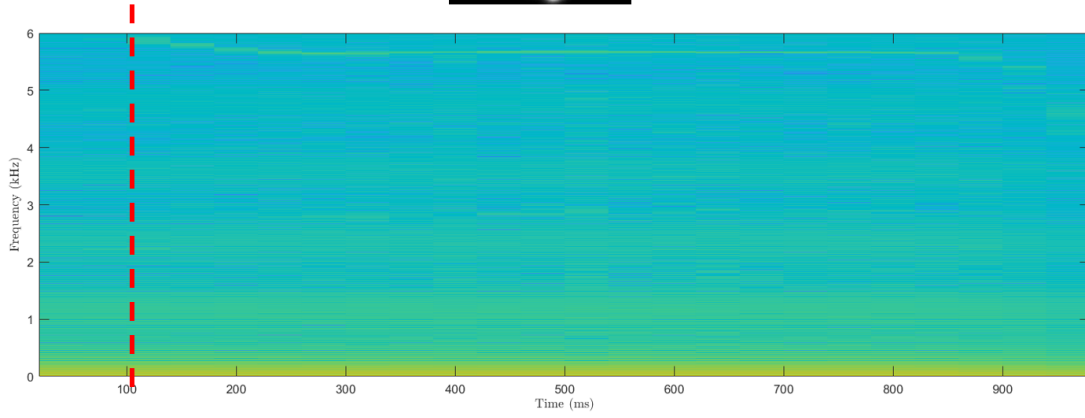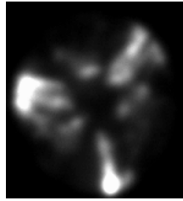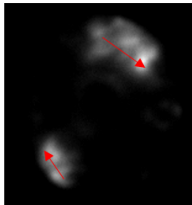
188

Three Node

Figure 113. Test 6 Mode Persistence

Two Wave
Rotating

One Wave
Rotating
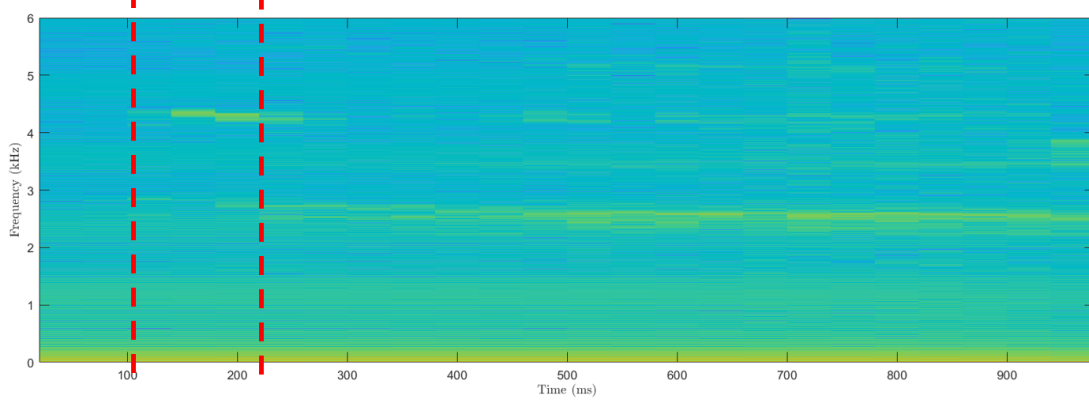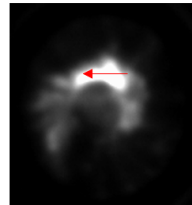
Figure 114. Test 10 Mode Persistence
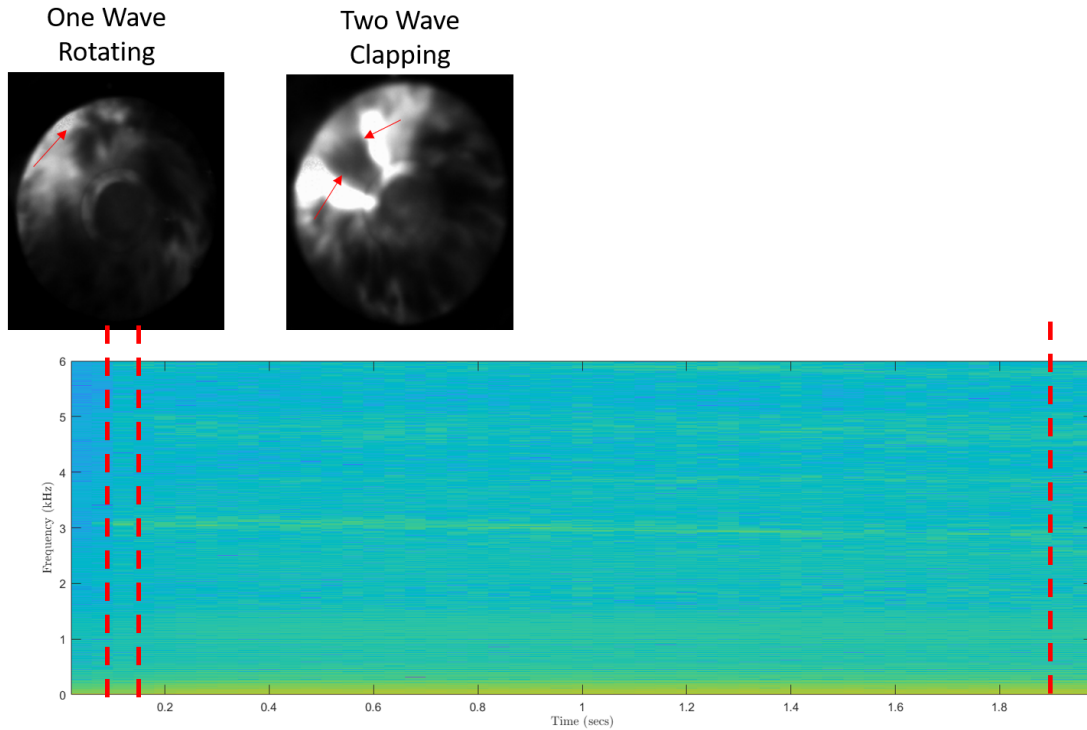
Figure 115. Test 11 Mode Persistence

[41] showed only two wave operation at this operating condition.

Figure 116 shows the modes observed in Test 12. Test 12 experienced a two wave rotating mode for the first $\approx 0.05s$, followed by a transition to a four wave, two node clapping mode for $\approx 0.2s$, and the transitioned back to a two wave rotating mode for the remainder of the run. Previous testing by Huff [41] showed only two wave operation at this operating condition. This test is exceptional for three reasons. First, it is the only test which ended in a two wave mode. Second, the two wave mode following transition appeared to have smaller secondary detonations running counter to the primary DW. These are not easily visible in individual photographs, but are more readily apparent in the video footage. Third, this is the only test which experienced the four counter-rotating wave mode, which formed two nodes as shown as the waves intersected. Eventually one pair of waves became stronger than their counter-propagating counterparts, and the clapping mode transitioned to a primarily

190
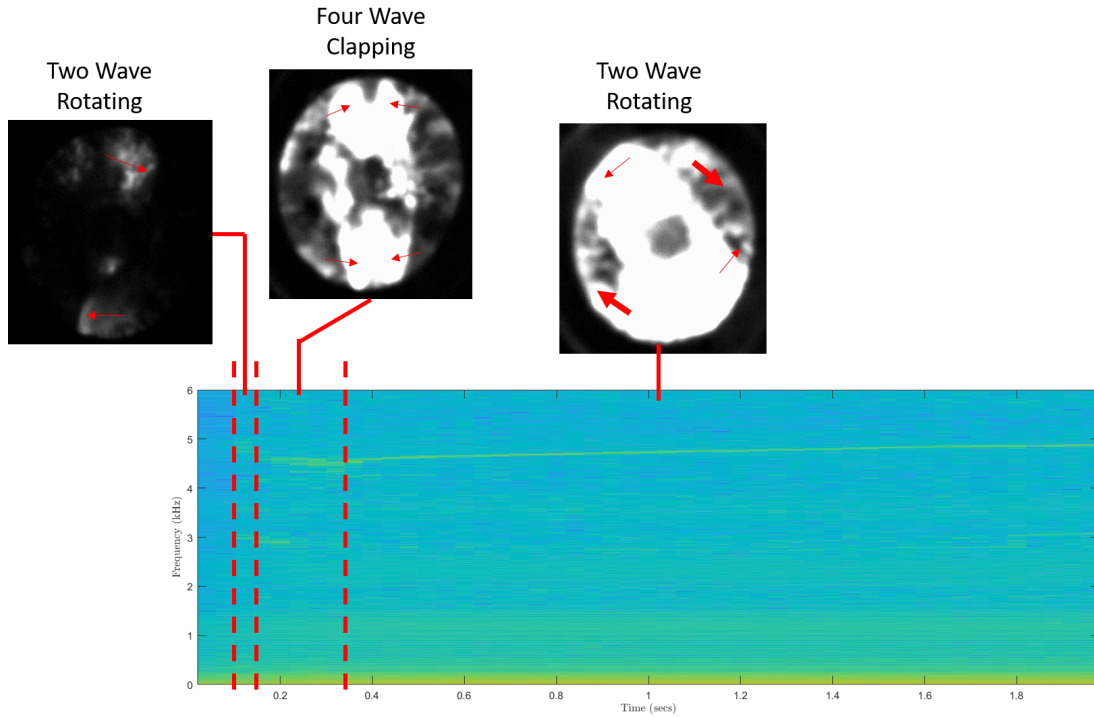
Figure 116. Test 12 Mode Persistence

rotating mode. Whereas previous two wave clapping modes, which formed one node upon intersection, occurred between one one wave rotating modes, this four wave, two node operation occurred in between nominal two wave operation. This suggests that the three node mode observed in Tests 5 and 6 may in fact be related to the three wave rotating mode, but that Tests 5 and 6 were unable to successfully transition to a three wave rotating mode for some reason.

Figure 117 shows the modes observed in Test 13. Test 13 initiated with a with a steady two wave rotating mode, which became progressively more unsteady, with the angle between detonation waves oscillating, before transition after $\approx 0.9s$ of operation. Previous testing by Huff [41] showed only two wave operation at this operating condition. In this unsteady operation, one wave would nearly catch up with the one in front of it before running into a the low detonability region following the former, then decreased in speed. The remainder of the test experienced a fluctuations

191
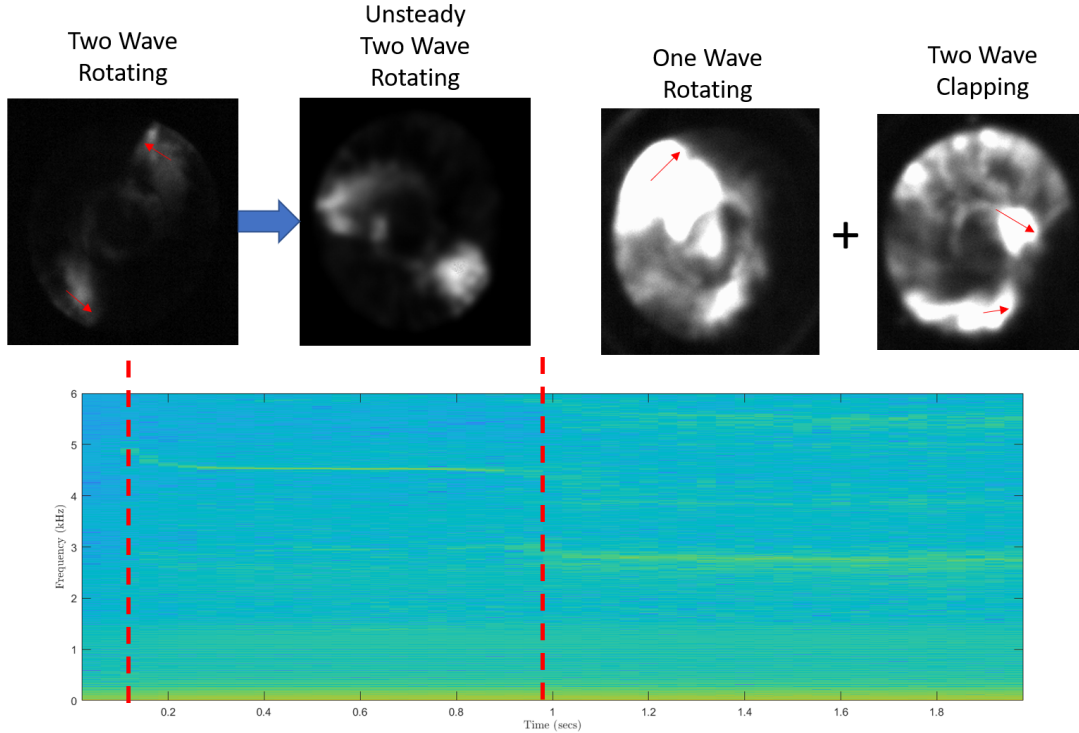
Figure 117. Test 13 Mode Persistence

between one wave rotating and two wave clapping modes.

Figure 118 shows the modes observed in Test 14. Test 14 initiated with a two wave rotating detonation mode which persisted for $\approx 0.4s$ before degenerating into transient modes for the remainder of the run, which could consist of a mixture of one wave, two wave clapping, two wave rotating, and other undefined modes for brief periods, $\mathcal{O}1cycle$. Previous testing by Huff [41] showed only two wave operation at this operating condition.

Figure 119 shows the modes observed in Test 15. Test 15 initiated with a two wave rotating detonation mode which persisted for $\approx 0.35s$ before degenerating into a combination of two wave rotating and transient modes for the remainder of the run. The two wave modes following transition could last several dozen cycles, and the transient mode operation was similar to that observed in Test 14. Previous testing by Huff [41] showed only two wave operation at this operating condition.

192
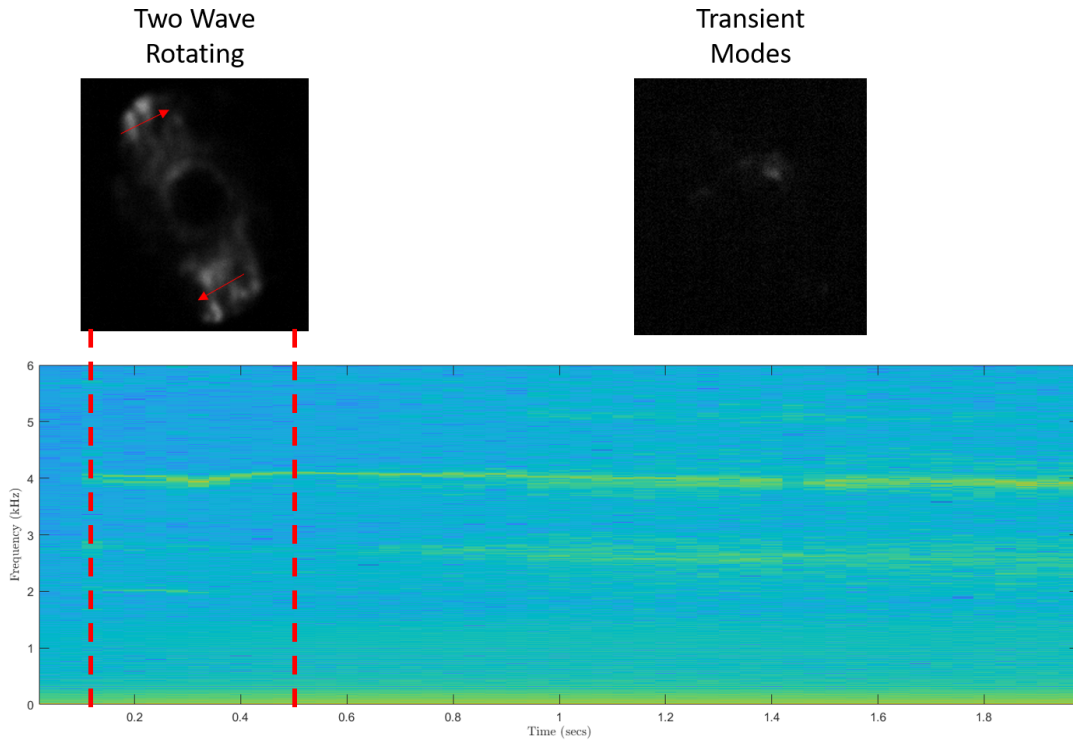
Figure 118. Test 14 Mode Persistence

Figure 119. Test 15 Mode Persistence

193

Figure 120. Test 16 Mode Persistence

Figure 120 shows the modes observed in Test 16. Test 16 initiated with a two wave rotating detonation mode which persisted for $\approx 1.2s$ before degenerating into transient modes for the remainder of the test. Previous testing by Huff [41] showed only two wave operation at this operating condition.

Figure 121 shows the modes observed in Test 17. Test 17 initiated with a two wave rotating detonation mode which persisted for $\approx 0.2s$ before degenerating into transient modes for the remainder of the test. Previous testing by Huff [41] showed only two wave operation at this operating condition.
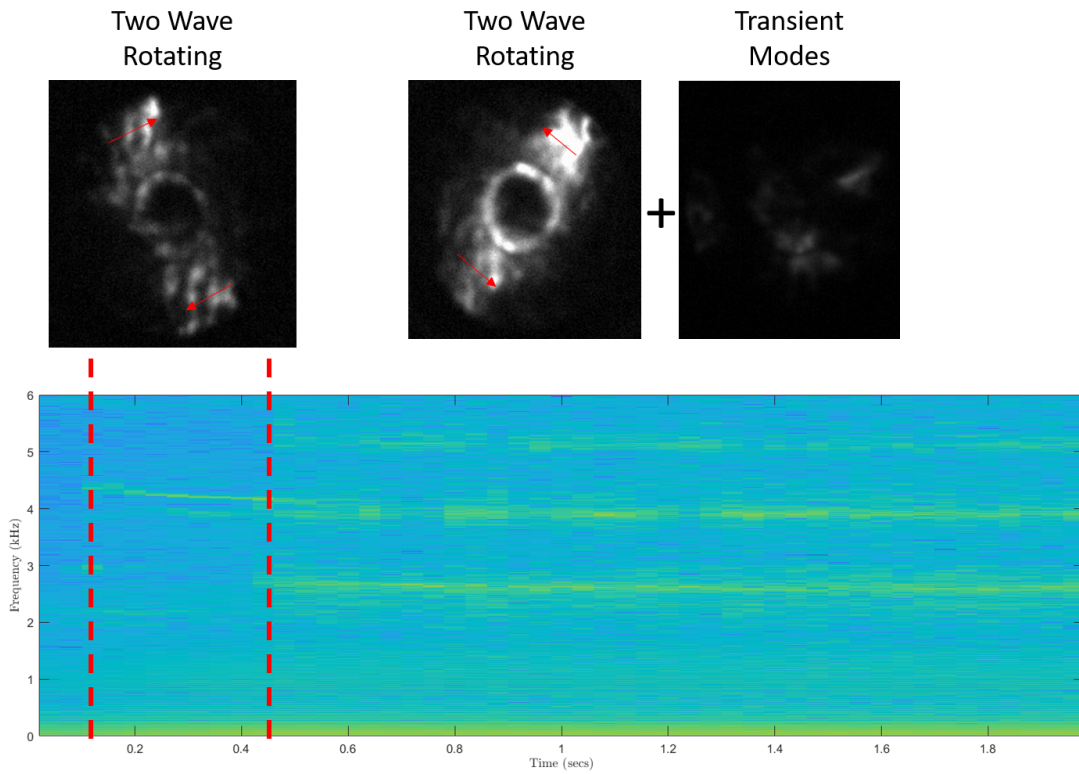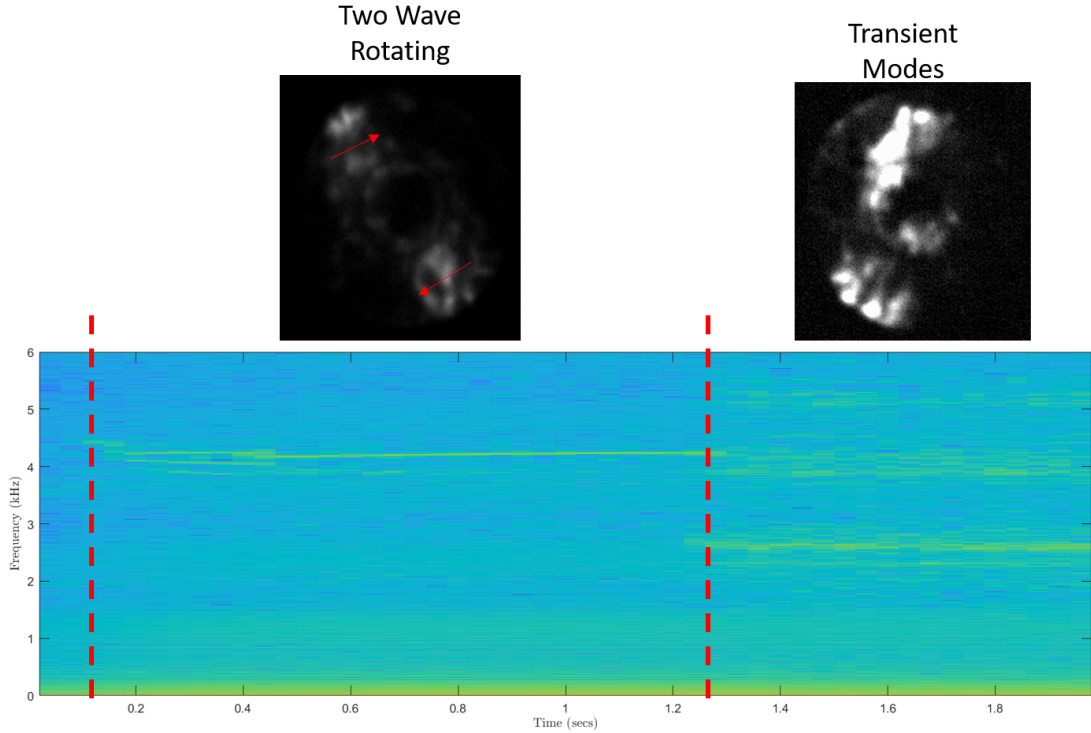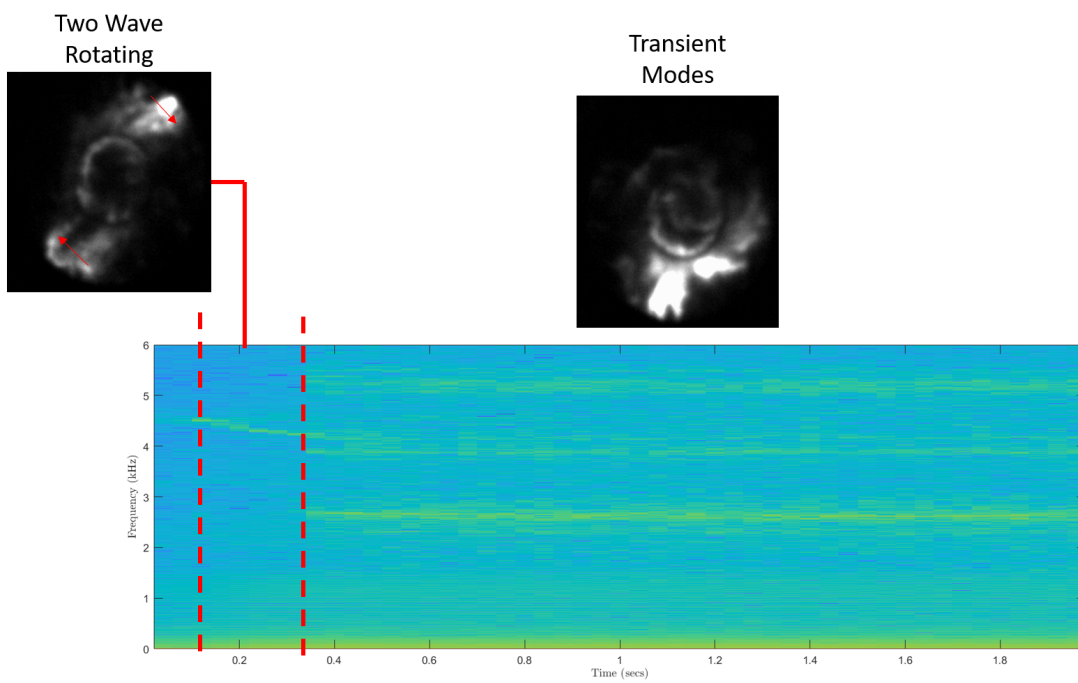
Figure 121. Test 17 Mode Persistence

Appendix B. Theoretical Detonation Velocity

This section gives an overview of the theoretical response of the detonation wave velocity $v_{D,CJ}$ to initial pressure, temperature, and equivalence ratio as calculated with NASA CEA and the CalTech Shock and Detonation (SD) Toolbox as a means to study the sensitivity of the DW speed to these parameters. The observed wave speeds from the present work fell below the CJ wavespeed. Based on observation of the high speed video, it was believed that mixing of the product gases with the reactant mixture may have occurred, which may have in turn reduced the wave speed. To simulate the effect of products from previous cycles recirculating back into the reactant mixture within an RDE, the effect of reintroducing products into the reactant mixture was also explored with the SD Toolbox.

To gain insight into the expected behavior of the RRDE, as well as its sensitivity to initial the reactant mixture, a theoretical examination of Detonation Wave (DW) characteristics was conducted using NASA's Chemical Equilibrium with Applications on-line program, CEARUN, using its detonation solver. H_2 was selected as the fuel, with air selected as the oxidizer; no trace species were added. The input parameters were varied over the ranges $0.1 \leq \phi \leq 2$, $300K \leq T_1 \leq 1400K$, and $1Bar \leq P_1 \leq 12Bar$. Ideal Chapman–Jouguet (CJ) performance was examined for $v_{D,CJ}$, as this parameter was selected as a figure of merit for RRDE performance. Specifically, the achieved detonation velocity normalized by the ideal detonation velocity, $\left(\frac{v_D}{v_{D,CJ}}\right)$, is frequently reported in literature. Additionally, the speed of sound in the products $a_{2,CJ}$ was examined. For most observed detonations in RRDEs, $v_D < v_{D,CJ}$, and therefore $\frac{v_D}{v_{D,CJ}} < 1$. As a check, it is also desired that $v_D > a_{2,CJ}$, or equivalently $\frac{v_D}{v_{D,CJ}} > \frac{a_{2,CJ}}{v_{D,CJ}}$, as a DW that propagates faster than $a_{2,CJ}$ can be confirmed to be a detonation, as opposed to high-speed deflagration.

To determine which parameters are most important to detonation velocity, ex-

amining the variation of the the detonation velocity as a function of the variables of interest was performed. $v_{D,CJ}$ and $a_{2,CJ}$ have a strong functional dependency on ϕ at ambient conditions as shown in Figure 122(a). However, the normalized quantity $\left(\frac{a_2}{v_D}\right)_{CJ}$ shows a weak dependence under these conditions as shown in Figure 122(b). Figures 122(c) and (d) show that the initial pressure has little effect on either $v_{D,CJ}$ or $\left(\frac{a_2}{v_D}\right)_{CJ}$. Figure 122(e) shows that both $v_{D,CJ}$ and $a_{2,CJ}$ have a dependence on initial mixture temperature, with $v_{D,CJ}$ tending to decrease with increasing T_1 and $a_{2,CJ}$ tending to increase with T_1. Figure 122(f) shows the normalized quantity $\left(\frac{a_2}{v_D}\right)_{CJ}$ increased with T_1.

$v_{D,CJ}$ and $a_{2,CJ}$ are most sensitive to changes in ϕ. The global ϕ of reactants entering the RRDE is well controlled as discussed in Chapter III, and thus variations in ϕ can be easily accounted for in calculations. However, due to potential mixing of reactants with products prior to arrival of the DW, and potential secondary burning, the actual or effective ϕ of the reactant mixture is unknown. Due to the sensitivity of $v_{D,CJ}$ to the value of ϕ, this has the potential to have a large impact on the observed v_D as compared to the $v_{D,CJ}$ value computed with the global ϕ or reactants entering the detonation channel. CEARUN computes detonation parameters from a simplified 1-D type analysis with ideal reactants that are not mixed with products to any degree, which deviates from the actual behavior within an RDE detonation channel. Because the effective ϕ will be lower than the ideal ϕ with such mixing and secondary burning, the observed v_D is likely to be lower than the value of $v_{D,CJ}$ calculated with the ideal ϕ.

The pressure of the reactant mixture is expected to be above ambient, but as these theoretical calculations show, initial pressure has little impact on the quantities of interest. Due to their storage, the reactants are expected to have a total temperature near the ambient temperature, although heat transfer and mixing as described
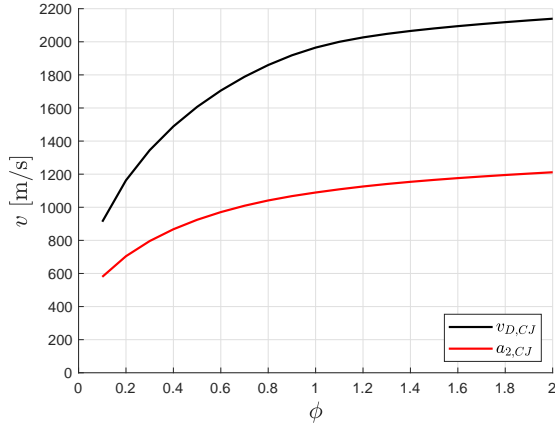
(a) $P_1 = 1.0132 Bar$, $T_1 = 300K$
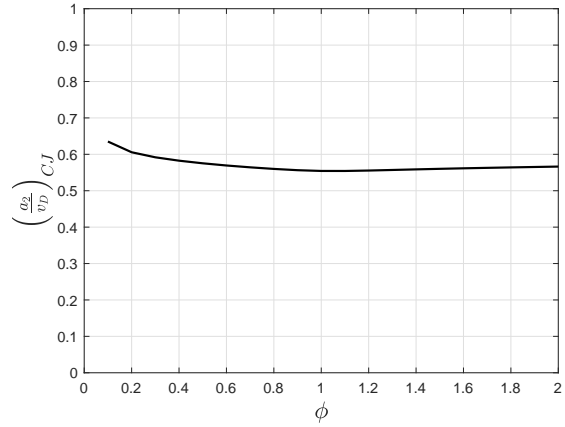
(b) $P_1 = 1.0132 Bar$, $T_1 = 300K$
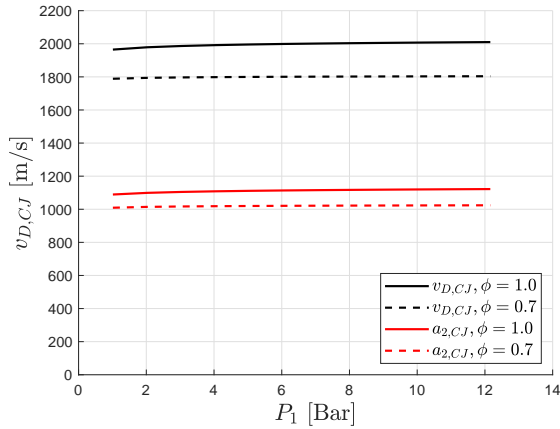
(c) $T_1 = 300K$
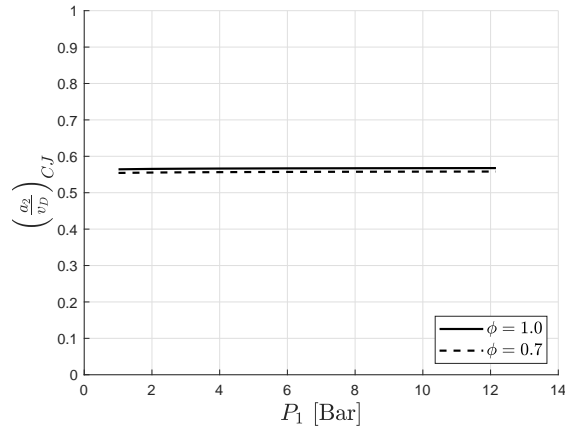
(d) $T_1 = 300K$
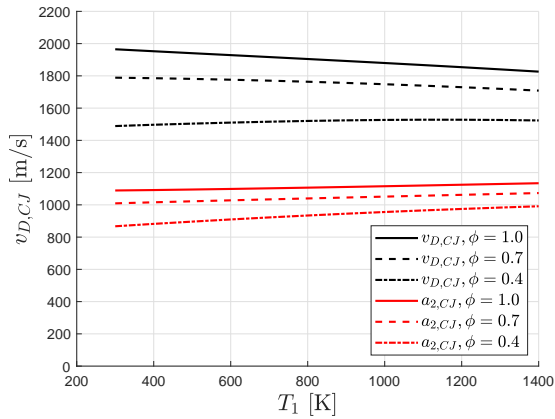
(e) $P_1 = 1.0132 Bar$
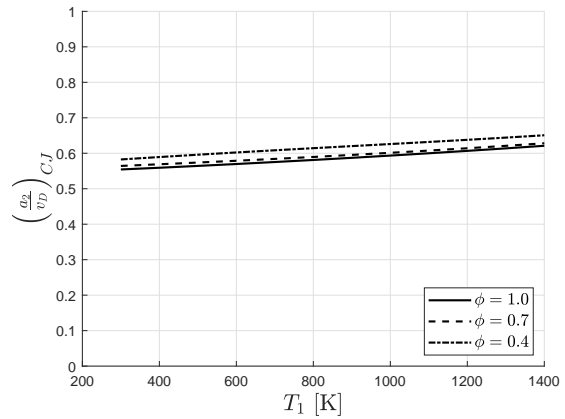
(f) $P_1 = 1.0132 Bar$

Figure 122. Left: Theoretical $v_{D,CJ}$ and $a_{2,CJ}$ from NASA CEARUN [9, 10]. Right: $\left(\frac{a_2}{v_D}\right)_{CJ}$ derived from curves on the Left.

198

previously may increase the reactant temperature. The degree to which the reactant temperatures vary from the ambient temperature is dependent upon a number of factors, such as flow behavior within the RRDE and thus a specific temperature at which the reactants attain before being consumed is difficult to determine. However, 122(e) shows that $v_{D,CJ}$ is expected to decrease and $a_{2,CJ}$ is expected to increase as the initial reactant temperature increases, and the observed behavior is expected to show similar trends. Therefore, heating of the reactants as they enter the RRDE will decrease $v_{D,CJ}$. However, heating nominally $300K$ reactants by $1000K$ was projected to decrease $v_{D,CJ}$ by less than 10% for $\phi = 1$, the most sensitive case considered. While the degree of pre-DW reactant heating is currently unknown, it is assumed that conductive or radiative heat transfer within the gaseous reactant mixture does not increase the temperature by more than this much in the short time before the next DW arrives.

Further theoretical performance was conducted using the 17 September 2018 release of the California Institute of Technology Shock and Detonation (SD) Toolbox in MATLAB 2018b [95]. This toolbox interfaced with Cantera-2.4.0-64x and Cantera-Python-2.4.0-x64-py3.7 [96], which in turn operated from Python-3.7.1-amd64. For use with detonations, the SD toolbox offers many of the same capabilities as NASA's CEARUN, but with a MATLAB script interface, allowing greater automation beneficial to examination of a large test matrix.

Figure 123(a) shows the change in v_D as a function of both P_1 and T_1 at $\phi = 1.0$. Over this range, v_D shows a dependency on T_1 for the entire range, but P_1 has a relatively minor impact on v_D for $P_1 > 1Bar$. The total variation in v_D from $1-15Bar$ was less than 7% for $T_1 = 1800K$, the most sensitive case considered, with less than 3% variation for $T_1 = 300K$, the least sensitive case. Having demonstrated the lack of sensitivity to P_1, its value was held constant at $P_1 = 1Bar$ for the remainder of
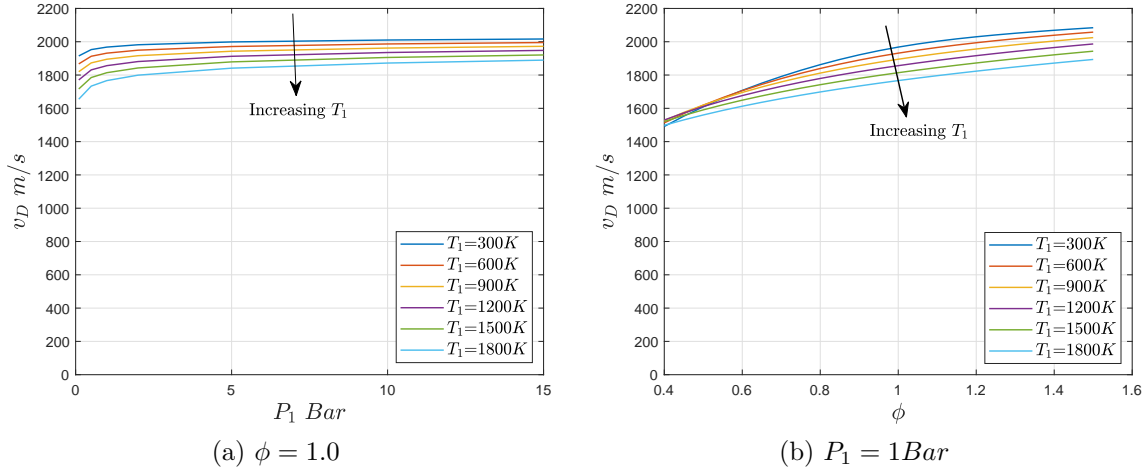
Figure 123. Theoretical v_D in an H_2-Air mixture from CalTech's Shock and Detonation Toolbox 2018 (MATLAB) in Cantera 2.4.0x64 for Python 3.7.1x64 [95, 96]. Equilibrium solution utilized.

this study.

Figure 123(b) shows the change in v_D as a function of both ϕ and T_1 at $P_1 = 1[Bar]$. These trends show that T_1 impacted v_D, but that this effect was reduced away from $\phi \approx 1.2$. Over the range of $T_1 = 300 - 1800K$, at $\phi = 1.2$ the change in temperature affected v_D by $\approx 10\%$.

v_D tended to increase as ϕ increased. Over the range of parameters of interest, v_D was most sensitive to ϕ, varying by $\approx 20-30\%$ over the range considered, followed by T_1 at $\approx 10\%$, and least by P_1 at $< 7\%$. These trends are similar to the findings with NASA CEARUN found previously. However, the SD Toolbox allowed for automated data collection over a larger test matrix, allowing a more thorough examination.

While previous analyses have shown the dependency of the detonation on the global parameters of the reactants being supplied assuming a 1-D CJ DW, the reality of the flow within the device is considerably more complicated. The reactants in an RRDE are in constant motion, and the possibility for mixing of the reactants with products from previous DWs exists. To quantify the effect of re-ingesting products into the reactant mixture, a modified script was used. This script initiated a detona-

tion with the global reactant mixture with molar fractions Y_1 based on T_1, P_1, and ϕ, which produced products with an equilibrium composition giving molar fractions Y_2. These products were then mixed with reactants such that $Y = (n-1)Y_1 + nY_2$, where n is the fraction of the new reactant mixture that is comprised of products from the previous detonation. This new reactant mixture was then supplied as the reactant mixture for the next detonation. This process was then repeated ten times, with the value of v_D and the chemical composition of the products observed to reach a steady value in this interval. It is important to note that these detonation velocities **are** Chapman-Jouguet velocities for the mixtures they were calculated with, which simply happen to be different mixtures than the reactant mixtures globally entering the reactor.
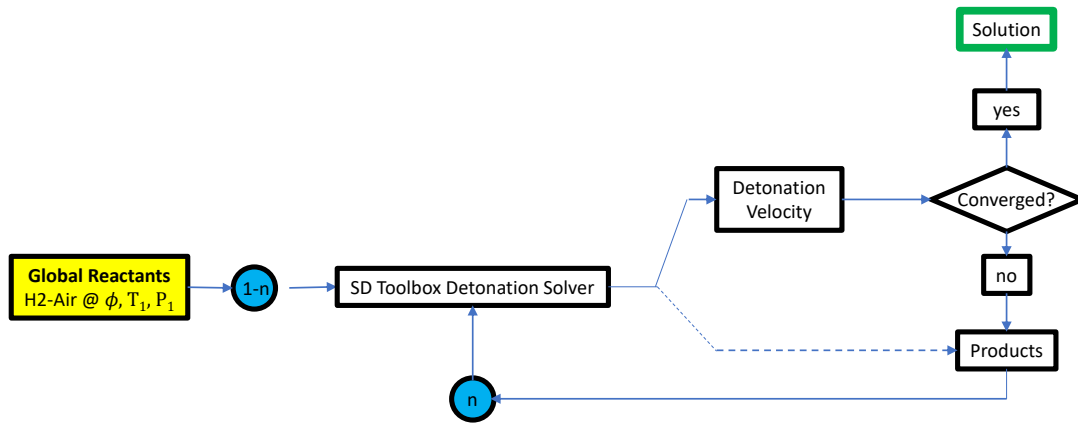
Figure 124. Diagram of solution method.

The effects of introducing products into the reactant mixture are shown in Figure 125(a). The values of P_1 and T_1 were held constant at $P_1 = 1Bar$ and $T_1 = 500K$. The value of ϕ corresponds to the ϕ of the global reactant mixture as opposed to the local ϕ experienced by the DW, which is different based on the excess fuel or oxidizer left over from the previous detonation. Introducing reactants into the products proved capable of being the dominant variable affecting wave speed, depending on the value of n. For instance, at $\phi = 1$ a reactant mixture composed of half global reactants and

half products ($n = 0.5$) resulted in a $v_D = 1562 \ m/s$, whereas a pure global reactant mixture ($n = 0.0$) resulted in a $v_D \approx 1943 \ m/s$.

(a) $P_4 = 1Bar, \ T_1 = 500K$ (b) $P_4 = 1Bar, \ T_1 = 500K$
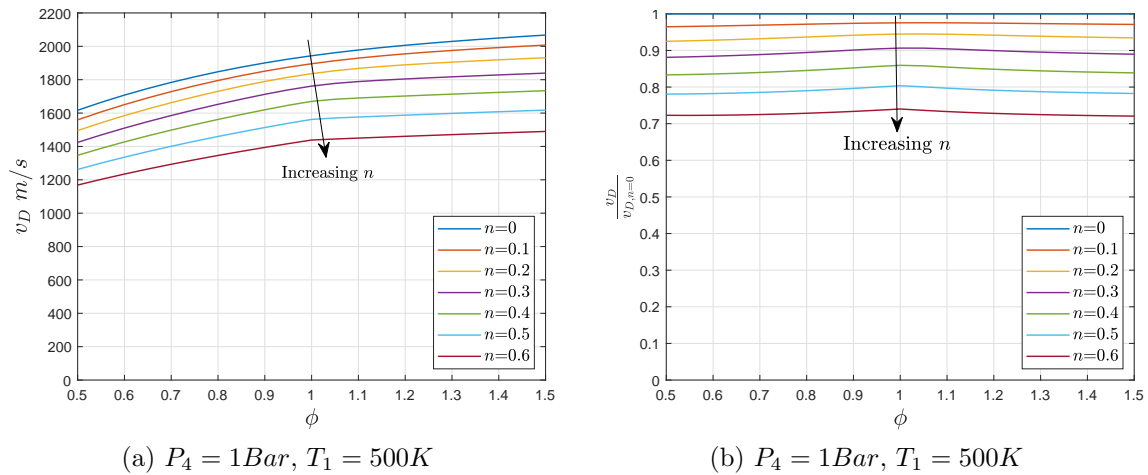
Figure 125. Theoretical v_D in an $H_2 - Air$ mixture with re-ingested products from CalTech's Shock and Detonation Toolbox 2018 (MATLAB) in Cantera 2.4.0x64 for Python 3.7.1x64 [95, 96]. Equilibrium solution utilized.

When v_D is normalized by the detonation velocity of the pure global reactant mixture ($v_{D,n=0}$) as a function of ϕ as shown in Figure 125(b), the reduction in $\frac{v_D}{v_{D,n=0}}$ is almost entirely dependent on n, with little variance across the range of ϕ of interest. This parameter is of particular interest, as it is common to report experimental detonation velocities normalized by their Chapman-Jouguet velocities, which are calculated based on the global reactants flowing into the test article. In general, the degradation of $\frac{v_D}{v_{D,n=0}}$ becomes more pronounced as n increases. Whereas $n = 0.1$ produces a deviation of $\approx 3\%$, a half and half mixture with $n = 0.5$ results in a deviation of $\approx 21\%$ of the v_D typically calculated simply based on the global reactants.

While this analysis shows the effects of varying n for any generic detonation, application to any given device requires estimation for the value of n, which will likely be specific to the device in question. Furthermore, without higher fidelity flow modeling there are currently no procedures to estimate the value of n.

Additionally, modeling the initial temperature as $500K$ for all mixtures is a first-order accurate assumption; given a better model for the state of the post-expansion products, which will depend on the geometry and flow field in question, the mass-averaged temperatures and heat capacities of the incoming reactants and the re-ingested products could be used to provide a better approximation of the effective mixture temperature.

Bibliography

1. Wintenberger, E. and Shepherd, J. E., "Thermodynamic Cycle Analysis for Propagating Detonations," *Journal of Propulsion and Power*, Vol. 22, No. 3, May 2006, pp. 694–697.

2. Nakagami, S., Matsuoka, K., Kasahara, J., Kumazawa, Y., Fujii, J., Matsuo, A., and Funaki, I., "Experimental Visualization of the Structure of Rotating Detonation Waves in a Disk-Shaped Combustor," *Journal of Propulsion and Power*, Vol. 33, No. 1, 2017, pp. 80–88.

3. Lu, F. K. and Braun, E. M., "Rotating Detonation Wave Propulsion: Experimental Challenges, Modeling, and Engine Concepts," *Journal of Propulsion and Power*, Vol. 30, No. 5, Jul 2014, pp. 1125–1142.

4. AFRL/RD, "Laser Weapons Systems (OPS-15-1038)," 2015.

5. DefenseTech, "Air Force Wants a Laser Weapon on AC-130J Gunship," 2015.

6. "Combined Heat and Power Technology Fact Sheets Series: Gas Turbines (DOE/EE-1330)," U.S. Department of Energy, 2016.

7. Turns, S. R., *An Introduction to Combustion : Concepts and Applications.*, McGraw-Hill series in mechanical engineering, Boston : WCB/McGraw-Hill, c2000., 3rd ed., 2012.

8. Vincenti, W. G. and Kruger, C. H., *Introduction to Physical Gas Dynamics*, Malabar, Florida : Krieger, 2002, c1965., 2002.

9. Gordon, S. and Mcbride, B. J., "NASA RP-1311 Computer Program for Calculation of Complex Chemical Equilibrium Compositions and Applications Part 1: Analysis," Tech. rep., NASA, Cleveland, Ohio, 1994.

10. McBride, B. J. and Gordon, S., "NASA RP-1311 Computer Program for Calculation of Complex Chemical Equilibrium Compositions and Applications Part 2: Users Manual and Program Description," Tech. rep., NASA, Cleveland, Ohio, 1996.

11. Snyder, C., "CEARUN," `https://cearun.grc.nasa.gov/`, NASA Glenn Research Center, Cleveland, OH.

12. Lee, J. H., *The Detonation Phenomenon*, Cambridge ; New York : Cambridge University Press, 2008., 2008.

13. Chapman, D., "On the Rate of Explosion of Gases," *Philosophical Magazine*, Vol. 47, 1899, pp. 90–103.

14. Jouguet, E., "On the Propagation of Chemical Reactions in Gases," *Journal de Mathématiques Pures et Appliquées*, Vol. 1, 1906, pp. 347–425.

15. Babbie, C. A., King, P. I., Hoke, J. L., and Schauer, F. R., "Effect of Elevated Mixture Pressure and Equivalence Ratio on Hydrogen-Air Detonation Cell Size," *54th AIAA Aerospace Sciences Meeting*, AIAA 2016-0442, San Diego, California, Jan 2016.

16. Stamps, D., Benedick, W., and Tieszen, S., "Hydrogen-Air-Diluent Detonation Study for Nuclear Reactor Safety Analyses," Tech. rep., Sandia National Laboratories, Albuquerque, NM, 1991.

17. Lee, J. H., "Dynamic Parameters of Gaseous Detonations," *Annual Review of Fluid Mechanics*, Vol. 16, 1984, pp. 311–336.

18. Vasil'ev, A. A., "Geometric Limits of Gas Detonation Propagation," *Combustion, Explosion and Shock Waves*, Vol. 18, No. 2, 1982, pp. 245–249.

19. Radulescu, M. I. and Lee, J. H., "On the Hydrodynamic Thickness of Cellular Detonations," *Combustion, Explosion, and Shock Waves*, Vol. 41, No. 6, 2005, pp. 745–765.

20. Maxwell, B. M. N., Bhattacharjee, R. R., Lau-Chapdelaine, S. S., Falle, S. A., Sharpe, G. J., and Radulescu, M. I., "Influence of Turbulent Fluctuations on Detonation Propagation," *Journal of Fluid Mechanics*, Vol. 818, 2017, pp. 646–696.

21. Radulescu, M. I., Sharpe, G. J., Law, C. K., and Lee, J. H., "The Hydrodynamic Structure of Unstable Cellular Detonations," *Journal of Fluid Mechanics*, Vol. 580, 2007, pp. 31–81.

22. Strehlow, R. A. and Crooker, A. J., "The Structure of Marginal Detonation Waves," *Acta Astronautica*, Vol. 1, No. 3, 1974, pp. 303–315.

23. Babbie, C. A., King, P. I., Stevens, C. A., Hoke, J. L., and Schauer, F. R., "Experimental Measurement of Hydrogen-Air Detonation Cell Size at Elevated Initial Pressures," *53rd AIAA Aerospace Sciences Meeting*, AIAA 2015-0634, Kissimmee, Florida, Jan 2015.

24. Knysttautas, R., Guirao, C., Lee, J. H., and Sulmistras, A., "Measurements of Cell Size in Hydrocarbon-Air Mixtures and Predictions of Critical Tube Diameter, Critical Initiation Energy, and Detonability Limits," *Dynamics of Shock Waves, Explosions, and Detonations*, edited by R. Soloukhin, A. Oppenheim, N. Manson, and J. Bowen, Progress in Astronautics and Aeronautics, American Institute of Aeronautics and Astronautics, Jan 1985, pp. 23–37.

25. Edwards, B. D., "Maintained Detonation Waves in an Annular Channel: A Hypothesis Which Provides the Link Between Classical Acoustic Combustion Instability and Detonation Waves," *Symposium (International) on Combustion*, Vol. 16, Jan 1977, pp. 1611–1618.

26. Ciccarelli, G., Ginsberg, T., Boccio, J., Economos, C., Sato, K., and Kinoshita, M., "Detonation Cell Size Measurements and Predictions in Hydrogen-Air-Steam Mixtures at Elevated Temperatures," *Combustion and Flame*, Vol. 99, No. 2, 1994, pp. 212–220.

27. Thomas, L., Schauer, F., Hoke, J., and Naples, A., "Buildup and Operation of a Rotating Detonation Engine," *49th AIAA Aerospace Sciences Meeting including the New Horizons Forum and Aerospace Exposition*, AIAA 2011-0602, Jan 2011.

28. Rankin, B. A., Fotia, M. L., Naples, A. G., Stevens, C. A., Hoke, J. L., Kaemming, T. A., Theuerkauf, S. W., and Schauer, F. R., "Overview of Performance, Application, and Analysis of Rotating Detonation Engine Technologies," *Journal of Propulsion and Power*, Vol. 33, No. 1, 2017, pp. 131–143.

29. Zhou, R., Wu, D., and Wang, J., "Review Article: Progress of Continuously Rotating Detonation Engines," *Chinese Journal of Aeronautics*, Vol. 29, Feb 2016, pp. 15–29.

30. Mattingly, J. D., Boyer, K. M., and von Ohain, H., *Elements of Propulsion: Gas Turbines and Rockets.*, AIAA education series, Reston, VA : American Institute of Aeronautics and Astronautics, Inc., [2016], 2nd ed., 2016.

31. Bohan, B. T. and Polanka, M. D., "Analysis of Flow Migration in an Ultra-Compact Combustor," *Journal of Engineering for Gas Turbines and Power*, Vol. 135, No. 5, Apr 2013, pp. 51502–51511.

32. Barr, L., "Pulsed Detonation Engine Flies Into History," Tech. rep., 88th Air Base Wing Public Affairs, 2008.

33. Rouser, K. P., King, P. I., Schauer, F. R., Sondergaard, R., and Hoke, J. L., "Unsteady Performance of a Turbine Driven by a Pulse Detonation Engine," *48th AIAA Aerospace Sciences Meeting Including the New Horizons Forum and Aerospace Exposition*, Aerospace Sciences Meetings, AIAA 2010-1116, Orlando, Florida, Jan 2010.

34. Huff, R., Polanka, M. D., McClearn, M. J., Schauer, F. R., Fotia, M. L., and Hoke, J. L., "A Disk Rotating Detonation Engine Part 1: Design and Buildup," *2018 AIAA Aerospace Sciences Meeting*, AIAA 2018-0633, Kissimmee, Florida, Jan 2018.

35. McClearn, M. J., Schauer, F. R., Huff, R., Polanka, M. D., Hoke, J. L., and Fotia, M. L., "A Disk Rotating Detonation Engine Part 2: Operation," *2018*

AIAA Aerospace Sciences Meeting, AIAA 2018-1607, Kissimmee, Florida, Jan 2018.

36. Naples, A. G., Hoke, J. L., Battelle, R., Wagner, M., and Schauer, F. R., "Rotating Detonation Engine Implementation into an Open-Loop T63 Gas Turbine Engine," *55th AIAA Aerospace Sciences Meeting*, AIAA 2017-1747, Grapevine, Texas, Jan 2017.

37. Bykovskii, F., Vasil'ev, A., Vedernikov, E., and Mitrofanov, V., "Explosive Combustion of a Gas Mixture in Radial Annular Chambers," *Combustion, Explosion, and Shock Waves*, Vol. 30, No. 4, 1994, pp. 510–516.

38. Bykovskii, F., Mitrofanov, V., and Vedernikov, E., "Continuous Detonation Combustion of Fuel-Air Mixtures," *Combustion, Explosion, and Shock Waves*, Vol. 33, No. 3, 1997, pp. 344–353.

39. Bykovskii, F., Zhdan, S., Vedernikov, E., Samsonov, A., and Zintsova, A., "Detonation Combustion of a Hydrogen-Oxygen Mixture in a Plane-Radial Combustor with Exhaustion Toward the Center." *Combustion, Explosion, and Shock Waves*, Vol. 52, No. 4, Jul 2016, pp. 446–456.

40. Nakagami, S., Matsuoka, K., Kasahara, J., Matsuo, A., and Funaki, I., "Visualization of Rotating Detonation Waves in a Plane Combustor with a Cylindrical Wall Injector," *53rd AIAA Aerospace Sciences Meeting*, AIAA 2015-0878, Kissimmee, Florida, Jan 2015.

41. Huff, R., *Design, Buildup, and Testing of a Radial Rotating Detonation Engine for a Compact Auxiliary Power Unit*, Master's thesis, Air Force Institute of Technology, 2018.

42. Huff, R., Schauer, F., Boller, S. A., Polanka, M. D., Fotia, M., and Hoke, J., "Exit Condition Measurements of a Radial Rotating Detonation Engine Bleed Air Turbine," AIAA SciTech Forum, AIAA 2019-1011, Jan 2019.

43. Boller, S. A., Polanka, M. D., Huff, R., Schauer, F., Fotia, M., and Hoke, J., "Experimental Flow Visualization in a Radial Rotating Detonation Engine," *AIAA Scitech 2019 Forum*, AIAA SciTech Forum, AIAA 2019-1253, Jan 2019.

44. Huff, R., Polanka, M. D., McClearn, M. J., Schauer, F., Fotia, M. L., and Hoke, J., "A Disk Rotating Detonation Engine Driven Auxiliary Power Unit," *2018 Joint Propulsion Conference*, AIAA 2018-4879, Jul 2018.

45. Higashi, J., Ishiyama, C., Nakagami, S., Matsuoka, K., Kasahara, J., Matsuo, A., Funaki, I., and Moriai, H., "Experimental Study of Disk-Shaped Rotating Detonation Turbine Engine," *55th AIAA Aerospace Sciences Meeting*, AIAA 2017-1286, Grapevine, Texas, Jan 2017.

46. Schwer, D. and Kailasanath, K., "Numerical Investigation of Rotating Detonation Engines," *46th AIAA/ASME/SAE/ASEE Joint Propulsion Conference & Exhibit*, AIAA 2010-6880, Jul 2010.

47. Sichel, M. and Foster, J., "The Ground Impulse Generated by a Plane Fuel-Air Explosion with Side Relief," *Acta Astronautica*, Vol. 6, No. 3, 1979, pp. 243–256.

48. Yu, K. H., Burr, J., and Fievisohn, R. T., "Fundamental Structure of High-Speed Reacting Flows : Supersonic Combustion and Detonation, AFRL-AFOSR-VA-TR-2016-0195," Tech. rep., 2016.

49. Houim, R. W. and Fievisohn, R. T., "The Influence of Acoustic Impedance on Gaseous Layered Detonations Bounded by an Inert Gas," *Combustion and Flame*, Vol. 179, 2017, pp. 185–198.

50. Stevens, C. A., Fotia, M. L., Hoke, J. L., and Schauer, F. R., "Comparison of Transient Response of Pressure Measurement Techniques with Application to Detonation Waves," *53rd AIAA Aerospace Sciences Meeting*, AIAA SciTech Forum, AIAA 2015-1102, Kissimmee, Florida, Jan 2015.

51. White, F. M., *Viscous Fluid Flow*, McGraw-Hill Series in Mechanical Engineering, Boston, 3rd ed., 2006.

52. Naples, A. G., Hoke, J. L., and Schauer, F. R., "Quantification of Infinite Line Pressure Probe Response to Shocks and Detonation Waves," *2018 AIAA Aerospace Sciences Meeting*, AIAA 2018-1886, Kissimmee, Florida, Jan 2018.

53. Englund, D. R. and Richards, B. W., "NASA-TM-83582, The Infinite Line Pressure Probe," Tech. rep., NASA, 1984.

54. Naples, A., Knisely, A. M., Hoke, J., and Schauer, F., "Infinite Line Pressure Probe and Flush Transducer Measurements in a Rotating Detonation Engine Channel," *AIAA Scitech 2019 Forum*, AIAA SciTech Forum, AIAA 2019-2022, Jan 2019.

55. Holman, J. P., *Experimental Methods for Engineers*, McGraw-Hill series in mechanical engineering, Boston : McGraw-Hill, 2001., 7th ed., 2001.

56. Schauer, F. R., Miser, C., Tucker, K., Bradley, R., and Hoke, J. L., "Detonation Initiation of Hydrocarbon-Air Mixtures in a Pulsed Detonation Engine," *43rd AIAA Aerospace Sciences Meeting and Exhibit*, AIAA 2005-1343, Reno, Nevada, 2005.

57. Andrus, I. Q., King, P., Fotia, M., Schauer, F., and Hoke, J., "Experimental Analogue of a Pre-Mixed Rotating Detonation Engine In Plane Flow," *53rd AIAA Aerospace Sciences Meeting*, AIAA SciTech Forum, AIAA 2015-1105, Jan 2015.

58. Andrus, I. Q., King, P. I., Polanka, M. D., Schauer, F. R., and Hoke, J. L., "Design of a Premixed Fuel–Oxidizer System to Arrest Flashback in a Rotating Detonation Engine," *Journal of Propulsion and Power*, Vol. 33, No. 5, Jul 2017, pp. 1063–1073.

59. Modest, M. F., *Radiative Heat Transfer*, Academic Press, New York, 3rd ed., 2013.

60. Walsh, K. T., Long, M. B., Tanoff, M. A., and Smooke, M. D., "Experimental and Computational Study of CH, CH*, and OH* in an Axisymmetric Laminar Diffusion Flame," *Symposium (International) on Combustion*, Vol. 27, No. 1, 1998, pp. 615–623.

61. Luque, J., Jeffries, J. B., Smith, G. P., Crosley, D. R., Walsh, K. T., Long, M. B., and Smooke, M. D., "CH(A-X) and OH(A-X) Optical Emission in an Axisymmetric Laminar Diffusion Flame," *Combustion and Flame*, Vol. 122, No. 1, 2000, pp. 172–175.

62. Rankin, B. A., Richardson, D. R., Caswell, A. W., Naples, A., Hoke, J. L., and Schauer, F. R., "Imaging of OH* Chemiluminescence in an Optically Accessible Nonpremixed Rotating Detonation Engine," *53rd AIAA Aerospace Sciences Meeting*, AIAA SciTech Forum, AIAA 2015-1604, Jan 2015.

63. "IR Optical Materials," Tech. rep., ISP Optics and Lightpath Technologies, 2018.

64. "Plexiglass Sheets, Fiberglass, UHMW, Polycarbonate & Engineering Plastics," http://www.plasticgenius.com/2011/05/infrared-and-ultraviolet-transmission.html, 2011.

65. Yin, Z.-Q., Li, D.-S., Meng, J.-L., and Lou, M., "Discharge Coefficient of Small Sonic Nozzles." *Thermal Science*, Vol. 18, No. 5, Sep 2014, pp. 1505–1510.

66. Szaniszlo, A. J., "NASA-TN-D-7848 Experimental and Analytical Sonic Nozzle Discharge Coefficients for Reynolds Numbers up to 8 x 10 to the 6th Power," 1975.

67. Bergman, T. L., Lavine, A. S., Incropera, F. P., and DeWitt, D. P., *Fundamentals of Heat and Mass Transfer*, Wiley, Hoboken, NJ, 7th ed., 2011.

68. Wolański, P., "Detonative Propulsion," *Proceedings of the Combustion Institute*, Vol. 34, No. 1, 2013, pp. 125–158.

69. Hargus, W. A., Schumaker, S. A., and Paulson, E. J., "Air Force Research Laboratory Rotating Detonation Rocket Engine Development," *2018 Joint Propulsion Conference*, AIAA Propulsion and Energy Forum, AIAA 2018-4876, Jul 2018.

70. Sziroczak, D. and Smith, H., "A Review of Design Issues Specific to Hypersonic Flight Vehicles," *Progress in Aerospace Sciences*, Vol. 84, 2016, pp. 1–28.

71. Glassman, A. J., Katsanis, T., McNally, W. D., Prust, H. W., Roelke, R. J., Goldman, L. J., Rohlik, H. E., Colladay, R. S., Szanca, E. M., and Schum, H. J., "NASA-SP-290: Turbine Design and Application," Tech. rep., Lewis Research Center, Cleveland, Ohio, 1972.

72. Theuerkauf, S. W., *Heat Exchanger Design and Testing for a 6-Inch Rotating Detonation Engine*, Thesis, Air Force Institute of Technology, 2013.

73. Theuerkauf, S., King, P., Schauer, F., and Hoke, J., "Thermal Management for a Modular Rotating Detonation Engine," *51st AIAA Aerospace Sciences Meeting including the New Horizons Forum and Aerospace Exposition*, Aerospace Sciences Meetings, AIAA 2013-1176, Jan 2013.

74. Theuerkauf, S. W., Schauer, F., Anthony, R., and Hoke, J., "Average and Instantaneous Heat Release to the Walls of an RDE," *52nd Aerospace Sciences Meeting*, AIAA SciTech Forum, AIAA 2014-1503, Jan 2014.

75. Duvall, J., Chacon, F., Harvey, C., and Gamba, M., "Study of the Effects of Various Injection Geometries on the Operation of a Rotating Detonation Engine," *AIAA SciTech Forum*, AIAA 2018-0631, Kissimmee, Florida, 2018.

76. Genin, F. and Menon, S., "Dynamics of Sonic Jet Injection into Supersonic Crossflow," *Journal of Turbulence*, Vol. 11, No. 4, 2010, pp. 1–30.

77. Seiner, J. M., Dash, S. M., and Kenzakowski, D. C., "Historical Survey on Enhanced Mixing in Scramjet Engines," *Journal of Propulsion and Power*, Vol. 17, No. 6, Nov 2001, pp. 1273–1286.

78. Li, L.-Q., Huang, W., and Yan, L., "Mixing Augmentation Induced by a Vortex Generator Located Upstream of the Transverse Gaseous Jet in Supersonic Flows," *Aerospace Science and Technology*, Vol. 68, 2017, pp. 77–89.

79. Li, L.-Q., Huang, W., Yan, L., and Li, S.-B., "Parametric Effect on the Mixing of the Combination of a Hydrogen Porthole with an Air Porthole in Transverse Gaseous Injection Flow Fields," *Acta Astronautica*, Vol. 139, 2017, pp. 435–448.

80. Huang, W., Tan, J.-G., Liu, J., and Yan, L., "Mixing Augmentation Induced by the Interaction Between the Oblique Shock Wave and a Sonic Hydrogen Jet in Supersonic Flows," *Acta Astronautica*, Vol. 117, 2015, pp. 142–152.

81. VanLerberghe, W. M., Santiago, J. G., Dutton, C. J., and Lucht, R. P., "Mixing of a Sonic Transverse Jet Injected into a Supersonic Flow." *AIAA Journal*, Vol. 38, No. 3, Mar 2000, pp. 470.

82. Fujii, J., Kumazawa, Y., Matsuo, A., Nakagami, S., Matsuoka, K., and Kasahara, J., "Numerical Investigation on Detonation Velocity in Rotating Detonation Engine Chamber," *Proceedings of the Combustion Institute*, Vol. 36, No. 2, Jan 2017, pp. 2665–2672.

83. Andrus, I. Q., Polanka, M. D., King, P. I., Schauer, F. R., and Hoke, J. L., "Experimentation of Premixed Rotating Detonation Engine Using Variable Slot Feed Plenum," *Journal of Propulsion and Power*, Vol. 33, No. 6, Jul 2017, pp. 1448–1458.

84. Rodgers, C. and Johnson, D., "APU Fuel Efficiency and Affordability for Commercial Aircraft," *23rd Joint Propulsion Conference*, AIAA 1987-1907, Jun 1987.

85. Turk, M. and Zeiner, P., "Advanced Technology Payoffs for Future Rotorcraft, Commuter Aircraft, Cruise Missile, and APU Propulsion Systems," *22nd Joint Propulsion Conference*, AIAA 1986-1545, Jun 1986.

86. Rodgers, C., "Secondary Power Unit Options for Advanced Fighter Aircraft," *21st Joint Propulsion Conference*, AIAA 1985-1280, Jul 1985.

87. Marcy, R., "Gas Generator Design for a Wide Variety of APU Applications," *9th Propulsion Conference*, AIAA 1973-1169, Nov 1973.

88. McKenna, R., Hagemann, D., Loken, G., Jonakin, J., Baughman, J., and Lance, R., "An Improved APU for the Space Shuttle Orbiter," *21st Joint Propulsion Conference*, AIAA 1985-1481, Jul 1985.

89. Moffat, R. J., "Describing the Uncertainties in Experimental Results," *Experimental Thermal and Fluid Science*, Vol. 1, Jan 1988, pp. 3–17.

90. "Vision Research, Inc. Phantom 1 Megapixel v-Series Cameras Data Sheet," `https://www.phantomhighspeed.com/products/cameras/vseries/v711`, 2016.

91. "Garrett Advancing Motion Product Catalog, Vol 8," `https://www.garrettmotion.com/wp-content/uploads/2018/05/Catalog-Volume-7_Rebrand_GAM.pdf`, 2018.

92. Cho, K. Y., Codoni, J. R., Rankin, B. A., Hoke, J., and Schauer, F., "Effects of Lateral Relief of Detonation in a Thin Channel," *55th AIAA Aerospace Sciences Meeting*, AIAA SciTech Forum, AIAA 2017-0373, Jan 2017.

93. Wilson, D. G. and Korakianitis, T., *The Design of High-Efficiency Turbomachinery and Gas Turbines*, MITP, 2014.

94. Paxson, D. E. and Kaemming, T. A., "Foundational Performance Analyses of Pressure Gain Combustion Thermodynamic Benefits for Gas Turbines," *50th AIAA Aerospace Sciences Meeting including the New Horizons Forum and Aerospace Exposition*, Aerospace Sciences Meetings, AIAA 2012-0770, Nashville, Tennessee, Jan 2012.

95. Browne, S., Ziegler, J., and Shepherd, J., "Numerical Solution Methods for Shock and Detonation Jump Conditions (GALCIT Report FM2006.006 Rev. 2015)," Tech. rep., California Institute of Technology, Pasadena, CA, 2004.

96. Goodwin, D. G., Moffat, H. K., and Speth, R. L., "Cantera: An Object- Oriented Software Toolkit for Chemical Kinetics, Thermodynamics, and Transport Processes," `https://www.cantera.org`, 2018.

Vita

Captain Scott A. Boller graduated in 2013 from the University of Michigan in Ann Arbor, MI with a Bachelor of Science in Engineering degree in aerospace engineering, and was subsequently commissioned as a Second Lieutenant in the United States Air Force at AFROTC Detachment 390, University of Michigan, Ann Arbor, Michigan. He was first assigned to the Air Force Life Cycle Management Center at Warner-Robins AFB, GA in 2014 as a C-130 Structural Engineer, where he provided engineering support for field units, as well as serving as an Aircraft Battle Damage Repair (ABDR) instructor. Following a deployment to Southwest Asia as a Depot Liaison Engineer for the 386th Expeditionary Maintenance Group, in 2017 Captain Boller entered the Air Force Institute of Technology at Wright-Patterson AFB, OH in pursuit of a Masters of Science degree in aeronautical engineering, with an emphasis in air-breathing propulsion systems. Upon graduation, he will be assigned to the Air Force Research Laboratory at Wright-Patterson AFB, OH.

REPORT DOCUMENTATION PAGE

Form Approved
OMB No. 0704–0188

1. REPORT DATE *(DD–MM–YYYY)*	2. REPORT TYPE	3. DATES COVERED *(From — To)*
08-02-2019	Master's Thesis	Sept 2017 — Mar 2019

4. TITLE AND SUBTITLE

FLOW BEHAVIOR IN
RADIAL ROTATING DETONATION ENGINES

5a. CONTRACT NUMBER

5b. GRANT NUMBER

5c. PROGRAM ELEMENT NUMBER

6. AUTHOR(S)

Scott A. Boller

5d. PROJECT NUMBER

5e. TASK NUMBER

5f. WORK UNIT NUMBER

7. PERFORMING ORGANIZATION NAME(S) AND ADDRESS(ES)

Air Force Institute of Technology
Graduate School of Engineering and Management (AFIT/EN)
2950 Hobson Way
WPAFB OH 45433-7765

8. PERFORMING ORGANIZATION REPORT NUMBER

AFIT-ENY-MS-19-M-205

9. SPONSORING / MONITORING AGENCY NAME(S) AND ADDRESS(ES)

Air Force Research Lab Aerospace Directorate
Combustion Branch, Turbine Engine Division
1790 Loop Road North
WPAFB OH 45433-7765

10. SPONSOR/MONITOR'S ACRONYM(S)

AFRL/RQTC

11. SPONSOR/MONITOR'S REPORT NUMBER(S)

12. DISTRIBUTION / AVAILABILITY STATEMENT

DISTRIBUTION STATEMENT A:
APPROVED FOR PUBLIC RELEASE; DISTRIBUTION UNLIMITED.

13. SUPPLEMENTARY NOTES

14. ABSTRACT

Recent progress has been made in demonstrating Radial Rotating Detonation Engine (RRDE) technology for use in a compact Auxiliary Power Unit with a rapid response time. Investigation of RRDEs also suggests an increase in stable operating range, which is hypothesized to be due to the additional degree of freedom in the radial direction which the detonation wave can propagate. This investigation seeks to determine if the detonation wave is in fact changing its radial location. High speed photography was used to capture chemiluminescence of the detonation wave within the channel to examine its radial location, which was found to vary based on operating condition. One wave detonations tended to operate near the inner radius of the channel near the nozzle, whereas two wave detonations tended to operate near the outer radius of the channel. Normalized detonation velocity was found to increase with detonation radius, from $< 0.5 v_{D,CJ}$ near the inner radius to $0.7 v_{D,CJ}$ near the outer edge. Additionally, the power generation of the RRDE integrated with a radial inflow turbocharger was examined over a broad range of reactant mass flow rates, equivalence ratios, and compressor and turbine back pressures. The addition of a flow straightening device was shown to have no appreciable impact on performance. Compressor back pressure was found to increase performance but placed the compressor near its surge line, whereas turbine back pressure decreased performance. Repeatability was found to be within $\approx 5\%$ of the best fit line.

15. SUBJECT TERMS

Rotating Detonation Engine, Radial Rotating Detonation Engine, Disk Rotating Detonation Engine, Detonation, Combustion, Propulsion, Pressure-Gain Combustion, Flow Visualization

16. SECURITY CLASSIFICATION OF:			17. LIMITATION OF ABSTRACT	18. NUMBER OF PAGES	19a. NAME OF RESPONSIBLE PERSON
a. REPORT	b. ABSTRACT	c. THIS PAGE			Dr. Marc D. Polanka, AFIT/ENY
U	U	U	U	234	19b. TELEPHONE NUMBER *(include area code)* (937) 255-3636, x4714; marc.polanka@afit.edu

Standard Form 298 (Rev. 8–98)
Prescribed by ANSI Std. Z39.18